THE UNIVERSITY OF
WARWICK

University of Warwick institutional repository: http://go.warwick.ac.uk/wrap

A Thesis Submitted for the Degree of PhD at the University of Warwick

http://go.warwick.ac.uk/wrap/57931

This thesis is made available online and is protected by original copyright.

Please scroll down to view the document itself.

Please refer to the repository record for this item for information to help you to cite it. Our policy information is available from the repository home page.

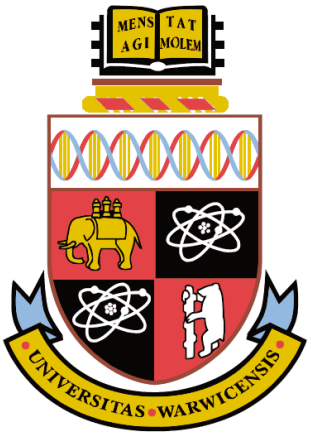

Advanced Methods in Fourier Transform Ion Cyclotron Resonance Mass Spectrometry

By

Yulin Qi

A thesis submitted in partial fulfillment of the requirements of the degree of

Doctor of Philosophy in Chemistry

University of Warwick, Department of Chemistry

April, 2013

Acknowledgements

It is my pleasure to acknowledge a number of people who supported and helped me during the whole period of my Ph.D. study at the University of Warwick. Foremost, I would like to express my deepest gratitude to my superior, Prof. Peter B. O'Connor, for giving me the opportunity to join his group and the financial support to finish my study. I greatly appreciate the encouragement of scientific method, flexibility, and independence you allowed me at different stages during my research. His patient guidance and valuable insights helped me immensely towards becoming a thorough and confident scientist. It has been an honor to be his student and great privilege to work with him.

I am sincerely grateful to Dr. Steve L. Van Orden, Dr. Christopher J. Thompson, and Dr. Joseph E. Meier for their knowledge, advice, and patience on discussing the details of FT-ICR data processing and the phase correction project I carried on. They are always available for answering my questions and reviewing my papers. Without their help, I can never go such far on the FT-ICR phase correction project. I really enjoyed and learnt so much from them.

I would like to thank Prof. Peter J. Sadler and Dr. Zhe Liu for their time and efforts on the collaboration project I worked on. Thank you for kindly sharing the novel Iridium(III) anticancer complexes, so that I can blaze a new trail in my Ph.D. research.

I am also fortunate to have such supportive and helpful working environment created by all the past and present members in O'Connor's group at Warwick, Dr. David Kilgour, Dr. Maria van Agthoven, Dr. Tzu-Yung Lin, Rebecca Wills, Andrea Lopez-Clavijo, Pilar Perez Hurtado, Juan Wei, Andrew Soulby, Samantha Benson, and Chris Wootton. In particularly, I would like to thank Dr. Mark Barrow and Dr. Huilin Li for teaching me how to use the instruments, their expertise and experience are precious for me to start my experiment at the early stage.

Very importantly, I am indebted to my father and my mother for their endless love and continuous encouragement in all these years. My special gratitude goes to my loving and patient wife, Lulin Zhang. Her company and support are very important to me.

Finally, I would like to thank the University of Warwick, the University of Warwick Department of Chemistry, and the Warwick Centre for Analytical Science (EPSRC funded EP/F034210/1) for supporting the research.

Declaration

I hereby declare that except where specific reference is made to other sources, the work contained in this thesis is the original work of the author. It has been composed by myself and has not been submitted, in whole or part, for any other degree, diploma, or other qualification.

Yulin Qi

April, 2013

The thesis has been partially/entirely reproduced from the following publications:

1. **Qi, Y.**; Thompson, C.; Van Orden, S.; O'Connor, P., Phase Correction of Fourier Transform Ion Cyclotron Resonance Mass Spectra Using MatLab. *J. Am. Soc. Mass Spectrom.* **2011,** *22* (1), 138-147. link
2. **Qi, Y.**; Barrow, M. P.; Van Orden, S. L.; Thompson, C. J.; Li, H.; Perez-Hurtado, P.; O'Connor, P. B., Variation of the Fourier Transform Mass Spectra Phase Function with Experimental Parameters. *Anal. Chem.* **2011,** *83* (22), 8477-8483. link
3. **Qi, Y.**; Barrow, M. P.; Li, H.; Meier, J. E.; Van Orden, S. L.; Thompson, C. J.; O'Connor, P. B., Absorption-Mode: The Next Generation of Fourier Transform Mass Spectra. *Anal. Chem.* **2012,** *84* (6), 2923-2929. link
4. **Qi, Y.**; Witt, M.; Jertz, R.; Baykut, G.; Barrow, M. P.; Nikolaev, E. N.; O'Connor, P. B., Absorption-Mode Spectra on the Dynamically Harmonized Fourier Transform Ion Cyclotron Resonance Cell. *Rapid Commun. Mass Spectrom.* **2012,** *26* (17), 2021-2026. link
5. **Qi, Y.**; Li, H.; Wills, R. H.; Perez-Hurtado, P.; Yu, X.; Kilgour, D. P. A.; Barrow, M. P.; Lin, C.; O'Connor, P. B., Absorption-Mode Fourier Transform Mass Spectrometry: the Effects of Apodization and Phasing on Modified Protein Spectra. *J. Am. Soc. Mass Spectrom.* **2013,** *24* (6), 828-834. link
6. **Qi, Y.**; Liu, Z.; Li, H.; Sadler, P. J.; O'Connor, P. B., Mapping the Protein-Binding Sites for Novel Iridium(III) Anticancer Complexes Using Electron Capture Dissociation. *Rapid Commun. Mass Spectrom.* **Acceptd**.
7. **Qi, Y.**; O'Connor, P. B., Data Processing in Fourier Transform Ion Cyclotron Resonance Mass Spectrometry. *Mass Spectrom. Rev.* **Submitted**.

Abstract

Mass spectrometry (MS) is a powerful analytical technique used to characterize various compounds by measuring the mass-to-charge ratio (*m/z*). Among different types of mass analyzers, Fourier transform ion cyclotron resonance mass spectrometer (FT-ICR MS) is the instrument of choice for those working at the forefront of research, as it offers incomparable mass accuracy, resolving power, and the highest flexibility for hybrid instrumentation and fragmentation techniques.

The FT-ICR MS requires professional and careful tuning to achieve its superior performance. Our work aims to review, develop and apply advanced methods to improve the data quality of FT-ICR and push the limits of the instrument.

FT-ICR spectrometry has been limited to the magnitude-mode for 40 years due to the complexity of the phase-wrapping problem. However, it is well known that by correcting phase of the data, the spectrum can be plotted in the absorption-mode with a mass resolving power that is as much as two times higher than conventional magnitude-mode. Based on the assumption that the frequency sweep excitation produces a quadratic accumulation in an ion's phase value, a robust manual method to correct all ions' phase shifts has been developed, which allows a broadband FT-ICR spectrum to be plotted in the absorption-mode.

The developed phasing method has then been applied to a large variety of samples (peptides, proteins, crude oil), different spectral acquisition-mode (broadband, narrowband), and different design of ICR cells (Infinity cell,

ParaCell) to compare the performance with the conventional magnitude-mode spectra. The outcome shows that, by plotting the absorption-mode spectrum, not only is the spectral quality improved at no extra cost, but the number of detectable peaks is also increased. Additionally, it has been found that artifactual peaks, such as noise or harmonics in the spectrum can be diagnosed immediately in the absorption-mode.

Given the improved characteristics of the absorption-mode spectrum, the following research was then focused on a data processing procedure for phase correction and the features of the phase function. The results demonstrate that in the vast majority of cases, the phase function needs to be calculated just once, whenever the instrument is calibrated. In addition, an internal calibration method for calculating the phase function of spectra with insufficient peak density across the whole mass range has been developed. The above research is the basis of the Autophaser program which allows spectra recorded on any FT-ICR MS to be phase corrected in an automated manner.

Table of contents

Chapter 2

Data Processing in Fourier Transform Ion Cyclotron Resonance Mass Spectrometry

Chapter 3

Phase Correction of Fourier Transform Ion Cyclotron Resonance Mass Spectra using a Quadratic Least Square Fit and Iteration

Chapter 7

Variation of the Fourier Transform Mass Spectra Phase Function with Experimental Parameters

List of Figures

List of Tables

List of Schemes

List of Abbreviations

ACN	Acetonitrile
Asp	Aspartic acid
CAD	Collisionally activated dissociation
CaM	Calmodulin
CI	Chemical ionization
DC	Direct current
ECD	Electron capture dissociation
EI	Electron impace
ESI	Electrospray ionization
FT-ICR	Fourier Transform Ion Cyclotron Resonance
FWHM	Full width at half maximum
Glu	Glutamic acid
ICR cell	Ion cyclotron resonance cell
IRMPD	Infrared multi-photon dissociation
LC	Liquid chromatography
MALDI	Matrix assisted laser desorption
Met	Methionine
MS	Mass spectrometry
m/z	Mass-over-charge
MS^n	Tandem mass spectrometry
NMR	Nuclear magnetic resonance
ppb	Parts per billion
ppm	Parts per million
PTMs	Post-translational modifications

RP	Resolving power
RF	Radio frequency
RMS	Root mean square
SORI	Sustained off-resonance irradiation
S/N	Signal-to-noise ratio
T	Tesla
TOF	Time-of-flight

Chapter 1

Introduction to Mass Spectrometry

1.1 Significance

Mass Spectrometry (MS) is an analytical technique that measures the mass-to-charge (*m/z*) of the molecules.[1-2] The history of MS began a century ago: in 1917, a prototype of the modern mass spectometer was designed by Arthur. J. Dempster, which he called a “positive ray spectrograph”, because it records *m/z* by photography.[3] Shortly thereafter, in 1918, Francis. W. Aston reported his first mass spectrograph.[4] In recognition of his contribution, Aston was rewarded the Nobel Prize in Chemistry in 1922 for his discovery, “by means of his mass spectrograph, of isotopes, in a large number of non-radioactive elements, and for his enunciation of the whole number rule.”[5] Rapid progress in the following decades has contributed significantly to the MS techniques, through developments in electronics, instrumentation, application, and theory development, making MS one of the most powerful analytical methodologies today for identifying the elemental composition of unknown compounds.

Mass spectrometry is now used extensively in the field of pharmaceuticals, healthcare, industry, military, natural resources, and environmental management. The widespread adoption of MS is often due to its superior selectivity, sensitivity, and accuracy compared to other techniques. For example, an analyte at a concentration of one part-per-billion (ppb) can be detected and distinguished within a complex chemical mixture,[6] while the fine

structure of isotope peaks in the mass spectra of peptides can be measured with a mass error of less than 200 ppb.[7]

1.2 Introduction to Mass Spectrometry

A mass spectrum is a graph of ion intensity as a function of *m/z* (where *m* is a molecular weight in Daltons, and *z* is the integer number of elementary charge; 1 Da≈1.6x10^{-17} kg, 1 unit charge≈1.6x10^{-19} Coulombs). The accurate measurement of mass can be used to provide the molecular weight and elucidate the structural details of the analyte. Such mass information is acquired from the observed behavior of gaseous charged particles in electric or combined electric and magnetic fields. For this reason, every mass spectrometer must contain two major components: the ionization source, and the mass analyzer.

1.3 Major Ionization Techniques

Only charged particles can be detected by mass spectrometers; therefore, the first step in MS is to ionize sample molecules. A variety of ionization techniques has been used for the conversion of neutral molecules present in the gas or solution phase into charged particles, and among them, electron impact (EI) and chemical ionization (CI) are classic ionization methods. However, these two methods require samples to be volatile and often break bonds in the molecular ions due to the higher energy applied during ionization. The development of soft ionization methods have enabled intact ions produced from large nonvolatile and fragile molecules such as proteins.[8] Currently, matrix

assisted laser desorption ionization (MALDI)[9-11] and electrospray ionization (ESI)[12] are the preferred methods for bio-molecular mass analysis.

1.3.1 Electron Ionization

Electron ionization (EI, also referred as electron impact) is a classic ionization method in which the gas phase molecules are interacted with energetic electrons to produce ions.[13] The sample for EI is introduced either in gas form via capillary or evaporated from a direct injection probe. In many applications, EI is coupled with gas chromatography for sample separation prior to MS detection (GC-MS). In the EI source, the sample collides with a beam of 70 eV electrons to ionize the sample molecule by detachment of an electron:

$$M + e^- \rightarrow M^{+\bullet} + 2e^- \qquad (1.1)$$

The EI process generates a radical molecular ion, $M^{+\bullet}$, which is often not stable and tends to fragment. For this reason, EI mass spectra are often characterized by intense fragment ions and small molecular ion peaks, and fragment ions can be used to analyse the structure of an analyte molecule.

1.3.2 Chemical Ionization

For chemical ionization (CI), the ions are generated by colliding the analyte with reagent gas (such as methane, ammonia). The reagent gas molecules are first ionized by EI and further undergo ion-molecule reactions with themselves and the molecules of analyte. The mechanism can be described as follows (in this case, methane is used as the reagent gas):

$$CH_4 + e^- \rightarrow CH_4^{+\bullet} + 2e^- \qquad (1.2)$$

$$CH_4^{+\bullet} + CH_4 \rightarrow CH_5^+ + CH_3^\bullet \qquad (1.3)$$

$M + CH_5^+ \rightarrow CH_4 + MH^+$ (1.4)

The molecular species (MH^+) generated in CI are protonated even-electron molecules, rather than odd-electron molecular ions ($M^{+\cdot}$) like EI. Therefore, compared with EI, the CI molecules species are relatively more stable, which yield less fragmentation, and usually result in a simpler mass spectrum. In summary, CI is particularly useful for providing molecular weight information but also requires volatile and stable samples.[14-15]

1.3.3 Matrix Assisted Laser Desorption Ionization

The matrix assisted laser desorption ionization (MALDI) method (Figure 1.1) was first introduced by Hillenkamp and Karas in 1985, who then demonstrated the ability of this technique to ionize intact proteins of up to 67 kDa.[9-10, 16] Later in 1988, Tanaka applied a similar method to ionize large proteins and polymers, with mass over 100,000 Da.[11] Since then, MALDI has been widely applied in the analysis of biomolecules, such as peptides, proteins, DNA, and large organic molecules.[17-20]

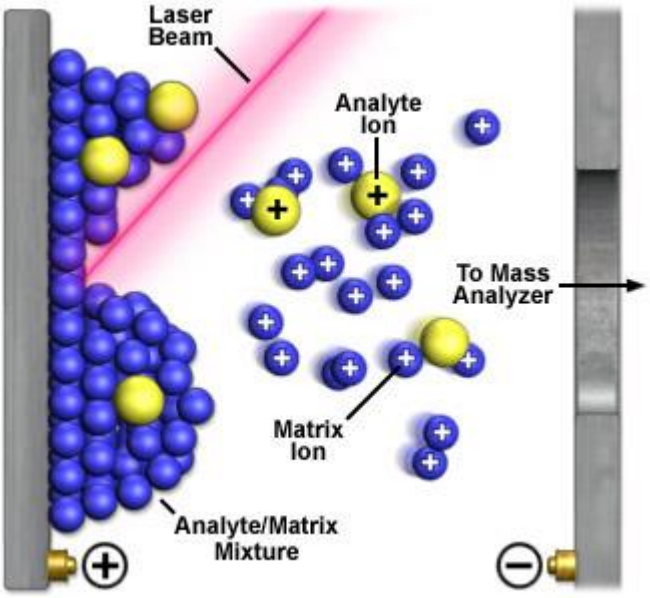

Figure 1.1 Diagram of the MALDI process (see http://www.magnet.fsu.edu/education/tutorials/tools/ionization_maldi.html for information, accessed 21st Feb, 2013)

During MALDI, the analytes are usually co-crystallized with a matrix compound--a small aromatic organic acid (most commonly used matrices include alpha-cyano-4-hydroxycinnamic acid, 2,5-dihydroxybenzoic acid, and sinapinic acid), the structures of which is optimized to absorb the laser at certain wavelength and transfer the energy to the analyte. General speaking, the analyte is first mixed with excess of matrix and irradiated with UV or IR laser light. The matrix then absorbs energy from the laser, and its upper layer will be ablated. Vaporized mixtures of matrix molecules (in both neutral and ionized forms) and neutral sample molecules are then formed in gas phase, followed by proton transfer that results in the ionized analytes. However, the exact mechanism of MALDI is still unclear; major debate lies on whether the charge transfer happens during the desorption event, or results from evaporation of charged matrix-analyte clusters (like the ESI mechanism).[21-22]

In summary, MALDI is a soft ionization technique, which is particularly suitable for non-volatile samples, such as biomolecules and polymers. And furthermore, MALDI generates mostly singly-charged species; thus greatly simplifies the spectra interpretation. The other attributes of MALDI are its high sensitivity, tolerance to salt adducts, and the ability for *in situ* ionization within biological tissues, make MALDI the ideal ionization technique for biological mass spectrometry imaging.[23-24]

1.3.4 Electrospray Ionization

Electrospray ionization (ESI, Figure 1.2), invented by Fenn in late 1980's,[12] together with MALDI, are the two revolutionary ionization techniques in MS. The development of ESI and MALDI made the analysis of bio-macromolecules possible in MS and contributed to the increasing understanding of the biological machinery of living organism. To recognize the contributions, Fenn and Tanaka were awarded the Nobel Prize (Chemistry) in 2002 for the development of soft desorption ionization methods in MS analysis.

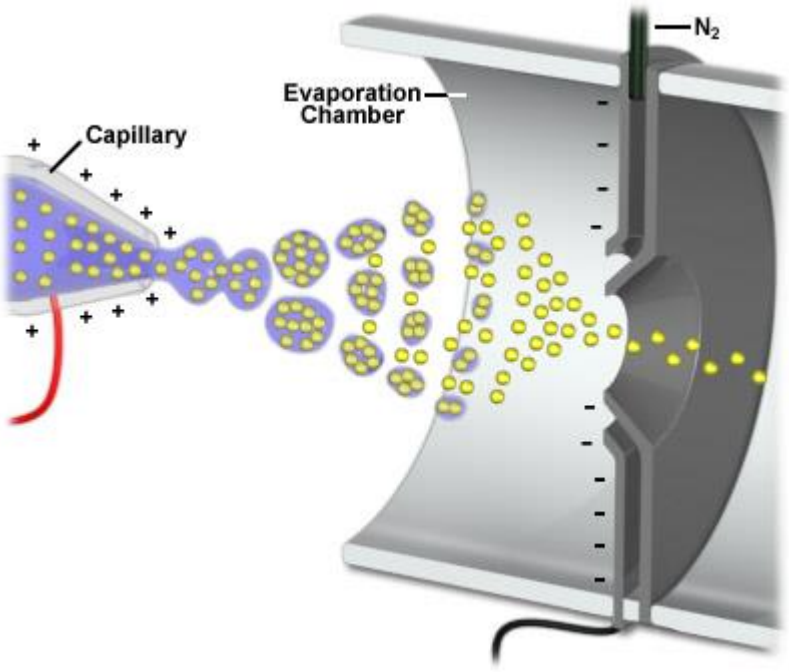

Figure 1.2 Diagram of the principle of ESI (see http://www.magnet.fsu.edu/education/tutorials/tools/ionization_esi.html for information, accessed 21st Feb, 2013)

Both positive– and negative–ion mode spectra can be obtained via ESI. For positive-ion mode, the samples are generally dissolved in an easily evaporated solvent, such as a mixture of 50:50 methanol/water with a small amount of acid (e.g., 1% formic acid or acetic acid) to enhance protonation, while for negative-ion mode, 0.1% ammonium hydroxide is often added for deprotonation.

As is shown in Figure 1.2, the solution is loaded into a capillary tube held at a high electrical potential (several kV). The resulting strong electric field between the capillary and the counter electrode (e.g. orifice) induces charge accumulation at the liquid surface located at the tip of the capillary, which releases small charged droplets. With the evaporation of the solvent from the droplet, the radius of the droplet decreases and the charge density increases.

When the droplet radius reaches the Rayleigh limit, the Coulombic repulsion exceeds the surface tension and leads to a “Coulombic explosion”, releasing smaller sized offspring ions. This process continues until the solvent is completely evaporated and the charged ions are generated. To ensure only ions are guided into the MS system, a countercurrent flow of dry curtain gas (normally nitrogen) is used at the interface to facilitate droplet evaporation and sweep away the uncharged particles.[25] And additionally, a sheath gas is also applied coaxially to reduce the radial dispersion of the spray.[26]

The unique advantage of ESI is that ions are formed in multiple charge states; the high charge not only improves the detection of the ion signal, but also allows the analysis of molecules with high molecular weight. Like MALDI, ESI is also a soft ionization technique which normally produces intact molecular ions, and for this reason, ESI can be used to analyze a variety of samples, including peptides, proteins, petroleum, polymers, organometallics, organic compounds, etc.[12, 27-30]

1.4 Mass Analyzers

The ionized analytes are directed into the mass analyzer region by the electric potential, and separated according to their *m/z* by manipulation of the electrical and magnetic field applied. The mass information on the ions is then recorded as electronic signals, and plotted in the mass spectrum. There are many types of mass analyzers available, with their unique advantages and limitations. The principles of several commonly used mass spectrometers will be introduced briefly. First of all, it is important to define several major

properties which describe the performance of a mass spectrometer: mass accuracy, resolving power, dynamic range, sensitivity, and scanning speed.

Mass accuracy is the accuracy of measured *m/z* value by the instrument, and it is defined by calculating the difference between the experimental value and the theoretical value, in part per million (ppm) units:[31]

$$\text{Mass accurancy} = \frac{m_{\text{exp}} - m_{\text{the}}}{m_{\text{the}}} \times 10^6 \quad \text{in parts per million (ppm)} \qquad (1.5)$$

Resolving power (*RP, m/*Δm_{FWHM}), where *m* is the *m/z* value in the center of the peak and Δm is its full width measured at half maximum (FWHM), is the ability of a mass spectrometer to distinguish two very close peaks in a spectrum. Consequently, a higher resolving power means a better ability to resolve closely separated peaks.

The dynamic range is a measure of the detection range of a detector, which is calculated by the ratio of the highest detectable ion signal and the lowest one. The sensitivity is the ratio of measured ion signal to the sample concentration. The scanning speed is the rate at which the analyzer measures over a particular mass range.

1.4.1 Quadrupole Mass Analyzer

The quadrupole is the most widespread mass analyzer; it was utilized with EI sources first in the 1950's.[32] Later since the 1990's, the quadrupole has been adapted to ESI source. The major factors that make quadrupole the most popular mass analyzer is that: First, it is cheap compared to other instruments. Second, it can be operated in a relatively high vacuum pressure (~10^{-6} mbar), which makes it compatible with high flow rate atmospheric pressure ion sources and cheaper pumping systems. Third, the quadrupole possesses a wide *m/z*

range up to 4 kDa, which is suitable for most routine research in pharmaceuticals, healthcare and industry.[33-35]

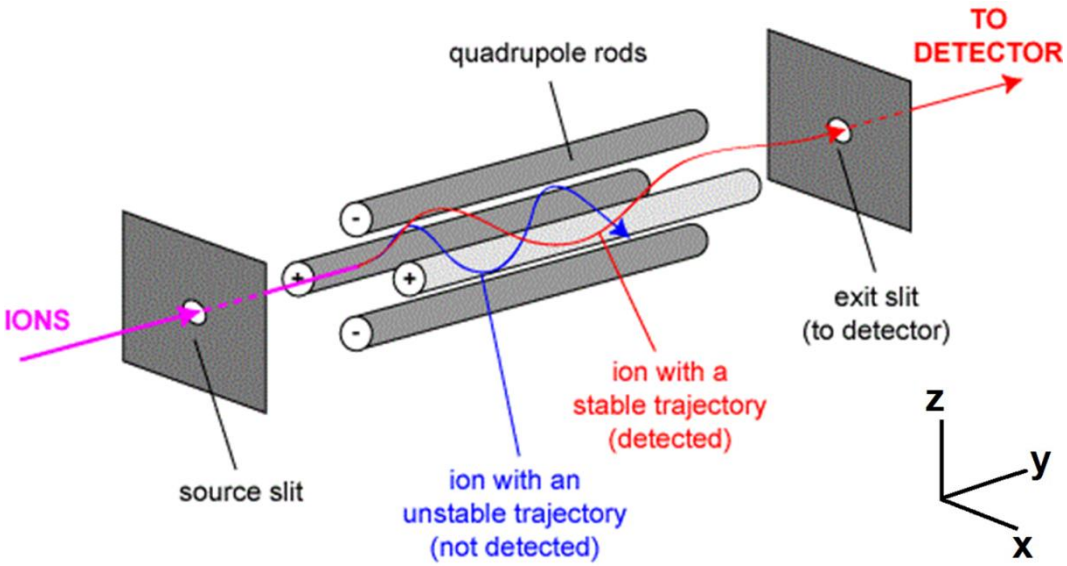

Figure 1.3 The scheme of a quadrupole device, the two opposite rods in the quadrupole have a potential of +(U+Vcos(ωt)) (labelled '+') and the other two -(U+Vcos(ωt)) (see http://www.chm.bris.ac.uk/ms/theory/quad-massspec.html for information, accessed 25th Feb, 2013).

A quadrupole mass analyzer consists of four parallel metal rods with each opposite pair being electrically connected. As shown in Figure 1.3, the ions enter and travel in the z direction, oscillate in the x-y plane, and only ions with stable trajectories can pass through the quadrupole and be detected. The ion's trajectory during the time (t) is controlled by the radio frequency (RF) voltage (V) and a direct current (DC) voltage (U) applied to each pair of rods:

$$\frac{d^2x}{dt^2} + \frac{2ze}{mr_0^2}(U - V\cos\omega t)x = 0 \qquad (1.6a)$$

$$\frac{d^2y}{dt^2} - \frac{2ze}{mr_0^2}(U - V\cos\omega t)y = 0 \qquad (1.6b)$$

where ω is the angular frequency, and r_0 is the half distance between the two opposing rods. The above equations can be rearranged and solved according to the Mathieu equation (Eq.1.6c),[36] and the result shows that ion's trajectory stabilities are determined by the two characteristic values a and q which are related to DC potential U and the magnitude of RF frequency V:

$$\frac{d^2u}{d\xi^2} + (a - 2q\cos 2\xi)u = 0 \qquad (1.6c)$$

$$a = \frac{8eU}{mr_0^2\omega^2} \qquad (1.6d)$$

$$q = \frac{4eV}{mr_0^2\omega^2} \qquad (1.6e)$$

For different masses, the bounded solution to the Mathieu equations results in a different stability diagram as shown in Figure 1.4.[36]

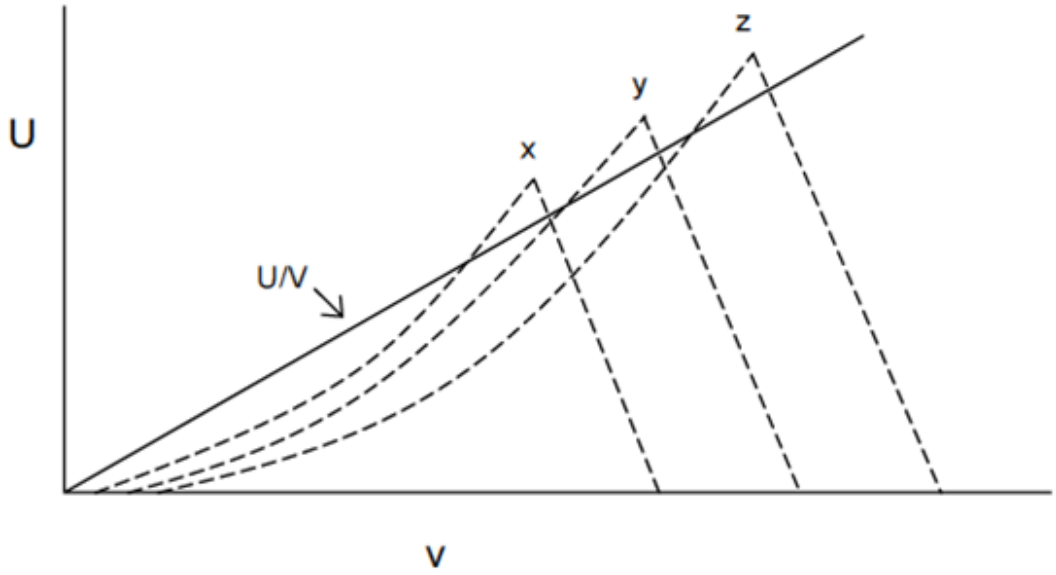

Figure 1.4 Theoretical stability diagram of three *m/z* values, where x<y<z.

Ions with different *m/z* values will have different stability areas in a quadrupole. Specific U and V values allow ions within a narrow *m/z* range to fly through a stable trajectories in the quadrupole and reach the detector;

meanwhile the ions with *m/z* values outside this range have unstable trajectories, and will strike the rods before detection. Such a feature is the basis for ion isolation, as is shown in the stability diagram, when a constant U/V value is kept during operation, the U/V line only crosses the vertices of the stable areas, and therefore, only the ion with a specific *m/z* value is transmitted. By adjusting the the U/V value, the resolution of the quadrupole can be varied. And when the DC potential is turned off, the quadrupole acts as a RF only ion guide, which allows all ions above a certain *m/z* value passing through.

Compared to the other mass analyzers, quadrupoles is easy to build, robust, and relatively cheap. In practice, a quadrupole normally has an upper *m/z* limit of ~4000, a mass resolution below 3000, a typical mass accuracy about 100 ppm, and a scanning speed for ~1 second for the entire mass range.[37] Due to the low cost, quadrupoles are often used as ion guides, ion selectors, and ion storage devices in hybrid mass spectrometers, rather than being as stand-alone mass analyzers.

1.4.2 Quadrupole Ion Trap Mass Analyzer

The quadrupole ion trap mass analyzer was invented by Wolfgang Paul who was awarded the Nobel Prize (Physics) in 1989 for his contribution. The operation principle of a quadrupole ion trap is similarly to a quadrupole mass analyzer, but the ions are trapped in the ion trap rather than passing through it as in the quadrupole mass analyzer.

An ion trap consists of two hyperbolic endcap electrodes and a ring electrode in between the end-cap electrodes (Figure 1.5). Ions are trapped in the three dimensional electric field by applying oscillating RF voltages to the

ring electrode and non-oscillating, static DC voltage to the end-cap electrodes. And the ions can be ejected through a small hole in the end-cap electrode to the detector by changing the radio frequency of the auxiliary AC electric field applied to the end-cap electrodes.[38-39]

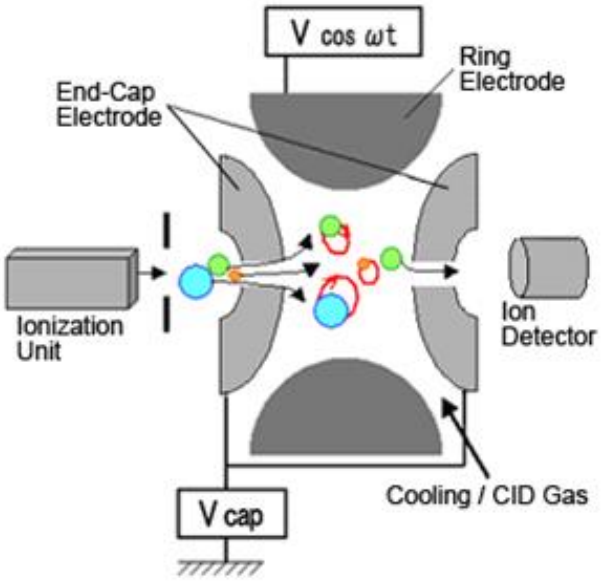

Figure 1.5 Diagram of an ion trap mass analyzer (see http://www.shimadzu.com/an/lcms/support/intro/lib/lctalk/61/copy_of_61intro.html for information, accessed 25th Feb, 2013).

The performance of an ion trap is also very similar to a quadrupole mass analyzer. Ion trap has poor mass accuracy (~100 pm), low mass resolving power (~4000), slow scanning speed (~1 second for the entire mass range), and *m/z* range of up to ~4000. Like quadrupoles, ion traps are also low-cost instruments, but theoretically, ion traps have higher analytical sensitivity than quadruples due to their ability to accumulate ions.

1.4.3 Time-of-Flight Mass Analyzer

A time of flight (TOF) mass analyzer separates the ions by their flight time through a field-free flight tube.[40-41] In a TOF MS, ions generated from the ion source are directed into the instrument by electric fields and then separated in a field-free flight tube based on their *m/z* values. The TOF mass analyzer measures the *m/z* based on the flight time of an accelerated ion travelling through the flight tube.

The ion's flight time can be calculated based on the length of the flight tube (L) and the velocity (v) as:

$$t = \frac{L}{v} \qquad (1.7a)$$

where the velocity can be acquired from ion's initial kinetic energy:

$$E = \frac{mv^2}{2} = zeV \qquad (1.7b)$$

Then the flight time (t) can be derived as:

$$t = \sqrt{\frac{mL^2}{2zeV}} \qquad (1.7c)$$

where *m* and *z* are the mass and charge of the analyte ion, and V is the accelerating potential. From Eq.1.7, it is obvious that lighter ions travel faster then heavier ions. The ion flight time in the tube is typically in the level of ~100 μs; which makes the scanning speed of TOF analyzers very fast. The pressure in the drift region is in the range of 10^{-7} mbar so that the ions are allowed to drift with a minimum number of collisions with background gas.[37]

A TOF analyzer couples well with a MALDI ionization source, because it works in a pulsed mode. Continuous ionization sources (e.g., ESI) can also be coupled to TOF analyzers, with special gating methods applied.

The major advantage of TOF analyzer is its very fast scanning speed, and therefore, it can be easily adapted to the liquid chromatography (LC) system for high throughput analysis. Besides that, since almost all the ions flying through the tube can be detected, TOF instrument have high sensitivities and require relatively small amount of samples, and theoretically, there is no mass range limitation for TOF. A modern TOF instrument can easily reach a resolving power of 20,000 and mass accuracy of <10 ppm and a scan time of 100 us.[37]

1.4.4 Fourier Transform Ion Cyclotron Resonance Mass Analyzer

The Fourier Transform Ion Cyclotron Resonance (FT-ICR) MS, introduced in 1974 by Comisarow and Marshall,[42-43] determines the *m/z* of the analyte ions by measuring their cyclotron frequency in a magnetic field.[44-45] Among all different types of mass analyzers, the FT-ICR is capable of achieving the highest performance in terms of mass accuracy and resolving power, yet it is a complicated and an expensive system requiring particular expertise. All experiments presented in this thesis were performed on a solariX FT-ICR mass spectrometer with a 12 T actively shielded magnet (Bruker Daltonik GmbH, Bremen, Germany), and the details on FT-ICR instrument and data processing will be discussed in Chapter 2.

1.5 Overview of This Thesis

This thesis focuses on the study of advanced methods to improve the data quality of FT-ICR instrument, involving a detail review on FT-ICR data processing (Chapter 2), the development, application, and advantages of a novel phase correction method to present the FT-ICR spectra in the

absorption-mode (Chapter 3-7), and a study on mapping the protein binding sites of novel iridium-based anticancer complexes using the electron capture dissociation (Chapter 8). And Chapter 9 is the conclusions and future work. Overall, this thesis demonstrates the importance on data processing for the FT-ICR mass spectrometry to achieve the ultra-high performance.

Chapter 2

Data Processing in Fourier Transform Ion Cyclotron Resonance Mass Spectrometry[1]

2.1 Introduction

In the past two decades, mass spectrometry[1] has developed extensively in the fields of pharmaceuticals, healthcare, industry, forensics, natural resources, and particularly in the study of proteins and complex mixtures.[2, 33-35] Among different varieties of commercially available mass analyzers, Fourier Transform Ion Cyclotron Resonance Mass Spectrometer (FT-ICR-MS or FTMS) is a preferred instrument at the forefront of research. The FT-ICR offers ultra-high mass resolving power (RP>100,000 routinely, and >20,000,000 in the newly designed ICR cell),[46] flexibility for hybrid instrumentation,[47-48] and additionally, its compatibility with a diverse range of fragmentation methods, such as sustained off-resonance irradiation collision activated dissociation (SORI-CAD),[49] multiphoton infrared dissociation (IRMPD),[50] and electron capture dissociation (ECD)[51] makes FT-ICR ideal for tandem mass spectrometric analysis (MS/MS) of large and complex molecules.

During the 40 years since its inception,[43] a number of FT-ICR review articles and book chapters have been written contributing to the aspects from instrumentation to application.[32, 44-45, 52-55] However, most of the literature is directed to specific areas assuming the readers are practitioners, while the principles of how FT-ICR spectra are generated and processed are lacking.

---

[1] This chapter has been partially/entirely reproduced from
Qi, Y.; O'Connor, P. B., Data Processing in Fourier Transform Ion Cyclotron Resonance Mass Spectrometry. *Mass Spectrom. Rev.* **2013**, submitted, Wiley.

This chapter is aimed of beginners without prior experience in the field, focuses on FT-ICR data processing, and explains the procedures step by step for users with the goal of maximizing spectral features such as mass accuracy, resolving power, dynamic range, and limits of detection.

2.2 Ion Motion

Mass spectrometers analyze ions in the gas phase to obtain the mass-to-charge ratio (*m/z*); therefore, a mass spectrum is a graph of ion intensity as a function of *m/z*. In FT-ICR, ions are normally ionized externally from an ion source,[10, 12] accumulated in the ion optics,[56-57] and transferred into the ICR analyzer (also referred as "cell"). The ICR cell is mounted within a spatially uniform magnetic field, *B* from the superconducting magnet, and an electric field, *E* from two opposed conductive trapping plates. Figure 2.1 shows a schematic of a closed cylindrical cell used in FT-ICR,[58] similar to the Infinity cell, manufactured by Bruker Daltonics.[59]

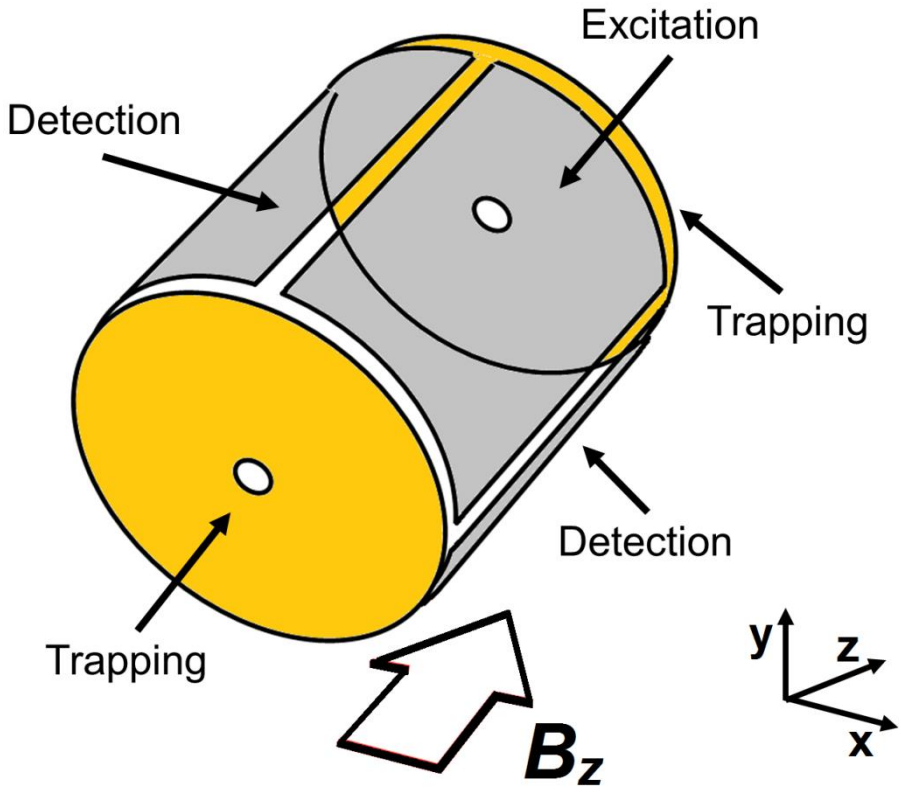

Figure 2.1 Schematic representation of a closed cylindrical cell. The cell is aligned with the bore of the magnet so that the magnetic field axis is coaxial with the trapping axis (*z*-axis). In this particular example, the excitation plates are located along the *y*-axis and the detection plates along the x-axis. The trapping electrodes are located at each end of the cell.

A charged particle, such as an ion, experiences a "Lorentz Force" (Eq2.1a) in the magnetic field, results in a circular motion with a perpendicular speed, *v*, and the ion will have a fundamental oscillation frequency, known as the "cyclotron motion" given by Eq2.1c:

$$F_{Lorentz} = qv \times B \qquad (2.1a)$$

$$F = ma = \frac{mv^2}{r} = \frac{m(\omega_c r)^2}{r} = qvB \qquad (2.1b)$$

$$\omega_c = \frac{qB}{m} \qquad (2.1c)$$

where ω_c, q, B, and m are cyclotron frequency, elementary charge of the ion, strength of magnetic field, and mass of the ion (all in SI units, measured in Hertz (Hz), Coulombs (C), Tesla (T), and kilograms (kg) respectively), and F is the force acting on an ion. Eq2.1c reveals that the ion's cyclotron frequency is independent of its velocity, and hence, independent of kinetic energy. This extraordinary characteristic is one of the key reasons why FT-ICR is capable of ultra-high resolving power, as most other types of mass spectrometers differentiate ions' *m/z* values by the spread of their kinetic energies. Meanwhile, according to Eq2.1, the ions can only be confined in the xy-plane in the cell, which means they are not stable in the z direction. For this reason, a DC voltage (V_T) which varies quadratically with axial z position (to a first order approximation) is applied on the trapping plates of the ICR cell in order to stabilize ion's motion along the magnetic field direction. This electric field results in the ion's trapping motion in the z direction, at an angular frequency, ω_z:[60]

$$\omega_z = \sqrt{\frac{2qV_T a}{ma^2}} \qquad (2.2)$$

in which α is the trapping scale factor, depending upon cell geometry, and a is the size (i.e., distance between the trap plates) of the ICR cell. Such oscillation in the z axis will perturb the ion's cyclotron motion; Hans Dehmelt pointed out that in three dimensions, the quadratic variation in electrostatic potential as a function of z is also accompanied by a quadratic variation as a function of radial position in the xy-plane:

$$\Phi(r,z) = V_T\left(\gamma + \frac{\alpha}{2a^2}(2z^2 - r^2)\right) \qquad (2.3)$$

in which γ is also a constant depending upon the cell geometry, and r is the radial distance between the ion and z axis [61]. This DC trapping potential results in a radially outward-directed electric force that opposes the inward-directed magnetic force, and therefore, in the xy-plane perpendicular to the magnetic field, the force acting on an ion becomes:

$$F = ma = m\omega^2 r = qB\omega r - \frac{qV_T\alpha}{a^2}r \qquad (2.4)$$

Eq2.4 is a quadratic equation on ω, and solving Eq2.4 for ω yields two rotational frequencies in the xy-plane--ω_c and ω_z:

$$\omega_+ = \frac{\omega_c}{2} + \sqrt{\left(\frac{\omega_c}{2}\right)^2 - \frac{\omega_z^2}{2}} \qquad (2.5a, \text{“reduced cyclotron frequency”})$$

$$\omega_- = \frac{\omega_c}{2} - \sqrt{\left(\frac{\omega_c}{2}\right)^2 - \frac{\omega_z^2}{2}} \qquad (2.5b, \text{“magnetron frequency”})$$

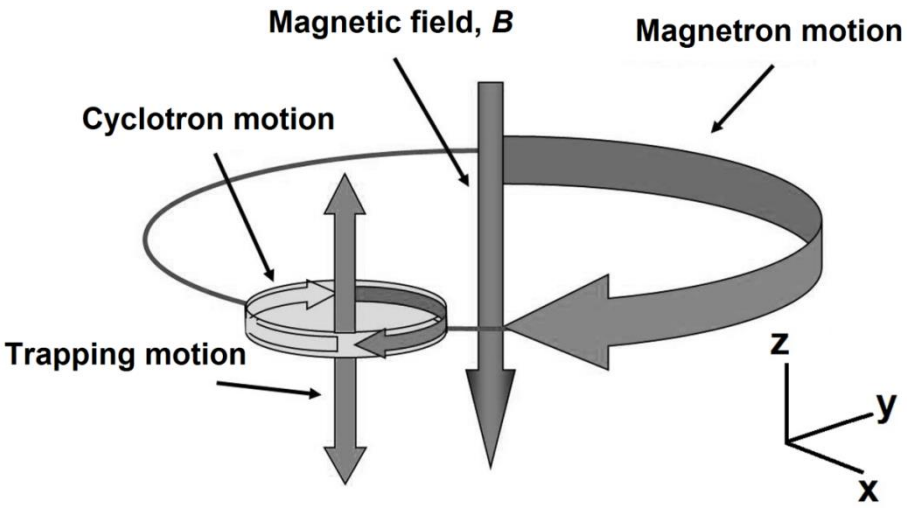

Figure 2.2 The three natural ion motional modes: cyclotron rotation, magnetron rotation, and trapping oscillation.

As is shown in Figure 2.2, in the ICR cell, the ions' motion is a combination of the three natural modes: 1) cyclotron motion in the xy-plane caused by the magnetic field; 2) magnetron motion, also in xy-plane, which is a drift of the cyclotron centre, and 3) trapping motion, which is a harmonic oscillation along the z-axis between the trapping plates. The corresponding frequencies of the three motions are functions of *m/q*; these motions are the basis for the FT-ICR to measure an ion's *m/z*. Among the three frequencies, the trapping frequency (<10 kHz) and magnetron frequency (<100 Hz) are the consequence of the trapping electric field applied which are much less than the cyclotron frequency (ranging from kHz to MHz), for this reason, trapping and magnetron frequencies are often ignored. However, the trapping electric fields do perturbs the ion's motion and affects the measurement of ion cyclotron frequency, and these can result in undesirable effects including radial ion diffusion, frequency shift, peak broadening, and sidebands on the peaks (discussed below).

2.3 Experimental

2.3.1 Pulse Program

Many mass spectrometers (e.g., magnetic sector, quadrupole, time-of-flight) are continuous mass analyzers, which means the events of ionization, isolation, and detection occur continuously and simultaneously at different parts of the instrument. By contrast, the FT-ICR is an ion trap; the above functions can be operated in the same space, but spread out in time; for this reason, the FT-ICR hardware is controlled by a series of events called a "pulse program". The pulse program is a flexible and compiled event sequence tailor-made either automatically or manually according to the requirements of

each experiment. A very basic pulse program consists of following events: cell quench, ion injection, excitation, and detection (Figure 2.3). The quench event is used to eject the ions left from the previous experiment by applying reverse voltages on two trapping plates (e.g., 10 V on the front plate and -10 V on the back plate). After the quench event, the ions of interest are then transferred and trapped in the ICR cell for analysis. Based on the basic pulse program, specific experiments can be triggered by the addition of conditional events (such as ECD or CAD) into the sequence. For example, two-dimensional MS/MS can be achieved by inserting a pair of excitation pulses with a delay time, between the ion generation and ion dissociation events;[62-63] double resonance MS/MS experiments can be done by adding a simultaneous on-resonance ejection event during ion dissociation.[64-65]

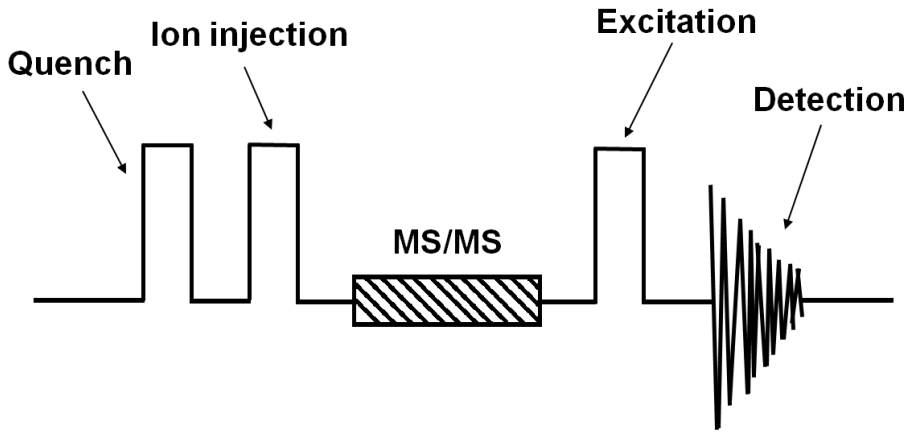

Figure 2.3 A simple experimental pulse program of FT-ICR

2.3.2 Ion Excitation and Detection

The ions oscillate at very small “thermal” cyclotron orbits. However, their initial packet radius in the ICR cell is defined by the phase space that they occupied in the ion optics, and the initial radius is probably <1 mm, before being transferred into the ICR cell. For detection, a radio frequency (RF, Figure 2.4 top) potential is applied to the excitation plates in order to increase an ions’ cyclotron radius. When the RF excitation frequency equals the cyclotron frequency of the ion (Eq2.5a), the ion will absorb kinetic energy from the electric field and spiral up into a large cyclotron orbit with a diameter of typically 2-5 cm, depending on voltage, cell geometry parameters, and the excitation duration. Normally, in order to excite all the ions for detection, the applied RF pulse is a stepwise frequency sweep across the entire resonant frequency range of interest, and the amplitude of the pulse is usually a constant, known as an “RF chirp”.[42, 66] During the excitation event, ions that are off-resonance with the RF frequency do not absorb energy and remain at the center of the cell, when the cyclotron frequency is in resonance with the excitation frequency, ions of corresponding *m/z* rapidly spiral outwards coherently to a larger radius, so that a much more intense image current can be recorded by the detection plates.[67]

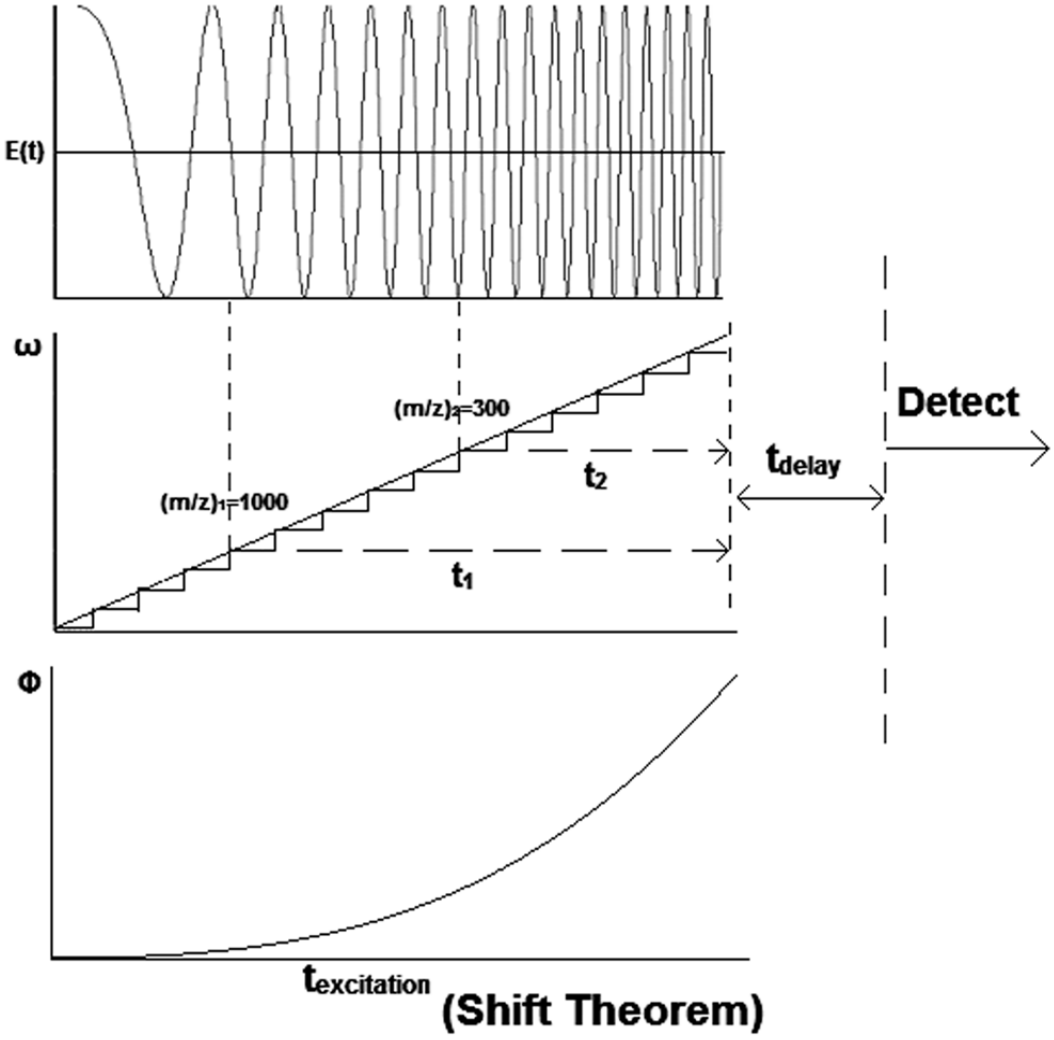

Figure 2.4 Top: time-domain profiles of the RF chirp for ion excitation. Middle: frequency for a linear polarized (upper line) or stepwise (lower line) frequency sweep. Bottom: quadratic phase accumulation for the stepwise frequency sweep. Reprinted from Qi *et al.*, 2011,[68] with permission from Springer, copyright 2011.

Through the RF chirp, ions of same *m/z* are excited coherently and undergo their motions as ion packets. Each ion packet has a resonance frequency (corresponding to *m/*z), and ions generate image current every time they pass the detection plates; thus the potential induced by the ion current is

recorded simultaneously as a function of time. As the ions' motion in the cell is periodic, the signal recorded is a composite sum of N_n sinusoidal waves with different frequencies in the time domain, and the intensity of the signal is damped with time following the approximate model:

$$F(t) = \sum_{n=1}^{N} K_n \cdot \exp(-t/\tau_n) \cdot \cos(\omega_n t) , \quad 0<t<T \qquad (2.6)$$

where K is the scaling factor which is proportional to the number of ions, T is the acquisition time of the signal, ω_n and τ_n are the frequencies and damping factors of the ions (mainly caused by collision with other ions and gas particles). Here, the detected ω_n is the ion's reduced cyclotron frequency (Eq2.5a), because the ideal cyclotron frequency is perturbed by the electric field. The recorded sinusoidal signal is then amplified, digitized, and stored for further processing by users.[69]

2.3.3 The Nyquist Theorem and Data Acquisition

In FT-ICR, the recorded sinusoid is called a "transient", "time domain data", or "free induction decay (FID)". In an actual experiment, the continuous image current detected cannot yield continuous time domain data; instead, it is sampled at a certain acquisition frequency to produce a discrete transient consisting of a finite number of data points. Due to the discontinuity of the data, the frequency used for sampling is crucial for reconstruction of the original signal. According to the Nyquist theorem, the required frequency for sampling must be at least twice the highest frequency being recorded in the transient. Otherwise, any frequency segment which exceeds the Nyquist frequency will "fold back", possibly multiple times, to a lower apparent frequency value in the acquired spectrum.[70-71]

The instrument software determines the sampling frequency, which is usually 2x of the highest frequency in the spectrum (corresponding to the lowest *m/z* cut-off). Similarly, the number of data points to be acquired in the transient is determined by the user prior to acquisition. And after that, the acquisition time (*T*) of the transient can be calculated from the sampling frequency and the data set size according to Eq2.7:

$$T = \frac{N}{f_s} \qquad (2.7)$$

in which N is the dataset size, and f_s is the sampling frequency. During acquisition, the time domain transient with a fixed data size is then digitized at the sampling frequency rate. For example, in the 4.6 sec transient used in Figure 2.5E, the lowest *m/z* being detected is 400, corresponding to the frequency of ~454,545 Hz, and therefore, the minimum sampling frequency required is 909,090 Hz, for a 4-mega-point dataset (4*1024*1024=4,194,304 data points), duration of the detection event, $T=N/f_s$=4194304/909090≈4.6 seconds.

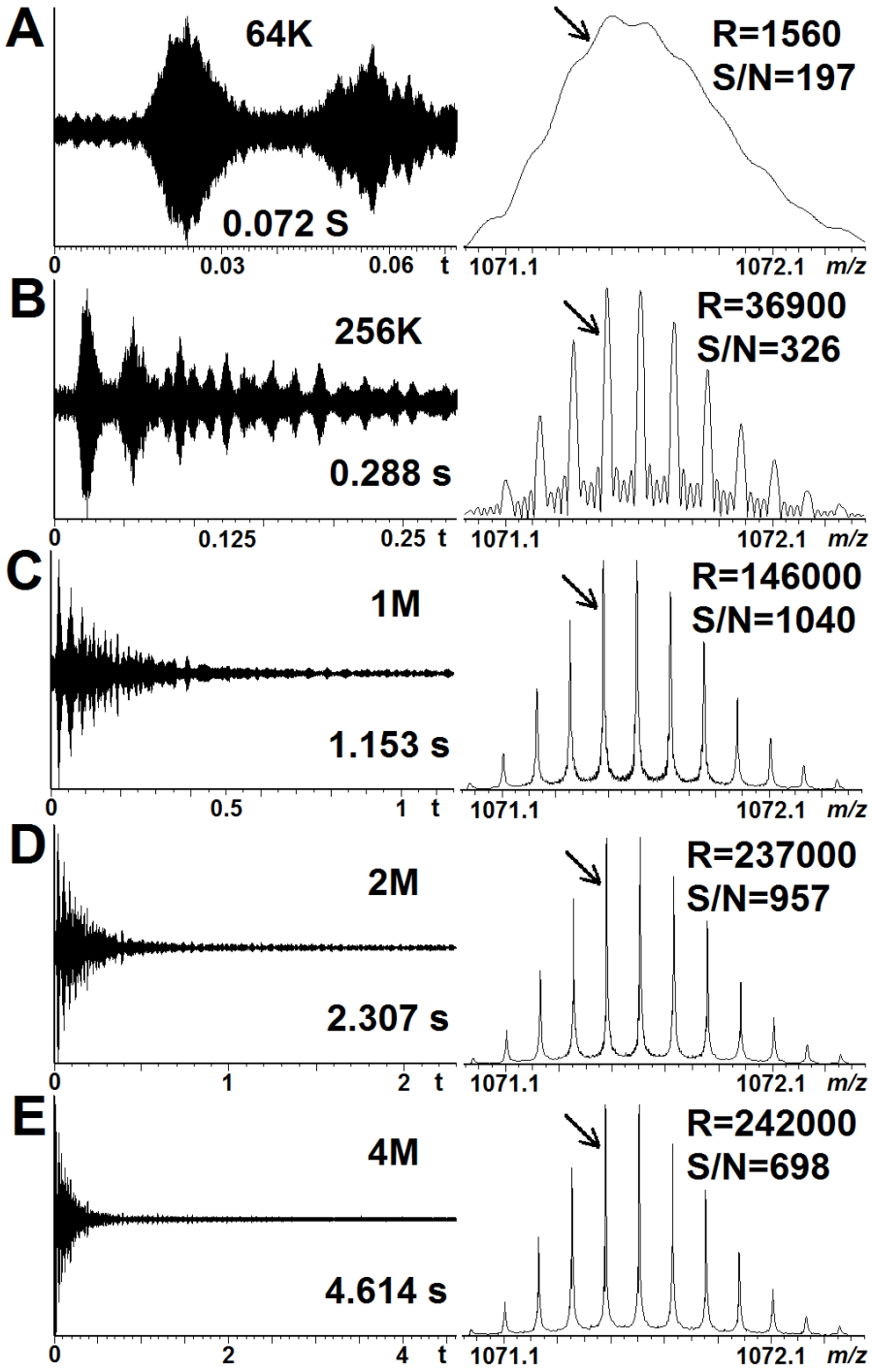

Figure 2.5 A ubiquitin data set (no apodization, one zero fill) demonstrates the transient duration (left), and its effect on the 8^+ isotopic peaks (right), the value of RP and S/N are measured for the labelled peak in each spectrum.

2.4 ICR Signal

2.4.1 Mass Accuracy and Resolving Power

Mass accuracy is the difference between the theoretical mass of an ion and its mass measured from the mass spectrometer, defined in Eq2.8:[31]

$$\text{Mass accuracy} = \frac{m_{\text{exp}} - m_{\text{the}}}{m_{\text{the}}} \times 10^6 \quad \text{in parts per million (ppm)} \qquad (2.8)$$

where m_{exp} is the m/z value of the peak obtained in the mass spectrum, and m_{the} is the theoretical m/z calculated for that species. The mass accuracy is important for determining the ion's elemental composition.[72] Most types of modern mass spectrometers (ion trap, quadrupole, time-of-flight) offer the mass accuracies in the level of at best tens of ppm in a limited mass range, whereas FT-ICR can achieve mass accuracy in sub-ppm, or even ppb (parts per billion) level in state-of-the-art instruments.[7, 73] With such extraordinary performance, the ion's elemental composition can be revealed without tandem MS experiments, and even the number of a certain atom, such as sulfur, in the formula can be counted.[74-75]

Mass measurement accuracy (MMA) is of course the key measurement parameter of a mass spectrometer, however, mass accuracy is dependent on the mass resolving power (RP) and signal-to-noise ratio (S/N), because a prerequisite for accuracy is that the peak of interest must be well resolved and distinguished from others. FT-ICR is known best for its ultra-high mass resolving power:

$$RP = \frac{m}{\Delta m} = \frac{\omega}{\Delta \omega} \qquad (2.9)$$

where m and ω are the m/z and frequency values for the peak of interest, Δm and $\Delta\omega$ are the peak width at half maximum (FWHM). The resolving power

is particularly important when peaks become close neighbours (e.g., isotopes of highly charged ions, complex mixtures). The isotopic pattern (^{13}C peaks) of multiply charged peptides or small proteins can be revealed when RP is above 10,000,[76] however, each of the isotope peaks other than the monoisotopic peak is composed of the much more complex fine isotope clusters, and the fine structures of isotopic distributions are generally only revealed when the resolving power is above 1,000,000.[7] As is shown in Figure 2.6, the fine structure of the A+3 isotopic clusters for substance P are baseline resolved at an average RP of around 4,000,000; note that even the ultra-low abundance trace isotopes are resolved.

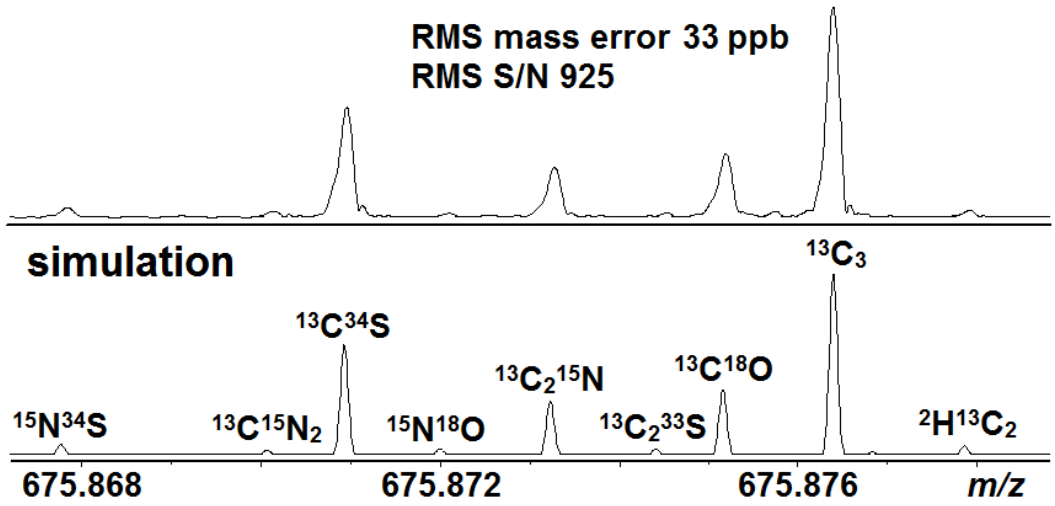

Formula	Measured m/z	Error (ppb)	Resolving power	S/N ratio	Calculated intensity	Measured intensity	Intensity difference
$^{15}N^{34}S$	675.867834	25	4.1M	118	5.9%	4.8%	-18.6%
$^{13}C^{15}N_2$	675.870143	58	4.1M	72	2.8%	3.0%	7.1%
$^{13}C^{34}S$	**675.870951**	**-19**	**4.0M**	**1363**	**60.7%**	**52.4%**	**-13.7%**
$^{13}C_2{}^{15}N$	**675.873268**	**25**	**4.0M**	**613**	**30.3%**	**23.7%**	**-21.8%**
$^{13}C^{18}O$	**675.875185**	**19**	**4.0M**	**781**	**36.2%**	**30.2%**	**-16.6%**
$^{13}C_3$	**675.876382**	**-25**	**4.1M**	**2607**	**100.0%**	**100.0%**	**0%**
$^{2}H^{13}C_2$	675.877895	61	4.7M	80	5.2%	3.4%	-34.6%
RMS		33		925			14%

Figure 2.6 Top: fine structure of A+3 isotopic clusters for substance P [M + 2H]$^{2+}$ ion, the recorded transient is 45 s long. Middle: simulation of the fine isotopic pattern. Bottom: details of peak assignment (peaks used for mass calibration are in bold). Reprinted from Qi *et al.*, 2012,[75] with permission from Wiley, copyright 2012.

The above spectrum shows the importance of resolving power for distinguishing the peaks with same integer *m/z* but different elemental compositions. The mass resolving power in FT-ICR can be estimated by applying Eq2.1 to Eq2.9:

$$RP = \frac{m}{\Delta m} = \frac{\omega}{\Delta \omega} = \frac{qB}{m\Delta\omega} \propto \frac{qBT}{mk} \qquad (2.10a)$$

$$\Delta\omega \propto \frac{k}{T} \qquad (2.10b)$$

in which *k* is a constant peak width, and the other variables were defined above. This peak width, *Δω*, is inversely proportional to the signal acquisition time, *T*, after the Fourier transform (FT). Therefore, the equations above reveal that the resolving power of any peak for a given *m/z* (*m* and *q* are fixed) is directly dependent on the magnetic field (*B*), duration of the transient (*T*), and the peak width constant (*k*). Among the three factors, building a higher magnetic field is the most straightforward way to improve resolution;[77] however, the expense of the magnet is the major part of the instrument cost, and increases dramatically for high field. Nevertheless, effort can be made to improve *T* and *k* by instrument tuning and data analysis.

2.4.2 Signal Acquisition, Resolving Power Vs Signal-to-Noise Ratio

Typically, the users tune the instrument to acquire a time-domain signal which lasts as long as possible. Figure 2.5 illustrates the effects of signal acquisition time on the resolving power and S/N. The original transient (Figure 2.5E) was recorded for 4.6 s (4 mega data points), then truncated to smaller data sizes (shorter acquisition times), Fourier transformed with one zero fill, and the value of RP and S/N on the labeled peak were measured for each spectrum. In the first 0.072 s of the transient, the peaks are not resolved, and the RP is 1560, which is far from sufficient to resolve the isotopes. For the 0.288 s transient, the RP increases to 36,900, the isotopes start to be split; meanwhile the shape of the peaks shows a typical sinc function (y=sin(x)/x). Overall, RP increases with the duration time of the transient, and the peak shape changes from a sinc function to a Lorentzian function (will discuss below). According to

Eq2.10a, a longer time domain signal is essential for achieving higher resolving power as RP increases linearly with *T*. Such an argument is only partially right. By truncating the transient and monitoring the corresponding peak in Figure 2.5, the resulting value of RP and S/N are plotted versus *T* to show a clear trend. In Figure 2.7, the increase of resolving power is almost linear during the first 2 s in the transient which agrees with Eq2.10, however, the slope starts to drop quickly after that, and the resolving power measured at the maximum 4.6 sec transient even decreases.

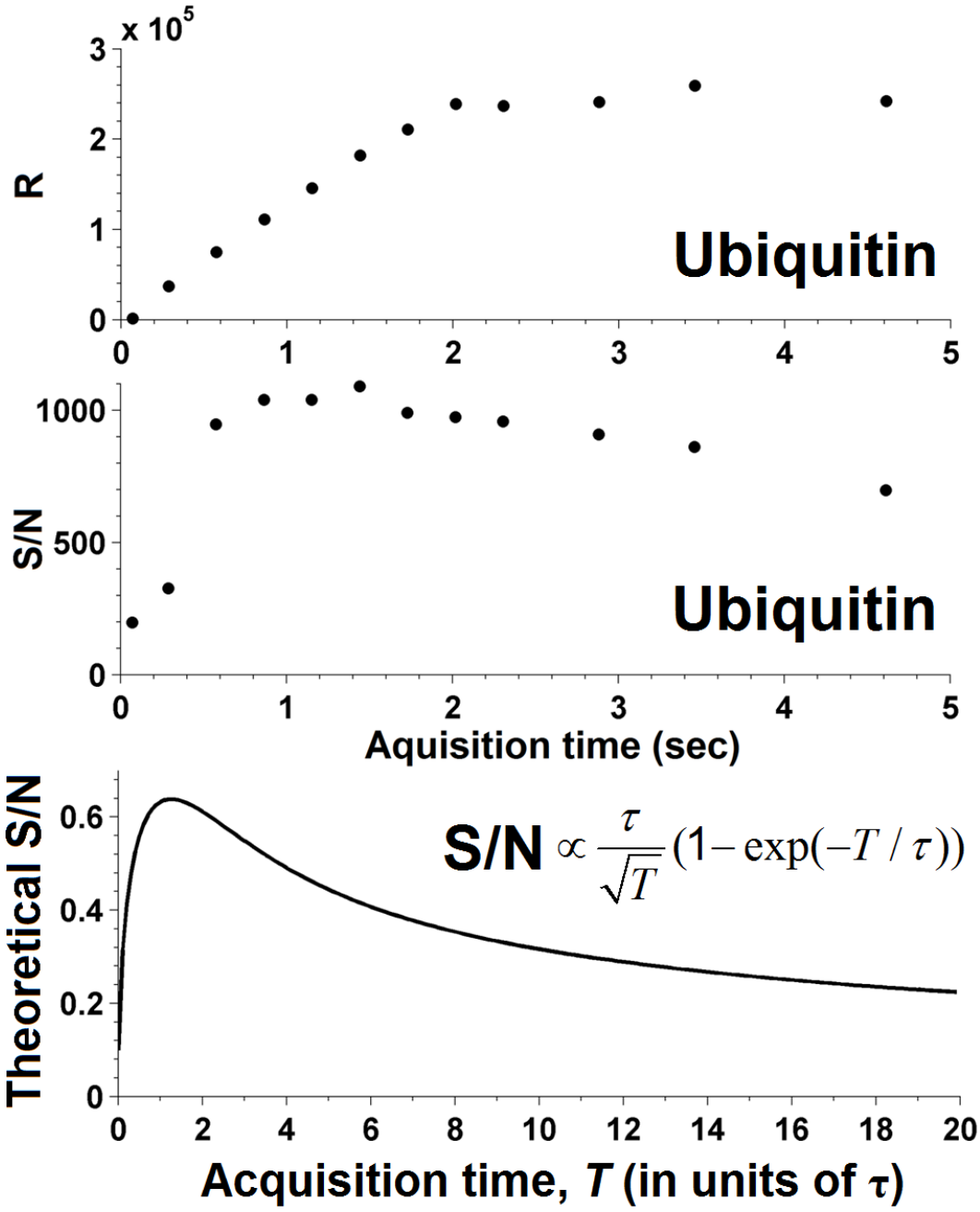

Figure 2.7 Top and middle: plot of transient acquisition time versus mass resolving power and S/N for the peak labelled in Figure 5 for the ubiquitin spectrum. Bottom: Relative S/N of a single transient as a function of data acquisition time, *T*, at a fixed damping factor, τ.

Such a non-linear variation of the resolving power results from the damping of the transient. After the excitation event, the ions' coherent motion will

experience frequent collision with other ions and gas particles, which speeds up the magnetron expansion and affects ions' cyclotron motion.[78-80] In an ICR cell, the trapping potential is nearly hyperbolic in the center, but becomes substantially anharmonic as radius increases. For a cubic cell, this results in a "squaring-off" of the electric potential near the edges. With substantial magnetron expansion or axial excitation, the ions will be exposed to increasingly inhomogeneous electric fields in both cyclotron and trapping motions, and therefore, the coherent ion packets dephase rapidly during the ion detection event, and results in an exponential damping on the signal intensity.

For a single scan transient (Eq2.6), assuming the scaling factor K=1 for simplicity, the amplitude factor $exp(-t/\tau)$ can be integrated, which results in the accumulated signal amplitude during the acquisition period, T (Eq2.11a). Knowing the noise level accumulated in the time-domain is proportional to the square root of T, and therefore, the variation of the time-averaged S/N for a single scan transient is revealed in Eq2.11b:

$$\text{signal intensity} \quad \propto \int_0^T \exp(-t/\tau)dt = \tau(1-\exp(-T/\tau)) \qquad (2.11a)$$

$$\text{S/N} \propto \frac{\tau}{\sqrt{T}}(1-\exp(-T/\tau)) \qquad (2.11b)$$

The theoretical plot (Figure 2.7 bottom) shows that at a fixed damping factor, the S/N of a spectrum saturated at around T=τ, and start to decrease afterwards. In a real experiment, the Coulombic repulsion and inhomogeneous electric field in the cell will cause an ion's frequency to shift and peak broadening, which further attenuate the S/N. Therefore, for the experimental data of ubiquitin, neither the resolving power nor S/N increases monotonically with the transient length.

Furthermore, Figure 7 also show that the resolving power of a peak is maximized at longer acquisition times than S/N, which means the optimal data acquisition time for the two parameters are not the same. So, how best can we balance RP and S/N during data acquisition? With a fixed frequency and high pressure model, the product of RP and S/N shows that an experimental optimal acquisition period is three times of the signal damping factor (T=3τ),[81] and an ideal transient is close to the one in Figure 5E. However, the above conclusion is a theoretical calculation based on ideal conditions; in real experiments, the sample is complex; thus the damping factors varies significantly with different ions, and also varies with instrument conditions, therefore, when acquiring a spectrum, in addition to monitoring the *m/z* spectrum, it is important to monitor the transient at the same time.

2.4.3 Transient and Peak Shape

During signal detection, the ion packets lose coherence due to ion-ion/ion-neutral collisions and other interferences, which causes an exponential decrease on the signal intensity even under low space charge conditions. Performing an FT on the general time-domain signal (Eq2.6) yields the mathematical expression on the frequency spectrum (in the conventional magnitude-mode):

$$f_m(\omega') = \frac{(KN_0/2\pi)\tau}{[1+(\omega-\omega')^2\tau^2]^{1/2}} \times \left\{1-2\exp(-T/\tau)\cos[(\omega-\omega')T]+\exp(-2T/\tau)\right\}^{1/2} \quad (2.12)$$

in which ω is the frequency of the ion of interest, ω' is the observed frequency, and other variables were defined previously.

In order to study the peak shape in the frequency spectrum, two extreme models of transient were assumed by choosing the data acquisition time:[82] First,

the zero-pressure model ($T<<\tau$) assumes an absence of collisions and constant signal intensity during data acquisition. Second, the high-pressure model ($T>>\tau$) assumes an exponential damping on the transient during the data acquisition. By considering the acquisition time, the peak shape of the two models can be expressed as follow:

$$fm(\omega') = \frac{(KN_0/2\pi)\sqrt{2}}{|\omega-\omega'|}\{1-\cos[(\omega-\omega')T]\}^{1/2} \qquad (T<<\tau) \qquad (2.13a)$$

$$fm(\omega') = \frac{(KN_0/2\pi)\tau}{[1+(\omega-\omega')^2\tau^2]^{1/2}} \qquad (T>>\tau) \qquad (2.13b)$$

The two models and the corresponding peak shapes are plotted in Figure 2.8. The peak shape shows a typical sinc function for a short acquisition time, and approaches a Lorentzian function when the signal damps to zero, and a gradual change of peak shape can also be observed from Figure 2.5. The peak shape from a real experiment involves the characteristics from the both functions; however, in the above text, T is suggested to be ~3x of τ in order to achieve the best performance. If this is done, the Lorentzian function will account for most of the peak shape as can be seen in Figure 2.5E.

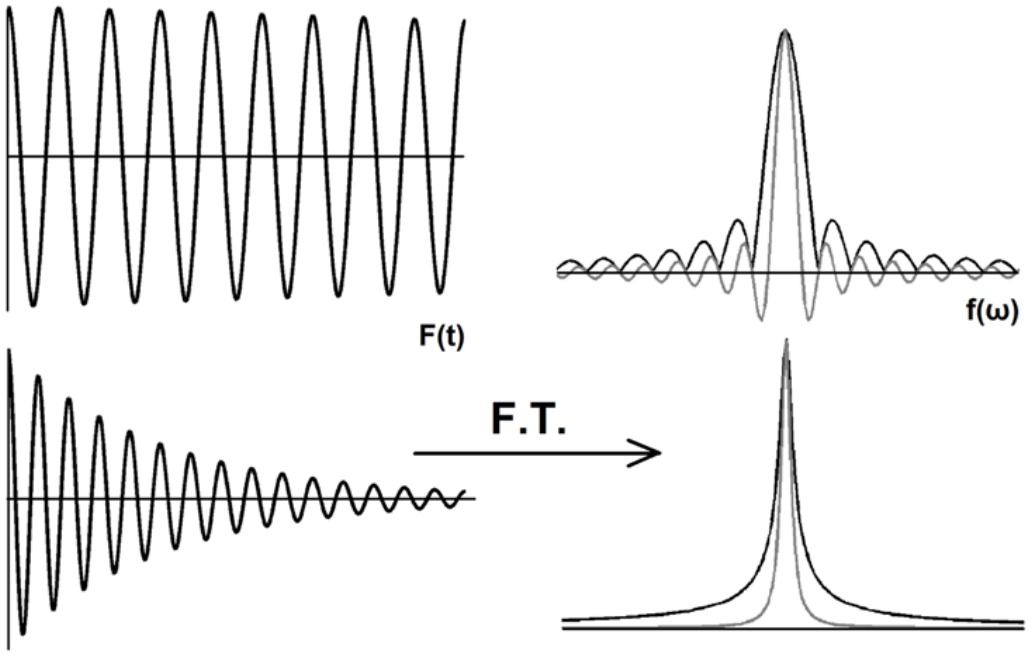

Figure 2.8 Simulated time-domain signals (left) and corresponding frequency-domain spectra after FT, with magnitude (black) and absorption-mode (gray) spectra (right). For $T<<\tau$, peak shape is Sinc function (top), for $T>>\tau$, peak shape is Lorentzian function (bottom). Adapted from Qi *et al.,* 2011.[83]

2.4.4 Data Size and Heterodyne Detection

According to Eq.10, the mass resolving power in FT-ICR is proportional to the duration of the transient. For this reason, high resolving power can be achieved by recording a transient as long as possible if it doesn't decay too much. In real experiments, the ion packets will gradually lose coherence during detection, and therefore, the effective transient that can be recorded is usually limited to several seconds, which occupies several megabyte (MB) of memory space. For example, in Figure 2.6, the 4.6 sec transient contains 4 mega data points (32 bit for each point) which requires ~16 MB computer memory.

Recently, Nikolaev *et al.* introduced the concept of a dynamically harmonized ICR cell, which has a space-averaging electric field instead of a truly quadratic field to retain an ion's cyclotron motion, and the original data shows that, by using the new cell, an ion transient can last for minutes without significant decay.[46] However, such an improvement on transient duration also creates a problem on data size. For example, in a 12 T instrument, the memory space required to record a 2 min transient with a low *m/z* cut-off at 200 is approaching 1 gigabyte (GB) according to Eq2.7. Even for a modern computer processor, 1 GB is too large to perform the FT, and additionally, the digitizers in the instrument only have a memory depth of a few million data points to store the transient.

To record a minutes-long transient for super-high mass resolving power, heterodyne mode (also called narrowband, mixer mode) can be applied for signal detection.[84] The heterodyne mode utilizes the trigonometric product-to-sum formula ($\cos\alpha*\cos\beta=[\cos(\alpha+\beta)+\cos(\alpha-\beta)]/2$), and the principle of heterodyne mode is illustrated in Figure 2.9. In the heterodyne mode, the original transient is multiplied by a reference frequency which is close to the signal of interest. Multiplying the signal frequency (f_1) with a reference frequency (f_2) results in a mixed signal with two frequency components: (f_1+f_2) and (f_1-f_2). By using a low-pass filter, the high frequency "carrier wave" component is discarded, and hence, the low frequency signal (f_1-f_2) which contains the information from f_1 to f_2 can be recorded at a much lower sampling rate, thus requiring less memory space. Meanwhile, as *m/z* is determined by frequency, the mass range detected in the heterodyne mode is also determined by the reference frequency applied, and therefore, the smaller (f_1-f_2) is, the

lower the sampling rate and narrower the mass range will be. For instance, if the frequency range of interest is 490-500 kHz (requires to be sampled at 1 MHz), by multiplying a reference frequency of 490 kHz, the resulting frequency range becomes 0 to 10 kHz, and the sampling frequency required is only 20 kHz, which is 1/50 of the original acquisition rate, for this reason, according to Eq2.7, the memory space required is also reduced to 1/50 of the original for the same total acquisition time.

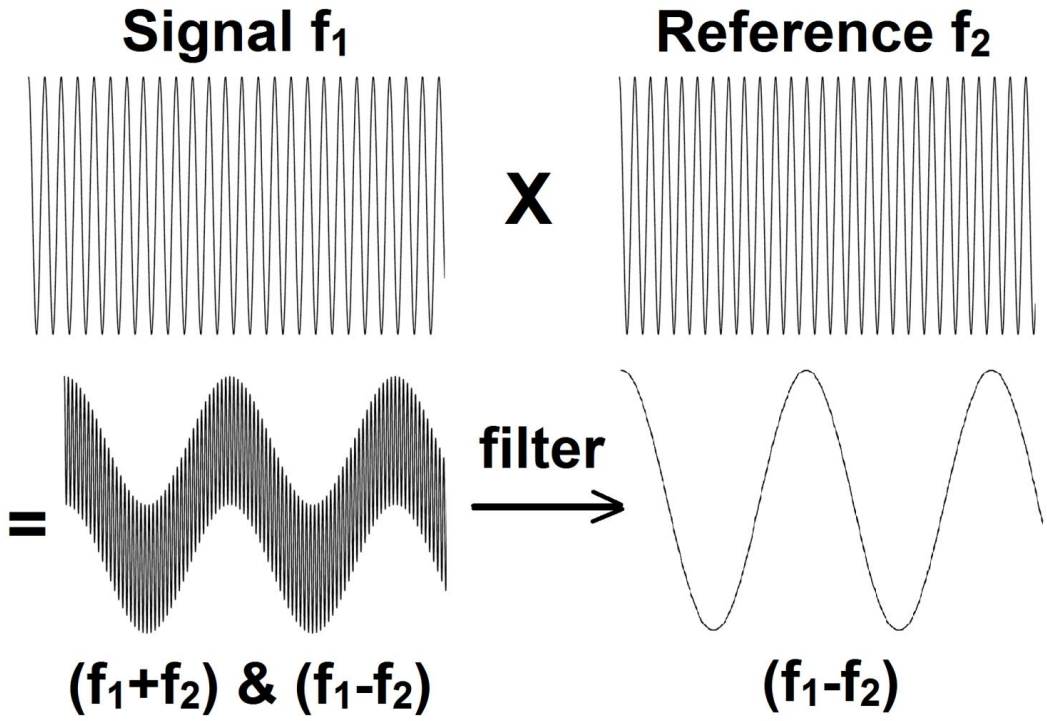

Figure 2.9 Principle of heterodyne mode detection.

2.5 Phase Correction

2.5.1 Fourier Transform, Magnitude-, and Absorption-Mode Spectrum

In FT-ICR, the original signal is a composite sum of sinusoidal waves with different frequencies recorded in the time-domain. Such a signal is Fourier

transformed to a frequency domain spectrum, (which can then be calibrated into the *m/z* domain).

Fourier transformation (symbolized as "FT[ ]") on a time domain signal, *F(t)*, produces a frequency spectrum with a complex output, *F(ω)*, consisting the absorption-mode spectrum, *A(ω)*, and the dispersion-mode spectrum, *iD(ω)*:[85]

$$\mathrm{FT}[F(t)]=F(\omega)=\int F(t)e^{-i\omega t}dt=\int F(t)(\cos\omega t-i\sin\omega t)dt=A(\omega)+iD(\omega)$$

(2.14a)

$$\phi(\omega)=\arctan[D(\omega)/A(\omega)] \qquad (2.14b)$$

$$M(\omega)=[\,(A(\omega))^2+(D(\omega))^2]^{1/2} \qquad (2.14c)$$

where the phase angle, *ϕ(ω)*, of the complex number can be calculated from the trigonometric relationship (Eq2.14b). Mathematically, *A(ω)* and *D(ω)* are the projection of *F(ω)* in the real and imaginary axis, which means they contain the same information with π/2 difference in phase.[86] However, as projection of *F(ω)* on the x- or y-axis ranges from positive to negative, both *A(ω)* and *D(ω)* have positive and negative values which makes their plots difficult to interpret (Figure 2.10). To overcome this problem, the absolute value of *A(ω)* and *D(ω)* is calculated (Eq2.14c) to yield a phase-independent magnitude-mode spectrum, *M(ω)*, which is plotted by all commercial and custom FT-ICR instruments.[87]

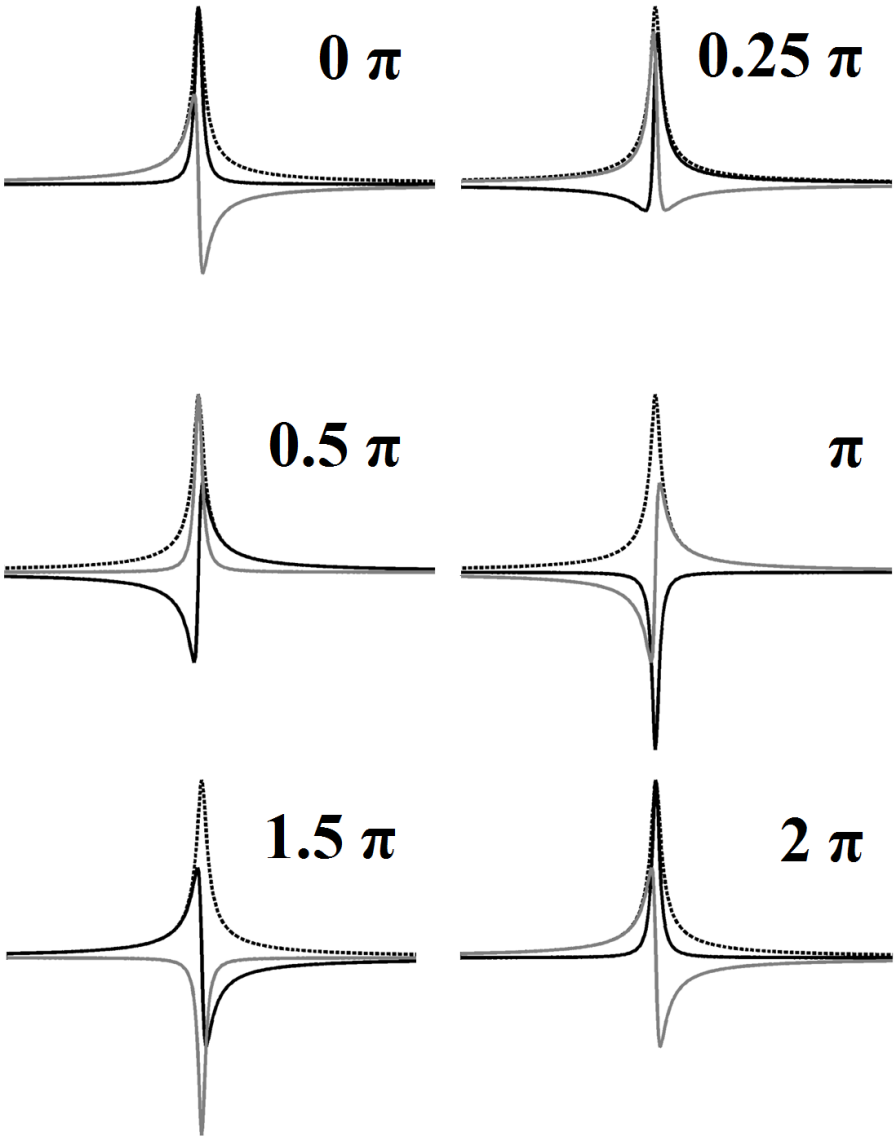

Figure 2.10 Peak shape of pure absorption- (black), dispersion- (grey), and magnitude-mode (dash line) spectra in Lorentzian function at different phase values.

2.5.2 Advantage of the Absorption-Mode

Development of FT-ICR is a history for pursuing higher resolving power.[88] Dating back to 1974, when the very first FT-ICR mass spectrum was obtained,[43] it was readily recognized that an absorption-mode spectral peak is inherently narrower than its corresponding magnitude-mode.[87] And through 40

years of research on this topic, it has been proved that the absorption-mode spectrum is preferable to the magnitude-mode for several reasons:

First, the peak width at half-maximum height (Δm) is narrower than its corresponding magnitude-mode by a factor depending on the damping of the transient (see Figure 2.8), from ~1.7 ($T>>\tau$, "Lorentzian" peak shape) to 2 ($T<<\tau$, "sinc" peak shape), without a concomitant loss in peak height.[83] In a real experiment, because the value of τ varies, the peak shapes in a spectrum are always a convolution of both a sinc and a Lorentzian function, and therefore, by plotting the absorption-mode spectrum, the theoretical improvement on resolving power is between 1.7 and 2.

Second, in absorption-mode, the S/N increases by $\sqrt{2}$. Phase correction aligns the data points (vectors) with the real axis of the complex space, and the noise from the imaginary part of the complex number does not get added into the absorption-mode spectrum. As the absorption-mode doesn't change the intensity of a peak, phase correction decreases the noise baseline level by $\sqrt{2}$ compared to magnitude-mode.[89] Such an improvement is equal to have a "quadrature detection" which requires two separate receiver coils for the instrument,[90] but here it is just data processing without extra cost.

Third, displaying the spectrum in absorption-mode can easily distinguish the common artifacts that exist in any FT-based mass spectrometer (FT-ICR, Orbitrap, and ion trap instruments), e.g., RF interference noise, harmonic, and intermodulation peaks. Such artificial peaks are usually immediately observed as they cannot be phased (Figure 2.11, details in section 2.9).

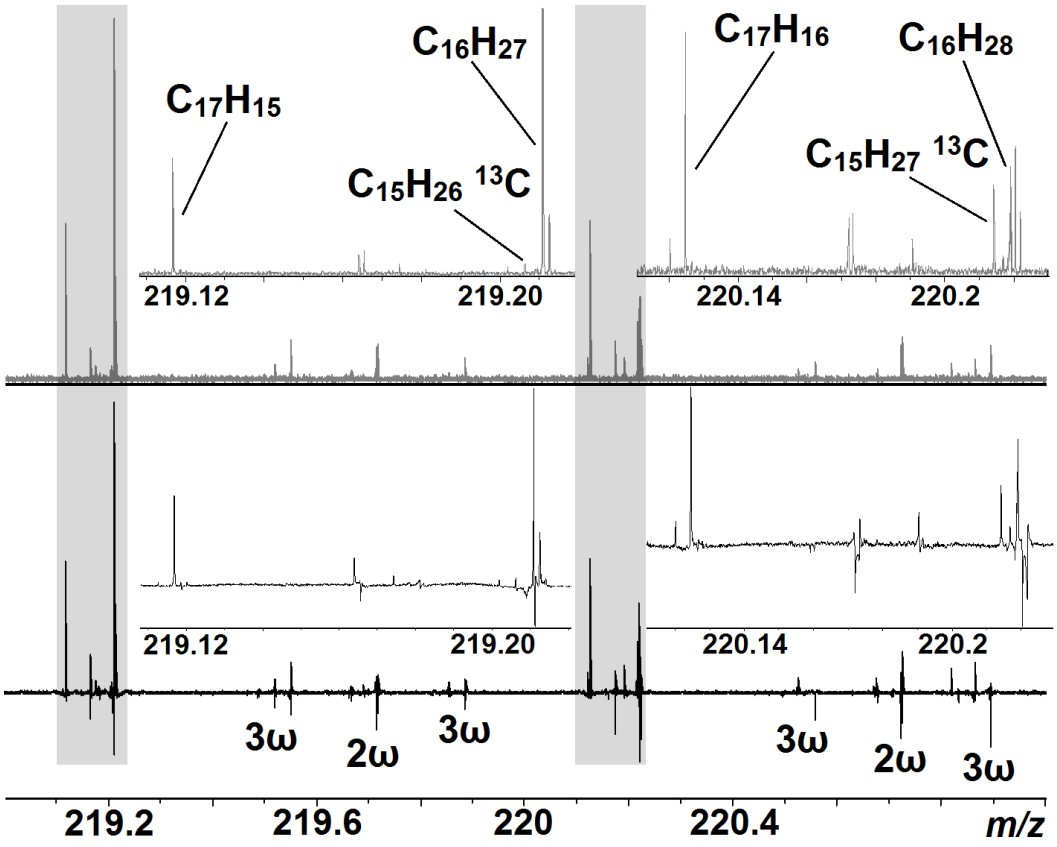

Figure 2.11 Close-up of an oil spectrum in both magnitude (grey) and absorption-mode (black), in *m/z* 219–221, showing the harmonics in a complex spectrum. Inset: zoom in on the shadow regions of two modes; only the labeled peaks are real peaks. Reprinted from Qi *et al.,* 2012,[75] with permission from Wiley, copyright 2012.

Fourth, during apodization,[71] a half window apodization is preferred in an absorption-mode spectrum for better peak shape and S/N, and the half window function retains the most intense signal at the beginning of the transient so that the absorption-mode signal will not be over-suppressed as often occurs in the magnitude-mode (see below for details on apodization). In summary, by plotting the spectrum in absorption-mode, the overall 'quality' of a spectrum can

be improved by more than 2x over the equivalent magnitude-mode at no additional cost.

2.5.3 Difficulties with Phasing

The absorption-mode spectrum offers a significant step towards improving the data quality of FT-ICR spectra. In Fourier transform nuclear magnetic resonance (NMR) spectroscopy, application of the absorption-mode was achieved in the 1970s.[91-92] Unfortunately, in FT-ICR, the pulse program involves a large and varying phase shift before the spectral acquisition event, and such a phase shift has hindered usage of the absorption-mode spectrum for almost 40 years.

The phase shift comes from two sources. First, for signal detection, ions in the ICR cell are excited to a larger orbital radius by a linear frequency sweep, and ions will undergo excitation once its cyclotron frequency matches the excitation waveform frequency. Thus, ions of different frequencies are excited at different times and accumulate a different total phase lag before the detection event. Second, because the amplitude of the excitation (*Vp-p*) is >100 V, whereas the signal from ions' image current is <mV, once the ions are excited, a delay time (in milliseconds) is required to settle the amplifiers before the detection event. During the delay time, all ions will continue their cyclotron motion and accumulate phase. In summary, before signal detection, all ions experience varying phase shifts, and any ion's phase, $\phi(\omega)$, is expected to vary with their excited frequencies; this phase shift follows a quadratic function:[93]

$$\phi(\omega) = -\frac{\omega_t^2}{2R} + \left(\frac{\omega_{final}}{R} + t_{delay}\right)\omega_t - \frac{\omega_0^2}{2R} + \varphi_0 \qquad (2.15)$$

where ω_0 and ω_{final} are the initial and final frequency of the frequency sweep applied, ω_t is the frequency when ions are excited at the time point t, R is its sweep rate, and φ_0 is the initial phase shift when the ions are transferred into the ICR cell (caused by the angular displacement between the excitation and detection electrodes). This function is the foundation to model and predicts ions' phase shifts in the ICR cell, and hence allows the phase shift to be assigned and corrected.

The wide range of the phase shift results in the "phase wrapping problem".[85] As any peak can be perfectly phased at a $\phi(\omega)$ between 0 and 2π, and this means that it is easy to phase a small *m/z* region in the spectrum, where the phase shift is <2π. However, according to trigonometric relationships, $\phi(\omega_i)=\phi(\omega_i)+2n_i\pi$ (Figure 2.10) for any integer n_i at any ω_i, which makes any phase angle beyond 2π return to 0-2π (known as phase wrapping). Consequently, it becomes essential to consider the additional $2n_i\pi$ into the phase angle for each peak in the spectrum. In FT-ICR, a typical excitation bandwidth ranges from kHz to MHz, which makes the accumulation of phase substantial (e.g., >10,000π for the *m/z* range from 200 to 2000 in a 12 T system). Finding the correct n_i for each peak (thousands of peaks in a spectrum) is crucial for phase correction, and this answers the question why virtually all FT-ICR instruments plot the spectrum in the magnitude-mode as calculating the phase shift accurately for each peak is difficult.

In recent years, general methods for producing absorption-mode spectra have been developed gradually. The method from Beu *et al.* requires a

specially modified instrument which can simultaneously excite and detect ions in the FT-ICR cell.[94] The method from Xian *et al.*[95-96] requires that the instrument records the experimental parameters and pulse program when the spectrum is acquired (e.g., excitation event, scan rate parameters, and the exact delay time between excitation and detection phase), to provide the accurate parameters for Eq2.15, which can then be used directly for phase correction. Unfortunately, commercial instruments either do not record these data or record it in an insufficient degree of accuracy, and apart from that, the parameters for Eq2.15 can be significantly different from the predicted values due to the image charge effect,[97] space charge, and other electric field inhomogeneities, which cannot be corrected by the above method.

2.5.4 Automated Broadband Phase Correction

The method, from Qi *et al.,*[68] generates a quadratic phase correction function of the following type:

$$\phi(\omega) = A\omega^2 + B\omega + C \qquad (2.16)$$

where *A*, *B*, and *C* are constants solved by quadratic least-squares fit and iteration. And the phased spectrum, *G(ω)*, can be produced by multiplying the raw spectrum, *F(ω)*, with the phase function, *ϕ(ω),* point-by-point (Eq2.17). The result, *G(ω)*, includes the pure absorption-mode, *A(ω)* (phase corrected), and pure dispersion-mode, *D(ω)* (π/2 different from the *A(ω)*), respectively.[98]

$$G(\omega) = F(\omega)\exp(-i\phi(\omega)) = \int F(t)e^{-i\omega t}e^{-i\phi(\omega)}dt = \int F(t)e^{-i(\omega t+\phi(\omega))}dt$$

(2.17)

Such a method only requires the ion transient and the spectral acquisition rate stored in the dataset, but no information from the pulse program is needed; therefore, this method allows phase correction to be largely automated to any FT-ICR spectrum worldwide. An automatic program--"Autophaser", based on advantages of this method has been developed, which provides a robust and rapid method for phasing FT-ICR data with minimal user interaction.[93]

2.6 Convolution and Apodization

2.6.1 Convolution and Convolution Theorem

Convolution is one of the most widely used concepts in conjunction with Fourier transform, because it greatly simplifies the calculation.[99] In mathematics, convolution is an operation on two time-domain function, *g(t)* and *h(t)*, which gives the integral over all space of one function as *u* multiplies another function at *t-u*:

$$g(t) \otimes h(t) = \int g(u)h(t-u)du \qquad (2.18a)$$

The convolution theorem states that the Fourier transform of a convolution is equal to the product of their Fourier transforms:

$$\mathrm{FT}[g(t) \otimes h(t)] = \mathrm{FT}[g(t)] \bullet \mathrm{FT}[h(t)] \qquad (2.18b)$$

and the theorem also works the other way around

$$\mathrm{FT}[g(t) \bullet h(t)] = \mathrm{FT}[g(t)] \otimes \mathrm{FT}[h(t)] \qquad (2.18c)$$

In any FT-based spectrometry, the observed response from an instrument can be regarded as convolution of the ideal time-domain response to an impulse excitation and the instrument excitation function,[100] and thus, the imperfect excitation can be deconvolved from the observed one in order to

recover the true signal.[101] The convolution theorem becomes important as it converts the integration into multiplication, simplifying the calculation.

2.6.2 Apodization

In spectroscopy applications, *g(t)* and *h(t)* from Eq2.18 have specific meanings, in which *g(t)* is usually a signal or data stream (e.g., Figure 12A), while *h(t)* is a response function, typically a curve which falls to zero in both directions from its maximum (e.g., Figure 12B). Normally, the response function is broader than the original signal, and thus, the effect of convolution is to smooth the raw signal *g(t)* in time according to the formula provided by the response function *h(t)*.

Spectra acquired from an instrument have a definite peak shape which associated with the instrument itself. As is mentioned above, in FT-ICR, the natural peak shape is a convolution of both sinc and Lorentzian functions (Figure 8), and the component from the sinc function contains undesirable sidebands at both sides of a peak, which cannot be avoided during spectral acquisition.[83] These wiggles contain no useful information but can interfere with the identification of adjacent peaks of low intensity. Therefore, during data processing, the time-domain transient is often multiplied by a window function prior to FT (Figure 12) to minimize the sideband intensities and smooth the line shape. Such procedure is called “apodization”, meaning "removing the feet", which is also an application of convolution theorem.[71] An optimal window function can smooth the sidebands but also inevitably degrades the S/N and resolving power of the spectrum.[102]

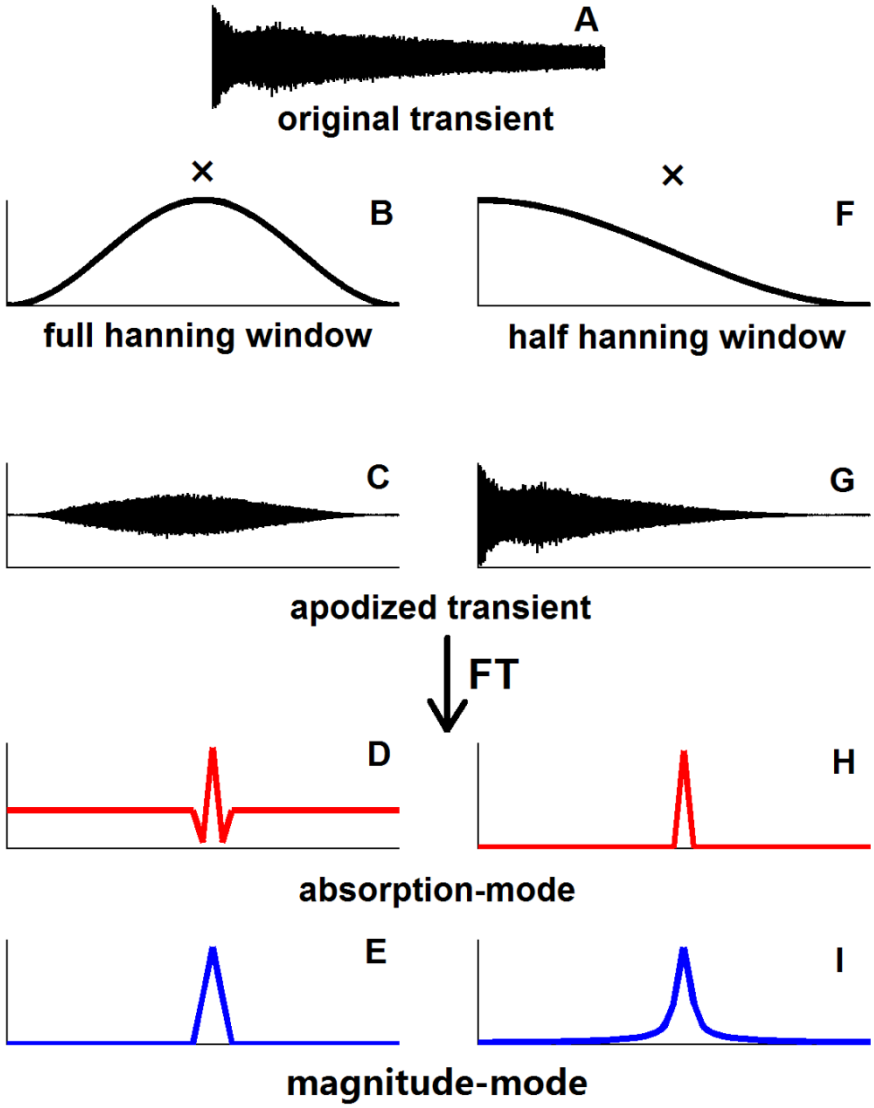

Figure 2.12 Transient, window function and its corresponding peak shape by simulation. A: original transient of a crude oil sample; B to E: full hanning window, apodized transient, and its corresponding peak shape in the absorption and magnitude-mode; F to I: half hanning window, apodized transient, and its peak shape in the absorption and magnitude-mode. Reprinted from Qi *et al.,*[89] with permission from American Chemical Society, copyright 2012.

The commonly used window functions in FT-ICR are listed in Table 2.1.[71] Theoretical treatments have been applied to FT-ICR transients in order to find the most advantageous window function.[103-104] Unfortunately, most window functions produce similar results in a given set of conditions, and the effect of apodization is largely dependent on the ratio of T/τ; however, it has been found that the magnitude- and absorption-mode spectra do better with different types of apodization.[105]

Name	Full (Magnitude-mode)	Half (Absorption-mode)
Rectangular	1	1
Cosine-bell	Cos(πn/N-π/2)	Cos(πn/2N)
Hamming	0.54-0.46cos(2πn/N)	0.54+0.46cos(πn/N)
Hann	0.5-0.5cos(2πn/N)	0.5+0.5cos(πn/N)
Gaussian	$\exp(-1/2((n-N/2)/kN/2)^2)$	$\exp(-1/2((n/2)/kN/2)^2)$
Blackman	0.42-0.5cos(2πn /N)+0.08cos(4πn/N)	0.42+0.5cos(πn/N)+0.08cos(2πn/N)
Triangle	1-|1-2n/N|	1-n/N

Table 2.1 Most commonly used apodization functions in FT-ICR, with the mathematical expressions for both full and half window. N is the total number of data points and n is the index of each data point $0 \leq n \leq N$.

The magnitude-mode plot is the standard spectrum produced by all commercial FT-ICR instruments (absorption-mode will be discussed in next section). A transient is a signal of the image current damping in the time-domain. By multiplying the transient with a window function as in Figure 2.12, the overall peak shape changes, which therefore affects the resolution, relative intensity, and S/N of the peaks after FT. In Figure 2.13, a crude oil spectrum was used for demonstration; the Fourier transformed spectra (plotted in same vertical scale)

show varying spectral intensity after apodization, because the window function changes the signal intensity at both the beginning and the end of the transient. By expanding the spectrum in the low *m/z* region (Figure 2.13J-L), it is clear to see that, after apodization, the sidebands of the peak are largely suppressed and the line shape becomes much smoother, while at the same time, the peak width is broadened. Such an effect is important for complex spectrum (e.g., from proteomics or petroleomics), where peak intensities vary over 1000x throughout these spectra. By using apodization, the low intensity peaks will suffer much less perturbation from adjacent intense peaks. When the peaks become dense in the high *m/z* region, apodization (especially a full window) suppresses the signal at the beginning of the transient, broadens the peak width, and consequently makes the doublet and triplet peaks unresolved (Figure 2.13M-O).

Apodization is a standard step during FT-ICR data processing, because it smooths the peak shape and facilitates the assignment. However, the benefit varies with the spectral conditions and also varies for different peaks in the same spectrum. Furthermore, the improved peak shape is generated at the cost of spectral resolution, and problems like frequency shifts, from image or space charge will often be “hidden”, as the peak shape is “smoothed out”. Thus, it is advisable to keep the raw spectrum and use apodization carefully.

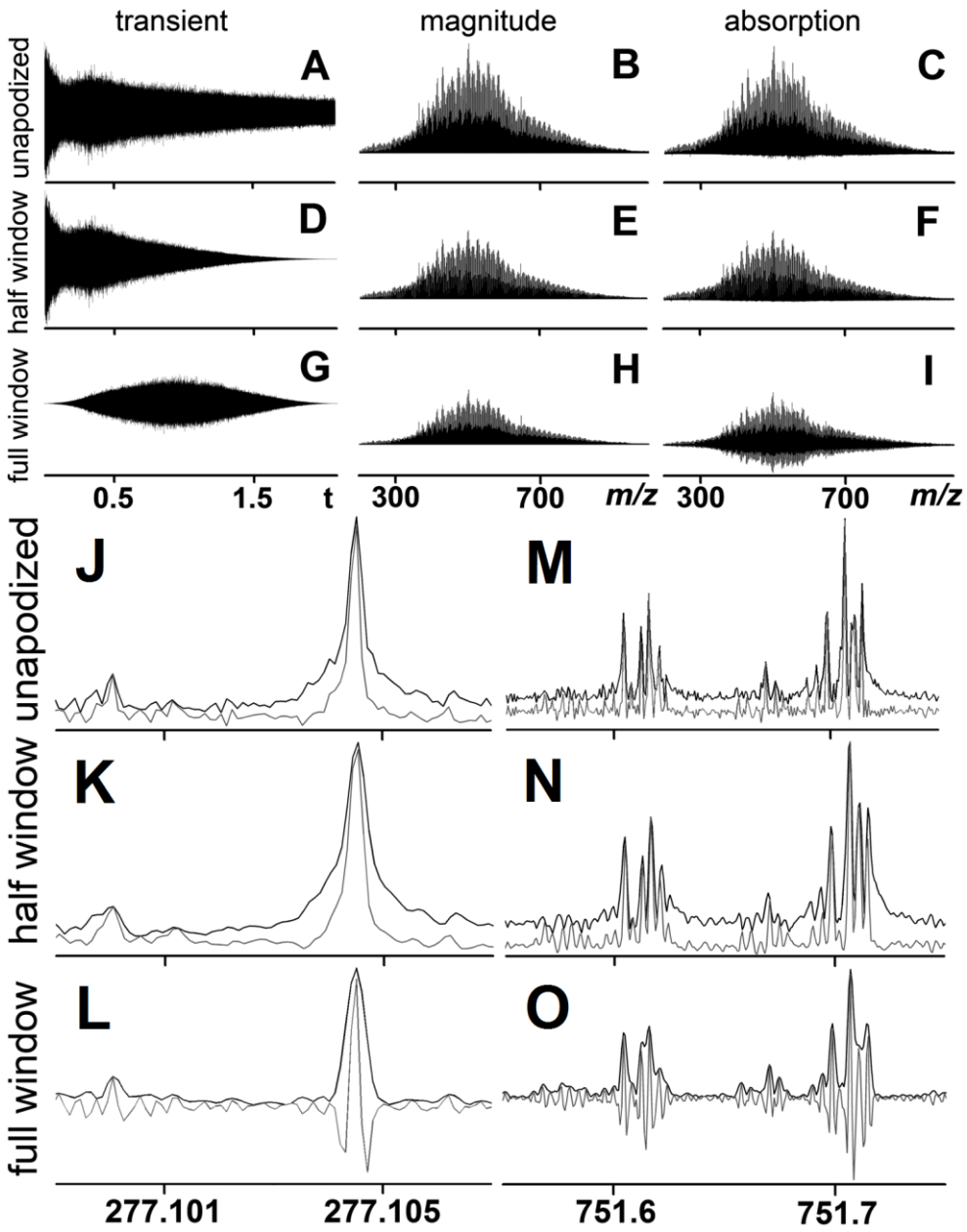

Figure 2.13 (A-C): Transient (left) and *m/z* spectra in magnitude- (middle) and absorption-mode (right) without apodization. (D-F): Transient and spectra with a half Hanning window apodization. (G-I): Transient and spectra with a full Hanning window apodization. (J-O): Close-up of two narrow *m/z* windows in both magnitude (black) and absorption-mode (grey). (J-L): *m/z* 414.308−414.335 with no apodization, half Hanning, and full Hanning apodization. (M-O): *m/z* 751.55−751.75 with no apodization, half Hanning, and

full Hanning apodization. Reprinted from Qi, et al.,[105] with permission from Springer, copyright 2013.

2.6.3 Full Window versus Half Window

Apodization reduces a peak's sidebands and smooth the line shape with a cost in S/N and resolving power. Although most window functions produce similar results, spectra in magnitude- and absorption-mode are affected differently by different types of window functions.

A window with its maximum at the beginning and minimum at the end is called "half window"; a symmetrical window with its minimum at two sides and its maximum in the middle is called "full window" (Figure 2.12). In the magnitude-mode plot, the full window after FT shows a narrower peak width and suppressed sidebands compared to the half window apodization, therefore, it is recommended in the magnitude-mode spectrum for best line shape and better resolving power. However, a full window function will generate large negative intensities in the absorption-mode after FT which is an interesting phenomenon reported by Comisarow *et al*. 24 years ago.[104] As is seen in Figure 13L&O, multiplying with a full window causes the peaks to show large negative intensities, which is a typical absorption-mode peak shape from a full window function. As the peaks become more closely spaced in the *m/z* domain, the negative sidebands start to interact with neighboring peaks and can severely distort the spectrum; such a problem can be fixed by using a half window function.[105] And in addition, the half window apodization in the absorption-mode normally results in a narrower peak width compared to a full window function in the magnitude-mode (Figure 12E&H).

An extra benefit is that the full window zeroes the signal at both beginning and end of the transient, while a half window function retains the most intense signal at the beginning. Therefore, using a half window apodization will cause less change in S/N and peak shape compared to the full window apodization. In summary, while no apodization is preferred for preservation of peak shapes and detection of space charge or electric field inhomogeneity effects, if apodization is required to facilitate peak picking and assignment, the full window and half window function are recommended for magnitude- and absorption-mode spectrum, respectively.

2.7 Zero Filling

2.7.1 Recovering the Information

As is mentioned above, during signal detection, a continuous image current cannot analytically be recorded as a continuous signal; instead, a discrete transient, *F(t)*, is sampled at 2x of the Nyquist frequency, and then recorded at *N* equally spaced intervals over the signal acquisition time, *T*: *F(t)=F(0), F(T/N), F(2T/N), F(3T/N),…,F((N-1)T/N)*. And FT on the discrete time-domain signal yields *N/2* complex data points at the frequency-domain,[106] with *1/T* Hz space interval: *f(ω)=f(0), f(1/T), f(2/T), f(3/T),…,f((N-1)/2T)*.

Initially, it appears like the information from the original transient will be lost during the FT process, as only *N/2* data points are generated. However, it should be noted that data in the frequency-domain are complex numbers, which contains two independent types of information: magnitude and phase. Furthermore, in the frequency domain, the highest frequency that can be recovered is the Nyquist frequency, which is the highest ion's frequency be

recorded in the spectrum. Hence, the spectral information is retained after the FT.

2.7.2 Recovering the Continuous Line Shape

The spectrum is plotted by connecting the individually discrete frequency points using a straight line; however, compared to a theoretical continuous spectrum, a straight line connection inevitably distorts the spectral line shape, as in most situations the signal frequency to be determined is not exactly the one of the frequency points used by the FT.[107-108]

For example, the peak apex in the discrete spectrum is not exactly its maxima in the continuous spectrum,[109] or the signal frequency deviates from the grid frequency of FT by a small value.[110]

Such distortion of line shapes causes peak broadening, auxiliary wiggles, and position shift, which will affect the “peak centroiding” algorithms for determining the peak location and intensity.[111-113] The most common interpolating procedure for “peak picking” is to fit the three highest points or more from a local peak to a pre-assumed peak shape (e.g., Parabolic, Gaussian, Lorentzian), and then calculate its theoretical apex.

Recovery of the continuous line shape can be greatly improved by zero filling, a method to extend the time-domain data by adding zeros at the end of the transient prior to FT. Consider if N zeros are added to the end of an N-points transient, the data size will then become 2N, therefore, the FT yields an N-points frequency spectrum, which is now equally spaced at the interval of *1/2T* Hz rather than *1/T* Hz. Although the time-domain is doubled, the frequency range of the resulting spectrum is still the same because the sampling rate of

the signal hasn't been changed. By doing this, the number of data points in the frequency spectrum is doubled, and a smoother line shape can be generated. Normally, the transient length is zero filled by a factor of 2^n, where n=1,2,3…, but in fact, n is valid for any positive value. If n approaches infinity, the discrete spectrum becomes identical to the true finite length continuous spectrum.

2.7.3 Number of Zero Fills

The discrete spectrum approaches the true continuous spectrum with infinite zero filling. However, each zero fill doubles the data size, and the computation time for FT increases substantially with the increasing data length.

In fact, zero filling is an interpolation of the existing data, rather than generating new information. Although zero filling is usually necessary to reduce the errors rising from the discrete line shape, to some extent, further zero filling is a waste of the computer memory. Such an effect is plotted in Figure 2.14, a 2 min transient of the reserpine $[M+H]^+$ ion was acquired using the harmonically compensated ICR cell,[75] the transient was recorded in heterodyne mode for 512 K data points. Notably, the signal of the transient almost didn't decay during the acquisition time; therefore, the low-pressure model can be applied here which predicts that the peak shape should have a typical sinc function. By setting the data points generated by FT, the connection between data size and spectral distortion is revealed from the corresponding spectra (plotted in the magnitude-mode). When the data points is truncated (64, 128, and 256 K), the peak shows poor, broad width and line shape, and each increase on data size can almost double the resolution of the spectrum; the peak starts to show a sinc function shape when the data points after FT equals the data points recorded in

the transient (no zero filling). After an extra zero fill, the peak shape becomes much smoother, and the resolving power increases just slightly. However, it is interesting to note that the increase reaches a plateau after two zero fills and the visual resolution of spectra are almost the same after that (2M and 32M spectra).

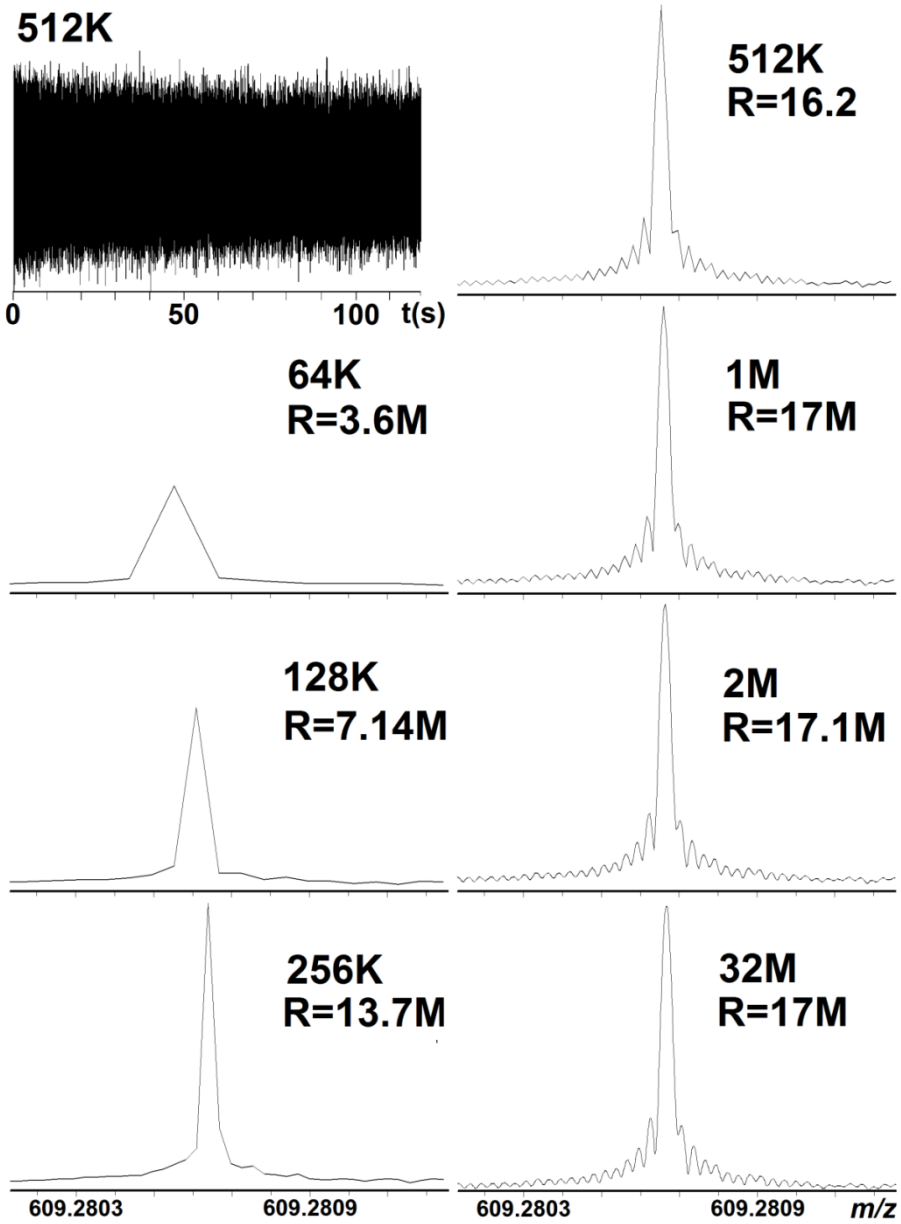

Figure 2.14 A two minute transient (512 K data points) of the reserpine $[M+H]^+$ ion acquired in heterodyne mode, and the corresponding *m/z* spectra with different number of zero fills in magnitude-mode.

Zero-filling is necessary for recovery of the information from a discrete signal; however, redundant zero fills also waste computation time without improvement in the spectral quality. Comisarow *et al.* have applied a theoretical calculation to estimate the maximum error on peak frequency and intensity from

a zero filled spectrum.[114] The maximum frequency error (Δf) occurs when the peak apex of a continuous spectrum falls exactly between two adjacent points in the discrete spectrum. As zero filling doubles the number of data points, the frequency error becomes $\Delta f / 2^{n+1}$ after n zero fills, which means even in the worst situation, each zero filling can still halves the frequency error. For determining the peak height, as is mentioned above, the peak shape varies depending on different models applied; the study measured the maximum error at different ratios of T/τ from 0 to 10. And the result shows that the all the errors in peak height are reduced to less than 2% by zero filling three times for the magnitude-mode spectrum, or four times for the absorption-mode spectrum (see below). Such a conclusion is drawn from the worst situation that the peak apex falls exactly between the two adjacent points in the discrete spectrum, and the ratios of T/τ is zero, which cannot happen in a real experiment. As is shown in Figure 2.14, even for a barely damped transient ($T/\tau \approx 0$), the peak shape and resolving power can be almost perfectly recovered by two zero fills.

2.7.4 First Zero Fill for the Absorption-Mode

Data from Comisarow *et al.* revealed that the absorption-mode spectrum required an extra zero fill compared to its corresponding spectrum in the magnitude-mode,[114] because the magnitude-mode spectrum contains two types of information: magnitude and phase, and calculation of the phase require the data points from both absorption- and dispersion-mode (Eq2.14b). If either of them is plotted separately, the information in the other will be lost, and therefore degrade the quality of the spectrum.[83] Fortunately, according to the

causality principle, the lost information on the absorption-mode spectrum can be recovered from the first zero fill.[106]

In theory, any function can be decomposed into the sum of an even and an odd function (Eq2.19):

$$x[n] = x_e[n] + x_o[n] \qquad (2.19a)$$

$$x_e[n] = \frac{x[n] + x[-n]}{2} \qquad (2.19b)$$

$$x_o[n] = \frac{x[n] - x[-n]}{2} \qquad (2.19c)$$

in which, x[n] is the original function, $x_e[n]$ and $x_o[n]$ represents its even and odd parts, and Eq2.19 is valid for any arbitrary function. Furthermore, if x[n] is causal (x[n]=0 when n<0, Figure 2.15a), it is then possible to recover x[n] from $x_e[n]$, or recover x[n] (n≠0) from $x_o[n]$ according to Eq2 .20.[115] And the validity of these relations is easily seen in Figure 2.15.

$$x[n] = 2x_e[n] \bullet u[n] - x_e[n] \bullet \delta[n] \qquad (2.20a)$$

$$x[n] = 2x_o[n] \bullet u[n] + x[n] \bullet \delta[n] \qquad (2.20b)$$

where

$$u[n] = \begin{cases} 0, n<0 \\ 1, n \geq 0 \end{cases} \qquad (2.20c)$$

$$\delta[n] = \begin{cases} 1, n=0 \\ 0, n \neq 0 \end{cases} \qquad (2.20d)$$

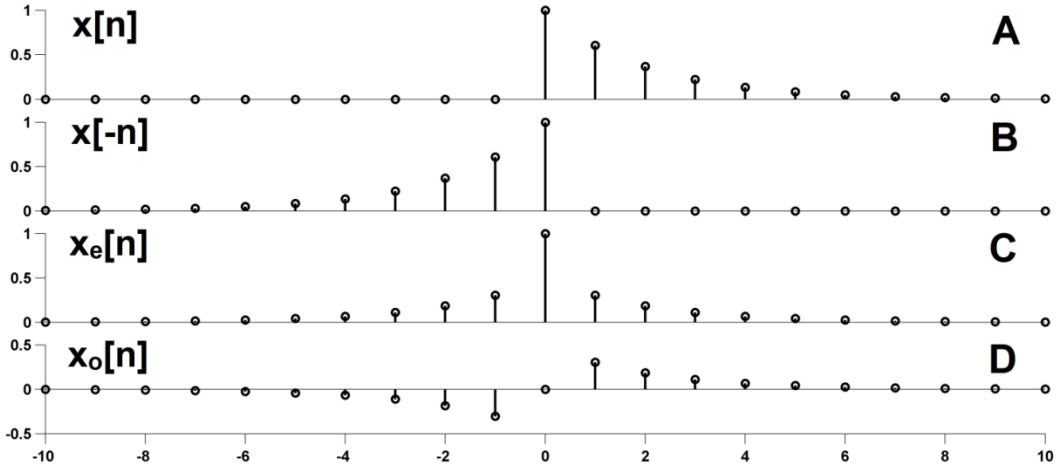

Figure 2.15 Even and odd parts of a causal sequence, x[n].

According to Eq.14a, it is obvious that A(ω) and iD(ω) are the even and odd parts of F(ω), which means that if the original signal F(t) is causal, F(ω) can then be recovered from either A(ω) or iD(ω).[116] However, the time-domain signal in the real world starts from t=0, in order to generate a causal signal, an equal length of zeros is added manually to F(t) by the first zero fill.

2.8 Space Charge and Mass Calibration

2.8.1 Calibration Functions

Operation of FT-ICR requires implementation of a mass calibration equation to convert experimentally measured frequencies of ions into the corresponding *m/z* value. Before the 1970's, the FT-ICR used a drift ICR cell, which measured the undisturbed cyclotron frequency of an ion (Eq2.1), however, the transient acquired was only in a few milliseconds in duration as the ions were not trapped in the z axis,[117] and thus the mass resolving power was no more than several hundred. In 1974, the trapped ion analyzer cell was introduced, in which ions can be confined in the z axis by applying an electric

field,[43] however in such a circumstance, the ion's motion is slightly distorted, and the frequency being detected is the "reduced cyclotron frequency" (Eq2.5a). In that paper, mass resolving power over 2500 was achieved at *m/z* 128, and the corresponding mass accuracy ranges from 7 to 151 ppm over the *m/z* 47 to 264. Later with the development of FT-ICR instruments, a mass resolving power over 10^5 at *m/z* 156 was obtained from a cubic trapped ion cell,[118] and such resolving power has been routinely achieved since the 1990's. Given a mass resolving power over 10^5, the isotopic distribution of multiply charged peptides or small proteins can be revealed in the spectrum,[76] extremely high mass accuracy becomes essential for unambiguously determining the elemental composition of the ions, and therefore, an accurate calibration function is required to convert the detected frequency of ions to their true *m/z*.

Typically, one of two calibration functions are commonly used for calibrating the FT-ICR spectrum: the Ledford equation[119] and the Francl equation,[118] both originate from the ion's motion in a spatially uniform magnetic field plus a three-dimensional axial quadrupolar electrostatic potential (Eq2.4). The frequency recorded during signal detection is the "reduced cyclotron frequency", ω_+, dividing Eq2.4 with *mr*, and replacing *q* with *ze* leads to the Ledford equation:

$$\frac{m}{z} = \frac{eB}{\omega_+} - \frac{eV_T\alpha}{a^2\omega_+^2} \qquad \text{or} \qquad \frac{m}{z} = \frac{A_{Ledford}}{\omega_+} - \frac{B_{Ledford}}{\omega_+^2} \qquad (2.21a)$$

in which

$$A_{Ledford} = eB \qquad (2.21b)$$

$$B_{Ledford} = \frac{eV_T\alpha}{a^2} \qquad (2.21c)$$

The other similar approach for mass conversion formula was proposed by Francl *et al*., which is derived from ion's magnetron motion. Substituting ω_z from in Eq2.5 results

$$\omega_{\pm}=\frac{\omega_c}{2}\pm\frac{\omega_c}{2}\sqrt{1-\frac{4V_T\alpha m}{zeB^2a^2}} \qquad (2.22a)$$

here, $eB^2a^2/4V_T\alpha$ is called the "critical *m/z*",[45] which is the upper *m/z* limit when ions can no longer be trapped in ICR cell (e.g., for a 9.4 T instrument, the *m/z* limit is ~5,000,000). Replacing the "critical *m/z*" term in Eq.22a results in a new expression for the magnetron motion, ω-:

$$\omega_{-}=\frac{\omega_c}{2}-\frac{\omega_c}{2}\sqrt{1-\frac{m/z}{(m/z)_{crit}}} \qquad (2.22b)$$

and assuming $m/z<<(m/z)_{crit}$, therefore, the Taylor approximation ($(1+x)^n\approx1+nx$, $x<<1$) can be applied to eliminate the square root in the equation:

$$\omega_{-}=\frac{\omega_c}{2}-\frac{\omega_c}{2}\sqrt{1-\frac{m/z}{(m/z)_{crit}}}\approx\frac{\omega_c}{2}-\frac{\omega_c}{2}\left(1-\frac{m/z}{2(m/z)_{crit}}\right)=\frac{V_T\alpha}{Ba^2} \qquad (2.22c)$$

the resulting Eq2.22c is also a good approximation of ion's magnetron frequency (independent of *m/z*). And the Francl equation is thus generated:

$$\omega_{+}=\omega_c-\omega_{-}=\frac{ezB}{m}-\frac{V_T\alpha}{Ba^2} \qquad (2.22d)$$

$$\frac{m}{z}=\frac{eB}{(V_T\alpha/Ba^2)+\omega_{+}}=\frac{A_{Francl}}{B_{Francl}+\omega_{+}} \qquad (2.22e)$$

in which

$$A_{Francl}=eB \qquad (2.22f)$$

$$B_{Francl}=\frac{V_T\alpha}{Ba^2} \qquad (2.22g)$$

In practice, although the calibration constants are in principle known, they are usually determined by calibration. Mass calibration consists of least

squares fitting for either Eq2.21a or Eq2.22e to the frequencies of two or more peaks of known *m/z* values to yield either constants $A_{Ledford}$ and $B_{Ledford}$, or A_{Francl} and B_{Francl}. This equation is then used to calculate the *m/z* scale from the known frequency scale. The two calibration functions above are essentially equivalent within the usual mass range and can be interconverted.[120] However, the Ledford equation can be used whenever the cyclotron motion is stable, namely, $m/z<(m/z)_{crit}$, while the Francl equation is used in a more restrictive condition given the prerequisite $m/z<<(m/z)_{crit}$, and consequently, the calibration error from the Francl equation increases monotonically with increasing *m/z*, and may fail at a sufficiently high value particularly in a small magnetic field instrument.

2.8.2 Space Charge Effect

The mass error from measurement caused by different experimental conditions and parameters from scan to scan (e.g., the trapping potential applied, stability of the magnetic field, variation of the ion population) is inevitable. Currently, it is possible to routinely achieve mass measurement accuracy (MMA) better than 1 ppm level over a broad *m/z* range via internal calibration.[121-122] However, such performance is also the lower limit of the two calibration functions above; routine MMA <0.1 ppm can hardly be achieved by a simple implementation of the two equations. The major contributor to mass errors below 0.1 ppm is attributed to the space charge effect rising from the columbic repulsion between ions during the detection of the time-domain signal.[123] Similar to the electric field applied, the ion space charge causes frequency shift, and such a perturbation is highly dependent on the total ion

number in the cell.[124] Although the sensitivity and dynamic range of the image current detector increases with the number of ions trapped in the cell, the accuracy of measurement tends to decrease significantly,[125] and in extreme cases, the space charge effect can cause the transient to collapse and die out in a very short time, a phenomenon called “the spontaneous loss of coherence catastrophe”.[126-127]

The space charge results from ions’ columbic interaction with each other. The total potential field from space charge that a charged particle experiences in a system can be calculated as:

$$\Phi(x, y, z) = \frac{q^2}{4\pi\varepsilon_0} \sum \frac{1}{r_i} \qquad (2.23)$$

Where x, y, z is the position of the particle, ε_0 is the permittivity constant, and r_i is its distance to the ith ions. Such a potential affects the quadrupolar potential gradient, the trapping potential applied in the ICR cell, and the image charge on the detection electrodes.[97]

Ledford and Francl equations can be adjusted to correct for a variation of the magnetic field strength, geometry of the ICR cell, trapping potential, and partially compensate for the influence from columbic interaction by assuming all the ions are in the same “global” space charge condition. However, apart from the “global” space charge, each ion cloud present in the cell also experiences “local” interactions with other ion clouds.[128] In 1983, Jeffries *et al.* have derived the analytical expression of ion’s frequency in a scanning ICR cell including the space charge effect:[123]

$$\omega_{\pm}' = \left(\frac{\omega_c}{2}\right)\left\{1 \pm \left[1 - 4\left(2qV_T\alpha / ma^2 + \rho q^2 G_i / \varepsilon_0 m\right) / \omega_c^2\right]^{1/2}\right\} \qquad (2.24)$$

where G_i is a geometry factor depending on the shape of the ion cloud, and other parameters have been defined above. Although the above expression has been proposed for 30 years, none of the commercial instruments apply the local space charge term, $\rho q^2 G_i/\varepsilon_0 m$ to mass calibration, and for this reason, there is room for considerable improvement in the MMA by using an additional calibration term to empirically correct for the “local” frequency perturbation.

2.8.3 Correcting for Ion Population and Local Space Charge

The conventional calibration functions struggle to achieve sub-ppm MMA. Due to space charge effects, particularly the “local” space charge, the number of ions trapped in the ICR cell should be considered during the measurement in order to achieve better MMA. In an FT-ICR experiment, the normal principle to achieve high MMA is to acquire spectra with small ion populations (minimize space charge), average the signal of multiple spectra, and mass calibrate internally. By contrast, external calibration can never provide accuracy better than a few ppm because the ion number for a measurement varies from experiment to experiment. Changes in both “global” and “local” space charge conditions can severely degrade the ability for the Ledford and Francl equation to accommodate the frequency shift.

Masselon *et al.* have pointed out that in addition to the “global” space charge for all the existing ions (which can be compensated by internal calibration), each individual ion cloud experiences different interactions with other ion clouds, called a “local” space charge effect, and this effect become crucial when the frequencies are measured to a precision better than 0.25 Hz (corresponding to a mass error of ~1 ppm depending on the magnetic field).

Furthermore, the space charge of local ion clouds varies with the specific ion abundance over a wide range.[128] To correct for such frequency shifts, the constant *B* in the Ledford equation is redefined by two separate parts:

$$B = B_{trap} + B_{sc} \qquad (2.25a)$$

$$B_{sc} = K \bullet I_{total} \qquad (2.25b)$$

here B_{trap} accounts for the term "$2qV_T\alpha/m$" (trapping potential and cell geometry) in Eq2.24, while B_{sc} represents for the term, $\rho q^2 G_i/\varepsilon_0 m$ (space charge). By assuming that the space charge is proportional to the total ion population (I_{total}), and utilizing the feature of FT-ICR spectrum that peak intensities are proportional to the total ion charges of the corresponding ions,[69] B_{sc} can be expressed in terms of I_{total} multiplied by a constant *K*. Wineland and Dehmelt have pointed out that an ion cloud of its individual *m/z* cannot affect itself mostly, for an exception see Wong & Amster, 2007.[129] Thus, ions of a certain *m/z* only experience interactions from other *m/z* clouds,[130] for this reason, the peak intensity of the ion clouds itself (I_i) should be subtracted from the function:

$$\frac{m}{z} = \frac{A}{f} + \frac{B + B_{total}}{f^2} - \frac{K \bullet I_i}{f^2} = \frac{A}{f} + \frac{B}{f^2} + \frac{C \bullet I_i}{f^2} \qquad (2.26)$$

The resulting new calibration law is proposed by Masselon *et al.*[128] By adding the term $C \cdot I_i/f^2$, the new function not only corrects the "global" space charge presents in the ICR cell environment, but also the accounts for the "local" space charge experienced by each individual ion cloud.

Following on Masselon's work, Muddiman *et al.* also reported a similar calibration law based on the Francl equation to correct both total ion abundance and individual ion abundance fluctuations.[131] By applying the new calibration law to a series mass spectra of singly charged polypropylene glycol (PEG) with

an average mass of 1000 Da, the mass accuracy can be improved by 2 fold using internal calibration, and over 10 fold using external calibration.[132]

2.8.4 Ion Population on External Calibration

As is mentioned above, internal calibration compensates for the "global" space charge effect because the ions being detected are exposed to an identical experimental environment, and therefore, the conventional calibration laws can routinely approach MMA of ~1 ppm level.[122, 133] Meanwhile external calibration only performs well when the calibrant and the analyte spectra are measured under the same conditions (e.g., same instrument, trapping potentials, excitation voltage, and transient duration); however, the ion population cannot always be reproduced from one experiment to another, especially in LC-MS, MALDI, and imaging experiments, whose chaotic nature produces scan-to-scan variations on the number of ions even for the same analyte.

When dealing with unknown samples, an external calibration function acquired using the same experimental parameters can be applied, and external calibration offers a simpler pulse sequence and higher throughout because an internal calibrant is not always feasible. However, if the space charge effect is ignored, the external calibration can result in mass errors of hundreds of ppm, and such error is even worse for spectra with a larger frequency range or with many components in the sample.

To employ external calibration on an unknown sample with decent MMA, new calibration equations sensitive to the ion abundance have been reported. In 1990, Cody patented a method which accounts for the differences on total

ion population between calibrant and analyte spectra. The difference on ion number was estimated by generating a calibration curve and comparing the trapping voltage to the total ion population for a calibrant compound, and then utilized to correct the analyte spectra, based on relative ion current and trapping voltages.[134] In 1999, Easterling *et al.* proposed a correction equation (Eq2.27) to predict the frequencies of the analyte when the space charge environment of the calibration spectrum is applied:

$$f_{est} = f_{mea} + c(I_{cal} - I_{ana}) \qquad (2.27)$$

here I_{cal} and I_{ana} refer to the total ion intensities of the calibrant and analyte spectrum, c is the slope of the frequency versus total ion intensity plot, f_{mea} is the measured frequency in the analyte spectrum, and the resulting f_{est} is the estimated frequency of the analyte if the space charge environment of the calibrant is applied. Therefore, f_{est} can be used in Eq.28 to determine a more accurate *m/z* value for external calibration.

$$\frac{m}{z} == \frac{A}{f_{est}} + \frac{B}{f_{est}^{2}} + \frac{C}{f_{est}^{3}} \qquad (2.28)$$

The above research shows that, in the absence of the correction strategy, the mass error can be as large as 220 ppm, however, by applying the new calibration law, Easterling and co-workers achieved a RMS mass error of 3.1 ppm from 20 measurements of the mass of bovine insulin B-chain (*m/z* ~3495) externally calibrated with polyethylene glycol (PEG) 3400. Later, based on the work from Easterling[124-125] and Masselon[128], Muddiman and co-workers developed a novel external calibration law utilizing multiple linear regression, thus allowed the mass error <1 ppm for automatic gain control FT-ICR measurements which also extends the dynamic range of the instrument for accurate mass measurement[132, 135]. Very recently, Smith *et al.* applied

Muddiman's multiple linear regression method to FT-ICR MS imaging spectrum [24], and demonstrated that ion abundance fluctuations in imaging can be corrected by addition of total and relative ion abundances terms. The external calibration over an entire tissue section obtained a RMS error of 0.158 ppm on 16,764 peaks,[136] which is even better than conventionally internal calibration. Such a result is attractive for high output imaging experiments because the external calibration is much more straightforward and can be employed easily in routine experiments.

For future work, to further improve the calibration law, efforts can be taken in the following directions: 1) To correct the ions' post-excite radius, as it has been reported that during signal detection, the uncertainty in cyclotron radius, namely, the peak intensities been acquired, varies by ±10%;[137-138] such an error certainly limits the estimation of ion population. 2) To consider the factor of ion kinetic energy, although the ion's cyclotron frequency caused by the magnetic field is theoretically independent of kinetic energy, the velocity fluctuations caused by ion optics during transfer still change the ion's axial kinetic energy and will more or less affect their cyclotron motions in the ICR cell.[139] 3) To account the ions with baseline intensity, as all estimation of "total ion number" fail for real samples, which have many components in the baseline which should be accounted for in mass calibration. 4) To correct the relativistic velocity induced mass defect caused by relativistic velocity, as Einstein's mass-velocity equation states that the mass of a body is not constant:

$$m = \frac{m_0}{\sqrt{1-\frac{v^2}{c^2}}} \qquad (2.29)$$

where m_0 is the rest mass of the body, v is its velocity, and c is the speed of light. In FT-ICR, an ion's cyclotron frequency is in the level of hundreds of kilo Hz, for example, in the 12 T instrument, an ion of *m/z* 230 has a cyclotron frequency of ~800,000 Hz. Assuming the ion is excited to an orbital of 1cm for signal detection; such an ion will travel at a velocity of ~50240 m/s, which causes a mass defect of 14 ppb according to Eq2.29. Currently, the field is struggling to routinely achieve the MMA in 0.1 ppm, which means the mass error induced by the above factors is negligible. However, physicists have achieved 0.1 ppb MMA in measuring single atom using a Penning trap (prototype of the ICR cell) for over 20 years,[140] which clearly points out the potential of FT-ICR performance, and at such level of accuracy, the relativistic correction will be important.

2.9 Artifacts in FT-ICR Spectra

2.9.1 Radio-Frequency Interference

The peaks in an FT-ICR spectrum represent the frequency of the ions' cyclotron motion, while artifacts that result from transient distortion and radio-frequency interference (RFI) also exist as peaks in the spectrum. The artifacts are inevitable spectral features; they contain no chemical information, but can complicate the task of data interpretation.

Artifacts induced by RFI are noise signals from the detection lines. In an FT-ICR instrument, power supplies, turbo pumps, RF oscillators, ion gauges, and even the DC voltages on the ion optics can be the source of RFI, and thus introduce electronic peaks into the final *m/z* spectrum. Typically, electronic peaks are single peaks without isotopic patterns; therefore, if the RFI peaks do

not overlap with real peaks, they can usually, but not always, be easily recognized in the spectrum.

2.9.2 Harmonics and Intermodulation Frequencies

The harmonics are the most common artifacts existing in any FT-based mass spectrometer (FT-ICR, Orbitrap, and ion trap). Different from the RFI, harmonic peaks are not real signals, they are generated inherently during the FT due to non-sinusoidal features of real signals. Odd harmonics are mostly generated by non-sinusoidal image current from finite-size detection electrodes, saturation of the amplifier, or overloading the analog-to-digital converter; even harmonics are mostly generated by non-zero magnetron radius, misalignment of the cell with the magnetic field, or imbalance of the excitation or detection amplifiers.[141-142]

Suppose that the original time-domain signal *f(t)* consists of two frequencies, ω_A and ω_B, with different amplitude A and B (Eq2.30a). When the signal is affected by the above reasons, the output becomes a non-linear signal, *f(t)'*, which can then be expressed as a power series of *f(t)* in general (Eq2.30b):

$$f(t)=A\cos(\omega_A t)+ B\cos(\omega_B t) \quad (2.30a)$$

$$f(t)' = c_1 f(t)^1 + c_2 f(t)^2 + c_3 f(t)^3 + \ldots + c_n f(t)^n \quad (2.30b)$$

If the first two terms in Eq.30b are considered and expanded by trigonometric relationships as *f(t)"*:

$$f(t)'' = c_1 A\cos(\omega_A t) + c_1 B\cos(\omega_B t) + c_2 A^2\cos^2(\omega_A t) + c_2 B^2\cos^2(\omega_B t) + 2c_2 AB\cos(\omega_A t)\cos(\omega_B t)$$
$$= c_1 A\cos(\omega_A t) + c_1 B\cos(\omega_B t) + \frac{c_2 A^2}{2}\cos(2\omega_A t) + \frac{c_2 B^2}{2}\cos(2\omega_B t) + c_2 AB\cos(\omega_A + \omega_B)t + c_2 AB\cos(\omega_A - \omega_B)t + \frac{c_2 A^2}{2} + \frac{c_2 B^2}{2} \quad (2.30c)$$

As is shown in Eq2.30c, in the approximation of the distorted transient, the real signals ω_A and ω_B are still present as the dominant frequencies, but many other frequencies are added, like $2\omega_A$ and $2\omega_B$ (referred as "harmonics"), $\omega_A+\omega_B$ and $\omega_A-\omega_B$ (referred as "intermodulation"). Although the intensity of the artifacts is usually minor, all these frequencies will still exist in the spectrum after FT.[143-144] When the spectrum is complex, these artifacts can overlap with real peaks, deteriorate the S/N, and cause confusion for data interpretation. Additionally, if the mass calibration applied includes the ion intensity term (see the previous section), all the artifacts will be accounted for the total ion population, and thus introduce error into the mass measurement.

The artifacts affect the performance of the FT-ICR instrument; unfortunately, they can never be avoided in the experiment. Generally, identifying RFI requires careful monitoring of the isotopic patterns, while identifying harmonics requires comparison and correlation of the peaks to higher *m/z* (lower frequency) primary signal peaks. The above methods can be time consuming, and are largely limited to simple mixtures, or clean samples, thus, can be very difficult for complex samples. By contrast, artifacts can be easily observed in the absorption-mode spectrum by their anomalous phase variation (Figure 2.11), because neither the harmonics nor RFI experiences ion's cyclotron motion in the ICR cell, and therefore, cannot normally be phased correctly using the instrument's current phase function [75].

2.10 Conclusions and Future Prospects

Being the most advanced mass analyzer, FT-ICR intricately couples the advanced physics techniques, instrumentation, and electronics with chemical

and particularly biochemical research. However, its software development lag relative to instrumentation due to the lack of sufficient attention and investment, and for this reason, there is much room for improvement. And additionally, professional skill is still the key to achieve high performance of FT-ICR. This chapter takes into account the non-ideal behaviour of magnetic and electric fields, explains the details of FT-ICR data processing, and thus can be used as a tutorial for practitioners to understand data processing in FT-ICR MS.

Chapter 3

Phase Correction of Fourier Transform Ion Cyclotron Resonance Mass Spectra using a Quadratic Least Square Fit and Iteration[2]

3.1 Introduction

3.1.1 Fourier Transform, Magnitude-, and Absorption-mode Spectrum

In FT-ICR, the original signal recorded in time-domain is a composite sum of sinusoidal waves with different ion cyclotron frequencies. Such signal is Fourier transformed to a frequency spectrum, therefore, components on the cyclotron frequency are extracted (which can be calibrated into the *m/z* domain).

Fourier transformation on a time domain signal, *F(t)*, produces the frequency spectrum in a complex output, *F(ω)*, consisting the absorption-mode spectrum, *A(ω)*, and the dispersion-mode spectrum, *iD(ω)*,[85]

$$F(\omega) = \int F(t) e^{-i\omega t} dt = A(\omega) + iD(\omega) \qquad (3.1a)$$

$$\phi(\omega) = \arctan[Im(\omega) / Re(\omega)] \qquad (3.1b)$$

$$M(\omega) = [\,(A(\omega))^2 + (D(\omega))^2\,]^{1/2} \qquad (3.1c)$$

where the phase angle, *ϕ(ω)*, of the complex number can be calculated from the trigonometric relationship (Eq.3.1b). Mathematically, *A(ω)* and *D(ω)* are the projection of *F(ω)* in the real and imaginary axis respectively, which means the two components contain the same information with π/2 difference in phase.[86] Apart from that, due to the accumulation on phase, the projection of *F(ω)*

---

[2] This chapter has been partially/entirely reproduced from
Qi, Y.; Thompson, C.; Van Orden, S.; O'Connor, P., Phase Correction of Fourier Transform Ion Cyclotron Resonance Mass Spectra Using MatLab. *J. Am. Soc. Mass Spectrom*. **2011**, 22 (1), 138-147. Copyright 2011, Springer.

ranges from positive to negative, which means neither *A(ω)* nor *D(ω)* can be plotted and interpreted straightforward (Figure 3.1). To solve this problem, the absolute value of *A(ω)* and *D(ω)* is calculated (Eq.3.1c) to yield a phase-independent magnitude-mode spectrum, *M(ω)*, which is plotted by all commercial FT-ICR instruments.

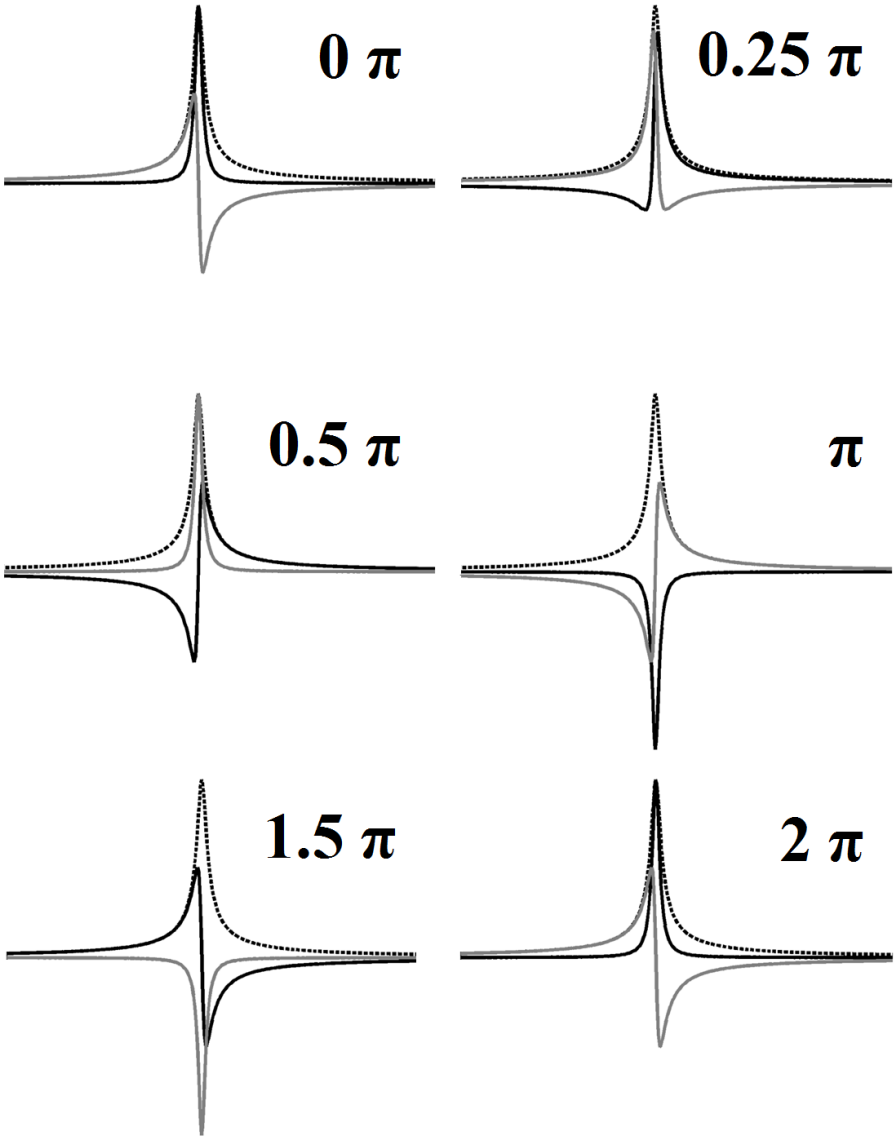

Figure 3.1 Peak shape of pure absorption- (black), dispersion- (grey), and magnitude-mode (dash line) spectra in Lorentzian function at different phase values.

3.1.2 Quadratic Phase Accumulation

The Fourier transform spectrum can be presented in the absorption-mode (common used in FT-NMR), magnitude-mode (FT-ICR), and the power-mode (engineering applications). The absorption-mode spectrum offers a significant step towards improving the data quality of FT spectrum. In FT-NMR spectroscopy, application of the absorption-mode was achieved in the 1970's.[91-92] Unfortunately, in FT-ICR, the pulse program involves a large and varying phase accumulation (~10^4 times over NMR) before the spectral acquisition event, and such an phase accumulation hinders the absorption-mode spectrum from widely application for almost 40 years.[87]

The phase accumulation comes from two sources. First, for signal detection, ions in the ICR cell are excited to a larger orbital by a linear frequency sweep, and ions will undergo excitation at different time points once its cyclotron frequency matches the excitation waveform. Second, because the amplitude of the excitation (*Vp-p*) is >100 V, whereas the signal from ions' image current is in mV level, once the ions being excited, a delay time (in milliseconds) is required to "cool down" the preamplifier before the detection event, and this delay time varies with different pulse sequences and different instruments (particularly from different manufacturers). During the delay time, all ions will continue their cyclotron motion and accumulate phase. Ignoring the image charge[97] and other field imperfections, the ion's theoretical phase accumulation in the ICR cell can be estimated as follow.[93]

In a linear frequency sweep, the frequency changes linearly with time:

$$\omega_t = \omega_0 + Rt \qquad (3.2a)$$

where R is the sweep rate, t is time, ω_0 and ω_t are the frequency of the sweep and time point 0 and t, respectively. And therefore, the phase of the waveform is the integral of frequency:

$$\varphi_t = \frac{R}{2}t^2 + \omega_0 t + \varphi_0 \qquad (3.2b)$$

Rearranging Eq3.2a, and substitute into Eq3.2b gives:

$$\varphi_t = \frac{\omega_t{}^2 - \omega_0{}^2}{2R} + \varphi_0 \qquad (3.2c)$$

Eq.3.2c is the initial phase of the ions when they are excited (at frequency ω_t). After this point, they are excited and continue to accumulate the phase, and the total phase shift is calculated by:

$$\phi(\omega) = \omega_t t_{total} + \varphi_t \qquad (3.2d)$$

$$t_{total} = t_{excite} + t_{delay} \qquad (3.2e)$$

where t_{total} is the sum of the time from excitation to the end of the frequency sweep (t_{excite}) and the delay time between the end of the frequency sweep and the beginning of the signal detection (t_{delay}). And t_{excite} can be calculated in terms of the parameters of the frequency sweep:

$$t_{excite} = \frac{\omega_{final} - \omega_t}{R} \qquad (3.2f)$$

where ω_{final} is the final frequency in the frequency sweep. Therefore, by combining Eq.3.2c, 3.2e and 3.2f into 3.2d:

$$\phi(\omega) = -\frac{\omega_t{}^2}{2R} + \left(\frac{\omega_{final}}{R} + t_{delay}\right)\omega_t - \frac{\omega_0{}^2}{2R} + \varphi_0 \qquad (3.2g)$$

Eq.3.2g reveals that, any ion's phase accumulation is expected to vary quadratically with its excited frequency. This function can therefore be used to

calculate the phase accumulation for any ion recorded in a broadband FT-ICR spectrum. If $\phi(\omega)$ is accurate enough, the phase corrected spectrum, $G(\omega)$, can be produced by multiplying $\phi(\omega)$ with the raw spectrum, $F(\omega)$, points by points (Eq.3.3). The result, $G(\omega)$, includes the pure absorption-mode, $A(\omega)_p$ (phase corrected), and pure dispersion-mode, $D(\omega)_p$ (π/2 different from the $A(\omega)_p$), respectively.[98]

$$G(\omega) = F(\omega)\exp(-i\omega) = \int F(t)e^{-i\omega t}e^{-i\phi(\omega)}dt = \int F(t)e^{-i(\omega t+\phi(\omega))}dt \quad (3.3a)$$

$$A(\omega)_p = Re(G(\omega)) = \cos(\phi)Re(\omega) + \sin(\phi)Im(\omega) \quad (3.3b)$$

$$D(\omega)_p = Im(G(\omega)) = \cos(\phi)Im(\omega) - \sin(\phi)Re(\omega) \quad (3.3c)$$

3.1.3 Methods for Phase Correction

During the last decade, general methods for phasing broadband absorption-mode spectra have also been developed.[68, 94-95] The method from Beu *et al.* requires a specially adapted instrument which can simultaneously excite and detect ions in the ICR cell, so that ions are recorded in the zero phase and the absorption-mode spectrum can be plotted straightforward after Fourier transform.[94] The method from Xian *et al*. requires that the instrument record the entire ion's excitation event with which the spectrum was recorded in order to provide the accurate parameters for Eq.3.2g in order to correct the absorption-mode spectrum.[95]

Both methods are successful but suffer from specific drawbacks which prevent them from being applied widely. First, no commercial instrument offers simultaneously excitation/detection or record the data of the ion excitation event in a sufficiently high degree of accuracy. And in additionally, even

specialized instruments can be home-built for the above purpose, the interference from the image charge effect or other field inhomogeneities will induce a small, but significant shift on ion's ICR frequency, and therefore, affect the accuracy of the phase function.

The third published method for phasing broadband absorption-mode spectra is from our group, which uses a quadratic least-square fit and iterations to form a phase function for any spectrum without specially modification on instrument or prior knowledge of the instrument pulse program.[68] Given the fact that ion's phase accumulated quadratically with its frequency, Eq.3.2g can be replaced by a general phase correction function of the type:

$$\phi(\omega) = A\omega^2 + B\omega + C \qquad (3.4)$$

where, *A, B* and *C* are coefficients which are solved for as part of the method; such function takes into account all the distortion on ion's frequency, variation on t_{delay}, and uncertainty on the recorded instrument parameters. By applying the general coefficients *A, B* and *C*, all the essential parameters required in Eq.3.2g can be ignored, and once the appropriate values for *A, B*, *C* are found; the general phase correction function can be applied directly to produce pure absorption-mode spectra.

3.1.4 Phase Wrapping

Except knowing ion's motion in the ICR cell, the "phase wrapping problem" is an added complication to overcome. As any peak can be perfectly phased at some $\phi(\omega)$ between 0 and 2π, and this means that it is easy to phase a single peak in the spectrum,[87] because the phase shift is <2π. However, according to the trigonometric relationship, $\phi(\omega_i)=\phi(\omega_i)+2n_i\pi$ (Figure 3.1) for any integer n_i at

any ω_i, and this makes any phase angle beyond 2π return to 0-2π (known as phase wrapping). Consequently, it becomes essential to consider the additional $2n_i\pi$ into the phase angle for each data point in the spectrum.

Compared to FT-NMR, phase wrapping effect makes it relatively difficult, to determine the variation of $\Phi(\omega)$ with frequency across the entire spectrum. In FT-ICR, a typical excitation bandwidth ranges from kHz to MHz, which makes the quadratic accumulation of phase very large (e.g., ~10,000π for the *m/z* range from 200 to 2000 in a 12 T system). Finding the correct n_i for each data point (over million points in a spectrum) is the crucial point for phase correction (Figure 3.2). Strictly speaking, the phase $\Phi(\omega)$ of a spectral peak can be determined only within 0 to 2π, so that Eq.3.4 should be replaced by Eq.3.5:

$$\phi(\omega_i) = A\omega_i^2 + B\omega_i + C + 2\pi n_i \qquad (3.5)$$

in which $0 \leq C \leq 2\pi$, and n_i is any integer representing the phase cycles, and finding the correct the n_i for each peak is crucial for phase correction (Figure 3.2). And it is because of this reason; the FT-ICR mass spectra have generally been limited to the magnitude-mode.

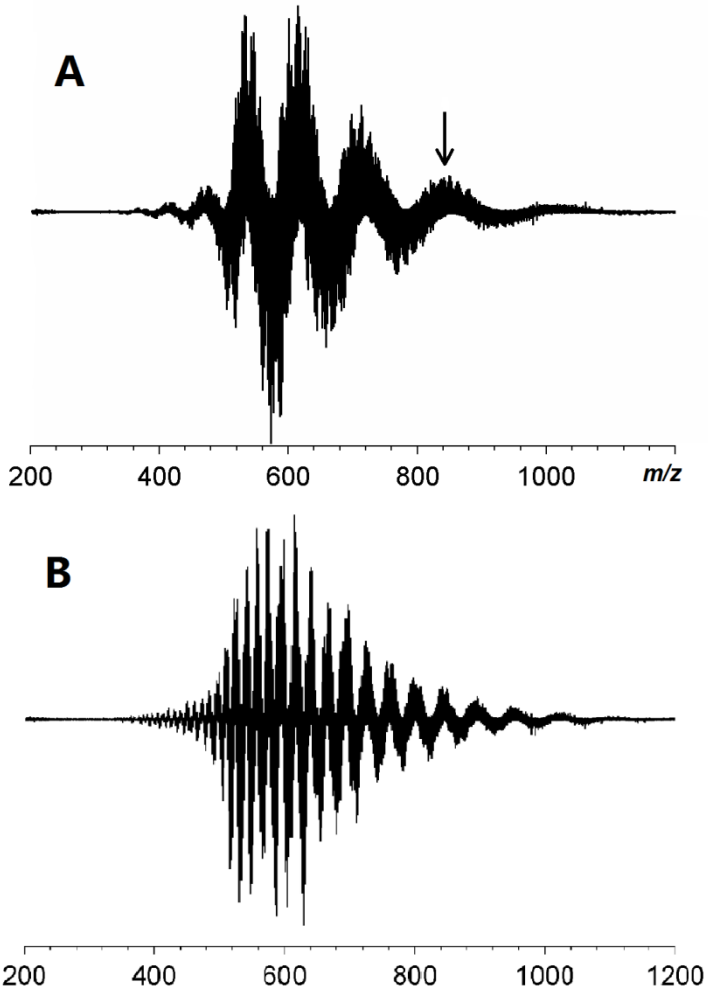

Figure 3.2 The absorption-mode, phase wrapped spectrum of an oil sample with labeled peak misphased by A) 4π and B) 10π, to show the complexity of correctly assigning the phase value of millions of data points varies up to 10,000π in an FT-ICR spectrum.

However, because any peak can be 'phased' iteratively, a set of phases, Φ_i, can be generated for a matched set of peaks in the frequency domain. Thus finding the correct $\Phi(\omega)$ for all values of ω_i, becomes a quadratic least squares fitting problem where the values of n_i can take on a range of specific integer values. The range of these n_i values can be readily approximated from the excitation duration and excite-detect delay time. Iterating through the expected

range of n_i values, phase correcting each iteration as in Eq 3.5, and checking the absorption-mode spectrum for symmetry around peaks and/or maximizing the positive signal amplitude is then straightforward.

In this chapter, a broadband phase correction method is demonstrated to phase a broadband FT-ICR absorption-mode spectrum using MatLab (MathWorks). The algorithm calculates the optimum value of $\Phi(\omega)$ for each individual data point in the spectrum so that the entire spectrum can be simply phased to the pure absorption-mode. This method is then tested for petroleum mixtures, proteins, and top-down electron capture dissociation (ECD) spectra, and yields a much improved peak shape in the spectra, particularly at the base of the peaks, compared to the corresponding magnitude-mode spectra.

3.2 Experimental Section

3.2.1 Sample Preparation

A crude oil standard sample (SRM 2721, light-sour) was purchased from NIST (Gaithersburg, MD, USA), and diluted 2000 times in a 85:15 methanol/toluene mixture used without additional purification. Ubiquitin (purchased from Sigma-Aldrich, Dorset) was diluted to 0.1 µM and 0.2 µM in a 50:50 water/methanol mixture for the molecular ion charge state distribution and 11^+ ECD spectra respectively. The ESI low concentration tuning mix is purchased from Agilent Technologies (Palo Alto, California, USA) without dilution. All solvents were HPLC-grade, obtained from Sigma-Aldrich Chemical Co. (Dorset, England).

3.2.2 Instrumentation

All spectra were recorded using a solariX 12T FT-ICR mass spectrometer (Bruker Daltonik GmbH, Bremen, Germany), equipped with an Infinity cell.[59] The oil sample was ionized using atmospheric pressure photoionization (PhotoMate APPI ion source, Syagen Technology, Inc., Tustin, CA, USA). The ubiquitin sample were ionized using electrospray ionization (Apollo II ion source, Bruker Daltonik GmbH, Bremen, Germany) for the molecular precursor ion spectrum first, and the 11^+ charge ion of ubiquitin was isolated in the quadrupole (Q1) of the solariX and transferred into ICR cell for ECD.[51]

Broadband frequency sweep (chirp) excitation (92-938 kHz for petroleum and 92-1250 kHz for ubiquitin, both at 125 Hz/μs sweep rate) was followed by a pre-scan delay of 3.5 milliseconds, and image current then was then detected to yield a 4 mega point (32-bit per data point) time-domain data set for each spectrum.

3.2.3 Data Process

The ICR transients were co-added (100 acquisitions for each to increase S/N), zero-filled twice, and fast Fourier transformed without apodization. The observed frequency is converted into *m/z* by means of a three term quadratic equation.[119, 145] The instrument was externally calibrated first using ESI tuning mix before each experiment. Then the oil spectrum was internally calibrated by assignment of a known $C_nH_{2n-16}S$ series throughout the *m/z* range from 200 to 900. The ubiquitin spectrum was calibrated internally using particular known *c/z·* fragments. All data sets were then processed using MatLab R2010a (MathWorks, Natick, MA, USA).

3.2.4 Theory

Eq.3.2a treated the frequency-sweep as a uniformly accelerated linear motion, and therefore the ion's phase accumulation can be assumed that increases quadratically with its corresponding frequency (similar to the linear distance travelled by an object with constant acceleration). In reality, e.g., the Bruker data system, the real excitation is generated in the instrument control software as a series of single frequency excitation events of identical length (Figure 3.3). For the spectra used here, there were approximately 1500-2000 frequency steps; each of 5 μs length. Note that in this work a true linear frequency shift is assumed, which may be a possible source of error; although it apparently is not significant (see below). In conclusion, the total cyclotron phase will be the sum of the quadratic phase accumulation during the frequency-sweep plus the linear increase between the instant of excitation and the onset of detection as shown in Eq.3.5, and such a function can be modeled as a general form in Eq.3.4.

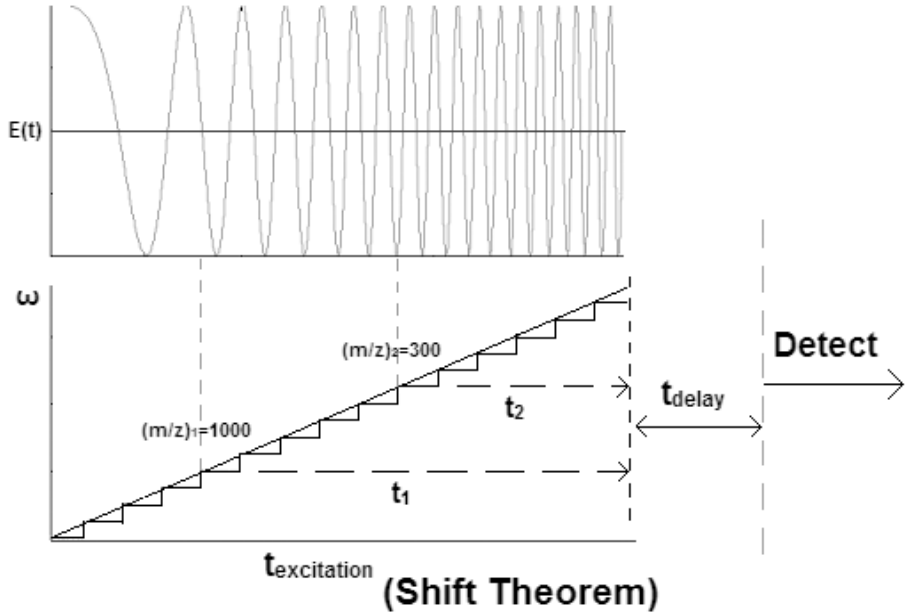

Figure 3.3 Top: Time-domain profiles of the excitation for frequency-sweep excitation. Bottom: Frequency for a continuous (upper line) or stepwise (lower line) frequency sweep.

3.2.5 Computational Algorithm in MatLab

The entire process of phasing the FT-ICR mass spectrum is operated within MatLab, the detailed explanation of the algorithm for each step is explained and all the MatLab code involved is listed in Appendix A.

Step 1: Read the data. The Bruker data folder (.m or .d extension) was set as the directory in MatLab. The ‘fopen’ command was used to open the file ‘fid’ for read operation. Then the data are zero filled once before the fast Fourier transform (FFT) in order to increase the sampling points of the spectrum and to recover the phase information if the spectrum is not plotted in the magnitude-mode. It should be noted that unlike the quadrature detection applied in NMR, the FT-ICR detection only records the signal as intensity versus time in a series of real numbers. For this reason, FT cannot distinguish

the rotation phase of the ions, and thus, results peaks in both positive and negative frequencies that are symmetrically centered at the zero point (0 Hz). This symmetry contains identical information, and therefore, the negative-frequency half of the data set was discarded.

Step 2: Generate the frequency basis set (N/2 values equally spaced between zero and half the Nyquist frequency) and calibrate the *m/z* domain. Most FT-ICR data systems do not save the spectral data as (x, y) pairs because the x value is easy to calculate. The x value for any display mode (*m/z*, Hz, points) can be calculated from the index of the point and an associated transformation/calibration function. The calibration function used by different instrumental companies varies, but are usually derived from either the Ledford[119] or Francl[118] equations. Calibration of FT-ICR spectrum was reviewed in Chapter 2, and all the calibration parameters needed are able to be found in the spectral dataset.

Step 3: Calculate an optimal phase, $\Phi(\omega_i) = \Phi(\omega_i) + 2n_i\pi$, for a set of arbitrarily chosen peaks. Several criteria were tested for estimating the best phase values and it was found to be better to divide the entire spectrum into several segments of smaller frequency range. Choose a segment of certain frequency range and begin by finding the apex of several peaks, get the real and imaginary values, and calculate their phase value. An initial segment from the middle of the frequency-sweep is recommended in order to reduce the first and second-order correction errors, and zero-filling is also suggested here to improve the apex picking accuracy. The optimal phase value for each peak is determined by manually picking the apex, but could be automated.

Step 4: Phase one region of a spectrum by iterating the successive values of n_i. Because the phase accumulation between adjacent peaks is generally low (several cycles), it is easy to estimate the value of n_i for a set of consecutive peaks in a narrow frequency range. After a list of peaks is generated (no more than 20 points), a quadratic least square fit is used to the above apex on their corresponding angular frequency and phase value pairs to generate $\Phi(\omega)$ according to Eq.3.4.

Step 5: Extend the range of the phase function. The phase function from step 4 is only a reasonable approximation within the narrow frequency range chosen. When applied to the whole spectrum, it will generate a 'phase-wrapping effect' (Figure 3.4). This indicates that some of the values of n_i from Eq.3.5 are incorrect. Fortunately, it is possible to estimate the number of cycles from the phase wrapping spectrum. For example, in Figure 3.4B, there are about two cycles shift for the marked point so that the phase wrapping is within 4π. To correct the phase function, one peak from the low frequency side was chosen (because a low frequency results in a small phase value, thus, minimizing the error), and its corresponding phase value from the function in step 4 was acquired. The correct phase value of that point is calculated by iteratively adding 2nπ (n is the phase cycle at that point) as shown in Figure 3.4. At each value of n, a new phase function is generated by quadratic least square fitting to the (ω, Φ) list, and these n values are iterated until the spectrum is fully absorption-mode in this region. This procedure is continued by adding successively more peaks until the entire FT-ICR spectrum can be phase corrected simultaneously (Figure 3.4D).

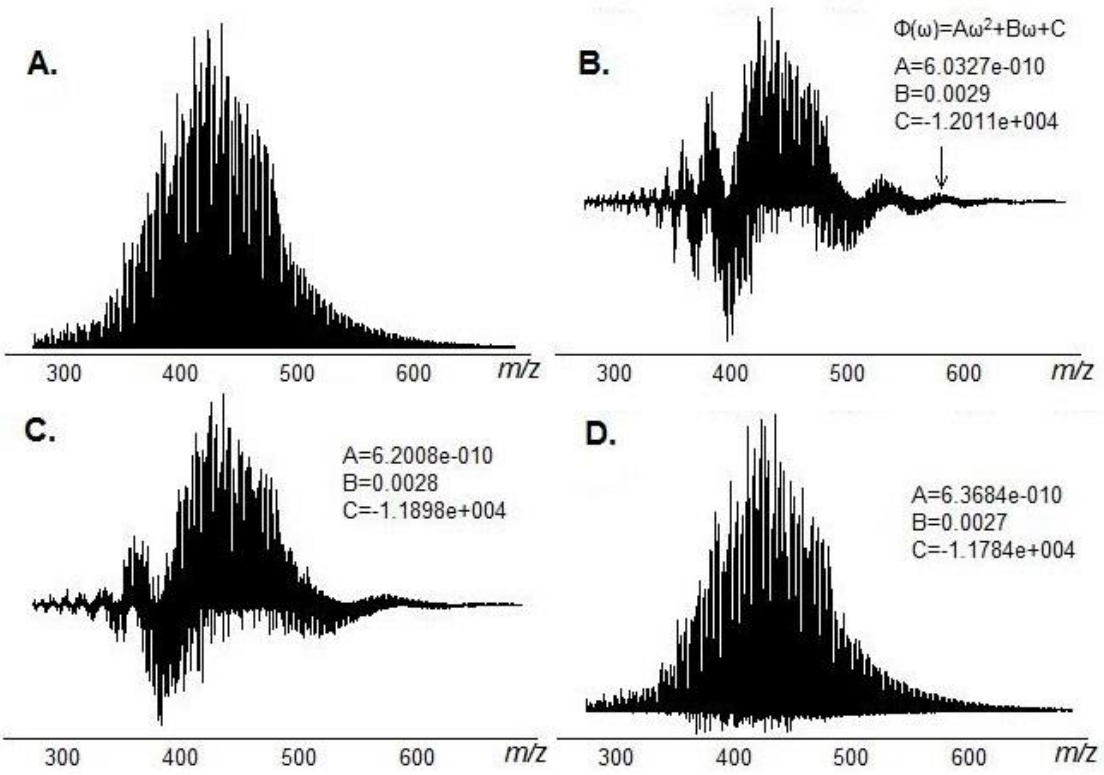

Figure 3.4 A) the magnitude-mode spectrum of an oil sample. B) the absorption-mode, phase-wrapped spectrum of petroleum (four cycles are apparent in the periodic phasing through the entire spectrum indicating slight errors with the phase function shown in the inset). The labeled point (arrow) is misphased by 4π, thus, this frequency and phase pair are added to the fitting list with the phase adjusted by adding 4π. C) and D) show further iterations, adding more peaks to the fitting list until the best fit (D) is obtained.

Step 6: The baseline of the peaks is corrected automatically using the MatLab command ‘msbackadj’ which estimates the lower frequency baseline roll within multiple shifted windows using a spline approximation, and then subtracts it.

3.3 Result and Discussion

3.3.1 Absorption-Mode versus Magnitude-Mode Display

The broadband phase-corrected absorption-mode spectra of crude oil sample are shown in Figure 3.5. In this case, the mass resolving power is increased by at least 50% for absorption-mode ($m/\Delta m_{50\%}$~850,000) compared to its corresponding magnitude-mode ($m/\Delta m_{50\%}$~500,000) (Figure 3.5, bottom inset). Several small, negative direction peaks in the absorption-mode spectrum result from their typical peak shape of a sinc function (details in Chapter 4).

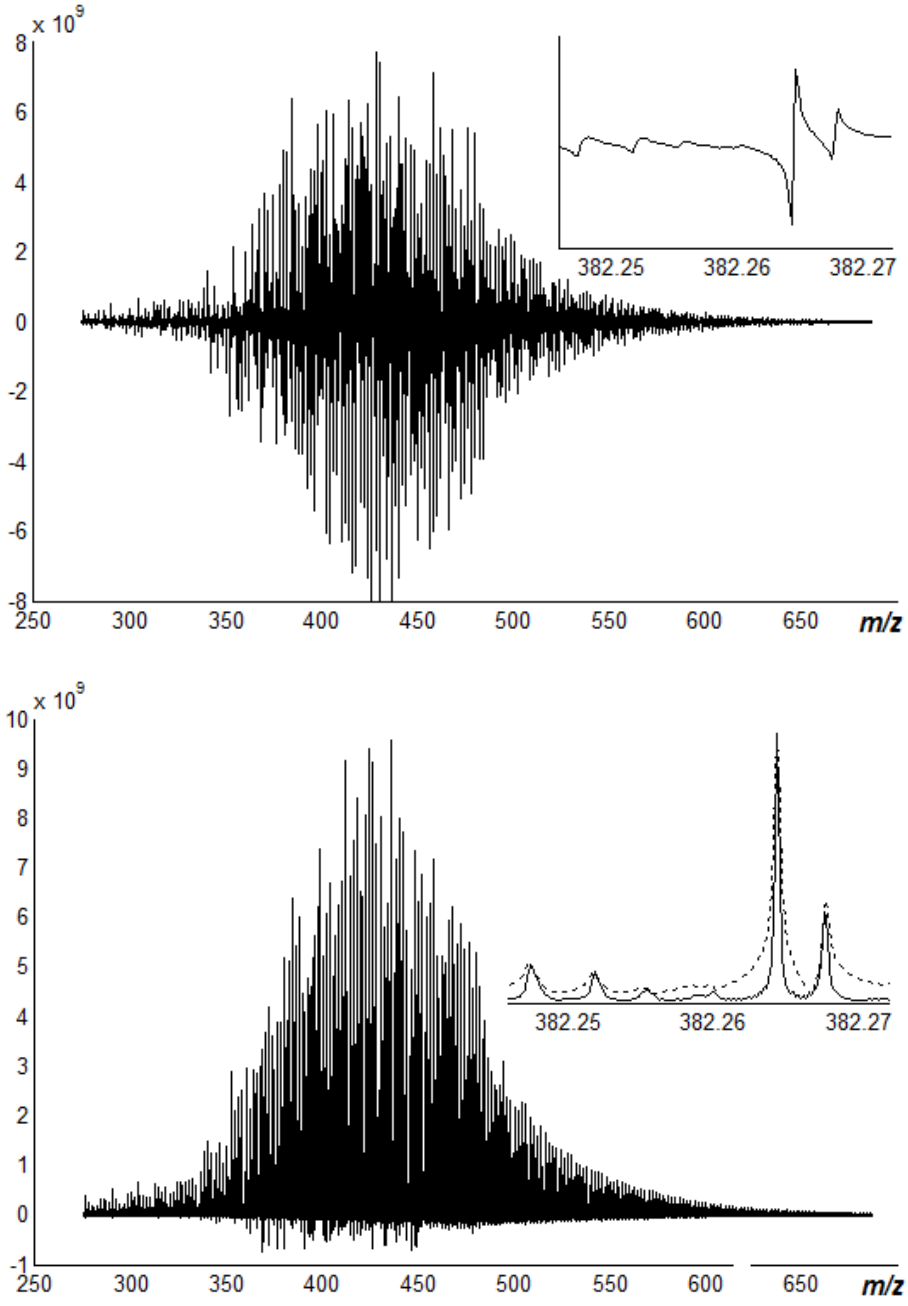

Figure 3.5 FT-ICR mass spectra of crude oil sample. Top: unphased absorption-mode spectrum following FFT. Bottom: phase-corrected absorption-mode spectrum, inset: magnitude-mode (dotted line, $m/\Delta m_{50\%}$~500k) versus absorption-mode (solid line, $m/\Delta m_{50\%}$~850k) spectra for some peaks extracted from the spectrum.

Regarding Figure 3.5, it is particularly interesting to note that the magnitude-mode spectrum (dotted line) and the absorption-mode spectrum (solid line) have significantly different peak shapes which manifest in some unusual baseline effects that are commonly observed in FT-ICR mass spectra. Note that the distortion of the spectrum is depending on the degree of peak overlap, the relative magnitudes of the overlapped peaks and the signal damping rate.[146] In particular, the "tails" of the magnitude-mode's Lorentzian/sinc convoluted function tend to distort the position of neighboring, smaller peaks. Because the “tails” of the dispersion-mode spectrum extend much farther than the “tails” of pure absorption-mode (Figure 3.1), and the magnitude-mode peak which is a summation of both part, must be farther apart for the same degree of overlap as absorption-mode peaks. This distortion suggests that the absorption-mode spectrum should provide better mass accuracy than the corresponding magnitude-mode, over and above the increase in mass accuracy associated with the improved resolving power, and more data will be demonstrated in the following chapters

3.3.2 Resolving power

Figure 3.6 shows the comparison of magnitude-mode and pure absorption-mode spectrum of an ECD spectrum on the 11^+ charged ubiquitin. Again, an over 50% higher mass resolving power for absorption-mode relative to magnitude-mode was observed and many overlapped isotopic peaks are now better resolved in the absorption-mode. Also notice that the peaks are separated far better at the base (Figure 3.6, bottom) as with Figure 3.5. As is commonly observed in unapodized FT-ICR spectra, the baseline of the

magnitude-mode isotopic distribution (Figure 3.6, bottom) rises and falls through the peak cluster due to the summation of the Lorentzian "tails" of the peak shape distributions. This effect is not observed in the absorption-mode spectrum, but a slight distortion of peak shape and a negative baseline drift (due to imperfect phase correction). This suggests that the narrower peak shape after phase correction may partially modifies the baseline shift, and investigation of the effect is still underway.

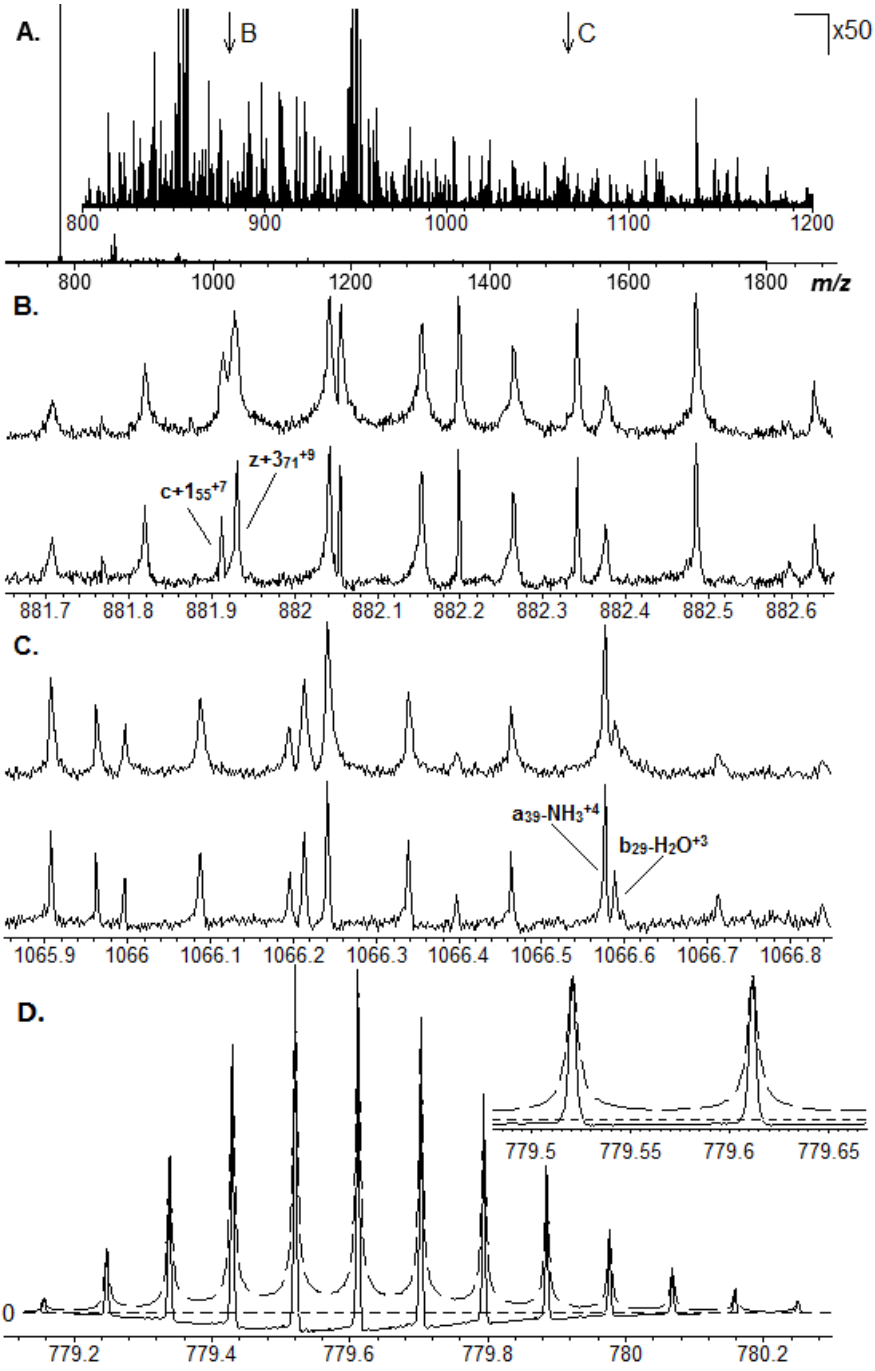

Figure 3.6 A) Magnitude-mode 11^+ ECD ubiquitin spectrum, zoom in to show peak density of the raw data. B) the absorption- (bottom) and magnitude- (top) mode spectrum of the region of (A) around *m/z* 882. C) the absorption- (bottom) and magnitude- (top) mode spectrum of the region of (A) around *m/z* 1066. D) the absorption- (solid) and magnitude- (dotted) mode spectrum of the precursor ion isotopic distribution at *m/z* 779-780.

3.3.3 Iteration

Figure 3.4 illustrates the phase iteration procedure. Figure 3.4A is simply the magnitude-mode spectrum, but Figure 3.4B shows the absorption-mode spectrum correctly phased only in a small region around *m/z* 450, with the rest of the spectrum periodically coming into and out of phase. The point marked with an arrow is misphased by 4π. When this frequency and phase are added to the fitting list, corrected by 2π and the quadratic least-squares fit is recomputed, the phase function shifts slightly (see the parameters in the inset) to form Figure 3.4C. Note that in Figure 3.5C, the periodicity of the absorption-mode spectrum has decreased. This iteration procedure is continued until the best absorption-mode spectrum is obtained (Figure 3.5D). It is clear from the small negative blips in Figure 3.5D that this phase function isn't perfect, which is due to the sinc function of peak shape in absorption-mode and the stepped frequency sweep excitation. However, this phase corrected absorption-mode spectrum represents a significant improvement over the magnitude-mode spectrum in terms of resolution and peak shape.

3.3.4 Centroiding

One significant source of error currently embedded in these calculations is related to the method used to calculate the peak centroid. The method currently used is the simplest method possible--defining the highest point on the peak (in magnitude-mode) as the apex of the peak. This method is not particularly accurate, but it improves dramatically with zerofilling, all the spectra shown in this chapter used two zerofills, thus lengthening the time-domain data set twice. While not currently tested, it seems likely that improvements can be made to

the peak centroiding algorithm, which will improve the accuracy of the ω/Φ pairs that are added to the least squares fit. Possible improved centroiding algorithms include use of a maximum likelihood peakfitting method,[147] a center-of-mass calculation, a least-squares fit to a Lorentzian (or Lorentzian/sinc) function, apodization and fitting to a Gaussian function, or even use of the shifted-basis method.[110] In this work, none of these centroiding algorithms have been tried, but they are an obvious next step.

3.3.5 Baseline correction

The baseline in magnitude-mode spectrum is obviously positive because magnitude-mode calculates the absolute value. While in absorption-mode, the noise is Gaussian distribution about the baseline (zero amplitude). Furthermore, the characteristics from sinc function introduce negative wiggles in both sides of the peak. Fortunately, some of these peak shape distortions can be corrected by standard baseline correction procedures. In MatLab, this can be done automatically using a command (see Appendix A) which fits the baseline to a cubic spline and then subtracts it from the signal to flatten the baseline drift. The absorption-mode spectrum after baseline correction shows an improvement in peak shape which would improve peak picking.

3.3.6 Algorithm speed

Currently, this method is user interactive, requires manual peak picking and phase assignment, so it is hardly fast. However, peak picking and centroiding can be standardized and automated, as can phase determination of individual peaks, so the bulk of the algorithm can be automated. Furthermore,

since the excitation pulse doesn't change from scan to scan, it is likely that an optimal phase function from one scan can be applied to the next scan directly. Errors from scan-to-scan will probably arise from space-charge effects, but these are expected to be minor and can be addressed using the same iterative method as above. Given the speed of Fourier transform, it is unlikely that these iterations will be far faster than the data acquisition event itself. The current results were performed offline as post-processing of existing transients, but once the phase function is known, phase correction requires a single point-by-point vector complex number multiplication on the transient, which takes less than a millisecond on modern processors. Thus, the method is, in principle, fast enough to be applied online on a chromatographic timescale. And to promote its application, an Autophaser program has been developed in our group.[93]

3.4 Conclusion

Here, the method to phase a broadband absorption-mode spectrum for several different samples by applying a quadratic least-squares fitting is demonstrated. The improvement in mass resolving power is significant compared with conventional magnitude-mode spectra particularly at the base of the peak. Additionally, the peak shape is greatly improved at the baseline except for a general negative drift which can be corrected. This method is applicable to top-down spectra and other complex spectra with a straightforward approach.

In theory, the largest resolution enhancement (a factor of 2) shall be achieved for on-line LC-MS, for which the time domain acquisition period can

be 1 s or lower (signal is not damped significantly). Furthermore, the absorption-mode display shows significant advantage in complex mass spectra, demonstrated here for petroleum and the ECD spectrum of ubiquitin, and will probably be applied to biological samples like proteomics, lipidomics and metabolomics.

Chapter 4

Absorption-mode: The Next Generation of Fourier Transform Mass Spectra[3]

4.1 Introduction

The FT-ICR is a high-performance mass analyzer capable of ultra-high mass accuracy, resolving power and sensitivity simultaneously.[44-45] In FT-ICR, the cyclotron resonance frequency is independent on ions' kinetic energy (kinetic energy only controls orbital radius), unlike most other mass analyzers, the precise determination of *m/z* is not affected by the kinetic energy. Consequently, a FT-ICR can routinely achieve mass accuracy below 1 ppm and resolving power ($m/\Delta m_{FWHM}$) above 10^6 under normal conditions. Additionally, the versatility and compatibility of FT-ICR to different ion fragmentation methods makes it an ideal instrument for tandem mass spectrometry analysis in proteomics,[148] metabolomics,[149] and petroleomics[35] to extract the maximum information possible from these complex samples.

In recent years, the development of FT-ICR has largely focused on instrumental improvements, e.g., increased magnetic field,[150] ion transfer and trapping efficiency,[151] and new cell designs to approach more harmonized ion motion at large cyclotron radius.[46, 152] However, research on electronics,[153-156] software, and data processing[127, 157-161] lags relative to instrumentation, and there is still much room for improvement. Among the above areas, phase

[3] This chapter has been partially/entirely reproduced from
Qi, Y.; Barrow, M. P.; Li, H.; Meier, J. E.; Van Orden, S. L.; Thompson, C. J.; O'Connor, P. B., Absorption-mode: The Next Generation of Fourier Transform Mass Spectra. *Anal. Chem.* **2012**, 84 (6), 2923-2929. Copyright 2012, American Chemical Society.

correction is a data processing method which significantly improves the performance of a FT-ICR spectrum without any additional cost on the instrument.[68, 83, 95]

It is well known that the mass resolving power of FT-ICR varies linearly with the applied magnetic field strength,[45] however, it is less widely appreciated that the resolving power can be enhanced by a factor up to 2 by phasing the raw data accurately and plotting in the pure absorption-mode, which has been a long standing problem for almost 40 years.[162-163] Recently this topic has been resurrected by two publications, first by F. Xian *et al*., using a detailed model of the excitation pulse from the experiment,[95] and second by Y. Qi *et al.*, using a quadratic least-squares fit, iterated over the entire phase range to form a full frequency shift function for the entire spectrum.[68] And very recently, it has been proved that the phase function can be optimized, and applied from experiment to experiment using different instrument parameters, regardless of the sample measured.[83]

This chapter aims to show the application of absorption-mode to the complex petroleum and protein spectra, demonstrates the advantages resulting from the increase of ~2 fold in resolution and √2 fold in the signal-to-noise ratio (S/N) simultaneously throughout the entire *m/z* range compared to the conventional magnitude-mode spectrum.

4.2 Theory: Advantages of the Absorption-Mode

The resulting absorption-mode spectrum shows several advantages over the conventional magnitude-mode: First, the peak width at half-maximum height is narrower than its corresponding magnitude-mode by a factor

depending on the damping of the transient, ranging from ~1.7 (signal acquisition time (T)>>signal damping factor (τ), 'Lorentzian' peak shape) to 2 ($T << \tau$, 'sinc' peak shape) without a concomitant loss on peak height (Figure 4.1, top),[82] which means that the mass resolving power, can be enhanced by the same factor. In a real experiment, because the value of τ varies, the peak shape of a spectrum is always a convolution of both a 'sinc' and a 'Lorentzian' function. Therefore, by plotting the absorption-mode spectrum, the theoretical improvement on resolving power is between 1.7 and 2.

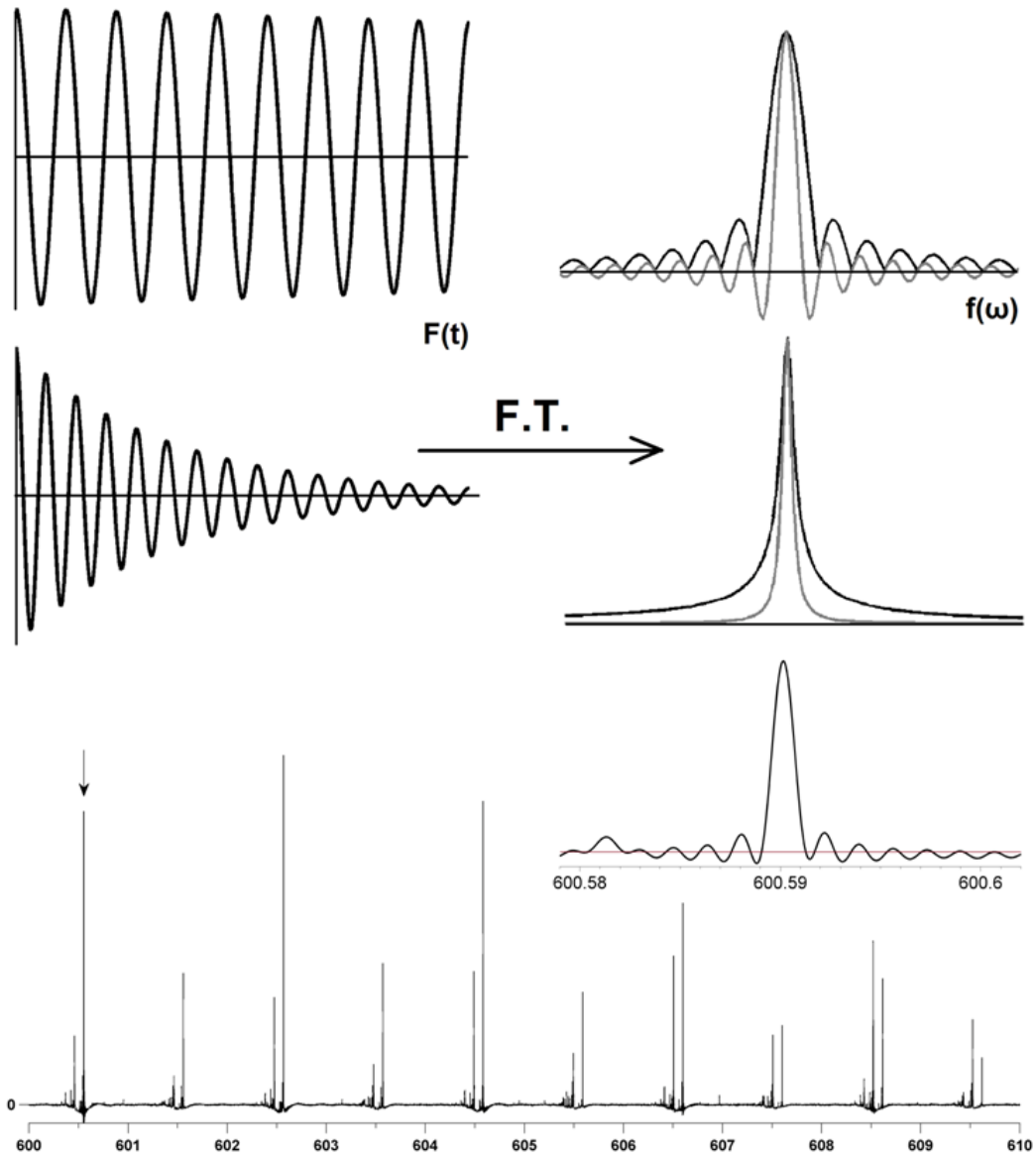

Figure 4.1 Top: simulated time-domain ICR signals (left) and frequency-domain magnitude (black) and absorption-mode (gray) spectra (right), for $\tau >> t$, sinc function (top), for $\tau << t$, Lorentzian function (bottom). Note that the sinc function has negative sidelobes in the absorption-mode after Fourier transform. Bottom: a small segment from the absorption-mode crude oil spectrum, inset: zoom in for the labeled peak to show the negative blips of a sinc function.

Second, the gain in resolving power is achieved without a concomitant loss on peak height, while at the same time the noise baseline level in the absorption-mode can be decreased by √2 compared to magnitude-mode. As Fourier transform produces complex numbers, both signal and noise level in a spectrum are defined herein by the root mean square value (RMS, Eq.4.1), where each data point is equal to '$a_n+i\cdot b_n$' for *M(ω)* and 'a_n' for *A(ω)*.

$$A(\omega)_{noise} = \sqrt{\frac{a_1{}^2 + a_2{}^2 + \ldots + a_n{}^2}{n}} \tag{4.1a}$$

$$M(\omega)_{noise} = \sqrt{\frac{(a_1{}^2 + a_2{}^2 + \ldots + a_n{}^2) + (b_1{}^2 + b_2{}^2 + \ldots + b_n{}^2)}{n}} \cong \sqrt{2} \times A(\omega)_{noise} \tag{4.1b}$$

In a phased spectrum, the value 'a_n' for the apex of a peak is equal to '$a_n+i\cdot b_n$' as phase correction aligns the vector with the real axis of the complex space so that the values of 'b_n' are zero. Meanwhile, it is known that the noise is randomly distributed throughout the signal, and cannot be phase corrected. Because noise is randomly distributed, under normal detection conditions, RMS ($\sum a_n$) is equal to RMS ($\sum b_n$). Thus, the noise level of magnitude-mode can be written in Eq.4.1b which is √2 times of the absorption-mode; therefore, the S/N of any peaks in absorption-mode is increased by √2x compared to magnitude-mode. Such an improvement is equal to have a "quadrature detection" which requires two separate receiver coils, but here it is just data processing without extra cost.

Third, for apodization,[71] a half window apodization is preferred in absorption-mode spectrum for better peak shape and S/N, and furthermore, the half window function retains the most intense signal at beginning of the

transient so that the absorption-mode spectrum will not be over-suppressed as often occurs in the magnitude-mode. The effects on apodization for FT-ICR spectra will be fully discussed in Chapter 5.

Finally, mass accuracy, defined as the proximity of the experimental measurement to the true value (exact mass),[31] which is the key measurement of a mass spectrometer. This value is affected by both resolving power and S/N mentioned in above and thus cannot be estimated and compared separately. However, given the combined effect of all the benefits mentioned above, the improvement on mass error is more than a simple sum of them. In order to demonstrate this improvement, the absorption-mode is applied to the spectra with the low *m/z* range (crude oil) and high *m/z* range (top-down protein), respectively, and compared with the conventional magnitude-mode spectra. In summary, the absorption-mode spectra are systematically found to be superior to magnitude-mode spectra.

4.3 Experimental Section

4.3.1 Sample Description and Preparation

A crude oil standard sample (SRM 2721, light-sour) was purchased from NIST (Gaithersburg, MD, USA), and diluted 2000 times in a 85:15 methanol/toluene mixture. Bovine calmodulin and ubiquitin were purchased from Sigma-Aldrich (Dorset, England), and diluted into 0.4 µM in a 50:50:1 acetonitrile/water/formic acid mixture. ESI-L low concentration tuning mix (for external calibration) is purchased from Agilent Technologies (Palo Alto, California, USA) and without dilution. All solvents were HPLC-grade, obtained from Sigma-Aldrich Chemical Co. (Dorset, England).

4.3.2 Instrumentation

All spectra were recorded using a solariX 12T FT-ICR mass spectrometer (Bruker Daltonik GmbH, Bremen, Germany), equipped with an Infinity cell.[59] The oil sample was ionized using atmospheric pressure photoionization (PhotoMate APPI ion source, Syagen Technology, Inc., Tustin, CA, USA). Both ubiquitin and calmodulin sample were ionized using electrospray ionization (Apollo II ion source, Bruker Daltonik GmbH, Bremen, Germany) for the molecular precursor ion spectrum first, and the 17^+ charge ion of calmodulin was isolated in the quadrupole (Q1) and transferred into the ICR cell for ECD experiment.[51] Broadband frequency sweep excitation (~1250-61 kHz (*m/z* 150-3000) at 125 Hz/μs sweep rate) was followed by a pre-scan delay of 3.5 milliseconds, and the image current was detected to yield a 4 mega point (32-bit per data point) time-domain data set for each spectrum.

4.3.3. Data Process

The ICR transients were co-added (100 acquisitions for each to increase S/N), apodized with an optimal window function[71, 164] (unless emphasized in the text): either a full Hanning (for magnitude-mode) or a half Hanning (for absorption-mode), zero-filled two times[106] and fast Fourier transformed in MatLab R2010a (MathWorks, Natick, MA, USA). The pre-processed data sets were then written in Xmass format with appropriate parameters based on the data, and loaded into Bruker DataAnalysis software for spectra deconvolution and peak detection (details are available in Appendix B).

The observed frequency is converted into *m/z* by means of a three term quadratic equation.[119, 145] The instrument was externally calibrated first using

ESI tuning mix before each experiment. Then the oil spectrum was internally calibrated by assignment of a known $C_nH_{2n-16}S$ series throughout the *m/z* range from 200 to 900. The calmodulin spectrum was calibrated internally using particular known *c/z·* fragments.

4.4 Result and Discussion

4.4.1 Peak Shape of a Sinc Function

Phase corrected spectra always show negative wiggles in both sides of the peak (Figure 4.1, bottom), because an absorption-mode spectrum has a peak shape of sinc function. In the previous study, negative-valued peaks were incorrectly attributed to the frequency sweep waveform and/or the centroiding algorithm used.[165] As mentioned above, the peak shape resulting from the Fourier transform is a convolution of both a 'sinc' and a 'Lorentzian' function; thus the negative wiggles are actually the nature of an absorption-spectrum which cannot be eliminated except by apodization.[71, 166] These wiggles are also present in the magnitude-mode spectrum, but are only positive valued because of the square calculation, however they will make the broadening of peak base much worse, distort neighbouring peaks, and can confound peak detection algorithms.[147]

4.4.2 Comparison of Noise Level

In order to test the √2 improvement on S/N mentioned in the theory section, both crude oil and ubiquitin charge state spectra were used; and for comparison purpose, neither of the spectra were apodized in order to retain the original signal intensity. In the oil spectrum, groups of peaks

corresponding to different classes appears every dalton (Da), thus the noise level (RMS) in a series of *m/z* windows of ~0.6 in the *m/z* region of ~300, 500, 700 and 900 were calculated respectively in both magnitude- and absorption-mode. In the precursor molecular ion spectrum of ubiquitin, a much broader *m/z* window can be included, thus a 5 Da noise window of ~555-560, 990-995, 1665-1670 and 2700-2705 were used respectively for calculation (Table 4.1). The S/N comparison between magnitude- and absorption- mode of the oil spectrum ranges from 1.32 to 1.51 due to insufficient of data points in a 0.6 Da window, however, the ratio approaches $\sqrt{2}$ in the smallest range of 300.30-301.05 (this range contains the most points) as the data point density increases inversely with the *m/z*. In the ubiquitin spectrum, this ratio is much close to $\sqrt{2}$, because much broader *m/z* windows could be chosen, thus increasing the averaging effect.

Table 4.1. Noise level (in RMS) of oil and ubiquitin charge states spectra in both magnitude and absorption-mode display.

Noise level (RMS) of crude oil spectrum			
***m/z* range**	**Magnitude-mode**	**Absorption-mode**	**Ratio**
300.30-301.05	699892.09	495412.99	1.41
500.56-501.1	836396.19	553054.63	1.51
699.71-700.30	938281.32	711066.96	1.32
899.98-900.56	965850.73	676193.80	1.43
Noise level (RMS) of ubiquitin charge states spectrum			
***m/z* range**	**Magnitude-mode**	**Absorption-mode**	**Ratio**
555-560	1099373.2806	777392.4059	1.41
990-995	1628990.0643	1152204.5984	1.41
1665-1670	1886997.2299	1335085.2547	1.41
2700-2705	2452423.2363	1735824.9276	1.41

4.4.3 Application on Protein

A top down ECD spectrum of calmodulin was analyzed, 288 c/z fragments were assigned with a RMS mass error of 0.90 ppm in the magnitude-mode (Figure 4.2A). Either the monoisotopic peak or the most intense peak (if monoisotopic peak wasn't clear) was used for assignment. Of the 147 inter-residue bonds in the protein, and 129 of them (88%) were detected in the spectrum which is already respectable cleavage coverage (the fraction of inter-residue bonds cleaved). These 288 fragments were also observed in the absorption-mode (Figure 4.2B) with a much smaller RMS error of 0.38 ppm. Furthermore, 40 new fragments were assigned with an RMS error of 0.67 ppm. All of the 40 new peaks were in the S/N range of ~2, or were closely overlapped with other peaks. These fragments contain 11 new inter-residue bonds which were not observed in the magnitude-mode (all new fragments were observed with more than one charge state), and the cleavage coverage of the spectrum was increased to 95% (note that the two prolines in calmodulin cannot be cleaved via ECD). The inset in Figure 4.2B shows one of the newly detected fragments, c_{78}^{9+}, with its simulated isotope pattern;[167] the isotope pattern of the c_{78}^{9+} peak is clearly visible in the absorption-mode, but impossible to discern in the magnitude-mode.

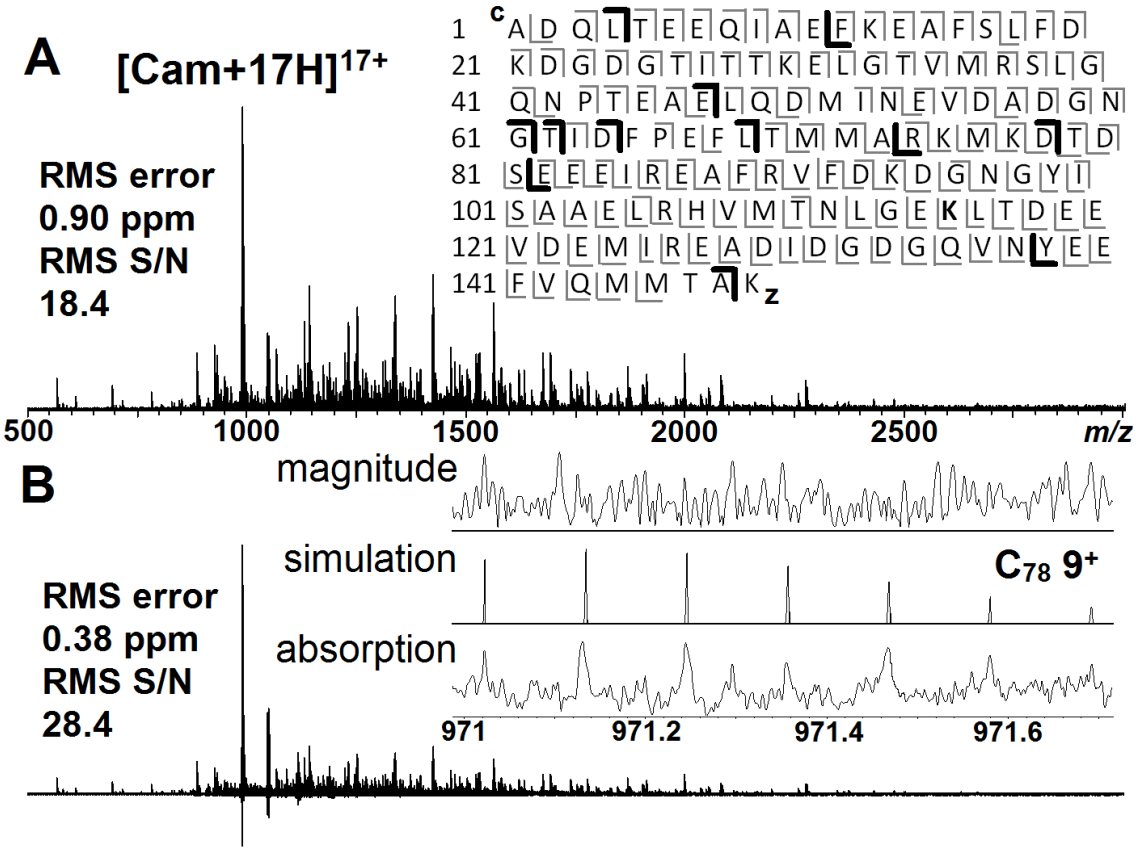

Figure 4.2 A: ECD spectrum of calmodulin $[Cam+17H]^{17+}$ in magnitude-mode with the RMS mass error and S/N labeled; inset: cleavage map (fragments observed in magnitude-mode are labeled in grey, new fragments in absorption-mode are in black). B: Spectrum in absorption-mode, inset: the c_{78}^{9+} fragment in magnitude (top), absorption-mode (bottom) and its isotope simulation (middle).

As is mentioned already, the absorption-mode spectrum has a lower noise level, thus the S/N of these peaks were calculated. Data in Figure 4.2 shows the absorption-mode increased the S/N (RMS value of all the peaks assigned) of the spectrum from 18.4 to 28.4 which is the reason for new peaks being detected. And it is interesting to note that the 1.54 times improvement is even greater than $\sqrt{2}$, value predicted in the theory section. The extra improvement is due to the use of a half window function in the absorption-mode, and detailed

discussion will be in Chapter 5. Finally, it is important to comment that the negative peak sidebands in the figures are the characteristics of absorption-mode peaks (a sinc function after Fourier transform)[83] which is also common in NMR spectra. For largely undamped signals, a sinc function represents the correct peak shape, although it is otherwise unusual in mass spectrometry.

Mass accuracy of the two modes has been studied in a recent paper,[83] and in that work only peaks with good peak shapes (S/N>10, *m/z*<1500) were chosen for comparison. It was actually surprising that absorption-mode gave similar mass-accuracy to magnitude mode for those well resolved peaks. Herein, the threshold of S/N was set to 2, and peaks with *m/z* up to 3000 were picked, and, under these conditions, a significant improvement was achieved in the mass accuracy in the absorption mode. The extra resolving power and S/N result in up to 2.4 times increase in mass accuracy, particularly for those peaks with low S/N or high *m/z* (Figure 4.3). The mass accuracy improvement in the absorption-mode is mostly in the region where the S/N is below 5 (Figure 4.3A) or *m/z* over 1000 (Figure 4.3B). These are the regions where the peaks start to distort significantly, and this tendency exists in both magnitude- and absorption-mode. However, the absorption-mode spectrum greatly reduces this effect and results in much better mass accuracy in this region.

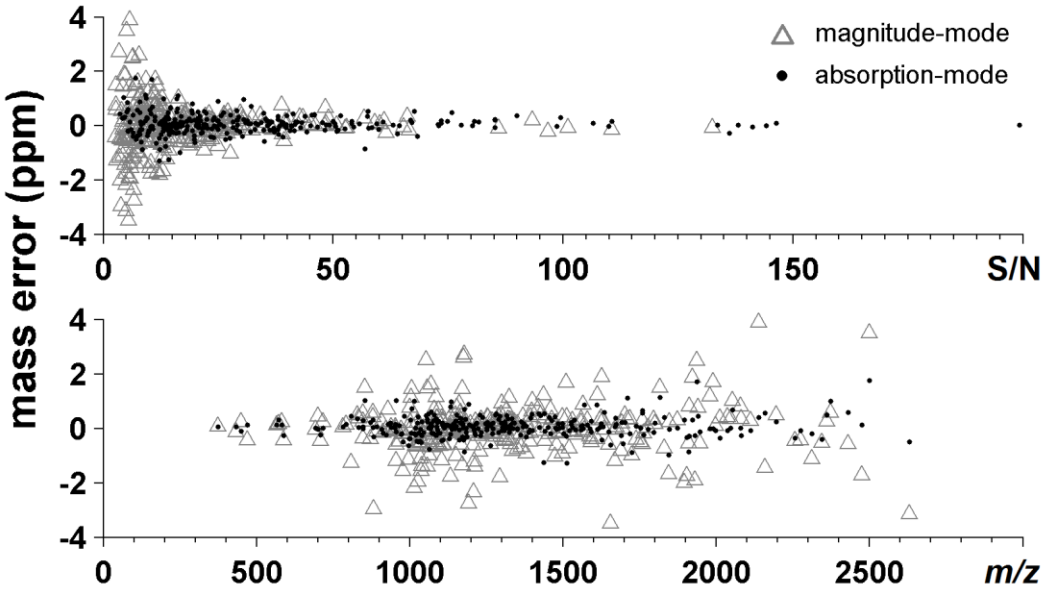

Figure 4.3 Mass error distribution (in ppm) versus S/N (top) and *m/z* (bottom) of the calmodulin spectrum for both magnitude- and absorption-mode.

4.4.4 Application to Petroleum

Direct analysis of crude oil without separation techniques is best performed in FT-ICR because it is an extraordinarily complex mixture, which therefore required the best possible analytical mass resolving power. However, the peaks in an oil spectrum appear regularly according to different compound classes (the heteroatom) and types (hydrogen deficiency).[35, 168] Similar to the results observed for calmodulin, the absorption-mode also works better for crude oil spectra in the low S/N and high *m/z* regions. The mass error distribution of the two display modes was plotted (Figure 4.4). Because the mass range here is below 1000 Da, better RMS error is achieved than with the calmodulin spectra (175 ppb for magnitude-mode and 99 ppb for absorption-mode) compared to the calmodulin spectra above. With the mass error at the sub-ppm level, systematic errors start to emerge.[169] Figure 4.4 shows a systematic variation in mass error across the entire *m/z* range, such

wavy distribution agrees with the work described by Savory *et al*.[169] This error distribution is possibly due to magnetron expansion caused by ions' different radii in the ICR cell;[170] however, as the magnetron frequency is fairly small (~1/10,000 compared to cyclotron frequency), so that this wavy distribution can only be observed when the mass accuracy is in 0.1 ppm level, and can be corrected internally using a "walking" calibration.[169]

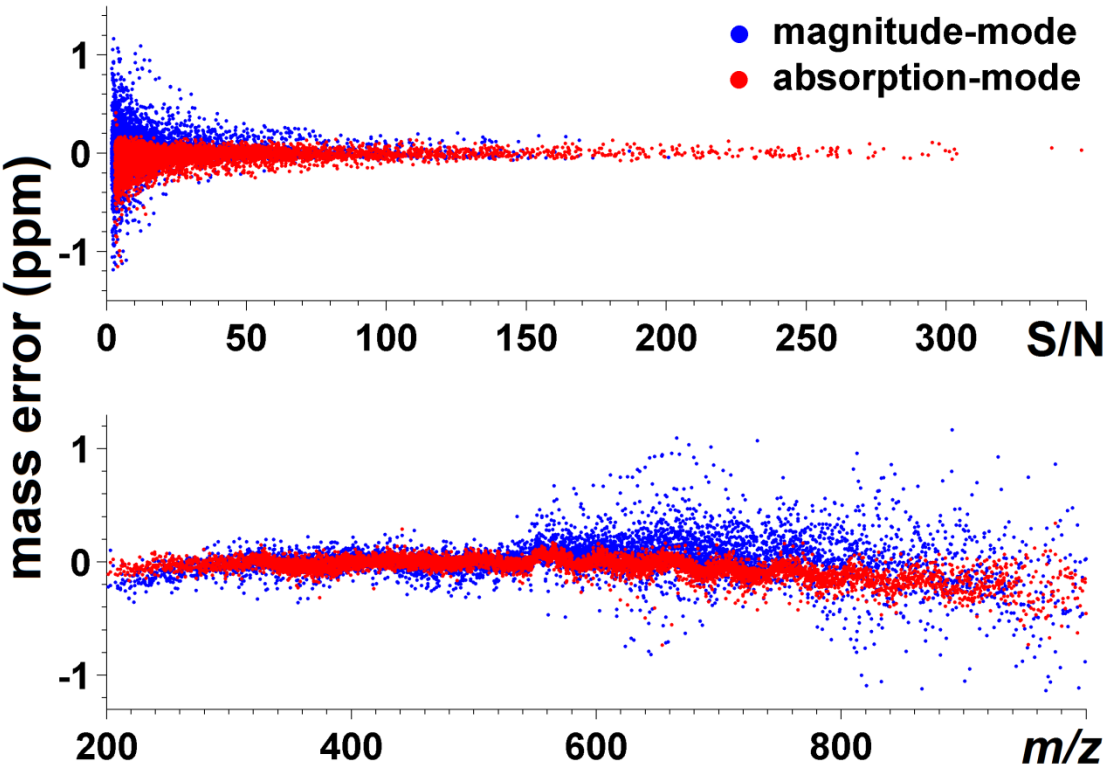

Figure 4.4 Mass error distribution (in ppm) of the crude oil spectrum versus S/N (top) and *m/z* (bottom) domain for both magnitude- and absorption-mode.

In the absorption-mode spectra, mass errors are lower, overall, than the errors in the magnitude-mode; however, a systematic shift in mass errors is observed in Figure 4.4, top for the very low S/N peaks in the absorption-mode. This shift is not caused by space-charge effects[126, 171] as the measured

frequency is a draft in the positive frequency direction. A possible source of this error may come from the use of a quadratic phase function. The phase function assumes that the ions' frequencies change linearly while the actual frequency sweep is stepwise (Figure 3.3 in chapter 3); consequently, this assumption slightly exaggerates the frequencies in the calculation. This error does not appear in the calmodulin spectrum, because this effect is not severe in high mass (low frequency) range (*m/z* 1000-3000 corresponds to the frequency of ~61-184 kHz). By contrast, peaks in the oil spectrum are within the *m/z* from 200 to 1000 which is much greater in frequency (~184-925 kHz), the higher frequencies used in oil spectra will certainly exaggerate the error, and the quadratic phase function does cause an asymmetric peak shape with a negative shift in the *m/z* in the absorption-mode spectrum (Figure B1, inset). Another possible source of error can be the centroiding algorithm from the Bruker Data Analysis software. All commercial FT-ICR programs are designed for magnitude-mode spectra by default, but the absorption-mode peak has negative sidebands and much narrower shape so that the conventional peak fitting algorithm is likely not the best choice for peak picking. Not surprisingly, all the peaks shifted in *m/z* are in the low S/N region--small peaks which would be affected by the sideband of the large peaks nearby. Therefore, a better peak fitting algorithm which utilizes the correct absorption-mode peak shape may correct this error.

For further study, several *m/z* windows in both low and high *m/z* regions were chosen to compare the performance of the two spectral modes. For the low mass range (Figure B1), although the peaks become sharper, there is little difference for the two modes. Because the 12 T instrument is sufficient to split

the fine structures, thus, the extra resolving power for use of absorption-mode does not result in any new information. However, at higher *m/z*, resolution drops and the number of possible elemental composition increase, and for this reason, the improvement becomes significant. Under these conditions, the absorption-mode resolves more peaks than the magnitude-mode, thus, much more information is now revealed (Figure 4.5), and close mass doublets unresolved in magnitude-mode now become resolved in the absorption-mode, thereby greatly increasing the mass accuracy and the number of unique elemental composition assignments (full assignment is in Table B1). This improvement is considered to be systematic; depending on the degree of peak distortion (e.g., small peaks partially overlapped by large peaks nearby will benefit most from the use of absorption-mode).

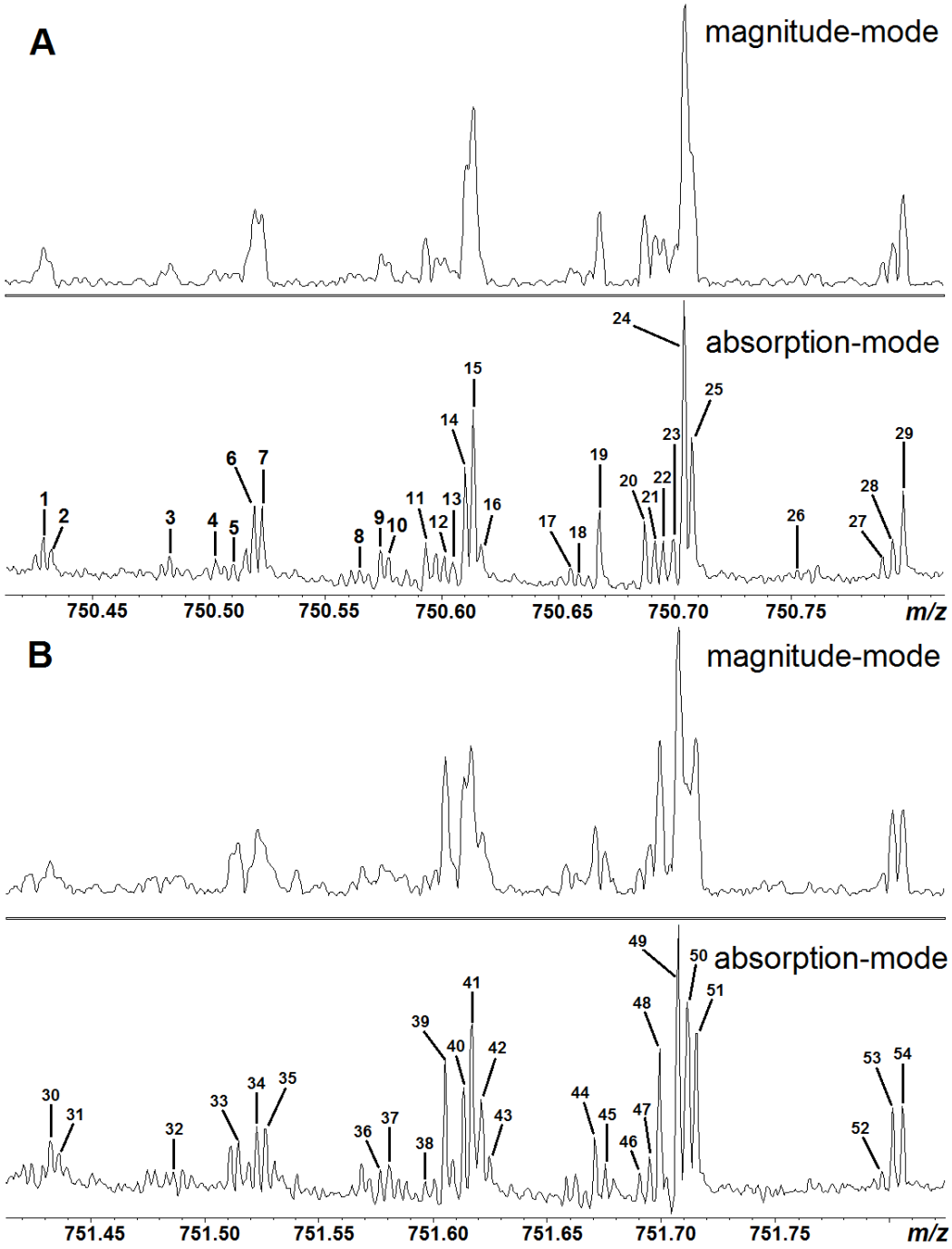

Figure 4.5 Zoom in of two narrow *m/z* windows in the oil spectrum, in both magnitude- and absorption-mode (A: *m/z* 750.41-750.82, B: *m/z* 751.41-751.83), the peak assignment is in Table B1.

Finally, this improvement in mass accuracy can be correlated to the compound's chemical information as is shown in Fig. 4.6A. In an oil sample, peaks appear regularly by compounds' hydrogen deficiency, heteroatom content and carbon distribution. Therefore, the absorption-mode spectrum may have marginal improvement for some classes of compounds, but substantial impact on others by improving peak shape (Figure B2). In the spectrum plotted in Figure 4.6A, the RMS mass errors for the whole spectrum in magnitude- versus absorption-mode were plotted for a series of molecular types, and the CH class shows only a 23% improvement in mass accuracy while the S_2 show a 64% increase. This systematic improvement is mostly possible because oil spectra are largely 'repeated' every 1 Da, with the various compound classes showing up at predictable regular positions relative to each other throughout the spectrum. Therefore, peaks of three adjacent classes: CH, S, and S_2 were chosen and monitored from *m/z* range 680-820, every 20 Da in the spectrum (Figure 4.6B). These three classes show significant differences in improvement ratio in Figure 4.6. This observation is muddled as there are controversies related to exactly how the compound 'class' is defined, but there is still an observable difference in mass accuracy between different compound classes in the petroleum sample.

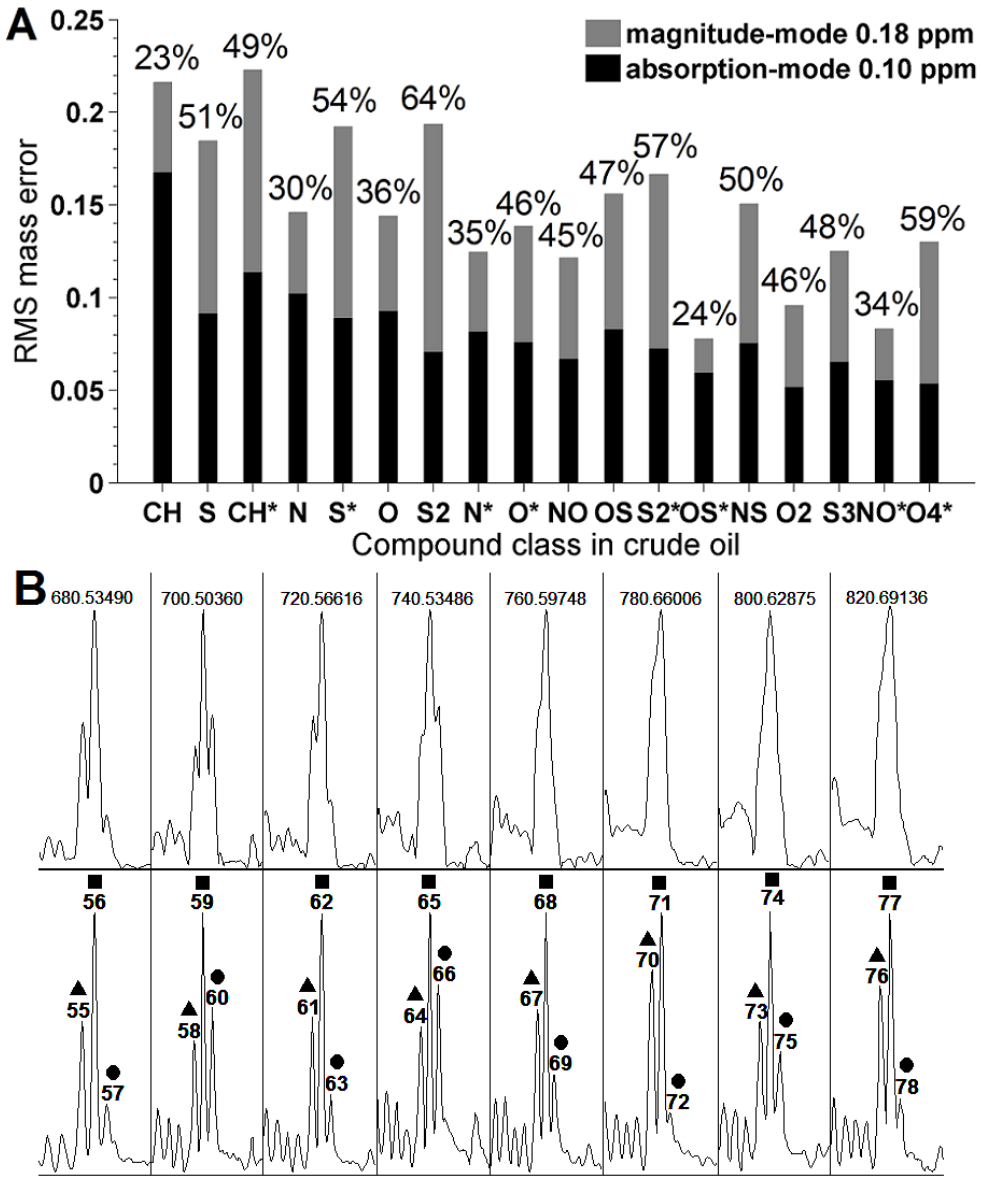

Figure 4.6 A: Histogram showing the improvement on RMS mass error for different compound classes ($C_nH_{2n+z}X$, where X represents the different classes listed in the horizontal axis) for the two mode of spectra (M* indicates the $[M+H]^+$ compounds as APPI generate both radical and protonated species); B: Zoom in of three adjacent classes: CH(▲), S(■), and S_2 (●) in both magnitude (top) and absorption-mode (bottom) in different *m/z* range, the measured mass of S class is labeled in the magnitude-mode, and the peak labeled in the absorption-mode are listed in Table B1.

4.5 Conclusion

Ultra-high resolving power is the key feature which distinguishes the FT-ICR from all other mass analyzers because the measurement of the mass of a peak is only confident, and mass accuracy can only be truly defined, when a peak is fully resolved. The importance of resolving power is best recognized in complex spectra (e.g., crude oil, top-down protein), which is why these samples are generally best analyzed using FT-ICR. However, physicists have achieved 0.1 ppb mass accuracy in measuring single atom using Penning traps (FT-ICR is fundamentally a Penning trap), whereas, in FT-ICR, the field is still struggling to routinely achieve 0.1 ppm level in routine experiment. In this chapter, the superior performance of the absorption-mode spectrum was successfully applied to crude oil and top-down protein spectra which may be a start to break the sub-ppm barrier.

Chapter 5

Absorption-Mode Fourier Transform Mass Spectrometry: the Effects of Apodization and Phasing on Modified Protein Spectra[4]

5.1 Introduction

Fourier transform ion cyclotron resonance (FT-ICR) mass spectrometry is used extensively in the field of proteomics, metabolomics, and petroleomics because of its superior mass resolving power, accuracy, and comparable sensitivity.[44-45] Furthermore, its compatibility with different fragmentation methods makes FT-ICR ideal for tandem mass spectrometric analysis of large biological molecules.[51, 172-173] The quality of a spectrum is the key for data interpretation, and in real experiments, not all protein fragments provide sufficient number of detectable multiple charge states for classic "deconvolution".[174] Furthermore, mass spectra from FT instruments often contain harmonic and noise peaks which leads to false results in the interpretation of complex spectra.[71, 144] Therefore, any method which could both increase the number of detectable peaks and identify any artificial peaks in a spectrum would be of great benefit in the study of complex samples.

Recently, different methods have been developed for phase correcting FT-ICR spectra, allowing the spectra to be displayed in the absorption-mode. The method by F. Xian *et al.*, uses a detailed model of the excitation pulse from each experiment.[95] Unfortunately, commercial instruments don't record these

[4] This chapter has been partially/entirely reproduced from
Qi, Y.; Li, H.; Wills, R.; Perez-Hurtado, P.; Yu, X.; Kilgour, D.; Barrow, M.; Lin, C.; O'Connor, P., Absorption-Mode Fourier Transform Mass Spectrometry: the Effects of Apodization and Phasing on Modified Protein Spectra. *J. Am. Soc. Mass Spectrom.* **2013**, 24 (6), 828-834. Copyright 2013, Springer.

data sufficiently accurate, and additionally, interference from the image charge effect or other field inhomogeneities induce space charge, can also affect the accuracy of the phase function.[93] Another method by Y. Qi *et al.*, uses quadratic least-squares fit and iteration to form a phase function for spectra from without prior knowledge of the instrument pulse program;[68] this method only requires the raw transient and calibration information, and allows phase correction to be largely automated for broad application.[93]

As noted in previous publications, compared to the conventional magnitude-mode presentation of spectra, the absorption-mode offers improvements in both the resolving power and the S/N of spectra: 1) the resolving power improves approximately by a factor of √3-2x, depending on the damping of the transient;[83] 2) the S/N increases by a factor of √2x, as phase correction aligns the data points (vectors) with the real axis of the complex space so that the values of the imaginary part become zero;[89] 3) the correlation between the intensities of the fine-structure isotopic peaks compared to their theoretical intensities improves by over 2x.[75] Apart from that, recent research shows that the artificial peaks in the spectrum (from harmonics or radio-frequency interference) can be easily distinguished in absorption-mode spectra as these peaks do not phase correctly. And furthermore, use of a half window apodization function retains the most intense signal at beginning of the transient so that the absorption-mode signal will not be over-suppressed as often occurs in the magnitude-mode (see below). Given the combined effect of all the factors described above, the overall ‘quality’ of an absorption-mode spectrum can be improved by much more than 2x over the equivalent magnitude-mode. And by using the absorption-mode spectrum, it is possible to

make many new peak assignments which could not be found using the magnitude-mode spectrum of the same data.

Previously, most demonstrations on absorption-mode spectra have used petroleum data where the *m/z* is below 1000, because calculation of the phase function initially requires a spectrum with a high peak density.[89, 95] This phase function could then be applied to other, low peak density spectra (e.g., protein spectra) in order to allow them to be displayed in absorption-mode. This approach is akin to external mass calibration in difficulty. In this chapter, a method for performing internal phase correction has been investigated, where the phase function is derived using ions of cesium perfluoroheptanoic acetate (CsPFHA), added into other samples as an internal calibrant. This chapter provides the first examples for phase correction of top-down spectra, ranging from small peptides (bombesin, digested collagen) to large proteins (calmodulin, hemoglobin tetramer), as well as a MS^3 spectrum of β2 microglobulin acquired from a different research laboratory. In these examples, the absorption-mode spectra display a significant number of additional low S/N and high *m/z* peaks, which were previously undetectable in the baseline, and so reveal much more information which was not apparent in the magnitude-mode spectra. Besides that, it is proved that the phase correction method can be applied to FT-ICR spectra worldwide, regardless of the experimental conditions and instrument parameters on which the spectrum was recorded, because this method is a post-process procedure requiring only the raw transient and calibration function, and to promote its application, an Autophaser program[93] will be available soon from our group.

5.2 Experimental Section

5.2.1 Sample Description and Preparation

Collagen, bombesin, calmodulin, hemoglobin, β2-microglobulin, trypsin, cesium iodide, and perfluoroheptanoic acid were purchased from Sigma Aldrich (Gillingham, UK); the crude oil standard (SRM 2721, light-sour) was purchased from NIST (Gaithersburg, MD, USA). The hemoglobin powder was diluted to 5 uM in 100 mM ammonium acetate (pH 6.8) for native state spectrum without desalting. Other samples were prepared according to general protocol, which can be found in previous publications.[89, 165, 175-178] The CsPFHA clusters (*m/z* up to 8000) were prepared according to the literature.[179] In order to generate sufficient peaks in the high *m/z* range for the calculation of phase function, CsPFHA ions were added to each experiment by dual-electrospray, to reduce the matrix effect.[180]

5.2.2 Data Processing

All spectra were recorded using a solariX 12 T FT-ICR mass spectrometer (Bruker Daltonik GmbH, Bremen, Germany), equipped with an Infinity cell.[59] 300 individual transients (2.3 s) of hemoglobin were collected and co-added. 40−300 individual transients (1.7 s) for the bombesin, collagen, calmodulin, microglobulin were collected and co-added. The acquired transients were then apodized by either a full Hanning window for magnitude-mode[103] or a half Hanning window for absorption-mode[104] (Figure 2.12) without any truncation of the signal, then zero-filled two times, and fast Fourier transformed in MatLab R2010a (MathWorks, Natick, MA, USA). The phase function was calculated utilizing the CsPFHA peaks across the entire spectrum. The pre-processed

data sets were then written in Xmass format with appropriate parameters based on the data, and loaded into Bruker DataAnalysis software for peak detection and spectral interpretation.[89]

5.3 Result and Discussion

5.3.1 Detecting the Harmonics and other Artefacts

Second, third, and higher harmonic peaks are common artefacts which always exist in FT-based mass spectrometer (e.g., FT-ICR, Orbitrap, and ion trap instruments, details in Chapter 2). In FT-ICR, odd harmonics are mostly generated by non-sinusoidal image current from finite size detection electrodes, while even harmonics are generated by non-zero magnetron radius or imbalance in the detection amplifiers.[71] In addition to harmonics, imperfect electronics (e.g., imbalance of the amplifiers, overloading the analog-to-digital converter, radio-frequency interference) can also result in artificial peaks in the recorded spectrum.[144] These artificial peaks contain no chemical information, but can greatly complicate the task of data interpretation, especially when the spectrum is complex. Figure 5.1 (left inset) expands the 3rd harmonic region in a top-down tandem mass spectrum of calmodulin bound with cisplatin; in the conventional magnitude-mode, the harmonics appear like a typical protein isotopic distributions. Generally, identifying the harmonics requires correlation of the peaks to higher *m/z* primary signals which is easily done in simple spectra, but this can be challenging for complex spectra. Here, in the absorption-mode, any artefacts can be directly recognized by the anomalous phase variation because they cannot be phased properly using the correct phase function. Therefore, by plotting the spectrum in the absorption-mode,

any artefacts can be easily recognized which facilitates data interpretation. Apart from that, it is interesting to note that the absorption-mode spectrum shows an oscillation at the baseline (Figure 5.1B), such oscillation is caused by two different sources: 1) a low periodic frequency oscillation (known as baseline roll);[96] and 2) distortion near signal peaks proportional to signal magnitude (known as sinc function deviations).[83] However, such baseline distortion can be removed or ameliorated by post-processing.[93, 96]

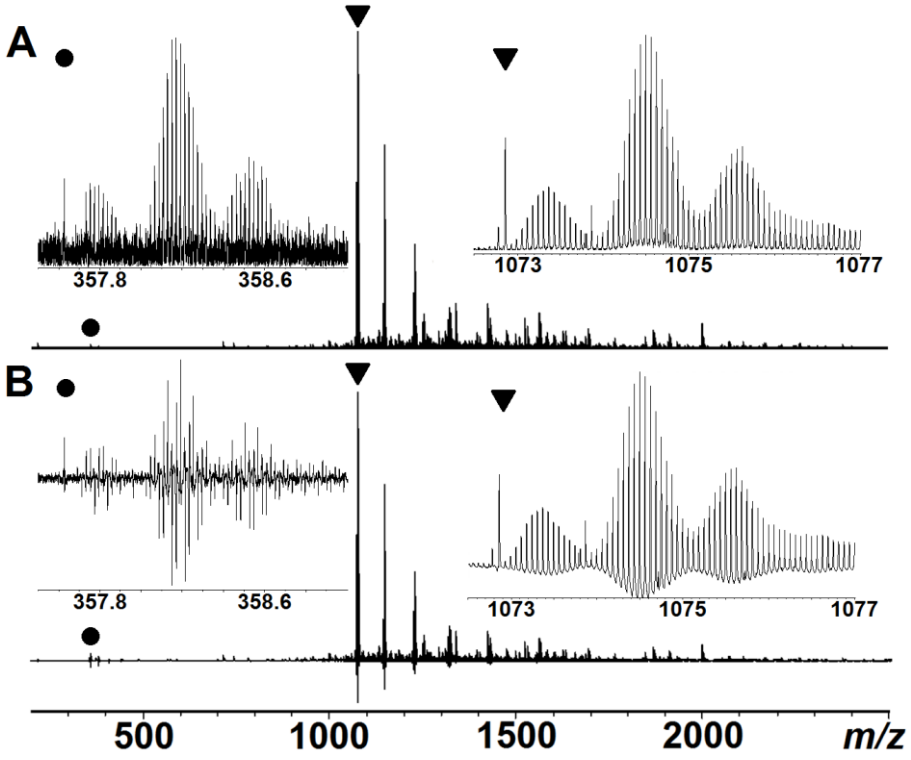

Figure 5.1 ECD spectrum of calmodulin+cisplatin mixture in both magnitude-(A) and absorption-mode (B). The inserts on the right are zoom in of the original peaks (labeled with a triangle in the spectra), and the inserts on the left are their 3rd harmonics (labeled with a dot).

5.3.2 Effects of Apodization

The Fourier transform generates undesirable sidebands at both sides of a peak, which interferes with adjacent peaks and affects the detection of low intensity peaks nearby, therefore, the time-domain transient is multiplied by a window function prior to Fourier transform in order to smooth the peak shape and minimize the sideband intensities (Figure 2.12).[71] This procedure is called “apodization”; an optimal window function removes the sidebands at a cost of S/N and resolving power. However, the effect of apodization is dependent on the ratio of sample acquisition time and its damping constant (T/τ), which varies significantly from spectrum to spectrum.

The window function also affects the relative intensity and S/N in a spectrum, for demonstration, the crude oil dataset from previous chapter[89] was re-plotted here. As is seen in Figure 5.2 A-I, the spectral intensity (using the same vertical scale) varies by applying different apodization functions: the full-window suppresses the signal at both the beginning and the end of the transient, while a half-window retains the intense part at the beginning. Furthermore, it should be pointed out that the full window function generates large negative intensities in the absorption-mode (Figure 5.2I), an interesting phenomenon which was first reported by Comisarow *et al*. 24 years ago,[104] and such a distortion is largely dependent on the density of peaks in the spectrum.

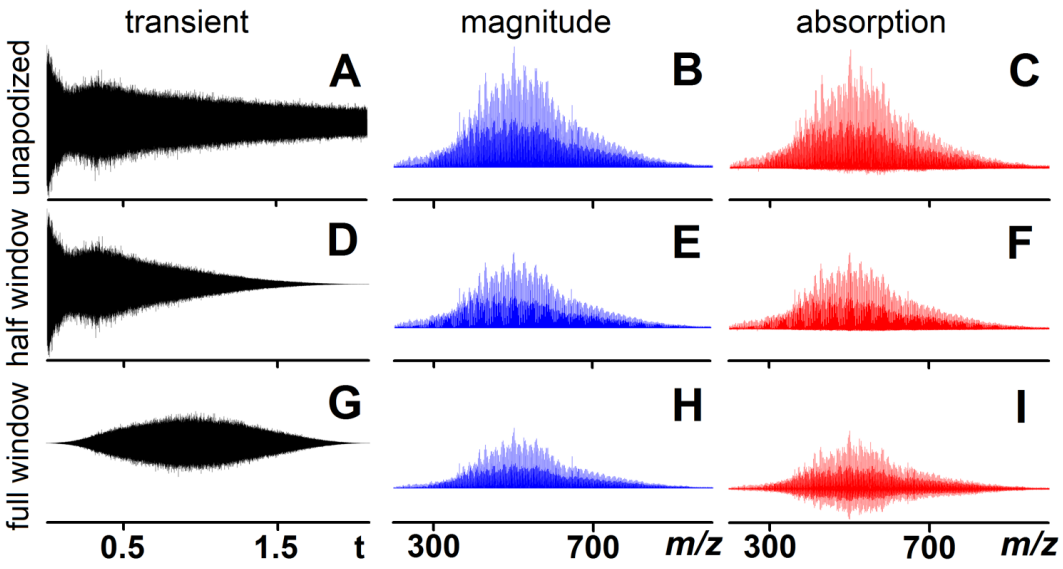

Figure 5.2 (A-C): Transient (black) and *m/z* spectra in magnitude- (blue) and absorption-mode (red) without apodization. (D-F): Transient and spectra with a half Hanning window apodization. (G-I): Transient and spectra with a full Hanning window apodization.

For further study, narrow *m/z* windows in both low and high *m/z* regions were expanded to compare the peak shape results from different window functions. As is shown in Figure 5.3A-F, both half and full windows smooth the peak shape compared to unapodized spectra, and the full window will have a narrower peak width than the half one. Additionally, the full window leads to large negative intensities in the absorption-mode, and thus, distorts the peak shape. In the low *m/z* region, when the peaks are well resolved, Figure 5.3C shows a typical absorption-mode peak shape from full window function. Meanwhile, when the peaks become dense in the high *m/z* region, the negative sidebands will interact with peaks nearby causing severe spectral distortion (Figure 5.3F). In conclusion, the full window apodization has a narrower peak width compared to the half window (Figure 2.12E&I), and thus

is recommended in the magnitude-mode spectrum for better resolving power and peak shape, meanwhile, the half window function is preferred in the absorption-mode for better peak shape and S/N.

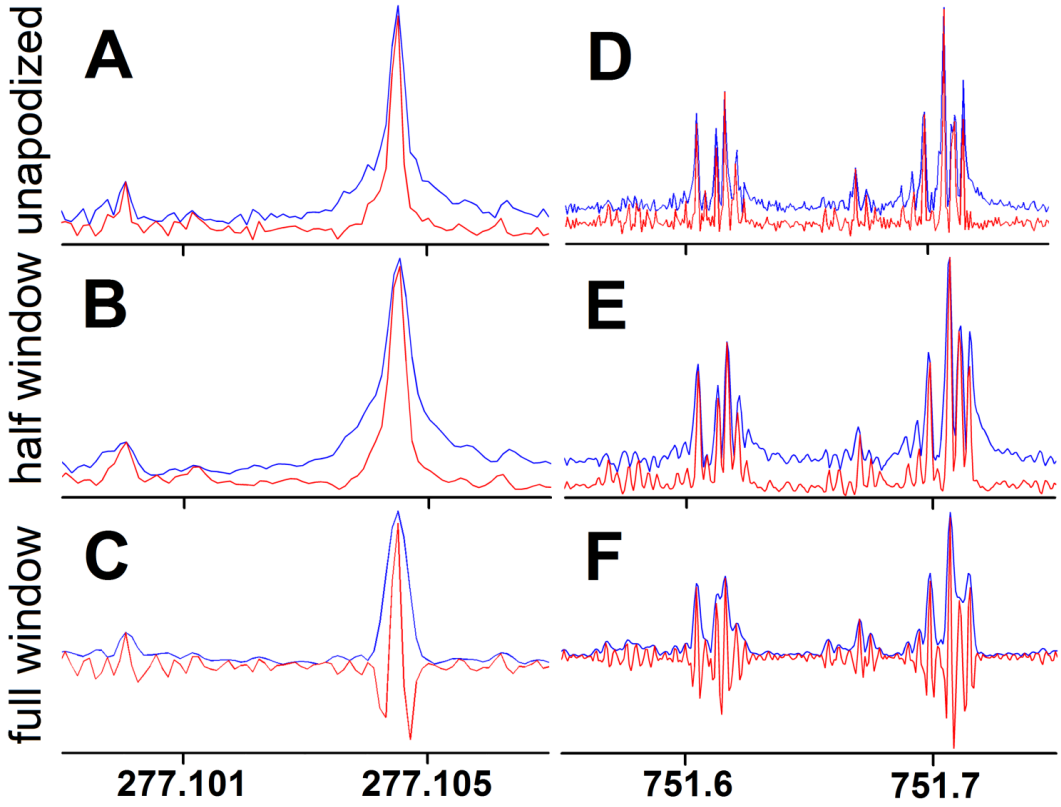

Figure 5.3 Close-up of two narrow *m/z* windows from Figure 5.2, in both magnitude- (blue) and absorption-mode (red). (A-C): *m/z* 277.099−277.107 with no apodization, half Hanning, and full Hanning apodization. (D-F): *m/z* 751.55−751.75 with no apodization, half Hanning, and full Hanning apodization.

Figure 5.4 shows a particularly difficult case involving the low charge states of intact hemoglobin (Hb, 65 kDa) by applying different window functions. Hb is an assembly of four subunits, each subunit is associated with

a heme group, and these allows study of non-covalent bond interactions.[181] During the experiment, the Hb powder was dissolved in ammonium acetate without desalting to deliberately complicate the spectrum, and a 2.3 s transient was recorded with the corresponding *m/z* spectra showing the peaks of Hb tetramer. As is seen in Figure 5.4, the distribution of each charge state was broadened significantly, as the presence of salts in the sample reduced the overall molecular ion abundances and distributed the signal of each charge state into many adducted forms (*m/z* 3800-4400). Because of the high mass and low charge for the adduct form, only FT-ICR offers sufficient performance to resolve the isotopic peaks. In the unapodized magnitude-mode (Figure 5.4C), peaks are partially overlapped, but they can be resolved and assigned the charge states, however, the use of apodization greatly decreases the resolution. When the same spectrum is plotted in the absorption-mode, the isotopes are almost resolved at the baseline, and there is no significant change in the unapodized and half window apodized spectra. Furthermore, a surprising effect was observed when the full window function was applied. In the magnitude-mode shown in Figure 5.4E, the isotopic peaks become unresolved. From Figure 5.4A, it is clear to see that the first beat pattern of the Hb tetramer appears within 0.01 s which is the most intense part of the transient, and the second one appears at ~1.4 s (the period agrees with the theoretic calculation). Consequently, a full window function zeros the signal at the beginning of the transient; such suppression effect is expected to vary with the ratio of T/τ. In certain cases, as is shown here, the full window function seriously degrades the performance of the spectrum because the S/N and resolution are significantly reduced. Therefore, in Figure 5.4H, when the same

phase correction was applied in the absorption-mode, the peaks were completely distorted. In summary, while lack of apodization is preferred, if apodization is needed for improvement of sidebands and peak shape for centroiding algorithms, a half window function is recommended for the absorption-mode spectrum.

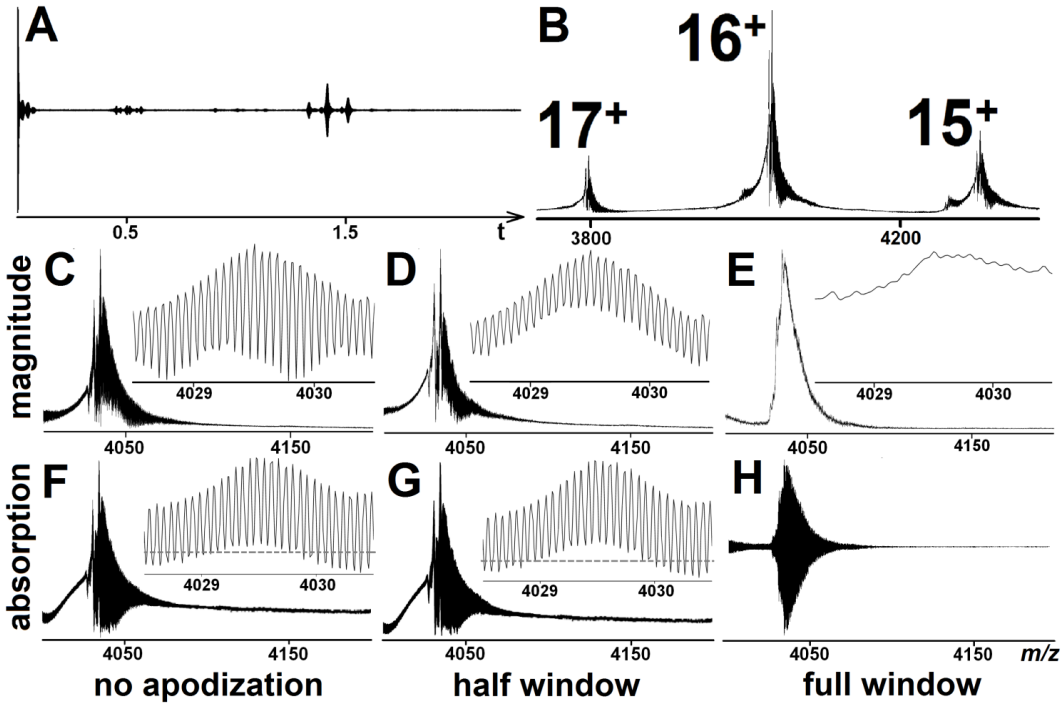

Figure 5.4 Transient and *m/z* spectra of hemoglobin tetramer with the charge states from 15 to 17. (A): original transient recorded for 2.3 s; (B): conventional magnitude-mode spectrum with no apodization. (C-E): Close-up of the 16^+ magnitude-mode spectra with no apodization, half window, and full window apodization (baseline of spectrum is the *m/z* axis). (F-H): Close-up of the 16^+ absorption-mode spectra with no apodization, half window, and full window apodization (baseline is labeled by dash).

5.3.3 Application to Modified Peptides and Proteins

For top-down spectra of small peptides, due to the low mass and charge state, the resolution of the 12 T instrument is sufficient to separate the individual isotopic peaks so that most fragments from inter-residue bond cleavage can be confirmed in top-down spectrum; however, in some cases, S/N is insufficient. When the peptides bind to the metallodrugs, the anomalous isotopic pattern of the metal ion tends to distribute signal of the original peaks into different modified forms, thus, reducing the overall ion abundances and shifting the m/z of all peaks.

Organometallic Ru complexes have been investigated as a potent anticancer agent,[182] and FT-ICR studies have provided insights into its preferred binding sites on proteins. As shown in Figure 5.5A&B, the ECD spectrum of Ru bound to bombesin yielded almost all the inter-residue bond cleavages. However, the S/N of a Ru modified bombesin are much lower than in the corresponding unmodified spectrum due to the broad isotope distribution of Ru, and additionally, the electrons are captured much more easily by metal ions, which reduces the probability of ECD cleavage on the peptide backbone. By presenting the spectrum in the absorption-mode, the S/N and isotope distributions were improved, and four new Ru-modified fragments were observed which were not detected previously in the magnitude-mode (Figure 5.5B). Note that the misalignment of peaks with the simulation is caused by hydrogen transfer between the c' and $z^{\cdot}$ ions.[183-184]

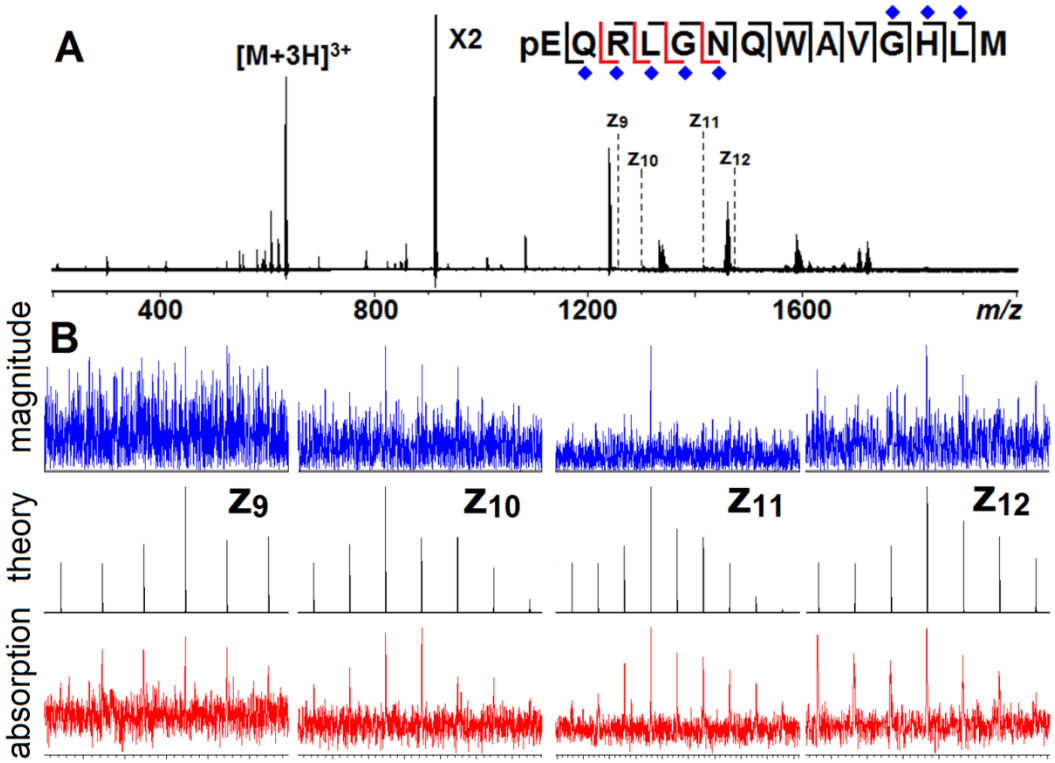

Figure 5.5 (A): ECD spectrum of Ru binding bombesin, with the cleavage map. Fragments observed in magnitude-mode are in black, new fragments in absorption-mode are in red, the Ru binding sites are labeled by diamond. (B): zoom in of fragment in magnitude- (top), absorption-mode (bottom), and its isotope simulation (middle).

The benefits of this spectral improvement can also be seen in the analysis of digested collagen. In magnitude-mode, 57 *c/z* fragments could be assigned,[175] accounting for 24 inter-residue bond cleavages (4 prolines in the sequence cannot be cleaved via ECD). As is shown in Figure 5.6A&B, the same fragments were also observed in the absorption-mode, but with a much smoother isotope distribution. Furthermore, 7 new fragments were detected, which were previously hidden in the noise in magnitude-mode.

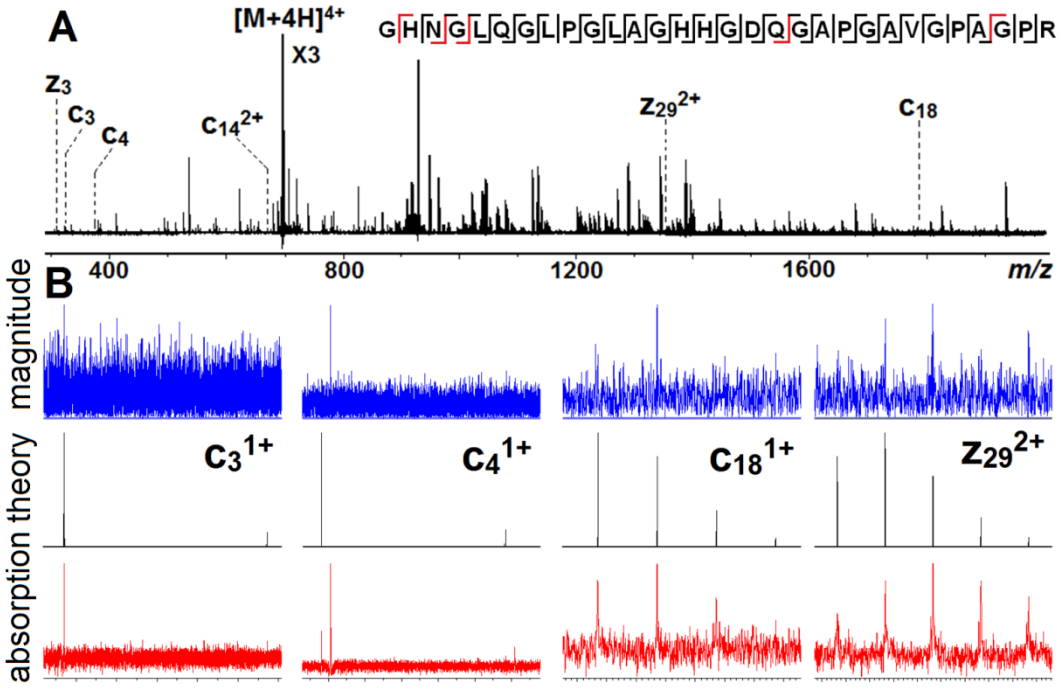

Figure 5.6 (A): ECD spectrum of collagen with the cleavage map (fragments observed in magnitude-mode are in black; new fragments in absorption-mode are in red, labeled in the spectrum). (B): zoom in of fragment in magnitude- (top), absorption-mode (bottom), and its isotope simulation (middle).

Investigating PTMs of large biological macromolecules is one of the most significant challenges facing MS analysis. Deamidation is, perhaps, the most common PTMs in proteins, which produces a mixture of asparagine (Asn), aspartic acid (Asp) and isoaspartic acid. Asn deamidation results in a 0.984 Da mass shift which is very close to the ^{13}C isotope of the unmodified form, which means there is only a 0.019 Da difference between the Asn and Asp isotopes.[185] Therefore, determining the extent of deamidation in a protein requires sufficient mass resolving power to separate the individual isotopic peaks. For example, Figure 5.7 shows an ECD spectrum (MS^3) on the b_{63}^{9+} fragment formed by CAD of β2 microglobulin; this spectrum was acquired by Yu

et al. from Boston University on their 12 T FT-ICR mass spectrometer.[178] The inset on the right is the expansion of the c_{25}^{4+} fragment to show the detailed peak splitting. For a 4^+ charge segment, the $\Delta m/z$ of Asn and Asp isotopes is ~0.0048, which is barely discernible in the magnitude-mode; by comparison, these peaks are clearly resolved in the absorption-mode due to the extra resolving power provided by phasing. The result not only shows a better peak splitting, but also illustrates that the phase correction method can be applied to the spectra acquired from different instruments without knowing precise details on experimental parameters.

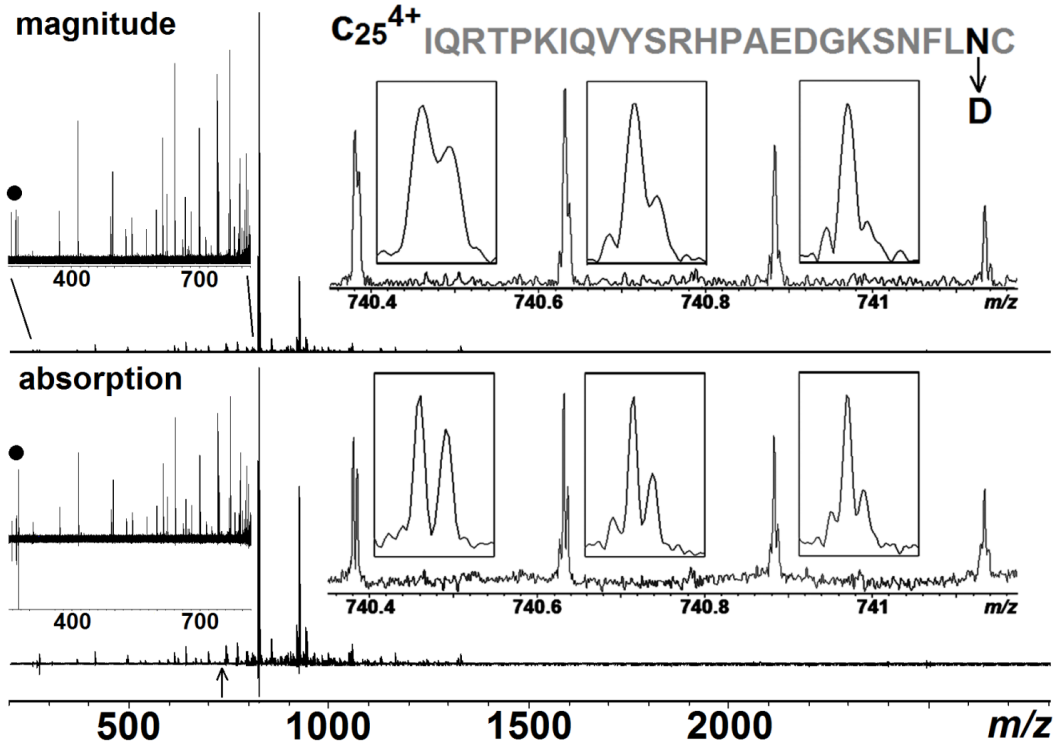

Figure 5.7 ECD spectrum (MS^3) of the b_{63}^{9+} fragment from β2 microglobulin in both magnitude- and absorption-mode. The inserts on the right are zoom in of the c_{25}^{4+} fragment (labelled with an arrow in the bottom) with its sequence and the deamidation site highlighted in black. The inserts on the left are zooms of *m/z* 250-820 to show the entire spectrum is properly phased, and the peaks labeled with a dot are 3rd harmonic peaks of the peaks in *m/z* ~823.

5.4 Conclusion

The absorption-mode spectra presented here represents a significant step towards improving the data quality of top-down spectra from modified protein at no extra cost. Phasing can be applied to petroleum, peptide, or protein transient without prior knowledge of instrumental conditions, and results in significant improvement in spectral qualities in terms of resolution, S/N, and mass accuracy. Phasing also allows immediate assignment of harmonics and noise peaks as they show an anomalous phase signature.

Chapter 6

Absorption-Mode Spectra on the Dynamically Harmonized Fourier Transform Ion Cyclotron Resonance Cell[5]

6.1 Introduction

The Fourier transform ion cyclotron resonance mass spectrometer (FT-ICR MS)[44-45] is superior to other mass analyzers in terms of flexibility, mass accuracy, and mass resolving power (RP, $m/\Delta m_{FWHM}$). Resolving power is particularly crucial because the assignment of peaks is only confident when peaks are fully resolved. The isotopic distribution of multiply charged peptides or small proteins is revealed when RP is above ~10,000;[76] however, each of the isotope peaks other than the monoisotopic peak is composed by the much more complex fine isotope clusters. Due to insufficient resolving power and minor abundance of some trace isotopes, the isotopologue peaks are often attributed as ^{13}C peaks, as the ^{13}C has relatively the highest abundance, even though the higher isotopic peaks in any distribution are more accurately represented by a series of "heavy" isotopes of varying masses. The fine structures of isotopic distributions are generally only revealed when the resolving power is above ~10^6, which can be achieved by state-of-the-art FT-ICR MS with careful tuning.[7, 74] The utility of the fine isotopic peak distribution is that it reveals the elemental composition without tandem MS experiments, and even the number of a certain atoms in the formula, such as

[5] This chapter has been partially/entirely reproduced from
Qi, Y.; Witt, M.; Jertz, R.; Baykut, G.; Barrow, M. P.; Nikolaev, E. N.; O'Connor, P. B., Absorption-mode spectra on the dynamically harmonized Fourier transform ion cyclotron resonance cell. *Rapid Commun. Mass Spectrom.* **2012**, 26 (17), 2021-2026.
Copyright 2012, Wiley.

sulfur, can be counted.[74] Obviously, the mass resolving power is a prerequisite to reveal the information within the fine isotope structure.

In FT-ICR, the mass resolving power ($m/\Delta m_{FWHM}$) of a given magnetic field, B, is defined in Eq. 6.1a (with the approximation of ω and $\Delta\omega$ defined in Eq. 6.1b and 6.1c):

$$RP = \frac{m}{\Delta m} = \frac{\omega}{\Delta\omega} = \frac{qB}{m\Delta\omega} \propto \frac{qBT}{mk} \qquad (6.1a)$$

$$\omega = \frac{qB}{m} \qquad (6.1b)$$

$$\Delta\omega \propto \frac{k}{T} \qquad (6.1c)$$

in which m, q, and ω are mass, charge and cyclotron frequency of the ion; Δm and $\Delta\omega$ are the peak width at half maximum in the m/z and frequency domain, respectively. The value of $\Delta\omega$ is inversely proportional to T (duration of the transient) after Fourier transform,[45] and the value of constant k varies, depending on the frequency stability of the signal and the model applied to describe the peak shape. From Eq.6.1a, it is obvious that building a higher magnetic field is the most direct way to improve RP, however, the cost of the magnetic field is not linear, and increases dramatically with B>12 T. Nevertheless, efforts can be taken to improve the other two factors, duration of the transient and the peak width constant.

In a given magnetic field, coherence of ions' motion and ultrahigh vacuum (~10^{-10} mbar) are the key factors to prolong the time-domain transient. In ICR cells, an electric field is applied to trap the ions in the axial direction. Thus, apart from the radial motion, ions also experience an axial oscillation; and the detection of "effective" cyclotron motion will be affected if the electric field is not

perfectly harmonized. The ideal electric field should be a hyperbolic geometry distribution so that the potential yields a harmonic restoring force like a spring, and ions are oscillating back and forth at a reduced cyclotron frequency independent of the axial position.[60] However, the effective hyperbolic region in the conventional ICR cells, such as cubic,[186] simple cylindrical,[187] or Infinity cell[59] are only ideal near the centre of the cell, while ions are usually detected at ~50% of the cell radius for improved sensitivity. Due to the limited homogeneity region, the interior of the cell cannot be used effectively, and either the ions are confined to a smaller volume at the centre of the cell and are more likely to be influenced by space-charge effects,[126] or excited to a high orbit where the cell's electric field inhomogeneities will cause loss of coherence on ions' motion and therefore decrease the resolving power and signal intensity. Furthermore, if ions are far away from the detecting plates, the sensitivity of the signal detection is also decreased. The above drawbacks limit the duration of the signal, and the effective transient signal recorded in the above cells are usually detectable for only a few seconds. The conventional cylindrical cell was modified by adding compensation rings which improved the electric field homogeneity over an orbit.[152, 188-189] Recently, Nikolaev and co-workers proposed the concept of a dynamically harmonized ICR cell, which creates a space-averaging potential distribution instead of a truly harmonic field.[46] The original data shows that the novel design extends the region of ideal electric field to almost the entire volume of the ICR cell, and the ion transient can last for minutes with minor decay in a 7 T instrument.

In an FT-ICR experiment, ions of different *m/z* are excited by a broadband frequency sweep, and the coherent motion of the ions generate the induced

current signals, which are then be recorded by the detecting plates in the cell. The recorded signal can be written in Eq.6.2:

$$f(t) = N\cos(\omega t)\exp(-t/\tau), \qquad 0 \le t \le T \qquad (6.2)$$

in which *N* is a scaling factor of the signal depending on the number of ions, ω is the observed cyclotron frequency of the ions, τ is the relaxation time due to the ion-molecule collisions and loss of coherence, and *t* is any point in the time domain.[114] The recorded transient (a beat pattern with all different frequencies mixed together) is then Fourier transformed to obtain the signals in the frequency domain, and the separation of close frequencies depends on $\Delta\omega$, the peak width. The peak shape of the frequency spectrum can be modelled in two extreme conditions based on the damping of the transient: low-pressure or high-pressure limits.[82] The low-pressure model is applied when the signal acquisition time << the damping time, which results in the peak shape of a 'sinc' function, and the high-pressure model is applied when the signal acquisition time >> the damping time, which results a peak shape of a 'Lorentzian' function (Figure 4.1). Thus, the peak shape in a real experiment is always a convolution of both a 'sinc' and a 'Lorentzian' function,[83] and the data processing method called 'phase correction' narrows the peak shape, thus, improving the resolving power by a factor between √3 to 2.[89, 95]

In this chapter, the phase correction algorithm is applied to both narrowband (heterodyne-mode)[44] and broadband mode data from the dynamically harmonized cell in a 7 T instrument, and the data are presented to compare the performance of the spectra in magnitude- and absorption-mode.

6.2 Experimental Section

6.2.1 Sample Preparation and Instrumentation

A complex crude oil sample from Sinopec (Beijing, China) was diluted 10^4 times in a 50:50 methanol/toluene mixture, ionized using atmospheric pressure photoionization (APPI), 6.7 dB of in-cell sweep excitation power was applied to enhance the image current (for the study of harmonics), the spectrum was acquired in broadband mode with a detection *m/z* 150-3000 with 8M data points using a solariX 7 T FT-ICR (Bruker Daltonik GMBH, Bremen, Germany) with the new dynamically harmonized cell, and 170 individual transients were co-added to increase S/N. The spectra of resperpine $[M+H]^+$ ion and the spectrum of substance P $[M+2H]^{2+}$ ion on its third isotopic fine structure were acquired in narrowband mode, and only one transient is recorded. The details of the cell design, instrumentation, and experimental parameters of the narrowband mode spectra were described in detail elsewhere.[7]

6.2.2 Data Analysis

The recorded transients were zero-filled twice, and apodized with an optimal window function[71] (unless emphasized in the text): either a full Hanning (for magnitude-mode) or a half Hanning (for absorption-mode).[164] Phase correction was then processed in MatLab R2010a,[83, 165] and the absorption-mode spectra were then loaded into Bruker DataAnalysis (DA) software for interpretation (the MatLab script for reading the heterodyne-mode spectra, calculating the absorption-mode spectrum, and writing the data into DA format can be found in Appendix C and Ref [89]).

6.3 Result

6.3.1 Phase Correction in the Heterodyne-Mode

According to Eq.6.1a, high resolving power can be achieved by recording a long transient. For a single isotopic peak of reserpine, the ions' cyclotron motion continues for at least two minutes in the new cell (Figure 6.1), which requires sufficient digitizer memory (details see Chapter 2). For a modern processor, it is not difficult to handle billions of data points; however, modern digitizers are still limited to a few million data points of storage, thus, all the spectra from these experiments were sampled in the heterodyne-mode to record the extended length transients. To test the phase correction, a quadratic phase function is applied to the substance P spectrum while a constant phase correction is used in reserpine (as there is only one peak in the spectrum). The result shows that the reference frequency and low-pass filter involved in the heterodyne-mode do not import artefacts into the spectrum, therefore, the improvement of resolving power and signal-noise-ratio (S/N) of the absorption-mode can still be achieved in the narrowband mode spectra.

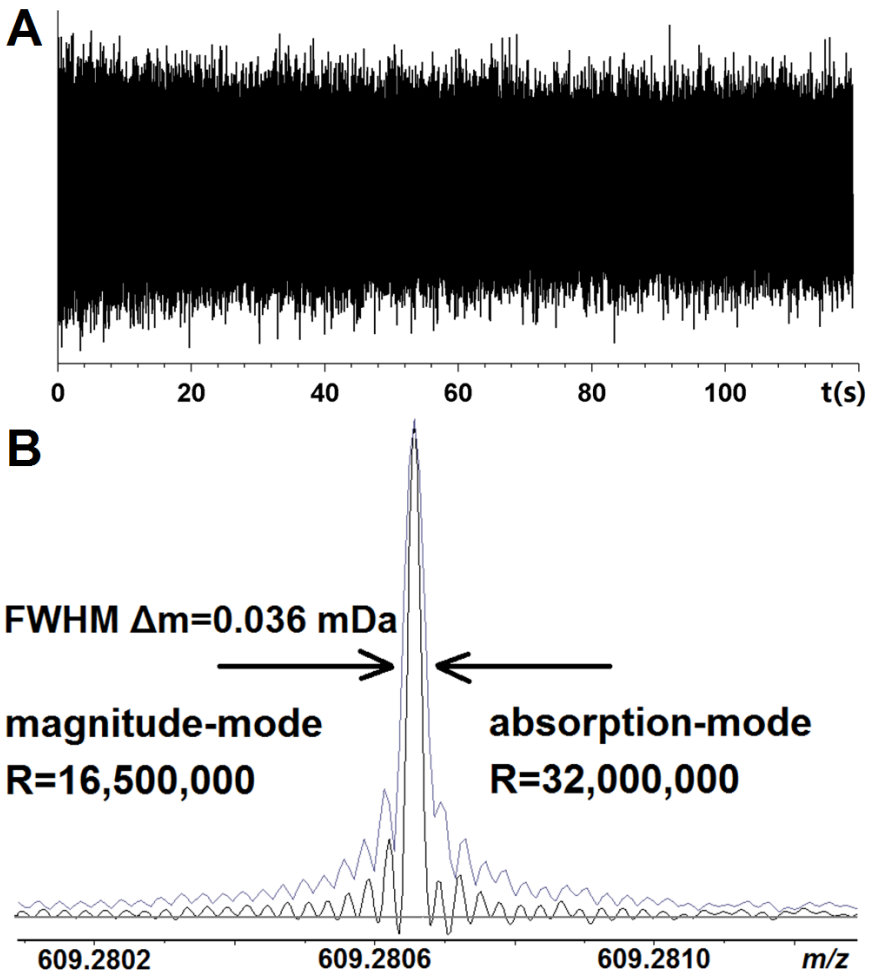

Figure 6.1 A: Time-domain transient of the resperine $[M+H]^+$ ion in heterodyne-mode, acquired for 2 min. B: Spectrum in both magnitude (grey) and absorption-mode (black), the peak width of the magnitude-mode is labeled.

6.3.2 Peak Shape and Mass Resolving Power

The harmonically compensated cell allowed recording of a 2 min, single scan transient of the reserpine (Figure 6.1), in addition, it is important to highlight that the intensity of the signal decays only ~30% during the detection; therefore, such a transient may last even longer. Due to the slow transient damping (τ estimated at >100 seconds), the low-pressure model can be applied here, and the sidelobes in the spectrum reveal a 'sinc' function peakshape--also showing that the signal has only partially damped. Resolving

power in the unapodized absorption-mode (~32M) here is 1.94x the unapodized magnitude mode (16.5M), which also approximates the theoretical value (2x) of the ‘sinc’ function.[83] Thus, with such essentially undamped transients on the dynamically harmonized cell, essentially the maximum improvement on resolving power (2x) can be achieved through phase correction. However, it should be pointed out that even though the 'sinc' function is the correct peakshape, it is also non-ideal as the sidelobes at the base will also interfere with small peaks nearby.

In Figure 6.2, the unapodized spectrum of the A+3 isotopic clusters for the doubly protonated substance P was plotted along with its simulated pattern.[190] In the magnitude-mode, the isotope peaks of $^{15}N^{34}S$ and $^{13}C^{15}N_2$ are partially hidden in the tail of the $^{12}C^{34}S$ peak, even though their mass resolving power is 4.3M and 2.7M, respectively. By contrast, these two isotopic peaks are well resolved in the absorption-mode where the resolving power increased to 8.1M and 9.1M primarily because the sideband distortion of the $^{12}C^{34}S$ peak is reduced. The negative intensity on the right of the $^{13}C_3$ isotope and the additional 'ringing' of the peak may be caused by coalescence of the closely spaced $^{17}O^{13}C_2$ isotope.[191] Overall, it is clear that the new cell increases the duration of the transient from seconds to minutes, therefore, fine structure of the isotope clusters can be revealed in routine experiments. However, 'ringing' artefacts from the ‘sinc’ function should also be noted, indicating a need to explore additional apodization functions[104] to reduce the sidebands, or to develop a peak picking algorithm specialized for such a peak shape.

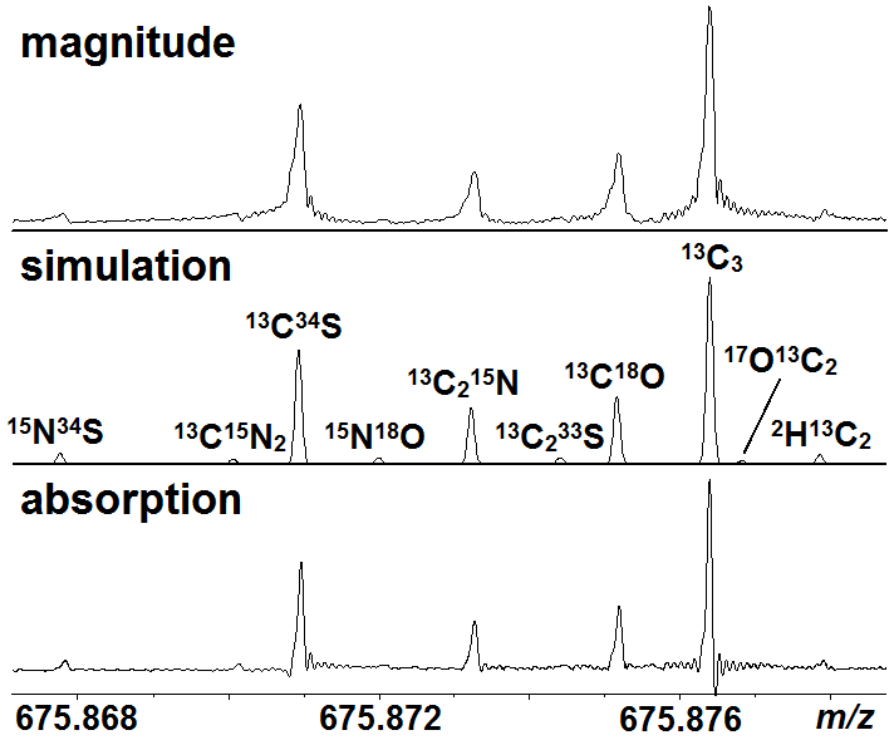

Figure 6.2 Fine structure of A+3 isotopic clusters for substance P$[M+2H]^{2+}$ ion, 45s transient, without apodization.

6.3.3 Mass Accuracy and Relative Peak Intensity

To avoid the 'ringing' artefacts of the sinc function, and to explore the issue of mass accuracy, the Hanning window function[71] (full Hanning for magnitude-mode and half Hanning for absorption-mode as previously reported[89]) was applied to the A+3 clusters of substance P (Figure 6.3); the apodization suppresses the sideband of the peaks at a cost of resolving power, as is obvious by comparison with Figure 6.2. The peaks in Figure 6.3 were assigned (details in Table 6.1). The mass resolving power and S/N in the absorption-mode spectra are systematically found to be superior to the magnitude-mode; however, the better performance doesn't result in a big difference in mass accuracy (33 ppb versus 25 ppb). This is because all peaks are resolved to the baseline, which means better resolving power cannot

improve the peak separations any more. In addition, the relative peak intensities of the assigned isotopes were also compared in Table 6.1, and it was found the RMS difference of the measured and theoretical values is reduced from 14% to 6% in the absorption-mode, because the half window function used in the absorption-mode preserves the most intense part of the transient at the beginning, and because the baseline noise is reduced by $2^{1/2}$ compared to the magnitude mode.[89] The improvement on peak intensity in the absorption-mode may also help to assign ambiguous peaks and count the number of ions. Moreover, the Hanning window function was chosen for comparison with existing literature.[164] In specific cases, other apodization functions may be preferable, but in all cases tested so far, the absorption-mode spectrum always yields higher resolving power than the magnitude-mode, as expected.

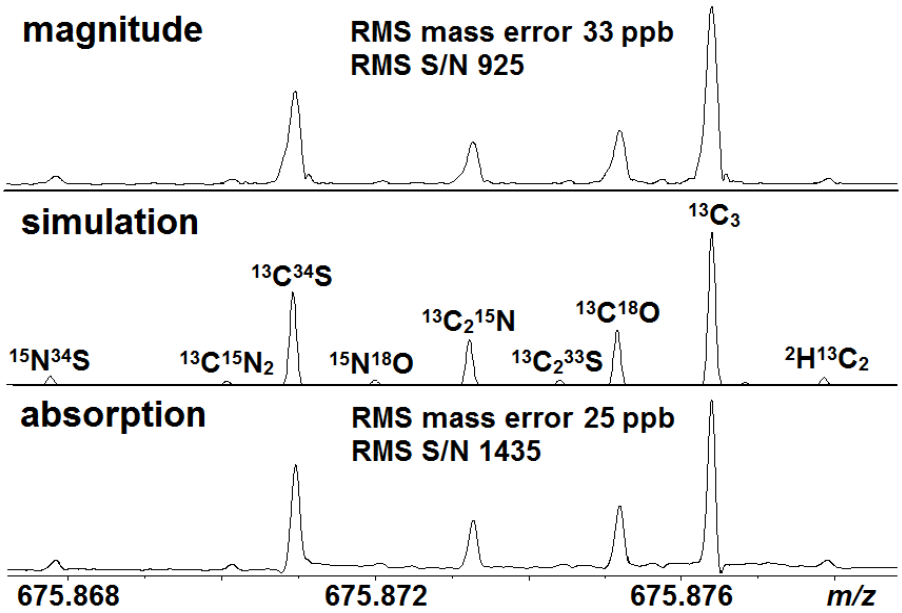

Figure 6.3 Same spectrum of Figure 6.2, with Hanning window function applied for apodization.

Table 6.1 Details of peak assignment for Figure 6.3 (peaks used for mass calibration are in bold).

Magnitude-mode							
Formula	**Measured m/z**	**Error (ppb)**	**Resolving power**	**S/N ratio**	**Theoretic intensity**	**Measured intensity**	**Intensity difference**
$^{15}N^{34}S$	675.867834	25	4.1M	118	5.9%	4.8%	-18.6%
$^{13}C^{15}N_2$	675.870143	58	4.1M	72	2.8%	3.0%	7.1%
$^{13}C^{34}S$	**675.870951**	**-19**	**4.0M**	**1363**	**60.7%**	**52.4%**	**-13.7%**
$^{13}C_2{}^{15}N$	**675.873268**	**25**	**4.0M**	**613**	**30.3%**	**23.7%**	**-21.8%**
$^{13}C^{18}O$	**675.875185**	**19**	**4.0M**	**781**	**36.2%**	**30.2%**	**-16.6%**
$^{13}C_3$	**675.876382**	**-25**	**4.1M**	**2607**	**100.0%**	**100.0%**	**0%**
$^{2}H^{13}C_2$	675.877895	61	4.7M	80	5.2%	3.4%	-34.6%
RMS		33		925			14%
Absorption-mode							
Formula	**Measured m/z**	**Error (ppb)**	**Resolving power**	**S/N ratio**	**Theoretic intensity**	**Measured intensity**	**Intensity difference**
$^{15}N^{34}S$	675.867834	12	5.7M	200	5.9%	5.0%	-15.3%
$^{13}C^{15}N_2$	675.870130	28	5.5M	138	2.8%	2.8%	0.0%
$^{13}C^{34}S$	**675.870958**	**-18**	**5.4M**	**2441**	**60.7%**	**61.2%**	**0.8%**
$^{13}C_2{}^{15}N$	**675.873269**	**22**	**5.3M**	**1131**	**30.3%**	**28.3%**	**-6.6%**
$^{13}C^{18}O$	**675.875186**	**19**	**5.2M**	**1474**	**36.2%**	**36.9%**	**1.9%**
$^{13}C_3$	**675.876382**	**-25**	**6.0M**	**3988**	**100%**	**100%**	**0%**
$^{2}H^{13}C_2$	675.877882	46	4.3M	191	5.2%	4.8%	-7.7%
RMS		25		1435			6%

6.3.4 Complex spectra

Application of the absorption-mode to a crude oil spectrum has been discussed in our previous paper; an improvement on mass accuracy from 23 to 64% was observed depending on compound classes,[89] and in that work, only the peaks assigned in both modes were counted. However, as is shown in Figure 6.4, the doublets and triplets unresolved in the magnitude-mode can often be assigned in the absorption-mode. In other words, the improvement in mass accuracy has meant that new assignments could be made which were not previously possible.

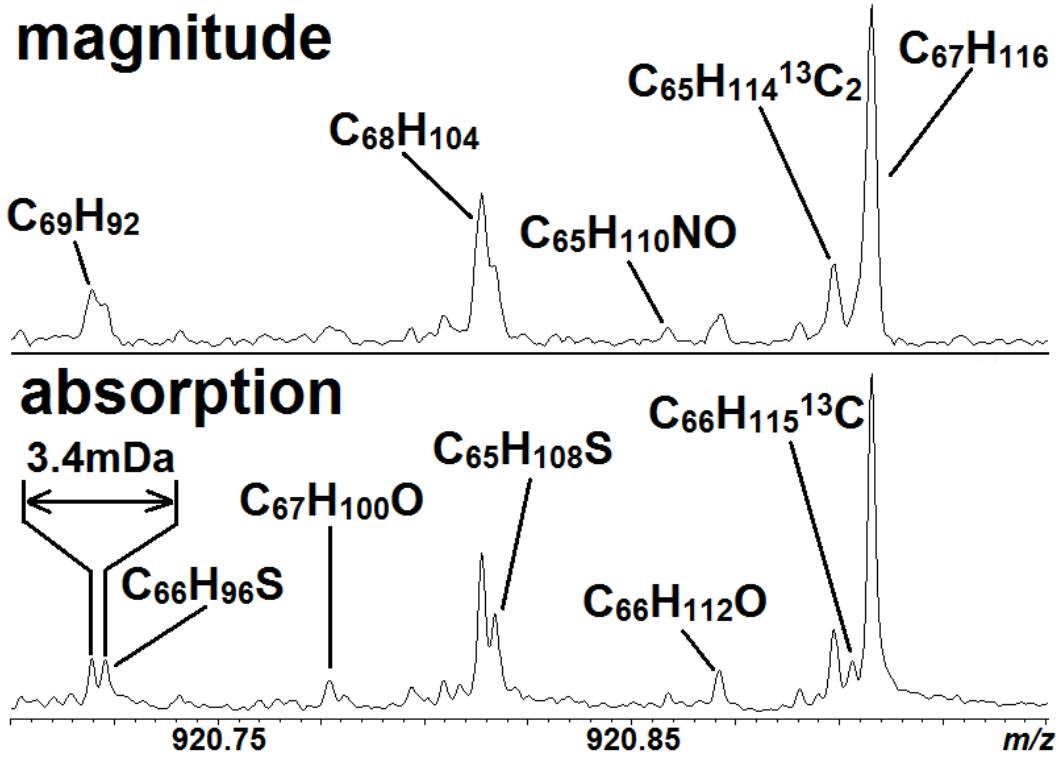

Figure 6.4 Close-up of a 0.25 *m/z* unit window from the crude oil spectrum in both magnitude- and absorption-mode.

In the previous chapter, it has been demonstrated that the artefacts in the FT-ICR spectra can be recognized immediately in the absorption-mode, and such an advantage was tested again using the crude oil spectra acquired from the new harmonically compensated ICR cell. For research purpose, the in-cell excitation voltage was set high deliberately to saturate the signal when acquiring the oil spectrum, thus generating unusually intense harmonics. The broadband oil spectrum acquired from the new cell is in Figure 6.5; the harmonic peaks appear similar to doubly- or triply- charged species in the conventional magnitude mode. Generally, identifying these harmonics requires comparison and correlation of the peaks to higher *m/z* (lower frequency) primary signal peaks. However, in the absorption-mode, they are easily recognized by their anomalous phase because such artefacts are not phased

correctly using the instrument's current phase function. To show this effect, a 2 *m/z* unit window is expanded in Figure 6.6. In the magnitude-mode all the peaks are positive; however, only 6 of them are real peaks which are easily observed in the absorption-mode. Such an advantage will certainly benefit the assignment of complex spectra by quickly identifying the artefact peaks.

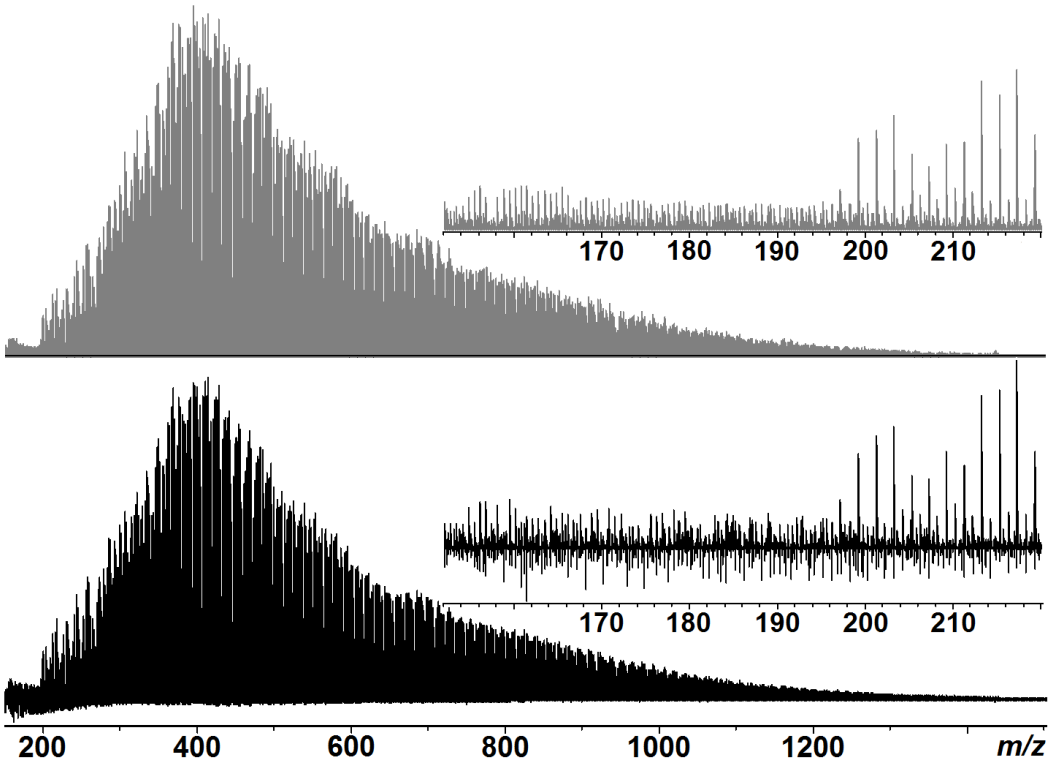

Figure 6.5 Oil spectrum in both magnitude- (grey) and absorption-mode (black), 6s transient with Hanning window function applied; inset, zoom in of *m/z* 150-220 showing the harmonic peaks in the spectrum.

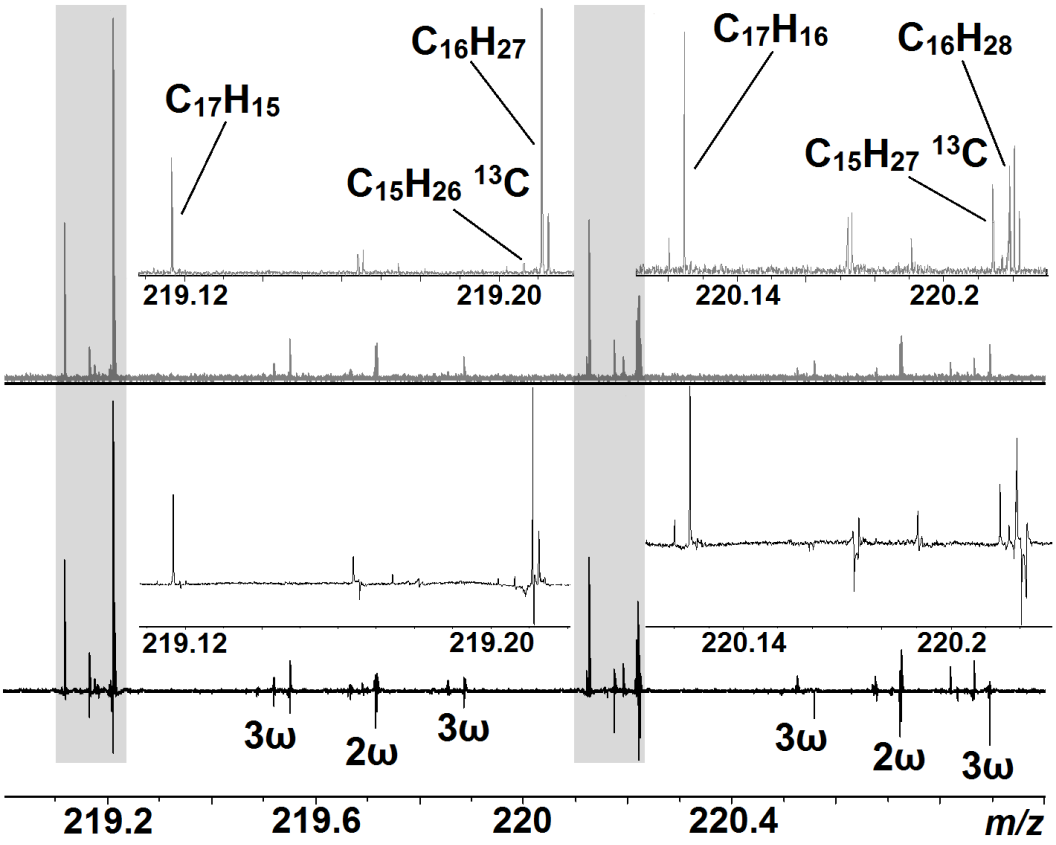

Figure 6.6 Close-up of Figure 6.5 (*m/z* 219-221) showing the harmonics, inset: zoom in on the shadow regions of two modes, only the labeled peaks are real peaks.

6.4 Conclusion

The new dynamically harmonized cell generates impressive performance in terms of transient signal length and resolving power, and when combined with the absorption-mode spectra, the data is improved even further. In particular, because the damping of the transient is greatly reduced so that the peak follows a classic 'sinc' function line shape, the absorption-mode improves resolving power by almost exactly 2-fold, while still reducing baseline noise by $2^{1/2}$, and improving the match with the theoretical intensities of the fine-structure of isotopic peaks by ~2x. Additionally, the absorption-mode spectra greatly

simplify the data interpretation, as the anomalous phase of noise peaks can be diagnosed immediately.

Chapter 7

Variation of the Fourier Transform Mass Spectra Phase Function with Experimental Parameters[6]

7.1 Introduction

The Fourier transform ion cyclotron resonance mass spectrometer (FT-ICR) is superior to all other mass analyzers in mass accuracy and resolving power.[44] Because it measures frequency, which is independent of the ions' velocity, the precise determination of mass-to-charge ratio (*m/z*) is not affected by the kinetic energy. Thus, a modern FT-ICR can routinely achieve mass accuracy less than 1 ppm and resolving power ($m/\Delta m_{FWHM}$) around 1,000,000 under normal conditions.[77, 171] Furthermore, the versatility and compatibility of FT-ICR to different fragmentation methods makes it an ideal instrument for tandem mass spectrometry analysis of large biological modules.[172] Although it is well known that the mass resolving power of FT-ICR varies linearly with the applied magnetic field strength,[45] it is less widely appreciated that the resolving power of FT-ICR can be enhanced by a factor up to 2 by phasing the magnitude-mode spectrum into the pure absorption-mode. And furthermore, the absorption-mode spectrum represents a significant step towards improving the data quality of FT-ICR spectrum at no extra cost.

Previous studies show that our phase correction method is a post-process procedure which only requires the ion transient to be multiplied by the correct

---

[6] This chapter has been partially/entirely reproduced from
Qi, Y.; Barrow, M. P.; Van Orden, S. L.; Thompson, C. J.; Li, H.; Perez-Hurtado, P.; O'Connor, P. B., Variation of the Fourier Transform Mass Spectra Phase Function with Experimental Parameters. *Anal. Chem.* **2011**, 83 (22), 8477-8483. Copyright 2011, American Chemical Society.

phase function point-by-point without prior knowledge of instrumental conditions. Such method is applicable to protein, petroleum, and other complex spectra with a straightforward approach. Therefore, once the phase function is known, it may be possible to automate broadband phase correction in routine work. This chapter aims to parameterize the phase function with variation of experimental conditions and apply the phase function from scan to scan and sample to sample in routine phase correction.

7.2 Theory

7.2.1 Variation of the Phase Function

Development of spectrometry always aims to pursue higher resolution.[88] Dating back to the very first FT-ICR mass spectra in 1974,[42-43] it was readily recognized that an absorption-mode spectral peak is inherently narrower than its corresponding magnitude-mode (which is phase independent),[87] and in FT-NMR spectroscopy, the phasing problem was solved in the 1970's.[91-92] Although the conceptual understanding is the same for both, the complexity is very different. In NMR, the phase varies over the spectrum by typically 0.1–0.3 π, far less than one cycle (2 π). While in FT-ICR, because the excitation bandwidth is three orders of magnitude broader (from kHz to MHz), the variance of phase value is much larger (e.g., ~10,000 π for the *m/z* range from 200 to 2000 in a 12 T instrument). It is important to note that any peak can be perfectly phased at some $\Phi(\omega_i)$ between 0 and 2 π, and this means that a small region around this peak, where phase variance is less than 2π (perhaps several Da), is also easily phased. Phase wrapping quickly complicates this (Figure 3.2), because $\Phi(\omega_i) = \Phi(\omega_i) + 2n_i\pi$ for any integer n_i at any ω_i, and the

phase variation for an entire spectrum is perhaps ~10,000 π. In order to solve the Φ(ω) for the entire *m/z* range, it is necessary to calculate all the individual values of n_i before fitting the phases into a quadratic function Φ(ω). Note: because every addition of a frequency/phase pair to the quadratic least squares fit also adds one value of n_i, the solution to the phase function equation is not unique being under-determined by exactly one degree of freedom. However, this lack of uniqueness is clearly characterized by the same phase wrapping problem in that the set of n_i integer values can always vary by +/- an integer, but their relative values remain constant.

7.2.2 Parameterization of the Phase Function

Because of linear frequency sweep excitation, the ions' corresponding phase angle, Φ(ω), is a quadratic function of the excitation frequency (Eq.7.1) and that such an equation could be used for phase correction,[95, 165] where A, B and C are the fitted constants.

$$\phi(\omega) = A\omega^2 + B\omega + C \qquad (7.1)$$

However, the previous published method is user-interactive;[68] requiring manual peak selection and phase assignment, and it was assumed that the phase function varies from experiment to experiment if the instrument parameters are changed which means the function needs to be recalculated every time. These drawbacks could potentially hinder the application of phase correction in routine work. However, because the bulk of the manual algorithm could be easily automated, and computation for the phase function only has to be done when the pulse sequence parameters are changed, it was likely that the function could be parameterized by adding a few correction factors. If so, then the phase

function could be applied directly to further scans without needing to be recalculated for each spectrum. Thus, a series of experiments were performed to test the variation of the phase function with particular experimental parameters such as trapping voltage, excitation amplitude, and space-charge.

In the ICR trap, the reduced ion cyclotron frequency (including the electric field and the effect of space-charge) can be written in Eq.7.2a (with ω_c and k defined in Eq.7.2b and c):[45, 60]

$$\omega_+ = \frac{\omega_c}{2}[1+(1-4k/\omega_c)^{1/2}] \qquad (7.2a)$$

$$\omega_c = \frac{qB_0}{m} \qquad (7.2b)$$

$$k = \frac{qV\alpha}{ma^2} + \frac{q^2\rho G_i}{\varepsilon_0 m} \qquad (7.2c)$$

$$\omega_+ = \frac{qB_0}{m} - \frac{\alpha V}{a^2 B_0} - \frac{V^2\alpha^2 m}{a^4 B_0{}^3 q}\cdots \qquad (7.2d)$$

in which B_0 is magnetic field; α is a scaling factor which depends on the trap geometry and ranges typically from 2 to 4; a is the characteristic dimension of the ICR trap usually defined as the distance between trapping plates; and V is the trapping potential applied to the ICR trapping plates. The last term in Eq.7.2c expresses the local space-charge component of the frequency shifts, where ρ represents the ion density, G_i the generalized ion cloud geometry correction factor, and ε_0 the permittivity of free space. As space-charge shifts are largely independent of m/z,[124, 133] the effect of electric field and space-charge are explored separately in the following section.

7.2.3 Variation of the Phase Function with Trapping Voltage

Variation of the trapping voltage changes the electric field contribution to the ions' frequencies (Eq.7.2a, and Eq.7.3c) and hence also alters the applied phase function. Thus, *k* in Eq.7.3a is substituted by the first term in Eq.7.2c, and Eq.7.2a can be expanded in a Taylor series to yield Eq.7.2d. In Eq.7.2d the third term can be ignored in routine calibration,[118-119] because it is less than $1/10^6$ of the second term in magnitude (the error caused by ignoring the 3rd term is sub-ppb). Additionally, because the phase variance over an entire spectrum is ~10^4 π, and because the phase function is quadratic, the order of magnitude error caused by neglecting the 3rd term of Eq.7.2d is squared (namely 10^{-12}), so that neglecting of this term in calculation of the phase function is perfectly valid. Therefore, the "ω" in the initial phase function (Eq.7.1) is substituted by the first two items of Eq.7.2d, which gives Eq.7.3.

$$\phi(\omega) = A\omega^2 + B\omega + C - \frac{2\alpha A}{a^2 B_0}\omega V + \frac{\alpha^2 A}{a^4 B_0{}^2}V^2 - \frac{\alpha B}{a^2 B_0}V \qquad (7.3)$$

The resulting equation is an optimized phase function with the correction factor for trapping potential, *V* (average of front and back plate, usually the same). The other parameters *α*, *a*, and B_0 are the constants of the instrument which can be easily acquired (see below).

7.2.4 Variation of the Phase Function with Total Ion Number

Frequency (and phase) of ions also vary with total ion number. Easterling and co-workers used the theoretical framework of the Eq.7.2 to demonstrate that the ion's frequency shift is linear proportional to the number of ions in the ICR cell, which is mostly independent of *m/z*.[124] In the hexapole (of FT-ICR),

the number of ions increases linearly with the accumulation time. As the trapped ions are analyzed, the space-charge is regarded as a constant shift from the ideal cyclotron frequency for ions of all masses in the cell on average, a “mean-field” approximation. Thus, we can rewrite the phase function as follow:

$$\omega_{new} = \frac{qB_0}{m} - \frac{\alpha V}{a^2 B_0} - \frac{q^2 \rho G_i}{\varepsilon_0 B_0} \equiv \omega - st, s = \frac{q^2 \rho G_i}{\varepsilon_0 B_0 t} \qquad (7.4a)$$

So, substituting Eq.7.4a into Eq.7.1

$$\phi(\omega) = A\omega^2 + (B - 2Ast)\omega + C + As^2 t^2 - Bst \qquad (7.4b)$$

Here, *s* is defined as a space-charge factor with the unit of ion density per time; *t* is the accumulation time in the hexapole; Eq.7.4b is the estimation of phase value with the “global” space-charge effect built in. Note: Eq.7.4 assumes that the beam current is constant, but Easterling *et al.* showed that space-charge frequency shifts are linear with total ion number,[124] so the same excitation can be used for varying beam current based on total ion number by redefining ‘t’ as the total ion number and ‘s’ as a parameterization constant. Both methods introduce some error into the phase function because the total space-charge effect is usually varies which will be discussed below.

In the following experiment, the phase function for the mass range of 200-2000 was calculated first from a crude oil sample and applied to small molecules and large proteins separately. The instrument parameters were changed from normal to extreme conditions (Figure 7.1) in order to detect the variation of phase corrected absorption-mode spectra.

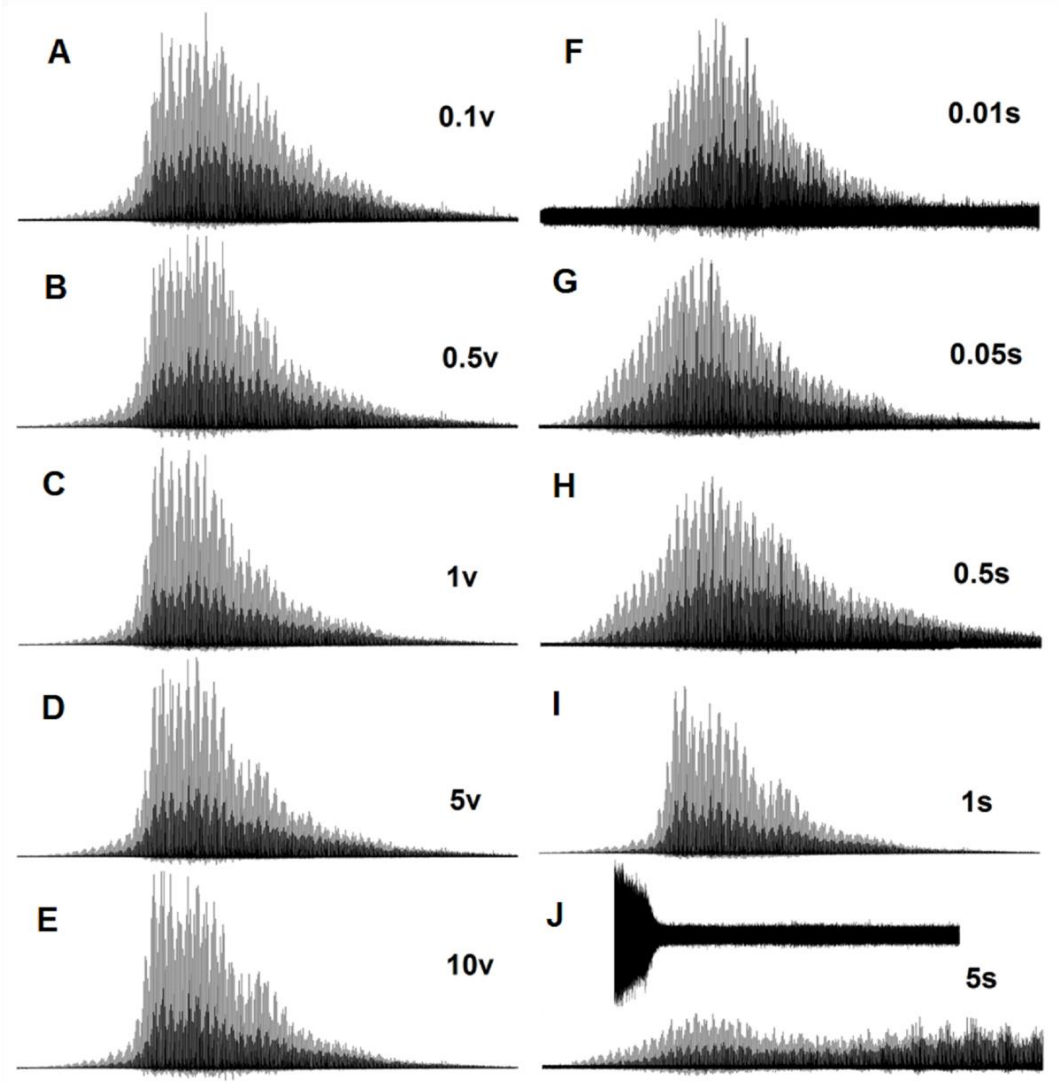

Figure 7.1 Left: phase corrected absorption-mode spectra with the trapping potential from 0.1-10 volt; Right: ion accumulation time form 0.01-5 s (with the transient in Fig. J).

7.3 Experimental Methods

7.3.1 Sample Description and Preparation

A crude oil sample (SRM 2721, light-sour) was purchased from NIST, diluted 2000 times in a 50:50:1 toluene/methanol/formic acid mixture. Ubiquitin, purchased from Sigma-Aldrich (Dorset, England) was diluted into 0.1 µM in a

50:50:1 water/acetonitrile/formic acid mixture. Collagen type I and sequencing-grade trypsin were purchased from Sigma-Aldrich; collagen was digested and then run at approximately 2.5 μM concentration in 50:50:1 methanol/water/formic acid. ESI-L low concentration tuning mix (external calibration) is purchased from Agilent Technologies (Palo Alto, California, USA) without dilution. All solvents were HPLC-grade, obtained from Sigma-Aldrich Chemical Co. (Dorset, England).

7.3.2 Instrumentation

All spectra were recorded using a SolariX 12T FT-ICR mass spectrometer (Bruker Daltonics, Bremen, Germany) by positive-mode Electrospray Ionization (ESI). Broadband frequency sweep excitation (92-922 kHz (*m/z* 2000-200) at 125 Hz/μs sweep rate) was followed by a pre-scan delay of 3.5 milliseconds, and image current detection to yield 4 mega-point time-domain data sets. The ion accumulation time in the hexapole was varied from 0.01 to 10 s, trapping voltage in the ICR cell from 0.1 to 10 volt, and excitation power from 10 to 100 volts. The data sets were co-added (10 acquisitions each to increase S/N), zero-filled, and fast Fourier transformed without apodization. All data sets were then processed using MatLab R2010a (MathWorks, Natick, MA, USA).

7.3.3 Mass Calibration

The observed frequency is converted into *m/z* by means of a three term quadratic equation.[119, 145] The instrument was externally calibrated first using ESI tuning mix before each experiment. The crude oil spectrum was internally calibrated by assignment of a known $C_nH_{2n-16}S$ series throughout the *m/z* range

from 200 to 800. Both ubiquitin and collagen spectra were calibrated internally using the molecular ions of different charge states.[133]

7.4 Result and Discussion

7.4.1 Optimize Phase Function

The original phase function for a *m/z* range from 200 to 2000 was calculated based on the oil spectrum (Figure 7.1A) using the quadratic least squares fit and iteration.[165] The instrument parameters from Figure 7.1B were then applied to acquire an ubiquitin molecular ion spectrum, and the absorption-mode spectrum of ubiquitin was then corrected using the same phase function from Figure 7.1B. As shown in Figure 7.2, the phase value of spectrum shifts constantly probably due to the slight difference in space-charge conditions; however, the variation of phase value for every point was definitely within one cycle (2 π) (Figure 7.2B). Therefore, the phase wrapping effect doesn't exist in the spectrum, which means that, using the same instrument parameters as before, the previous phase function can provide a very close approximation for the phase value of the new spectrum, and thus, the phase function can be reused easily from experiment to experiment. Correction of the phase function is achieved by choosing three (or more) peaks in the spectrum, calculating their phase values, and adding the resulting values to the predicted phase from the provisional phase function. A new, corrected phase function is then calculated by quadratic least squares fitting.

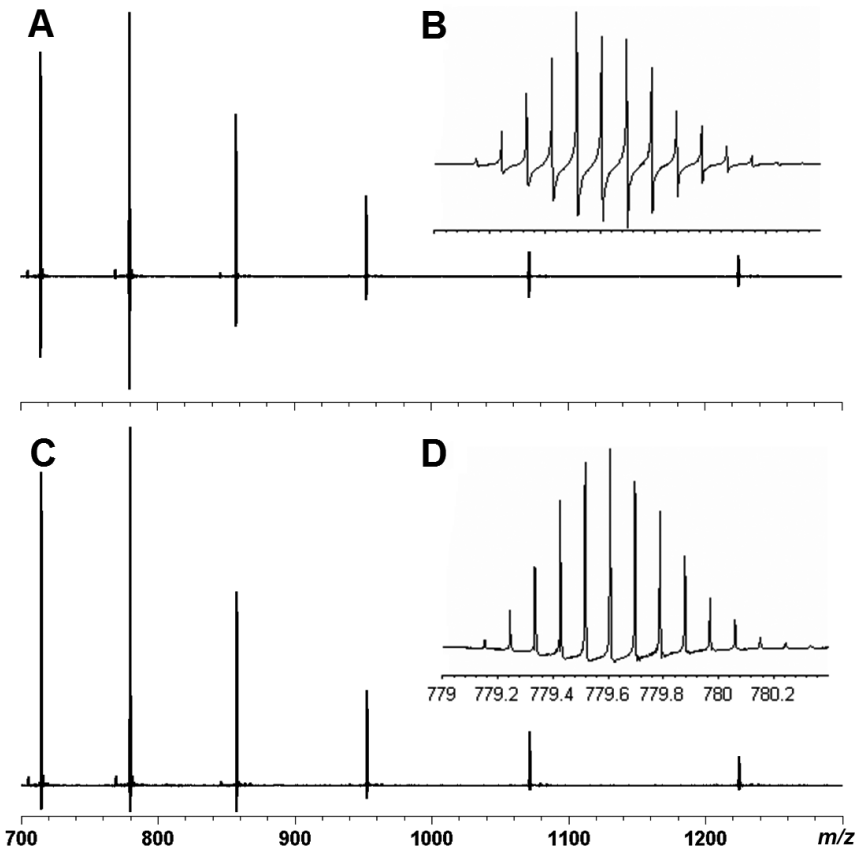

Figure 7.2 A: Ubiquitin charge state spectra in absorption-mode initially phase corrected using the phase function from the oil spectrum (Figure 7.1B) using the same instrument parameters; B: zoom in of the 11^+ charge isotope peaks (*m/z* ~779) in A; C: Rephased absorption-mode spectrum generated by correcting the phase value of 3 (or more) peaks in the spectrum and recalculating the quadratic phase function; D: zoom in of the 11^+ charge isotope peaks in C.

This result clearly shows that computation of the phase function must be done only when the pulse sequence is changed -- so that in the vast majority of cases, it only has to be calculated once whenever instrumental drift requires recalibration of the instrument. Since the original phase function is now defined, subsequent experiments endeavored to determine the phase function variance

as a function of the following parameters: trapping potential, accumulation times, and excitation power from normal to extreme conditions. Then the variance of the phase function was applied to correct the phase of spectra using the predicted functions mentioned above. The majority of the spectra used for demonstration were acquired from crude oil, because such samples have high intensity peaks throughout the entire mass range which would clearly capture any error resulting from incorrect phase correction.

7.4.2 Trapping Potential

Eq.7.3 is applied to predict the phase shift caused by variance of the trapping potential; the resulting spectra are shown separately (Figure 7.1, left). A rough estimation of Eq.7.2 tells that a change of 0.1 V in the trapping potential will cause a cyclotron frequency shift of several Hz, which is about 10 π for the frequencies used (Eq.7.3); as a consequence, the phase function varies significantly with a small change in trapping voltage. Figure 7.1 shows that a properly parameterized Eq.7.3 can effectively convert the phase function for different trapping potentials (from 0.1 to 10 volts). 10 volt is the maximum setting for the instrument used which is sufficient to show the relationship, particularly because detection is normally performed with a trapping potential below 1 volt.

7.4.3 Number of Ions

An important feature in Eq.7.4a is that the space-charge effect on the frequency is linear with the ion population, and moreover, the accumulation time is independent of *m/z*.[124] The value of "*s*" in Eq.7.4a is calculated by

choosing any peak in the spectrum and recording its observed frequency change with accumulation time; the value is acquired by linear regression with a related coefficient (R^2) greater than 0.99. Given the R^2>0.99, the error of the predicted phase value from Eq.7.4 is within 0.01 π, which is a sufficiently good approximation to eliminate the phase wrapping effect. With such an approximation, the exact phase value for each point can be easily calculated, thus, the entire *m/z* range is then re-phased as before. Figure 7.1 shows the application of Eq.7.4b with different ion accumulation times. As is shown, the phase function remains fairly stable throughout the entire time scale from 10 ms to 5 s of accumulation time. Surprisingly, the phase function is still stable even in the extreme space-charge condition which already shows the spontaneous loss of coherence catastrophe or “nipple effect” in the transient (Figure 7.1J).[126] However, in such an extreme case, the peak position shift and artifacts caused from the space-charge effect are much more severe than the phase correction itself.

7.4.4 Excitation Radius

Ideally, an ion’s frequency is a function of the excitation radius, but this is only true in a perfect, hyperbolic cell.[126, 192] The new shaped cell designs from Rempel,[152] Tolmachev[189] and Nikolaev[46] greatly improve the adherence to ideal. However, the data herein was generated from the Infinity cell,[59] in which the electric field is not shimmed in any way. An ion packet’s orbital radius is determined by the applied excitation potential; however, change of the cyclotron radius has effects on both the electric field and space-charge conditions which make prediction of exact cyclotron frequency difficult.

According to the experimental data, the shift of ion cyclotron frequency was recorded which roughly follows a quadratic relation with the ion excitation potential (Figure 7.3); however, these plots show that, in the Infinity cell, the resulting quadratic function varies substantially for different ions, and thus is not sufficiently accurate to reach a reliable prediction for ions' frequency to be used for a proper evaluation of the phase function. For that reason, the ion excitation potential was held as a constant throughout the experiment. Furthermore, since the newer, improved cell designs will largely eliminate this effect, a full evaluation of this multidimensional frequency shift function is not warranted at this time.

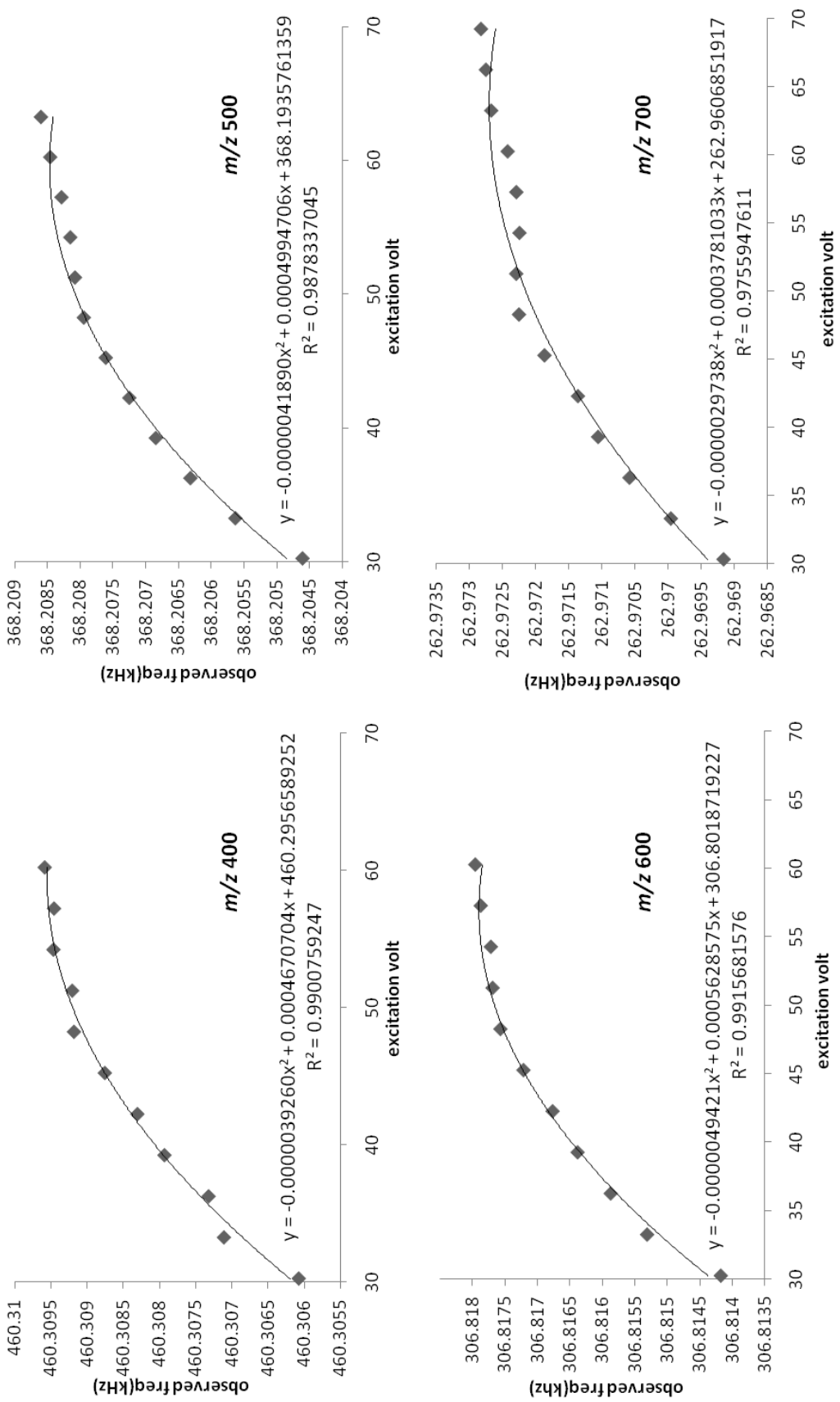

Figure 7.3 Plot of excitation potential versus observed frequency for the peak with *m/z* of ~400, 500, 600 and 700.

7.4.5 Effect of Zero filling on Absorption-Mode Spectra

During the FT data processing, the time-domain transient is recorded discretely and numerically transformed to generate a discrete *m/z* spectrum, thus mass error occurs when the apex of a continuous peak falls between two adjacent sampled points in the discrete spectrum. One solution is to use zero filling which is a computational trick used to increase the sampling points of a spectrum and also to recover the phase information if the spectrum is not plotted in the magnitude-mode (details in Chapter 2). Generally speaking, it can be viewed as adding N zeros at the end of N observed points in the time-domain (T) , thus, the Fourier transform is calculated at intervals of 1/(2T) rather than 1/T and visual resolution of the spectrum is doubled.[71]

As is demonstrated in Chapter 2, peak shape improve dramatically with the first zero filling and slightly with more zero fillings even when the worst situation is applied -- the ion transient barely decayed during the acquisition (sinc function peak shape, $T/\tau \approx 0$). For this reason, most FT-ICR data analysis zero fills the original N-points data once by default before the Fourier transform. Meanwhile, it's been proved by the NMR community that the causality principle requires one more zero fill for the absorption-mode spectrum to recover the phase information lost in the dispersion-mode. Such an argument is also true for FT-ICR, Figure 7.4 (inset) shows, for one zero filling, that the phase corrected absorption-mode spectrum exhibits less information than its corresponding magnitude-mode (the peak splitting is not well resolved), and a smaller and better resolved absorption-mode spectrum appears only with an extra zero filling. It is because FT generates complex numbers, which contain two independent types of information in the frequency spectrum: magnitude

and phase. By plotting the absorption-mode only (real part of the complex number), the phase information cannot be calculated. Therefore, when plotting the absorption-mode spectrum, an extra zero filling is required before FT to recover the lost information on phase.

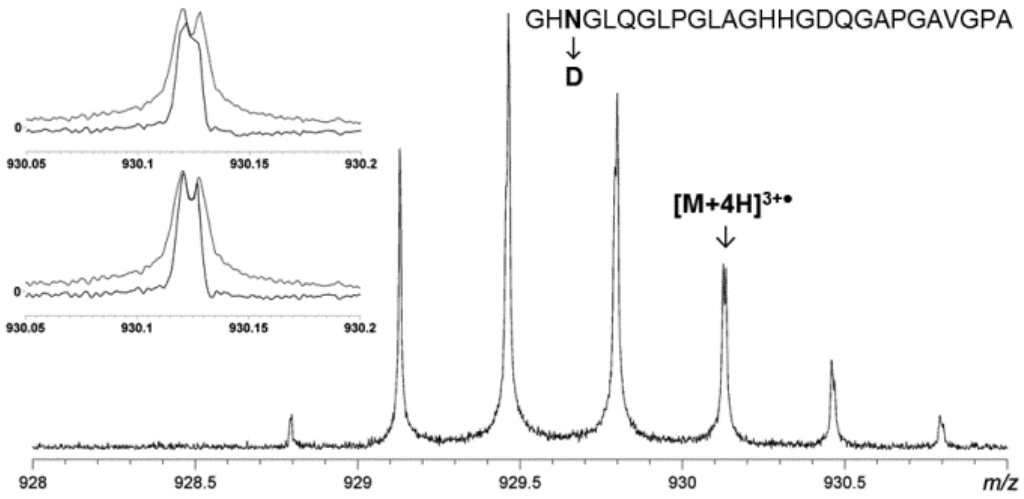

Figure 7.4 Isotopic distribution of a fragment from collagen; inset: 1N(top) and 2N(bottom) zerofills of the labeled peak in both magnitude- (grey) and absorption-mode (black) display, the left peak is the deamidated peptide, the right one with is the undeamidated precursor (A+4 isotope).

7.4.6 Magnetic Field and Geometry Factor

In most commercial FT-ICR instruments, the mass calibration from frequency to *m/z* consists of fitting either the Ledford (Eq.7.5)[119] or Francl equation,[118] and information on magnetic field and geometry factor are accommodated within the calibration parameters below, where *e* is the elementary charge.

$$m/z = \frac{A_{Ledford}}{\omega} + \frac{B_{Ledford}}{\omega^2} \qquad (7.5a)$$

$$A_{Ledford} = eT \qquad (7.5b)$$

$$B_{Ledford} = \frac{eV\alpha}{a^2} \qquad (7.5c)$$

The exact magnetic field of the instrument can be extracted from Eq.7.5b. And the geometry factor, *α*, is a constant depending on the shape of ICR cell (Infinity cell[59] in this project). Values of *α* for different ICR trap designs commonly used were listed in a recent review.[45] The value of "*α*" is determined by rearranging Eq.7.2d to yield Eq.7.6, and then plotting frequency versus trapping voltage.

$$\omega = -\frac{\alpha}{a^2 T}V + \frac{qB_0}{m} \qquad (7.6)$$

The slope ($-\alpha/a^2T$) and intercept (qB_0/m) were calculated using linear regression by varying the trapping potential, *V*, and monitoring the corresponding observed frequency, *ω*. The measurement was carried out by monitoring two peaks in the Agilent ESI tuning mix, with one in high mass range (reference *m/z*: 1821.9523), the other in low mass range (reference *m/z*: 622.0290). Table 7.1 lists the result and the value of α=2.841 was applied in the phase equations above.

m/z	1821.9523	622.0290
slope	-65.7687	-65.7641
intercept	635460.8161	861295.5848
R^2	0.99926970	0.99973292
α	2.8411	2.8409

Table 7.1 Calculated geometry factor for the Bruker Infinity cell

7.5 Conclusion

This chapter discussed the parameterization of broadband phase correction for FT-ICR mass spectra with trapping voltage, ion accumulation time, and excitation amplitude including experimental data and a theoretical treatment. These experiments show that the phase function can be applied directly from scan to scan and from sample to sample (with slight modification) in cases where 1) the pulse sequence doesn't change or 2) the pulse sequence change is limited to modest variation to trapping voltage or ion accumulation. The present method was successfully applied to complex crude oil spectra. It is clear that, within minor change on the instrument parameters, the phase function can be applied directly to almost all spectra with little effort. This broadband phase correction has the potential to be automated in routine work as is already done in NMR. The current results were performed offline as post-processing of existing transients, but once the phase function is known, and the parameterizations discussed above are applied, phase correction itself only requires a single point-by-point vector complex number multiplication on the transient -- which takes less than a millisecond on modern processors. Thus, the method is, in principle, fast enough to be applied online on a chromatographic timescale.

Chapter 8

Conclusions and Future Work

8.1 Conclusions

FT-ICR is the ideal instrument for forefront research, as it offers the best experimental performance,[46] flexibility for hybrid instrumentation,[47-48, 193] and compatibility with a diverse range of fragmentation methods. Being the most advanced mass analyzer, FT-ICR intricately couples the advanced physics techniques, instrumentation, and electronics with chemical and particularly biochemical researches. However, its software development lags relative to instrumentation due to the lack of sufficient attention and investment by instrument companies, and for this reason, there is much room for improvement.

Most data processing algorithms we are familiar with in FT-ICR are neither well studied nor taken seriously by practitioners; thus, professional skill is really the key to achieve high performance in FT-ICR. The first part of thesis work is theoretical, focusing on data processing, and explains the procedures step-by-step for users with the goal of maximizing spectral features, such as mass accuracy, resolving power, dynamic range, and detection limits.

The main body of the work includes the development and application of a novel data processing method--phase correction, which can significantly improve the performance of FT-ICR spectra without any recourse to costly instrumental upgrades. Instead of the normal magnitude-mode spectrum, it has been recognized for 40 years that presenting the FT-ICR spectrum in the absorption-mode offers up to a two-fold improvement in mass resolving

power.[87] Our research shows that a broadband FT-ICR mass spectrum can be phased using quadratic least-squares fit and iteration. Compared to general methods from other groups,[94-95] we proposed a post-processing method which only requires the ion transient of the spectrum, but no information from the experimental pulse program during the collection of the data is needed. Based on mathematical treatment and experimental data, it was proved that plotting the spectrum plotted in the pure absorption-mode improves not only resolving power ($\sqrt{3}$-2), but also S/N ($\sqrt{2}$), mass accuracy, and correlation of the peak intensities to the theoretical values. Finally, the developed phase correction method was applied to different spectral acquisition modes: broadband and narrowband, different design of ICR cells: Infinity cell[59] and ParaCell,[46] and various types of samples: petroleum, peptide, and protein acquired from different instruments. In these examples, the absorption-mode spectra reveal much more information which was not apparent in the same spectra plotted in the conventional magnitude-mode. And additionally, the spectral artefacts can be recognized immediately after phasing.

8.2 Future Work

Presenting the FT-ICR spectra in the absorption-mode represents a significant step towards improving the data quality. As such an improvement is made with no extra cost in instrumentation, it is worthwhile to apply and promote absorption-mode in routine experiments as is already done in NMR.

Currently, the presented method is user interactive, involves manual peak picking, phase assignment, and iteration, so it is hardly fast, and furthermore, there are potential drawbacks which prevent its broad application. First, as is

mentioned, the algorithm presented is manually intensive (taking over one hour to phase a single mass spectrum) for an expert user. Second, this method requires that the spectrum used to calculate a phase correction function has a sufficient peak density across the entire *m/z* range of interest (e.g., a petroleum spectrum), which means it may be limited in certain type of samples.

Generally speaking, in the future, an auto-model approach is required to speed the process of phase correction. Among the entire algorithm, peak picking and centroiding can be readily standardized and automated, as can phase determination of individual peaks, so the bulk of the algorithm can be automated. And phase correction itself only requires a single point-by-point complex number multiplication on the transient--which takes less than a millisecond on modern processors. The processing bottleneck of phasing lies in how to automate the iteration and tuning steps with minimal user input for solving the phase function. Additionally, the effect caused by space charge should also be looked into. As the number of total ions being trapped in the ICR cell varies from scan to scan, the resulting phase function also changes, even if the instrument pulse program remains the same. Sometimes it is necessary to re-solve the phase function for spectra acquired under the same experimental conditions; this can possibly cause a bottleneck for phasing the high output LC-MS or imaging-MS spectra.

Currently, the Autophaser algorithm, coded in LabVIEW software, is being built in our group. This program offers the advantages of the presented method, and incorporates a novel artificial intelligence based tuning method to solve the phase function with little user input. At this stage, phase correction is still a

post-processing method on the acquired transients, but the ultimate goal of this project is to build a phase correction program fast enough to be used on a chromatographic timescale.

Appendix A (Supporting information for Chapter 3)

I. MatLab code for phasing with full comments (start with %)

Step 1: Read the data

```
file = fopen('fid','r');
% open the file ‘fid’ for read operation.
fid=fread(file,'int32');
% read all data from fid as 32-bit integers
fclose(file);
% close the file, or you can’t read any more data from it.

spec = fft(fid,length(fid)*2);
% Fourier transform with one zero fill
spec=spec(1:length(spec)/2);
```

% discard the data in the negative half of the data, because FFT generates even symmetry data around the zero frequency point. This symmetry adds redundant information.

Step 2: Get the frequency, ω and calibrate *m/z* domain

% calibration the *m/z* domain data follows the calibration equation as approximate. Bruker uses a proprietary calibration function to generate the frequency and *m/z* domain corresponding to the intensities of the signal.

Step 3: Calculate an optimal phase, $\Phi(\omega_i)= \Phi(\omega_i)+2n_i\pi$ for a set of arbitrary chosen peaks

% find the apex of the chosen peaks, then calculate the phase value by Eq.3.1b, thus the phase is arctangent(Im(ω)/Re(ω)).

a=abs(spec(N));

r=real(spec(N));

j=imag(spec(N));

% N is the assigned peak apex in 'spec' file, a: absolute value of that point, r: real value and j: imaginary value.

% calculate the phase of this point

pN=atan(j/r);

% then iteratively calculate the phase values for the apex of adjacent peak, and Φ(ω) varies within one cycle for consecutive peaks.

Step 4: least square approximation of the quadratic in a small frequency domain

x=[w1 w2 w3...];

y=[p1 p2 p3...];

%y is phase values, pN, acquired in step 3, x is their corresponding angular frequency (frequency*2π) which is obtained by calibration from step 2.

para=polyfit(x,y,2);

%quadratic least square fit of (x, y) pairs for a quadratical function

ybest=polyval(para,x);

%ybest is the best fit for the function we get from the regression

plot(x,ybest,x,y,'o'), title('quadratic regression estimate'), grid

%plot the regression curve with the raw (x, y) pairs in spot.

A=para(1),B=para(2),C=para(3)

%output the parameters A, B and C for the phase function

%calculate the initial Φ(ω) function

RightPhase=A.*w.*w+B.*w+C;

% calculate the phase value for the corresponding frequency-domain

PhasedSpec=spec.*exp(-i.* RightPhase);

% correct the phase by rotating the raw data mathematically

plot(mz,abs(spec),mz,real(PhasedSpec))

% plot the magnitude-mode versus phased absorption-mode

Step 5: Extend the range of the phase function

% add additional apex outside the frequency domain in step 4 to the fit, the cycle between two phase values can be estimated as shown in **Figure 5**, go to step 4, and more frequency/phase pairs can be added continuously to increase accuracy, thus, phase the whole spectrum

Step 6: Baseline correction

baseline=msbackadj(index,real(PhasedSpec),'STEPSIZE',201,'WINDOWSIZE',50,'QUANTILEVALUE',0.01,'SHOWPLOT',1);

%the parameters 'STEPSIZE', 'WINDOWSIZE' and 'QUANTILEVALUE' are depending on the size of the data (see MatLab help file)

figure

plot(m,abs(spec),m,real(PhasedSpec),m,baseline)

%plot the baseline in the phase-corrected spectrum

Appendix B (Supporting information for Chapter 4)

Table B1. Peak assignment for both of the magnitude- and absorption-mode in Figure 4.5 and 4.6B, (H) indicates the $[M+H]^+$ ion as APPI generate both radical and protonated species.

No.	Formula	Magnitude *m/z*	Magnitude Error(ppm)	Resolving Power	Absorption *m/z*	Absorption Error(ppm)	Resolving power
1	$C_{52}H_{62}S_2$	750.42891	0.23	142036	750.42881	0.09	462321
2	$C_{49}H_{66}S_3$	N/A	N/A	N/A	750.43208	-0.05	430767
3	$C_{53}H_{66}OS$	750.48332	0.57	202042	750.48294	0.07	556289
4	$C_{52}H_{67}NS^{13}C$	750.50210	-0.17	206445	750.50267	0.59	488052
5	$C_{52}H_{67}S^{13}C_2(H)$	N/A	N/A	N/A	750.51028	-0.07	432098
6	$C_{54}H_{70}S$	750.51951	0.32	190526	750.51922	-0.07	447824
7	$C_{51}H_{74}S_2$	750.52251	-0.19	240450	750.52262	-0.04	438667
8	$C_{53}H_{72}O^{13}C_2$	750.56433	-0.20	103995	750.56458	0.13	394349
9	$C_{55}H_{74}O$	750.57369	0.36	119698	750.57339	-0.04	559554
10	$C_{52}H_{78}OS$	750.57608	0.39	109475	750.57574	-0.07	564271
11	$C_{54}H_{75}N^{13}C$	750.59281	0.07	262368	750.59282	0.08	594237
12	$C_{54}H_{76}{}^{13}C_2$	750.60078	-0.11	129258	750.60066	-0.27	400435
13	$C_{51}H_{80}S^{13}C_2$	750.60442	0.25	82907	750.60431	0.11	203587
14	$C_{56}H_{78}$	750.60989	0.12	270059	750.60978	-0.03	465720
15	$C_{53}H_{82}S$	750.61319	0.03	231954	750.61316	-0.01	453797
16	$C_{50}H_{86}S_2$	N/A	N/A	N/A	750.61647	-0.11	421143
17	$C_{53}H_{83}NO(H)$	750.65490	0.21	134739	750.65497	0.31	306785
18	$C_{52}H_{84}O^{13}C_2$	750.65801	-0.49	131634	750.65825	-0.17	289712
19	$C_{54}H_{86}O$	750.66738	0.08	262631	750.66729	-0.04	491425
20	$C_{53}H_{87}N^{13}C$	750.68672	0.08	255757	750.68671	0.07	542113
21	$C_{54}H_{87}N(H)$	750.69125	0.16	230714	750.69108	-0.07	603410
22	$C_{53}H_{88}{}^{13}C_2$	750.69484	0.11	162951	750.69468	-0.11	574782
23	$C_{54}H_{88}{}^{13}C(H)$	750.70024	1.35	192330	750.69895	-0.37	454660
24	$C_{55}H_{90}$	750.70385	0.20	206323	750.70364	-0.08	431678
25	$C_{52}H_{94}S$	N/A	N/A	N/A	750.70707	-0.01	418642

26	$C_{51}H_{96}O^{13}C_2$	750.75272	0.59	193032	750.75232	0.05	390112
27	$C_{52}H_{100}{}^{13}C_2$	750.78883	0.23	277594	750.78870	0.05	609322
28	$C_{53}H_{100}{}^{13}C(H)$	750.79325	0.16	249577	750.79313	0.00	532512
29	$C_{54}H_{102}$	750.79761	0.01	262868	750.79762	0.03	464459
30	$C_{51}H_{62}S_2{}^{13}C$	751.43211	0.01	211985	751.43220	0.13	388629
31	$C_{48}H_{66}S_3{}^{13}C$	N/A	N/A	N/A	751.43583	0.48	327196
32	$C_{52}H_{66}OS^{13}C$	N/A	N/A	N/A	751.48632	0.11	319875
33	$C_{53}H_{69}NS$	751.51440	-0.16	120344	751.51454	0.03	519623
34	$C_{53}H_{70}S^{13}C$	751.52292	0.39	123192	751.52263	0.00	494256
35	$C_{50}H_{74}S_2{}^{13}C$	N/A	N/A	N/A	751.52631	0.41	406248
36	$C_{54}H_{74}O^{13}C$	751.57726	0.65	105454	751.57657	-0.27	587620
37	$C_{51}H_{78}OS^{13}C$	N/A	N/A	N/A	751.58055	0.55	558309
38	$C_{53}H_{75}N^{13}C_2$	751.59635	0.32	323636	751.59631	0.27	438902
39	$C_{55}H_{77}N$	751.60509	0.05	246977	751.60499	-0.08	481803
40	$C_{55}H_{78}{}^{13}C$	751.61332	0.21	213808	751.61312	-0.05	514144
41	$C_{52}H_{82}S^{13}C$	751.61642	-0.15	213792	751.61666	0.17	412127
42	$C_{53}H_{82}S(H)$	751.62124	0.32	161567	751.62085	-0.20	371439
43	$C_{50}H_{86}S_2(H)$	N/A	N/A	N/A	751.62442	0.07	497812
44	$C_{53}H_{86}O^{13}C$	751.67074	0.09	266055	751.67061	-0.08	592419
45	$C_{54}H_{86}O(H)$	751.67512	-0.03	261794	751.67511	-0.04	767125
46	$C_{52}H_{87}N^{13}C_2$	751.69017	0.21	314777	751.69024	0.31	589260
47	$C_{53}H_{87}N^{13}C(H)$	751.69467	0.25	234627	751.69454	0.08	704647
48	$C_{54}H_{89}N$	751.69898	0.04	250615	751.69890	-0.07	486086
49	$C_{54}H_{90}{}^{13}C$	751.70721	0.20	219576	751.70703	-0.04	451729
50	$C_{55}H_{90}(H)$	N/A	N/A	N/A	751.71107	-0.61	300253
51	$C_{52}H_{94}S(H)$	751.71478	-0.16	161252	751.71491	0.01	441932
52	$C_{52}H_{99}{}^{13}C_2(H)$	751.79686	0.49	269921	751.79635	-0.19	722087
53	$C_{53}H_{102}{}^{13}C$	751.80094	-0.03	265603	751.80099	0.04	483275
54	$C_{54}H_{102}(H)$	751.80545	0.03	228116	751.80541	-0.03	479263
55	$C_{51}H_{68}$	680.53179	0.35	436358	680.53149	-0.10	504563
56	$C_{48}H_{72}S$	680.53496	0.04	283203	680.53490	-0.04	495066
57	$C_{45}H_{76}S_2$	680.53805	-0.36	271613	680.53824	-0.08	511475

58	$C_{53}H_{64}$	700.50054	0.41	256903	700.50020	-0.07	490922
59	$C_{50}H_{68}S$	700.50368	0.08	259273	700.50360	-0.03	482757
60	$C_{47}H_{72}S_2$	700.50689	-0.15	283878	700.50699	-0.01	470205
61	$C_{54}H_{72}$	720.56309	0.33	244947	720.56272	-0.18	467348
62	$C_{51}H_{76}S$	720.56624	0.02	245114	720.56616	-0.09	461176
63	$C_{48}H_{80}S_2$	N/A	N/A	N/A	720.56953	-0.09	498988
64	$C_{56}H_{68}$	N/A	N/A	N/A	740.53146	-0.13	507748
65	$C_{53}H_{72}S$	740.53495	0.03	178072	740.53486	-0.09	486221
66	$C_{50}H_{76}S_2$	N/A	N/A	N/A	740.53823	-0.09	469622
67	$C_{57}H_{76}$	N/A	N/A	N/A	760.59404	-0.15	427714
68	$C_{54}H_{80}S$	760.59752	0.00	133009	760.59748	-0.05	443772
69	$C_{51}H_{84}S_2$	N/A	N/A	N/A	760.60087	-0.03	427430
70	$C_{58}H_{84}$	N/A	N/A	N/A	780.65657	-0.23	425199
71	$C_{55}H_{88}S$	780.65992	-0.27	126483	780.66006	-0.09	430228
72	$C_{52}H_{92}S_2$	N/A	N/A	N/A	780.66350	0.01	344908
73	$C_{60}H_{80}$	N/A	N/A	N/A	800.62534	-0.15	395314
74	$C_{57}H_{84}S$	800.62882	-0.01	135350	800.62875	-0.10	426243
75	$C_{54}H_{88}S_2$	N/A	N/A	N/A	800.63205	-0.18	390608
76	$C_{61}H_{88}$	N/A	N/A	N/A	820.68784	-0.26	425247
77	$C_{58}H_{92}S$	820.69115	-0.34	122433	820.69136	-0.08	407644
78	$C_{55}H_{96}S_2$	N/A	N/A	N/A	820.69485	0.06	414786

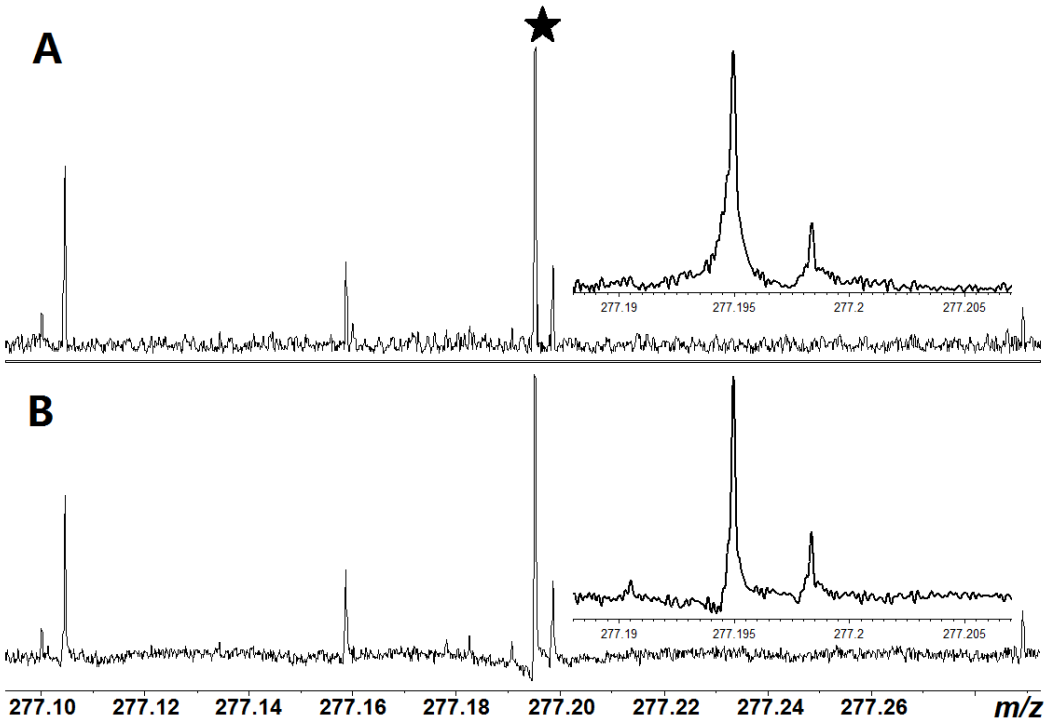

Figure B1. A: zoom in of oil spectrum in the low *m/z* region with magnitude-mode and, B: absorption-mode, inset: further zoom in of labelled peaks from the **unapodized** spectrum to show the wiggles and broad "tails". Note the asymmetric peak shape of the absorption-mode spectrum causes a slightly negative shift in *m/z* (mentioned in the text).

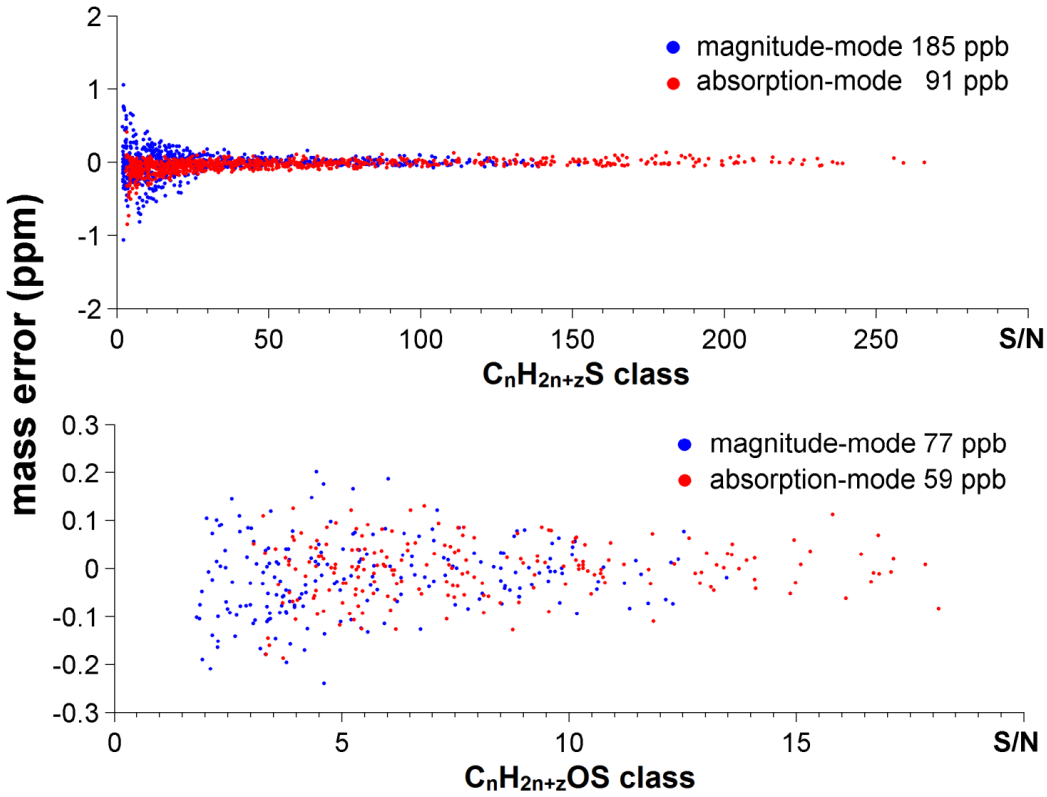

Figure B2. RMS mass error distribution to show the mass accuracy improvement for different compounds in the crude oil, huge for $C_nH_{2n+z}S$ (top), while intermediate for $C_nH_{2n+z}OS$ (bottom).

I. Load the Modified Spectrum into Bruker DataAnalysis Software

The raw transient ('fid' file) was processed and phase corrected using MatLab. The pre-processed file was then written in old Xmass format (Bruker), with appropriate parameters based on the data and a rescaled *m/z* range which is then readable by DataAnalysis for further analysis.

After phase correction, the real part of the spectrum (consisting of just the intensity values only) is written out as a 32 bit binary file (e.g., floats) with a file name of '1r'. In this case, the spectrum data is written in 32 bit using syntax '[phid] = newfid(sf);' (see section II)

Then all need to do is to create the corresponding ‘proc’ and ‘procs’ parameter files in the same directory as the ‘1r’ file. Users just have to make sure their parameters are set correctly and consistently with the original method file, so that DataAnalysis can calculate the right *m/z* array for the spectrum. Details of parameter settings are available from Bruker on request.

II. MatLab Functions ‘newfid’ with Full Comments (Start with %)

```
%#################################################################
%#                          function ‘newfid’
%#          usage: [phid] = newfid(sf);
%#          generate the transient (‘phid’) and absorption-mode (‘1r’) file for the phase corrected spectrum
%#          sf is spectrum after phase correction (complex number)
%#################################################################

function [phid]=newfid(sf);

% the MatLab syntax 'fft' (fast Fourier transform) and 'ifft' (inverse fast Fourier transform) generate even symmetry data around the zero frequency point which adds redundant information, thus this part of data is discarded during the data processing
sf2=rot90(sf);
sf2=rot90(sf2); % the negative half of data
```

```
sff=[sf;sf2]; % generate a symmetric spectrum for ifft (inverse fast Fourier transform)
newfid=ifft(sff);
newfid =real(newfid);
newfid = newfid (1:(length(phid)/2)); % discard the half of data

% generate the phase corrected transient file named 'phid'
fid=fopen('phid','w');
fwrite(fid, newfid,'int32');
fclose(fid);

% read the new transient (phid)
[fidspec,s,f,m]=readfid;

s=fft(fidspec,length(fidspec)*2); % zero fill
s=s((length(s)/2+1):length(s)); % discard the half of data
s=real(s);

%generate the '1r' file
fid = fopen('1r', 'w');
fwrite(fid, s, 'int32');
fclose(fid);
end
```

Appendix C (Supporting information for Chapter 5)

I. Load the Modified Spectrum into Bruker DataAnalysis Software

The raw transient ('fid' file) was processed and phase corrected using MatLab. The pre-processed file was then written in old Xmass format (Bruker), with appropriate parameters based on the data and a rescaled *m/z* range which is then readable by DataAnalysis for further analysis.

After phase correction, the real part of the spectrum (consisting of just the intensity values only) is written out as a 32 bit binary file (eg. floats) with a file name of '1r'. In this case, the spectrum data is written in 32 bit using syntax '[phid] = newfid(sf);

Then all need to do is to create the corresponding 'proc' and 'procs' parameter files in the same directory as the '1r' file. Users just have to make sure their parameters are set correctly and consistently with the original method file, so that DataAnalysis can calculate the right *m/z* array for the spectrum. Details of parameter settings are available from Bruker on request.

II. MatLab Functions 'newhyd' for Opening the Dataset Acquired in Narrowband, with Full Comments (Start with %)

```
%#####################################################################
%#                              function readhyd
%#       usage: [fidspec,s,f,m]=readhyd;
%#       plot the fid data, spectrum after Fourier transform and calibrate the
frequency and m/z
```

```
%#         domain
%#         fidspec--the fid data
%#         s--spectrum after fast Fourier transform
%#         f,m--frequency, m/z array
%#
%#         *for Bruker solarix file, narrowband mode only
%#####################################################################

function [fidspec,s,f,m]=readhyd(varargin)

if nargin~=0
   if exist(varargin,'file')==2
       infile = varargin;
   else
        disp('ERROR: file not found..please select now!');
        [filename,dirname]=uigetfile('*.*','Open file');
        infile=[dirname,filename];
   end
else
   [filename,dirname]=uigetfile('*.*','Open fid file');
   infile=[dirname,filename];
end

n=[varargin (2:end)];
```

```
fid=fopen(infile,'r');
fidspec=fread(fid,'int32');
fclose(fid);

o=fidspec(1:2:end);
e=fidspec(2:2:end);
e=e*i;
fidspec=o+e;

% half-hanning window apodization
idx=1:(size(fidspec));
z=size(fidspec);
z=z(1);
y=0.5+0.5*cos(pi.*idx./z);
y=y';
fidspec=fidspec.*y;

s=fft(fidspec,length(fidspec)*2); %zero fill for N,otherwise the spectrum will distorted
s=[s((size(s)/2+1):end);s(1:(size(s)/2))];
s=rot90(s);
s=rot90(s);
% calibration the freq and m/z
% details of calibration parameters are available from Bruker
End
```

Appendix D (Mapping the Protein-Binding Sites of a Novel Iridium(III) Anticancer Complex Using Electron Capture Dissociation)[7]

I. Introduction

Mass spectrometry (MS) has been recognized as a powerful tool for characterization of post-translational modifications (PTMs) due to its speed, accuracy, selectivity, and sensitivity for low concentration samples. Modified peptides and proteins can be easily identified by MS because of their mass shift and isotopic pattern change from specific modification, and the modification site can then be further located via tandem MS.

DNA is one of the most important targets for transition metal-based anticancer drugs. For example, the mechanism of action of cisplatin, a successful platinum(Pt)-based anticancer drug, involves coordination to the guanine base on DNA to form primarily 1,2- or 1,3-intrastrand crosslinks.[194] However, it is also important to understand their irreversible binding to the serum proteins since this may be involved in drug transport as well as side effects. Within one day of injection of cisplatin, 65-98% of the injected Pt is protein bound.[195-197]

Controlling the reaction of metallodrugs before they reach their target sites is vital for metallodrug design. Inert low spin d^6 transition metal complexes have become promising as they are highly selective inhibitors of protein kinases.[198] Organometallic Ru^{II} and Os^{II} arene complexes have shown potential as anticancer agent.[199-200] Also more recently, organometallic cyclopentadienyl Ir^{III}

[7] This chapter has been partially/entirely reproduced from
Qi, Y.; Liu, Z.; Li, H.; Sadler, P. J.; O'Connor, P. B., Mapping the Protein-Binding Sites for Novel Iridium(III) Anticancer Complexes Using Electron Capture Dissociation. *Rapid Commun. Mass Spectrom.* **Accepted on 02/June/2013.** Copyright 2013, Wiley.

complexes have been shown to have highly potent anticancer activity.[201] However, some of these complexes readily undergo ligands exchange and can potentially bind to both DNA and proteins.

Recent work has shown that the potent anticancer activity of $[(\eta^5\text{-}Cp^x)Ir(XY)Cl]^{0/+}$ (where Cp^x=pentamethylcyclopentadienyl (Cp*), tetramethyl(phenyl)cyclopentadienyl (Cp^{xph}) or tetramethyl(biphenyl)cyclopenta-dienyl (Cp^{xbiph}), XY=chelating ligand) is highly dependent both on the Cp* substituents and on the XY ligand.[202] For example, replacing the N,N chelating ligand 2,2'-bipyridine (bpy) with the C,N-chelating ligand 2-phenylpyridine (phpy) in Cp^*Ir^{III} complexes (Figure D1) decreases its IC_{50} value (concentration at which 50% of the cell growth is inhibited) from >100 μM to 10.8 μM for A2780 human ovarian cancer cells,[203] and furthermore, the biphenyl substitution on Cp* reduces the IC_{50} value to 0.7 μM (Figure D2).[204] Although DNA has been shown to be a potential target for this type of Ir^{III} complex, it is also important to investigate its binding sites on proteins.

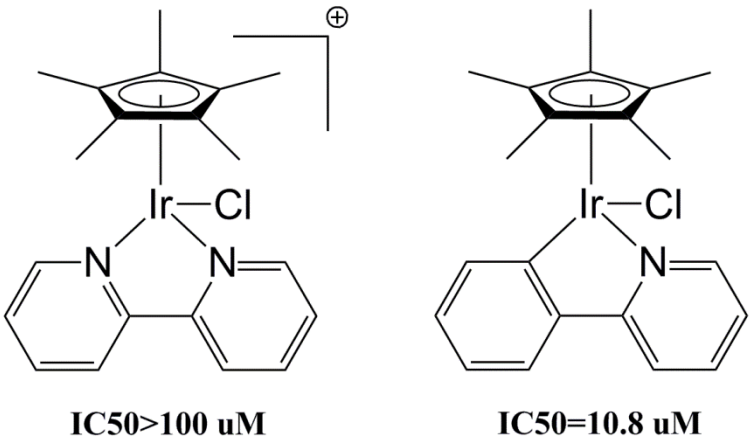

IC50>100 uM **IC50=10.8 uM**

Figure D1 Iridium(III) pentamethylcyclopentadienyl (Cp^x) complexes with IC_{50} values, (left) $[(\eta^5\text{-}C_5Me_5)Ir(bpy)Cl]^+$; (right) $[(\eta^5\text{-}C_5Me_5)Ir(phpy)Cl]$.[203]

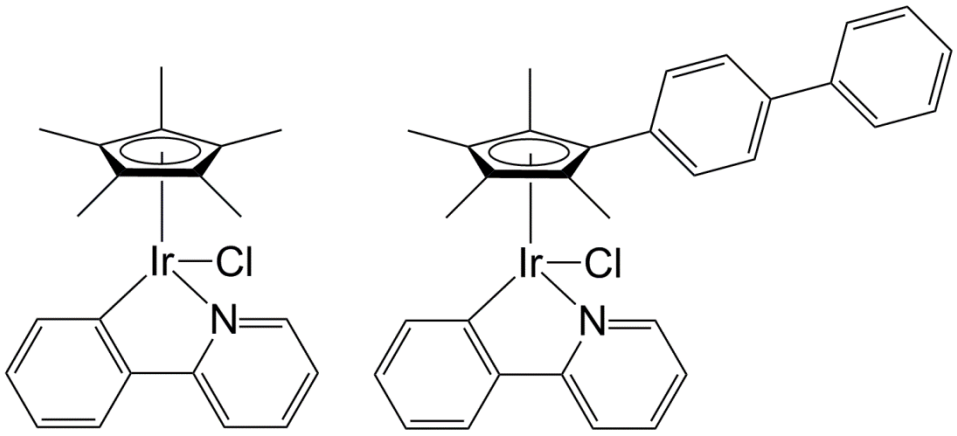

IC50=10.8 uM **IC50=0.7 uM**

Figure D2 Left: $[(\eta^5\text{-}C_5Me_5)Ir(phpy)Cl]$ (Ir_1), formula: $IrC_{21}H_{23}NCl$. Right: $[(\eta^5\text{-}C_5Me_4C_6H_4C_6H_5)Ir(phpy)Cl]$ (Ir_2), formula: $IrC_{32}H_{29}NCl$.[204]

Sulfur-containing ligands are often strong binding sites for the heavier transition metal ions. For example, the cysteine-rich proteins, metallothioneins, play a crucial role in resistance to and detoxification of cisplatin, as Pt often binds irreversibly to the thiolate sulphur of cysteine.[205] The sulphur of the

thioether methionine (Met) is also a strong binding site for Pt.[206] To understand the biological properties of metallated proteins is important to 1) define the coordination sites of the bound metal, and 2) determine which of the original ligands from the metallodrug are still bound in the protein complex. In this project, a Met rich protein--calmodulin (CaM, containing 9 Met out of 148 amino acid residues, which contribute ~46% of the exposed surface area of the hydrophobic patches on the surface) was chosen to investigate $Cp^{x}Ir^{III}$--protein interaction and compared with its interaction with cisplatin. The aim of the present work is to map the binding sites and possible intermediates for the Ir complex on CaM using Fourier transform ion cyclotron resonance (FT-ICR) tandem mass spectrometry.

II. Experimental Methods

Bovine calmodulin and trypsin (TPCK treated from bovine pancreas) were purchased from Sigma (Gillingham, UK). HPLC grade of acetic acid, methanol, and acetonitrile were obtained from Fisher Scientific (Pittsburgh, PA). [(η^5-C_5Me_5)Ir(phpy)Cl] (Ir_1) and [(η^5-$C_5Me_4C_6H_4C_6H_5$)Ir(phpy)Cl (Ir_2) were synthesized and characterized by published methods.[203-204]

Ir_1 and Ir_2 (Figure D2) were dissolved in a 50:50 methanol/water mixture to 1 mM for stock solutions. To retain the native state of CaM, reactions of protein with Ir complex were carried on in water. CaM (40 μM) was mixed with Ir_1 or Ir_2 (400 μM), and incubated at 37 °C for 24 h. To remove the free iridium complex and desalt, Amicon filters (MW cut off = 3 kDa, Millipore, Watford, U.K.) were used at 13,000 rpm for 30 min at room temperature, and washed three times with water. The samples were diluted to 0.5 μM with

50:50:1 acetonitrile/water/acetic acid mixture immediately before mass spectrometry analysis.

The CaM–Ir_1 mixture (molar ratio 1:10) was diluted to 20 μM with water and then subjected to trypsin digestion at a protein to enzyme ratio of 40:1 (w/w) at 37 °C for 4 h. 20 μM CaM without $Cp^{x}Ir^{III}$ complex was also digested under the same conditions for a blank experiment. The sample was diluted to 1 μM with 50:50:1 acetonitrile/water/acetic acid mixture immediately before mass spectrometry analysis.

The samples were ionized using nano-electrospray (nanoESI), and all spectra were recorded using a solariX 12T FT-ICR mass spectrometer (Bruker Daltonik GmbH, Bremen, Germany), equipped with an Infinity cell[59] and a CO_2 laser with 10.6 μm IR light (Synrad, Mukilteo,WA). In MS/MS mass spectrometry, the precursor ions were isolated in the first quadrupole and externally accumulated in the hexapole for 1–5 s. For CAD experiments, 0-10 eV collision energy was applied. For IRMPD, 0-200 ms IR laser irradiation was applied. For ECD experiments, the accumulated ions were transferred into the ICR cell, and irradiated with 1.4 eV electrons from a 1.7 A heated hollow cathode dispenser for 10–80 ms.[207] All spectra were internally calibrated using the unmodified $c'/z\cdot$ ions which were previously defined in the ECD spectra of CaM. Due to the H transfer between $c'/z\cdot$ ions in ECD experiments, the peak assignment was based on matching both the theoretic mass and the isotopic pattern. Either the monoisotopic peak or the most intense peak (if monoisotopic peak was not clear) was used for assignment in the peak list (Table D1-D4).

III. Result and Discussion

Ir_1 and Ir_2 (Figure D2) were incubated with CaM for 24 h and analyzed. Figure D3 shows the mass spectra of CaM on reaction with Ir_1 and Ir_2. Though the molar ratio of Ir to CaM was 10:1, the dominant peaks observed are still from different charge states of CaM without Ir adducts. Detailed analysis shows that only one Ir modified CaM species can be found for each charge state at very low signal intensity. As shown in Figure D3, the peaks for the Ir+CaM adducts were assigned as $[CaM+IrC_{21}H_{23}N+13H]^{14+}$ and $[CaM+IrC_{32}H_{29}N+13H]^{14+}$, suggesting that the Cl ligand is substituted by a CaM side chain ligand on binding. In contrast, when CaM reacts with cisplatin at a molar ration of 1:8, it was found that CaM can bind to 6-8 cisplatin molecules.[177] This phenomenon indicates that either the Ir binding is weak or the modified CaM adducts are unstable in the gas phase.

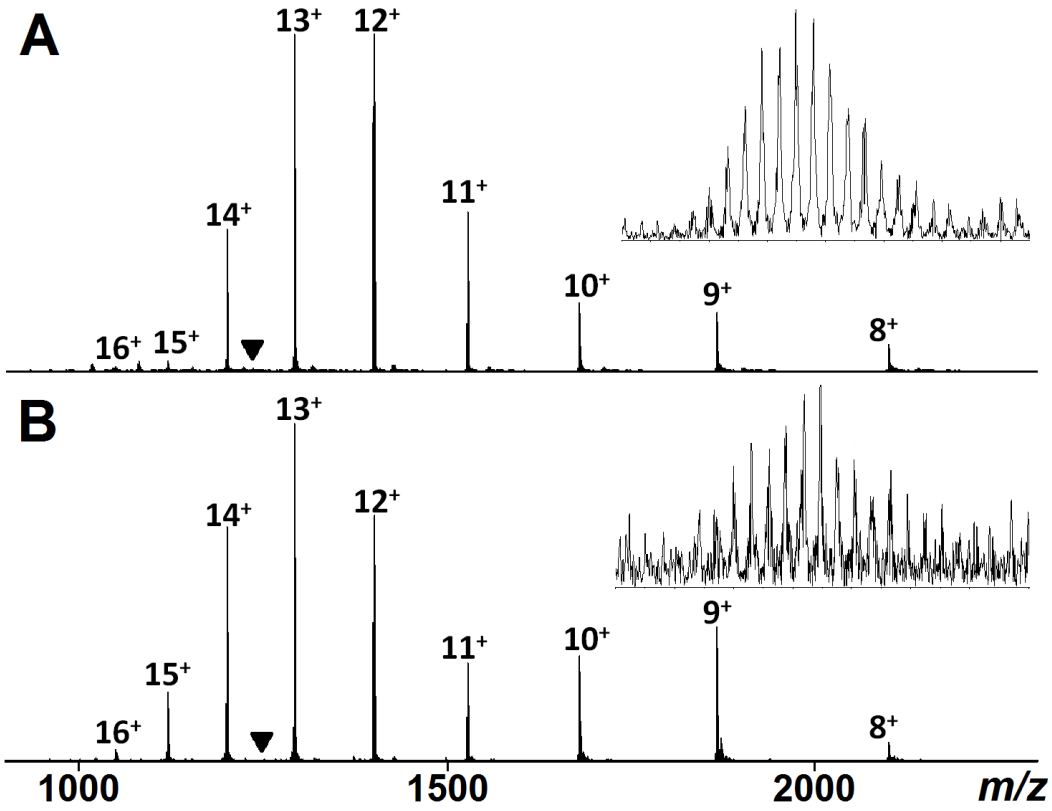

Figure D3 Spectra of intact CaM with $Cp^{x}Ir^{III}$ complexes at molar ratio of 1:10, with charge states of CaM labelled. (A) CaM-Ir_1, inset: zoom in of *m/z* 1233.9-1235.6 showing the isotopic pattern of $[CaM+IrC_{21}H_{23}N+13H]^{14+}$. (B) CaM-Ir_2, inset: zoom in of *m/z* 1243.8-1245.5 showing the isotopic pattern of $[CaM+IrC_{32}H_{29}N+13H]^{14+}$.

For MS/MS, the species of $[CaM+Ir\_1]^{17+}$ was isolated and subjected to collisionally activated dissociation (CAD) and infrared multiphoton dissociation (IRMPD). Unfortunately, both techniques failed to provide information on the Ir modification sites. In Figure D4, during the isolation of $[CaM+Ir\_1]^{17+}$ species, some of the Ir modification had already broken and dissociated to $[IrC_{21}H_{23}N]^{1+}$ (simply using Ir* in the latter text) and $[CaM+16H]^{16+}$ during external ion accumulation.[208] Applying 5 eV or 160 ms IR excitation energy caused almost

complete Ir* loss while the protein backbone still remains intact, so that no information about the binding site is retained; the same result was also obtained for the CaM+Ir_2 mixture. For a typical CAD experiment, >20 eV is required to cleave the protein backbone amide bonds.[177, 196] This phenomenon shows that Ir binding is much weaker than the amide bonds. Both CAD and IRMPD involve vibrational excitation; the fragmentation depends mostly on the amount of energy applied, which means that the weakest bond is cleaved first. Thus, by using conventional MS/MS methods, the information of Ir modification position is lost before the proteins' amide bonds are cleaved, and therefore, a different MS/MS technique is required to study the structure of $Cp^{x}Ir^{III}$--protein adducts.

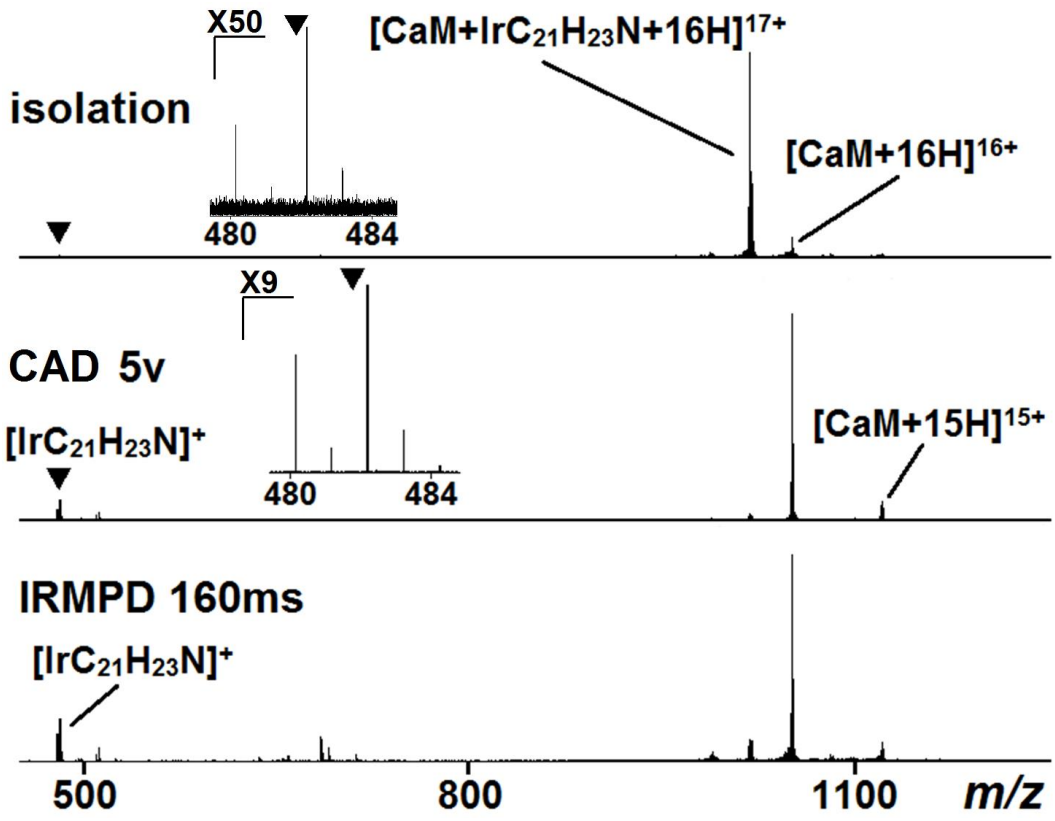

Figure D4 (top) isolation mass spectrum of $[CaM+IrC_{21}H_{23}N+16H]^{17+}$, with zoom in (50 times) the labeled $[IrC_{21}H_{23}N]^{+}$ isotopic species. (middle) CAD spectrum with zoom in (9 times) the labeled $[IrC_{21}H_{23}N]^{+}$. (bottom) IRMPD spectrum.

Electron-capture dissociation (ECD) is a technique that utilizes ion-electron recombination, and is believed to be non-ergodic.[209] In ECD, the cleavage happens prior to the redistribution of vibrational energy; thus labile groups and non-covalent bonds are preserved.[210] Again, the $[CaM+Ir^*]^{17+}$ was isolated, accumulated, and a top-down[211] ECD experiment was applied. As is shown on Figure D5A (full peak list in Table D1), the cleavage was observed on both the CaM+Ir* bond and the CaM backbone N-Cα bond. The Ir* fragment is still notable at *m/z* ~481, and careful analysis reveals that the Ir* fragment here is actually a combination pattern of $[IrC_{21}H_{23}N]^{+}$ (CAD caused by the voltage

and heating during ion transfer and accumulation) and $[IrC_{21}H_{23}N+H]^+$ (ECD mechanism, Scheme 8.1); here, FT-ICR successfully resolved the mass difference (4.47 mDa) between the two different isotopic species (Figure D5B, inset).

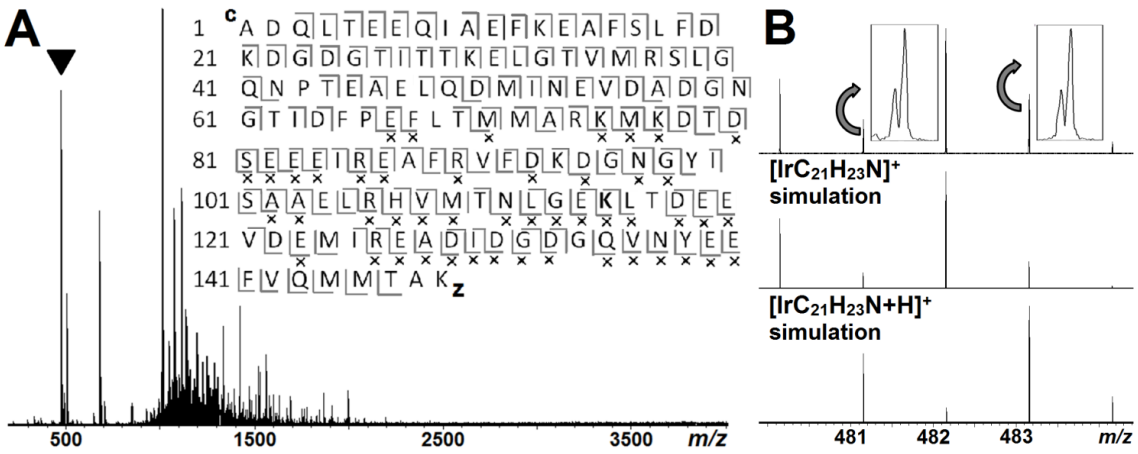

Figure D5 (A) ECD spectrum of $[CaM+IrC_{21}H_{23}N+16H]^{17+}$, inset: the corresponding fragmentation map, X represents $[IrC_{21}H_{23}N]^+$ modification (full peak list is available in Table D1). (B) top: expansion of the peak labelled with a "▼" from A, showing that this species is a combination of $[IrC_{21}H_{23}N]^+$ species and $[IrC_{21}H_{23}N+H]^+$, middle and bottom: isotope simulation of $[IrC_{21}H_{23}N]^+$ and $[IrC_{21}H_{23}N+H]^+$ species.

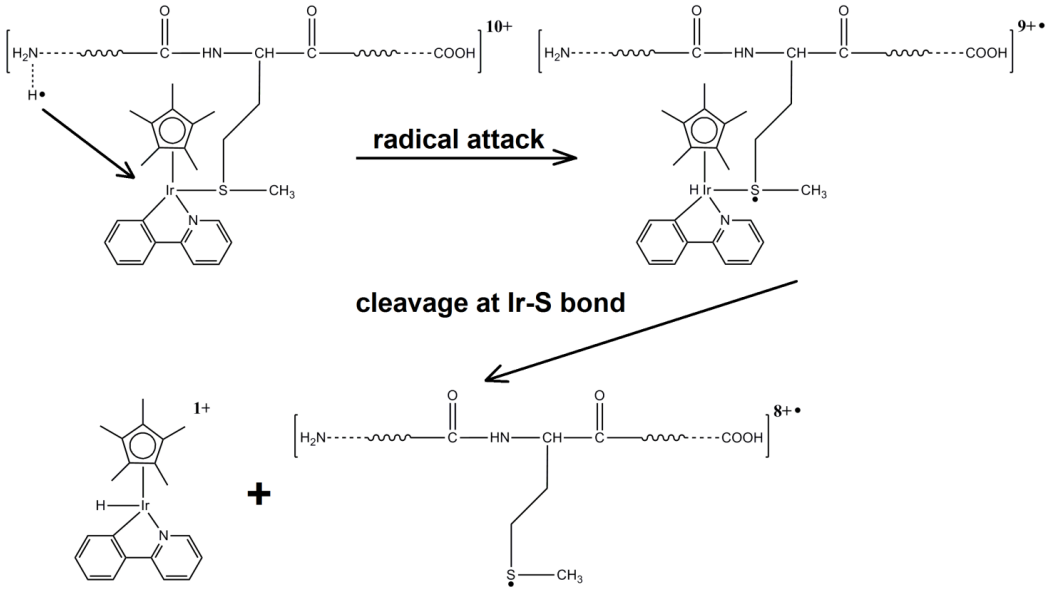

Scheme D1 Proposed mechanism of $[IrC_{21}H_{23}N+H]^+$ formed by ECD.

In addition to the CaM+Ir* cleavage, backbone cleavages of CaM with the Ir* modification attached were also observed in the spectrum. Overall, 129 cleavages from the total of 147 (88%) available N-Cα backbone bonds in CaM were assigned. By comparison, Li *et al.* reported that after CaM reacted with cisplatin, only 58% backbone cleavage was observed due to the cross-linking of Pt between Met109 and Met144, while as a control, 91% backbone cleavage was achieved on CaM without cisplatin adducts.[177] Here, the backbone cleavage of Ir*+CaM is close to that from unmodified CaM, which probably means the Cp^xIr^{III} complex does not crosslink CaM and limit its flexibility.[212] The same experiment was also performed on the CaM+Ir_2 mixture; however, the Ir modified CaM was barely observable after ion isolation, and thus, the signal intensity was insufficient for ECD. The hydrophobicity and bulkiness of the Ir_2 complex may limit its binding with CaM, which would explain this result.

In top-down tandem MS, the cleavage map for CaM+Ir_1 (Figure D5) shows that there is no Ir modification in the region of CaM(141-148); meanwhile, both modified and unmodified z9 ions are observed. This indicates that the Ir* binding site is either on the E140 residue or in the region of CaM(141-148). Interestingly, no Ir modified c fragments were observed in the top-down spectrum. Such an observation is consistent with Ir binding on CaM(140-148), near the C-terminus. However, due to the structure of the full size protein and the complexity of the top-down spectrum, these fragments may be too weak for detection or overlapped by more intense peaks. MS^3 is one option to locate the exact binding sites; however, the electrons are captured more easily by iridium and sulphur which makes the cleavage between CaM and Ir* adduct the major channel. For this reason, the backbone cleavage of CaM is suppressed, and the intensity of Ir modified ions is too low for a second ECD experiment.

To locate the exact binding sites, the Ir*+CaM mixture was trypsin digested into peptides for bottom-up MS analysis. Four Ir* binding peptides were identified; they are CaM(38-74), CaM(107-126), CaM(127-148), and CaM(75-148). The above modified peptides were then isolated and subjected to the ECD. The overall fragment peak intensity is fairly low; however, the characteristic isotopic pattern of Ir* adduct (Figure D5) and the accurate mass of FT-ICR assist the assignment of the fragments from ECD. For CaM(127-148)+Ir* (Figure D6), the fragment map clearly indicates that the Ir* coordinates to Met144 and/or Met145. Additionally, special fragments $[Ir^*+CH_3S]^{1+}$ and $[Ir^*+CH_3S+H]^{1+}$ were observed in the spectrum, which arise from the side chain loss of Met (Scheme D2); existence of these fragments proves that the Cp^xIr^{III} complex binds to Met.

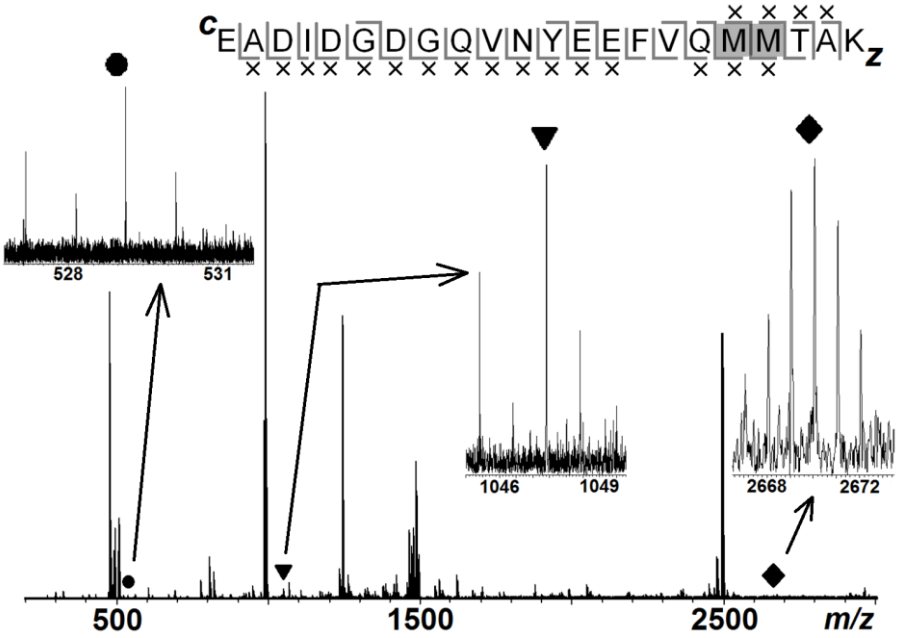

Figure D6 ECD spectrum of [CaM(127-148)+Ir$C_{21}H_{23}N$+2H]$^{3+}$ ion at *m/z* ~991. The insets are its corresponding fragmentation map, and characteristic fragments: ●[Ir*+CH_3S(+H)]$^{1+}$, ▼[z_5+Ir*]$^{1+}$, and ♦[c_{19}+Ir*]]$^{1+}$. Full peak list in Table D2.

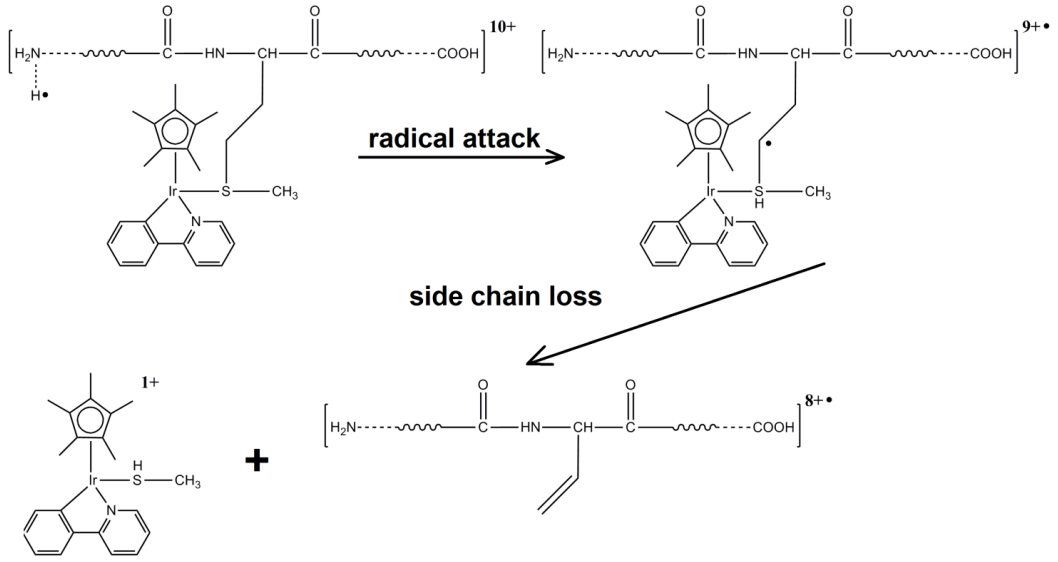

Scheme D2 Proposed mechanism of $[IrC_{21}H_{23}N+CH_3S+H]^+$ ions formed by ECD.

Apart from the primary binding site, other sites may also have affinity for Ir, giving a complicated mixture of CaM+Ir* products with the same elemental composition and mass, but different modification sites. Ir* modification is also observed on CaM(107-126) (Figure D7) and CaM(38-74) (Figure D8), and the binding sites were identified unambiguously as Glu120 and Asp64 from to the fragmentation map. In addition, side chain loss from Met (very low S/N) was also found in both peptides, indicating that Met51, Met71, Met72, Met109, and Met124 may also bind to Ir* after long reaction times or at a high molar ratio of Cp^xIr^{III}/protein.

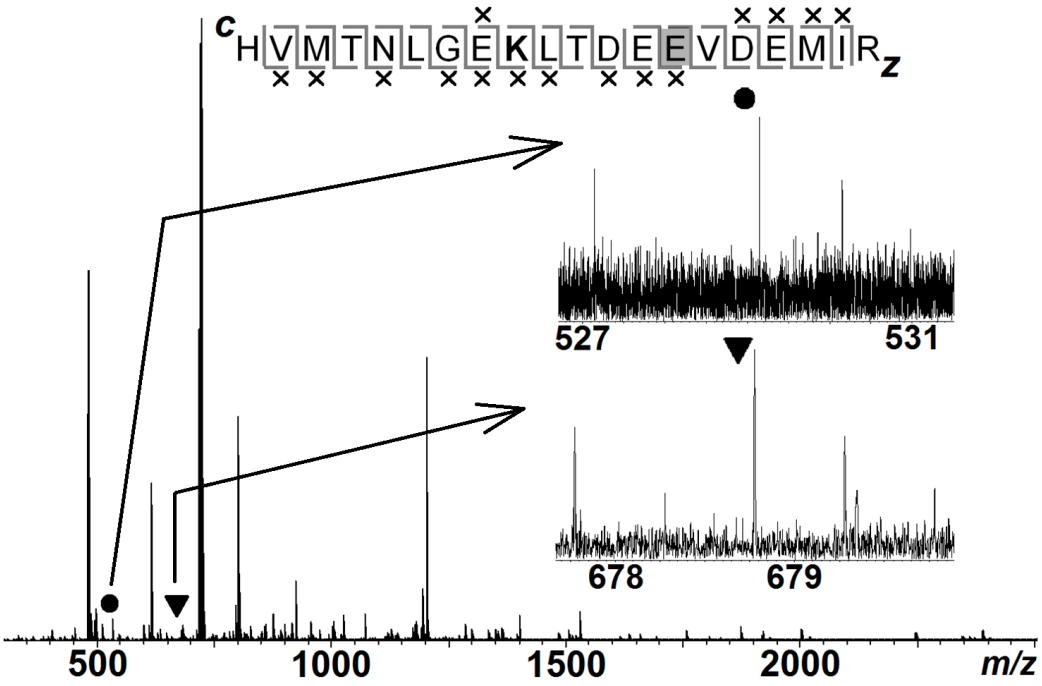

Figure D7 ECD spectrum of [CaM(107-126)+Ir$C_{21}H_{23}N$+3H]$^{4+}$ ion at *m/z* ~722. The insets are its corresponding fragmentation map, and characteristic fragments: ●[Ir*+CH_3S(+H)]$^{1+}$, and ▼[z_7+Ir*]$^{2+}$. Full peak list in Table D3.

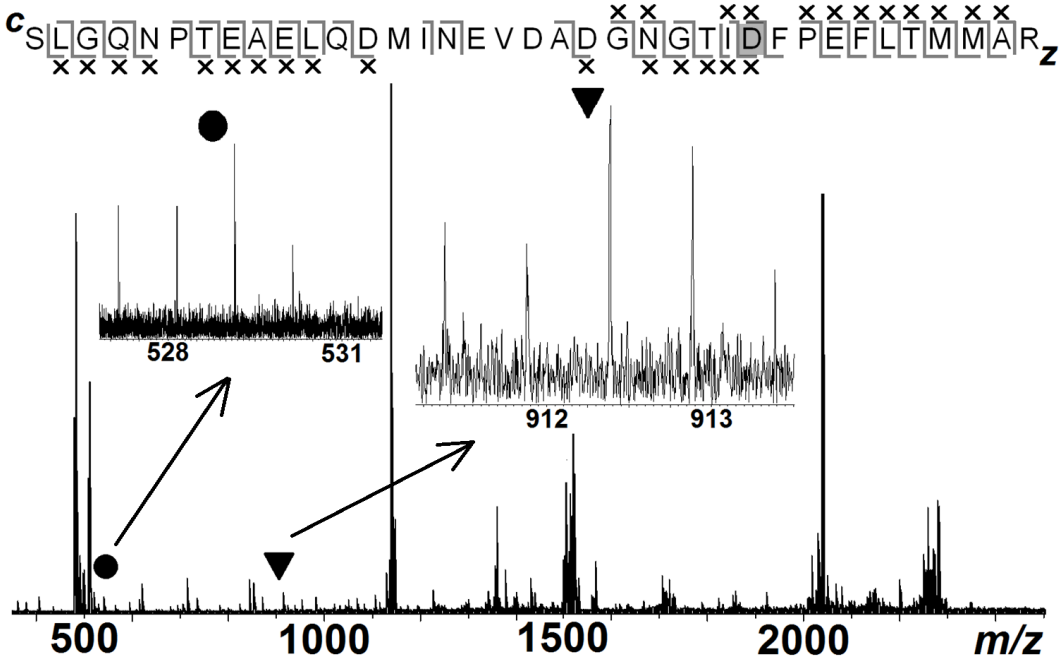

Figure D8 ECD spectrum of [CaM(38-74)+Ir$C_{21}H_{23}$N+3H]$^{4+}$ ion at *m/z* ~1139. The insets are its corresponding fragmentation map, and characteristic fragments: ●[Ir*+CH_3S(+H)]$^{1+}$, and ▼[z_{11}+Ir*]$^{2+}$. Full peak list in Table D4.

IV. Conclusion

The binding of metallodrugs to proteins can play an important role in their activation, transport, and excretion in vivo. Herein, the interaction between Cp^xIr^{III} complex and calmodulin was elucidated by ECD based tandem mass spectrometry, and the fragment [Ir*+CH_3S(+H)]$^{1+}$ was found which is a signature of Met binding. Although Cp^xIr^{III} can coordinate to proteins at a high molar ratio, the binding strength is fairly weak under the conditions used here, and thus, the binding sites cannot be assigned by conventional MS/MS methods. And additionally, unlike cisplatin, which preferentially binds to Met sites in a protein with displacement of all four ligands,[176-177] the Cp^xIr^{III} complex does not readily lose its chelated Cp^x ring or the phpy ligand.[202-203] Therefore, not just the Ir^{III} scaffold but its coordinated ligands remain intact, which may

explain its high anticancer activity. Finally, to the best of our knowledge, this is the first study in which the coordinative protein binding sites for an organometallic Ir^{III} complex have been located.

Table D1. ECD fragments of the $[CaM+IrC_{21}H_{23}N+16H]^{17+}$ ions for Figure D5, * indicates the masses used for internal calibration.

Assignments	charge	Theo. m/z	Exp. m/z	Error (ppm)
c3	1	*374.16702	374.16702	0.00
c4	1	*487.25109	487.25108	-0.02
c5	1	*588.29877	588.29877	0.00
c6	1	*717.34136	717.34134	-0.03
c7	1	*846.38395	846.38392	-0.04
c10	1	*1158.56371	1158.56366	-0.04
c11	1	1287.60630	1287.60575	-0.43
c12	1	*1434.67472	1434.67504	0.22
c13	2	781.88848	781.88847	-0.01
	1	*1562.76968	1562.76978	0.06
c14	1	*1691.81227	1691.81228	0.01
c15	2	881.92833	881.92859	0.29
	1	*1762.84939	1762.84978	0.22
c16	2	954.95863	954.95855	-0.08
	1	1909.91780	1909.91677	-0.54
c17	2	998.47464	998.47511	0.47
	1	1996.94983	1996.94901	-0.41
c19	2	1129.05479	1129.05493	0.12
	1	*2257.10231	2257.10226	-0.02
c20	2	*1186.56826	1186.56828	0.02
c21	2	*1250.61574	1250.61605	0.25
	1	2501.22758	2501.22847	0.36
c22	2	1308.12922	1308.12991	0.53
c23	3	891.42906	891.42944	0.43
	2	*1336.63995	1336.63983	-0.09
c24	2	*1394.15342	1394.15310	-0.23
c25	3	949.11298	949.11315	0.18
	2	*1422.66415	1422.66411	-0.03
c26	2	1473.18799	1473.18727	-0.49
c27	2	1529.73002	1529.72961	-0.27
c28	2	*1580.25386	1580.25397	0.07
c29	3	1087.52089	1087.52069	-0.18
	2	*1630.77770	1630.77746	-0.15
c30	3	1130.21921	1130.21917	-0.04
	2	*1694.82518	1694.82533	-0.09
c31	3	1173.23341	1173.23330	-0.09
	2	*1759.34648	1759.34634	-0.08
c32	3	1210.92810	1210.92807	-0.02
	2	1815.88851	1815.88906	0.30
c33	3	1229.93525	1229.93518	-0.06
	2	1844.39924	1844.39870	-0.29

c34	3	1263.95227	1263.95216	-0.09
	2	1895.42476	1895.42591	0.61
c35	3	1296.97507	1296.97519	0.09
c36	3	1340.65523	1340.65574	0.38
	2	2010.47921	2010.47969	0.24
c37	3	1392.68894	1392.68915	0.15
	4	1044.76852	1044.76850	-0.02
c38	4	1066.77737	1066.77720	-0.16
	3	1422.03406	1422.03468	0.44
c39	4	1094.79866	1094.79704	-1.48
	3	1459.72826	1459.72881	0.38
c40	4	1109.30375	1109.30377	0.02
	3	1478.73591	1478.73609	0.12
c41	5	913.25617	913.25650	0.36
	4	1141.31840	1141.31822	-0.16
	3	1521.42210	1521.42206	-0.03
c44	5	975.68485	975.68452	-0.34
	4	1219.35424	1219.35473	0.40
	3	1625.46989	1625.46956	-0.20
c45	5	1001.49337	1001.49349	0.12
	4	1251.36404	1251.36399	-0.04
	3	1668.48409	1668.48314	-0.57
c46	4	1269.37417	1269.37403	-0.11
	3	1692.16313	1692.16336	0.14
c48	5	1064.12612	1064.12595	-0.16
c49	6	908.98274	908.98291	0.19
	5	1089.73784	1089.73793	0.08
	4	1361.92048	1361.92042	-0.04
c50	4	1390.92805	1390.92792	-0.09
c51	6	1085.01962	1085.01916	-0.42
	5	1301.82209	1301.82114	-0.73
	4	1627.02579	1627.02561	-0.11
c52	5	1161.76880	1161.76899	0.16
	4	1451.95918	1451.95965	0.32
c53	6	987.14848	987.14849	0.01
	5	1184.57739	1184.57731	-0.07
	4	1480.46992	1480.47014	0.15
c54	4	1512.73057	1512.73043	-0.09
c55	5	1230.19959	1230.19915	-0.36
	4	1537.49767	1537.49703	-0.42
c56	5	1253.20498	1253.20485	-0.10
	4	1566.25441	1566.25446	0.03
c57	6	1056.34483	1056.34490	0.07
	5	1267.41234	1267.41231	-0.02
	4	1584.01361	1584.01357	-0.03
c58	5	1290.41773	1290.41743	-0.23

	4	1612.77035	1612.77063	0.17
c59	6	1085.01957	1085.01916	-0.38
	5	1301.82203	1301.82114	-0.68
	4	1627.02571	1627.02561	-0.06
c60	6	1104.02672	1104.02676	0.04
	5	1324.63061	1324.63084	0.17
	4	1655.53645	1655.53663	0.11
c61	5	1336.03490	1336.03483	-0.05
	4	1669.79181	1669.79808	3.75
c63	5	1378.86126	1378.86127	0.01
	4	1723.32475	1723.32433	-0.24
c64	5	1401.86664	1401.86745	0.58
c66	6	1209.24414	1209.24418	0.03
	5	1450.69088	1450.69132	0.30
	4	1813.11179	1813.11138	-0.23
c67	7	1055.07353	1055.07402	0.46
	6	1230.75124	1230.75095	-0.24
	5	1476.70003	1476.70020	0.12
c70	6	1290.95127	1290.95119	-0.06
	5	1548.94007	1548.94035	0.18
c71	6	1312.79135	1312.79132	-0.02
c72	6	1334.63143	1334.63138	-0.04
c73	6	1346.47095	1346.47159	0.48
c74	7	1176.42077	1176.41956	-1.03
	6	1372.32302	1372.32147	-1.13
c75	7	1195.14585	1195.14681	0.80
c76	8	1062.00961	1062.00977	0.15
	7	1213.58137	1213.58145	0.07
	6	1415.67705	1415.67754	0.35
c77	7	1232.02395	1232.02364	-0.25
	6	1437.02621	1437.02658	0.26
c78	8	1092.52523	1092.52485	-0.35
	7	1248.45637	1248.45654	0.14
	6	1456.36455	1456.36397	-0.40
c79	9	982.47298	982.47278	-0.20
	8	1105.15619	1105.15597	-0.20
	7	1262.89175	1262.89165	-0.08
	6	1473.03865	1473.03874	0.06
c80	8	1119.40917	1119.40965	0.43
	7	1279.32417	1279.32424	0.05
	6	1492.20987	1492.20979	-0.05
c81	8	1130.41357	1130.41300	-0.50
	7	1291.75732	1291.75612	-0.93
c82	8	1146.54389	1146.54376	-0.11
	7	1310.19198	1310.19193	-0.04
	6	1528.38943	1528.38954	0.07

c83	8	1162.67422	1162.67389	-0.28
	7	1328.62663	1328.62645	-0.14
	6	1549.89653	1549.89666	0.08
c84	8	1178.80454	1178.80482	0.24
	7	1347.06129	1347.06158	0.22
c85	8	1192.94005	1192.93963	-0.35
c86	10	970.26392	970.26382	-0.10
	9	1177.84764	1177.84793	0.25
	8	1212.45269	1212.45215	-0.45
	7	1385.51632	1385.51627	-0.04
c87	8	1228.58301	1228.58170	-1.07
	7	1403.95098	1403.95091	-0.05
c88	9	1100.07872	1100.07895	0.21
	8	1237.46265	1237.46210	-0.44
c89	8	1255.84621	1255.84600	-0.17
	7	1435.10891	1435.10870	-0.15
c90	9	1133.76423	1133.76356	-0.59
	8	1275.35825	1275.35848	0.18
c92	10	1045.20256	1045.20258	0.02
	9	1161.22426	1161.22342	-0.72
	8	1306.25139	1306.25168	0.22
c93	10	1056.70526	1056.70487	-0.37
	9	1174.00503	1174.00500	-0.03
	8	1320.62975	1320.62844	-0.99
c94	11	972.37771	972.37790	0.20
	10	1069.51476	1069.51464	-0.11
	9	1188.23781	1188.23752	-0.24
c96	11	988.01848	988.01860	0.12
	10	1086.71960	1086.71928	-0.29
	9	1207.35430	1207.35437	0.06
	8	1358.14768	1358.14759	-0.07
c97	9	1220.02573	1220.02459	-0.93
c100	11	1028.67410	1028.67415	0.05
	10	1131.44078	1131.44109	0.27
c101	11	1036.58610	1036.58624	0.14
c102	12	956.20762	956.20756	-0.06
	11	1043.04402	1043.04394	-0.08
c103	11	1049.50194	1049.50089	-1.00
c105	11	1071.51345	1071.51375	0.28
c106	12	995.39662	995.39621	-0.41
	11	1085.79566	1085.79582	0.15
c107	12	1006.81820	1006.81791	-0.29
c108	12	1015.07391	1015.07375	-0.16
c110	12	1034.41459	1034.41389	-0.68
	11	1128.36071	1128.35996	-0.66
c112	12	1053.34184	1053.34130	-0.51

c114	12	1068.84718	1068.84700	-0.17
	11	1165.92354	1165.92347	-0.06
c115	13	999.79349	999.79324	-0.25
c118	13	1025.11339	1025.11295	-0.43
c119	13	1035.11691	1035.11594	-0.94
c121	13	1052.66391	1052.66468	0.73
c125	13	1090.21730	1090.21712	-0.17
c126	14	1023.56666	1023.56660	-0.06
	13	1102.22508	1102.22479	-0.26
c129	14	1046.07385	1046.07373	-0.11
c130	14	1054.22288	1054.22297	0.09
c132	14	1066.44046	1066.44070	0.23
c133	14	1074.65668	1074.65735	0.62
z3	1	303.17887	303.17885	-0.07
z4	1	434.21936	434.21943	0.16
z5	1	565.25984	565.25986	0.04
z6	1	693.31842	693.31843	0.01
z7	1	792.38683	792.38719	0.45
z8	1	939.45525	939.45542	0.18
z9	1	1068.49784	1068.49790	0.06
z9+IrC21H23N	2	775.32163	775.32163	0.00
z10+IrC21H23N	2	839.84293	839.84291	-0.02
z11+IrC21H23N	2	921.37459	921.37454	-0.05
z12	1	1474.64669	1474.64648	-0.14
z12+IrC21H23N	2	978.39605	978.39617	0.12
z13+IrC21H23N	2	1027.93026	1027.92975	-0.50
z14	1	1701.77368	1701.77427	0.35
z14+IrC21H23N	2	1091.95955	1091.95988	0.30
z16	1	1873.82209	1873.82149	-0.32
z16+IrC21H23N	2	1178.48547	1178.48557	0.08
z17+IrC21H23N	2	1206.99620	1206.99639	0.16
z18	1	2046.87832	2046.87765	-0.33
z18+IrC21H23N	2	1264.50968	1264.50956	-0.09
z19+IrC21H23N	2	1321.05171	1321.05222	0.39
z20	1	2274.98933	2274.98673	-1.14
z20+IrC21H23N	2	1378.56519	1378.56529	0.07
z21+IrC21H23N	2	1414.08374	1414.08382	0.06
z22+IrC21H23N	2	1478.60504	1478.60517	0.09
z23	2	1315.58480	1315.58470	-0.08
z23+IrC21H23N	3	1038.10616	1038.10657	0.39
z25	2	1437.64707	1437.64691	-0.11
z26	2	1502.16837	1502.16879	0.28
z26+IrC21H23N	3	1162.49514	1162.49531	0.15
z27	2	1560.18352	1560.18371	0.12
z29	2	1673.73734	1673.73691	-0.26
z29+IrC21H23N	2	1914.80804	1914.80868	0.33

	3	1276.87445	1276.87434	-0.09
z30	2	1738.25864	1738.25824	-0.23
z30+IrC21H23N	3	1319.88865	1319.88884	0.14
z31	2	1795.77211	1795.77181	-0.17
z31+IrC21H23N	3	1358.23096	1358.23103	0.05
z33	2	1902.83798	1902.83729	-0.36
z33+IrC21H23N	2	2144.41049	2144.41185	0.63
	3	1428.60820	1428.60834	0.10
z34	3	1325.94284	1325.94291	0.05
	2	1988.41062	1988.41090	0.14
z34+IrC21H23N	3	1486.65672	1486.65681	0.06
	4	1115.24436	1115.24446	0.09
z35	3	1368.95704	1368.95736	0.23
	2	2052.93192	2052.93193	0.00
z35+IrC21H23N	3	1529.33636	1529.33711	0.49
z36	3	1387.96419	1387.96431	0.09
	2	2081.44265	2081.44228	-0.18
z36+IrC21H23N	3	1548.67808	1548.67784	-0.15
z37	3	1425.99333	1425.99314	-0.13
	2	2138.48636	2138.48731	0.44
z37+IrC21H23N	4	1190.03139	1190.03197	0.49
z38	3	1464.00844	1464.00857	0.09
	2	2195.50783	2195.50799	0.07
z38+IrC21H23N	3	1624.38708	1624.38650	-0.36
z40	3	1541.03591	1541.03586	-0.03
	2	2311.55191	2311.55108	-0.36
z40+IrC21H23N	4	1276.31323	1276.31237	-0.67
z41	3	1574.39317	1574.39306	-0.07
	2	2361.08612	2361.08313	-1.27
z41+IrC21H23N	4	1301.33127	1301.33005	-0.94
z42	3	1620.07947	1620.07976	0.18
	2	2430.11724	2430.11717	-0.03
z42+IrC21H23N	4	1335.59592	1335.59546	-0.34
z43	4	1254.33670	1254.33631	-0.31
	3	1672.11318	1672.11308	-0.06
z43+IrC21H23N	5	1099.89841	1099.89807	-0.31
z44	3	1709.80787	1709.80746	-0.24
z45	4	1314.86837	1314.86770	-0.51
	3	1753.15801	1753.15744	-0.33
z46	4	1332.62765	1332.62715	-0.38
	3	1776.50110	1776.50113	0.02
z46+IrC21H23N	4	1452.91213	1452.91232	0.13
	5	1162.73191	1162.73195	0.03
z47	4	1350.38692	1350.38697	0.04
	3	1800.18014	1800.18036	0.12
z47+IrC21H23N	5	1176.73858	1176.73835	-0.20

z48	4	1372.14493	1372.14432	-0.44
	3	1829.52676	1829.52626	-0.27
z50	4	1441.18178	1441.18303	0.87
	3	1921.23995	1921.24041	0.24
z51	4	1455.68799	1455.68765	-0.23
	3	1940.24710	1940.24689	-0.11
z51+IrC21H23N	5	1260.77875	1260.77873	-0.02
z52	5	1187.56043	1187.56007	-0.30
	4	1484.19872	1484.19865	-0.05
	3	1978.59587	1978.59574	-0.07
z52+IrC21H23N	5	1283.78809	1283.78802	-0.05
	6	1069.82399	1069.82412	0.12
z53	4	1498.45408	1498.45352	-0.37
z54	5	1221.97011	1221.97016	0.04
	4	1527.21082	1527.21086	0.03
z54+IrC21H23N	5	1318.19778	1318.19717	-0.46
	6	1098.66603	1098.66624	0.19
z55	5	1247.58910	1247.58807	-0.83
	4	1559.23456	1559.23417	-0.25
z56	5	1270.59449	1270.59355	-0.74
	4	1587.99130	1587.99137	0.04
	3	2116.98597	2116.98550	-0.22
z56+IrC21H23N	6	1139.18635	1139.18623	-0.11
z57	4	1624.75840	1624.75855	0.09
z58	4	1649.52550	1649.52582	0.19
z59	5	1351.04208	1351.04240	0.24
	4	1688.55078	1688.55079	0.01
z59+IrC21H23N	7	1034.05183	1034.05193	0.10
z60	5	1380.45576	1380.45574	-0.01
	4	1725.31788	1725.31720	-0.39
z62	5	1420.47170	1420.47170	0.00
	4	1775.33781	1775.33732	-0.28
z62+IrC21H23N	7	1083.64442	1083.64438	-0.04
z63	6	1210.07838	1210.07803	-0.29
z63+IrC21H23N	8	967.82741	967.82712	-0.30
z65	7	1071.80012	1071.80019	0.07
	6	1250.43282	1250.43330	0.38
	5	1500.11726	1500.11747	0.14
z65+IrC21H23N	8	998.09324	998.09281	-0.43
z66	7	1090.23478	1090.23419	-0.54
	6	1271.77269	1271.77252	-0.13
	5	1525.92578	1525.92560	-0.12
z66+IrC21H23N	7	1158.96875	1158.96859	-0.14
	8	1014.22357	1014.22360	0.03
z67	6	1293.44702	1293.44621	-0.63
	5	1551.93497	1551.93496	-0.01

z67+IrC21H23N	8	1030.47938	1030.47972	0.33
z68	6	1307.95236	1307.95186	-0.38
	5	1569.34137	1569.34104	-0.21
z68+IrC21H23N	8	1041.35838	1041.35882	0.42
z69	7	1137.67834	1137.67798	-0.32
	6	1327.12352	1327.12369	0.13
	5	1592.34676	1592.34622	-0.34
z69+IrC21H23N	8	1055.61126	1055.61132	0.06
z70	6	1343.96479	1343.96456	-0.17
z71	6	1363.13595	1363.13559	-0.26
	5	1635.56169	1635.56100	-0.42
z72	6	1384.48511	1384.48586	0.54
z72+IrC21H23N	9	976.78565	976.78582	0.17
z73	6	1406.32519	1406.32547	0.20
z73+IrC21H23N	9	991.34571	991.34568	-0.03
z74	7	1223.86477	1223.86360	-0.96
	6	1427.67435	1427.67351	-0.59
z74+IrC21H23N	9	1005.57848	1005.57862	0.14
z76	7	1256.31309	1256.31331	0.18
z78	8	1132.28540	1132.28626	0.76
	7	1293.89657	1293.89673	0.12
z78+IrC21H23N	10	954.04322	954.04287	-0.37
z81	8	1177.43575	1177.43542	-0.28
	7	1345.49659	1345.49683	0.18
z81+IrC21H23N	10	990.26363	990.26290	-0.74
z82	8	1193.44033	1193.44040	0.06
z92	8	1316.99447	1316.99383	-0.49
z99	8	1419.16138	1419.16019	-0.84
z107	10	1223.77139	1223.77171	0.26
	9	1359.74553	1359.74573	0.15
IrC21H23N	1	*480.14309	480.14311	0.04
IrC21H23N+H	1	481.15092	481.15094	0.04
			Mean (ppm)	-0.06
			St. Dv. (ppm)	0.40

Table D2. ECD fragments of the $[CaM(127\text{-}148)+IrC_{21}H_{23}N+2H]^{3+}$ ions for Figure D6, * indicates the masses used for internal calibration.

Assignments	charge	Theo. m/z	Exp. m/z	Error (ppm)
c6	1	618.27295	618.27296	0.02
c12	1	1294.55460	1294.55644	1.42
c13	1	1423.59719	1423.59807	0.62
c16	1	1798.77661	1798.77970	1.72
c17	1	1926.83519	1926.83197	-1.67
c18	1	2057.87568	2057.87222	-1.68
c18+IrC21H23N	1	2541.02502	2541.02089	-1.63
c19+IrC21H23N	1	2670.04985	2670.04945	-0.15
c20	1	2289.96384	2289.95793	-2.58
c20+IrC21H23N	2	1386.05240	1386.05242	0.01
c20+IrC21H23N	1	2771.09753	2771.10160	1.47
c21	1	2361.00095	2360.99924	-0.72
c21+IrC21H23N	2	1422.07487	1422.07524	0.26
z3	1	*303.17887	303.17886	-0.03
z4	1	*434.21936	434.21937	0.02
z4+IrC21H23N	1	914.36300	914.36313	0.14
z5	1	*565.25984	565.25982	-0.04
z5+IrC21H23N	1	1047.40582	1047.40628	0.44
z6	1	*639.31842	639.31858	0.25
z6+IrC21H23N	1	1175.46439	1175.46417	-0.19
z7	1	792.38683	792.38631	-0.66
z8	1	939.45525	939.45581	0.60
z9	1	*1068.49784	1068.49821	0.35
z9+IrC21H23N	1	1550.64382	1550.64519	0.88
z10	1	*1197.54043	1197.53985	-0.48
z10+IrC21H23N	1	1679.68641	1679.68677	0.21
z11	1	*1360.60376	1360.60408	0.24
z11+IrC21H23N	1	1842.74974	1842.74704	-1.47
z12	1	*1475.65451	1475.65444	-0.05
z12+IrC21H23N	1	1956.79267	1956.79212	-0.28
z13	1	1573.71510	1573.71377	-0.85
z13+IrC21H23N	1	2055.86108	2055.86100	-0.04
z14	1	*1701.77368	1701.77315	-0.31
z14+IrC21H23N	1	2183.91965	2183.92157	0.88
	2	1091.95955	1091.96097	1.30
z15	1	1758.79514	1758.79099	-2.36
z15+IrC21H23N	1	2240.94112	2240.94035	-0.34
z16	1	1873.82209	1873.82355	0.78
z16+IrC21H23N	1	2355.96806	2355.96985	0.76
	2	1178.48544	1178.48729	1.57
z17	1	1930.84355	1930.84966	3.16

z17+IrC21H23N	1	2413.99289	2413.98622	-2.76
z18	1	*2045.87049	2045.86889	-0.78
z18+IrC21H23N	1	2528.01647	2528.01659	0.05
	2	1264.50964	1264.51138	1.38
z19	1	2158.95456	2158.95107	-1.62
z19+IrC21H23N	1	2642.10390	2642.10757	1.39
	2	1321.05167	1321.05253	0.65
z20	1	*2273.98150	2273.97956	-0.85
z20+IrC21H23N	1	2757.13084	2757.13095	0.04
	2	1378.56515	1378.56621	0.77
z21	1	2345.01861	2345.02772	3.88
z21+IrC21H23N	1	2828.16796	2828.16161	-2.25
	2	1414.08370	1414.08482	0.79
IrC21H23N	1	*480.14309	480.14318	0.19
IrC21H23N+H	1	481.15092	481.15098	0.12
IrC21H23N+SCH3	1	527.13864	527.13874	0.19
IrC21H23N+SCH3+H	1	528.14646	528.14548	-1.86
			Mean (ppm)	0.04
			St. Dv. (ppm)	1.26

Table D3. ECD fragments of the $[CaM(107\text{-}126)+IrC_{21}H_{23}N+3H]^{4+}$ ions for Figure D7, * indicates the masses used for internal calibration.

Assignments	charge	Theo. m/z	Exp. m/z	Error (ppm)
c2	1	*254.16115	254.16111	-0.16
c3	1	*385.20164	385.20158	-0.16
c4	1	*486.24931	486.24927	-0.08
c5	1	*600.29224	600.29227	0.05
c6	1	713.37631	713.37668	0.52
c7	1	770.39777	770.39813	0.47
c8	1	899.44036	899.44105	0.77
c8+IrC21H23N	1	1380.57857	1380.57768	-0.64
c9	1	1069.58228	1069.58266	0.36
	2	535.29478	535.29473	-0.09
c10	1	1182.66634	1182.66689	-0.47
c11	1	*1283.71402	1283.71384	-0.14
c13	1	*1527.78355	1527.78329	-0.17
	2	764.39542	764.39560	0.24
c14	1	1656.82615	1656.82774	0.96
	2	828.91671	828.91646	-0.30
c15	1	1755.89456	1755.89341	-0.65
c16	1	*1870.92150	1870.92256	0.57
	2	935.96439	935.96503	0.68
c16+IrC21H23N	2	1176.53346	1176.53183	-1.39
c17	1	1999.96410	1999.96637	1.14
	2	1000.48569	1000.48632	0.63
c17+IrC21H23N	2	1241.55648	1241.55556	-0.74
c18	1	2131.00458	2131.00812	1.66
c18+IrC21H23N	2	1307.07672	1307.07766	0.72
c19	1	*2244.08865	2244.08603	-1.17
c19+IrC21H23N	2	1363.61876	1363.61632	-1.79
z2	1	*272.18429	272.18432	0.11
z3	1	*403.22478	403.22473	-0.12
z4	1	*532.26737	532.26734	-0.06
z5	1	*647.29431	647.29433	0.03
z6	1	*746.36273	746.36282	0.12
z7	1	*875.40532	875.40541	0.10
z7+IrC21H23N	2	678.77538	678.77532	-0.09
z8	1	1004.44791	1004.44827	0.36
z8+IrC21H23N	2	743.29667	743.29657	-0.13
z9	1	1119.47486	1119.47434	-0.46
z9+IrC21H23N	2	800.81015	800.80995	-0.25
z10	1	1220.52253	1220.52290	0.30
z11	1	1333.60660	1333.60701	0.31
z11+IrC21H23N	2	907.87601	907.87649	0.53

z12	1	*1503.74851	1503.74877	0.17
	2	752.37789	752.37763	-0.35
z12+IrC21H23N	1	662.30040	662.30149	1.65
z12+IrC21H23N	2	993.45088	993.45070	-0.18
z13	1	*1632.79110	1632.79090	-0.12
	2	816.89919	816.89847	-0.88
z13+IrC21H23N	2	1057.97217	1057.97200	-0.16
z14	1	1689.81257	1689.81327	0.41
z14+IrC21H23N	2	1086.48291	1086.48339	0.44
z15	1	1802.89663	1802.89876	1.18
z16	1	1916.93956	1916.93680	-1.44
	2	950.97342	950.97415	0.77
z16+IrC21H23N	2	1200.04421	1200.04346	-0.62
z17	1	*2017.98724	2017.98522	-1.00
z18	1	2150.03108	2150.02824	-1.32
z18+IrC21H23N	2	1316.09312	1316.08829	-3.67
z19	1	1124.55171	1124.55135	-0.32
z19+IrC21H23N	4	683.06403	683.06475	1.05
IrC21H23N	1	*480.14309	480.14307	-0.04
IrC21H23N+H	1	481.15092	481.15088	-0.08
IrC21H23N+SCH3	1	527.13864	527.13910	0.87
IrC21H23N+SCH3+H	1	528.14646	528.14587	-1.12
			Mean (ppm)	-0.05
			St. Dv. (ppm)	0.86

Table D4. ECD fragments of the [CaM(38-74)+Ir$C_{21}H_{23}N$+3H]$^{4+}$ ions for Figure D8, * indicates the masses used for internal calibration.

Assignments	charge	Theo. m/z	Exp. m/z	Error (ppm)
c2	1	*218.14992	218.14992	0.00
c3	1	275.17138	275.17144	0.22
c4	1	403.22996	403.22987	-0.22
c6	1	*614.32565	614.32569	0.07
c7	1	*715.37333	715.37346	0.18
c8	1	844.41592	844.41619	0.32
c9	1	915.45304	915.45210	-1.03
c10	1	*1044.49563	1044.49576	0.12
c11	1	1157.57969	1157.57742	-1.96
c12	1	1285.63827	1285.63689	-1.07
c15	1	1644.78976	1644.78658	-1.93
c16	1	1758.83269	1758.82961	-1.75
c20	1	2173.00775	2172.99896	-4.05
c22	1	2346.05616	2346.05355	-1.11
	2	1173.03172	1173.03347	1.49
c22+IrC21H23N	2	1413.59861	1413.60006	1.03
c23	1	2459.09909	2459.09272	-2.59
c23+IrC21H23N	2	1471.12399	1471.12816	2.83
c24	1	2516.12055	2516.11483	-2.27
c26	1	2730.25229	2730.24551	-2.48
c26+IrC21H23N	1	3212.39391	3212.38637	-2.35
	2	1606.70054	1606.70027	-0.17
c27+IrC21H23N	1	3327.42075	3327.42400	0.98
	2	1644.21401	1644.21346	-0.33
c29+IrC21H23N	2	1786.27460	1786.27666	1.15
c30	1	*3219.44637	3219.44402	-0.73
c30+IrC21H23N	2	1850.79590	1850.79410	-0.97
c31+IrC21H23N	2	1924.33011	1924.33190	0.93
c32+IrC21H23N	2	1980.87214	1980.87117	-0.49
c33	1	3580.64653	3580.63452	-3.35
c33+IrC21H23N	2	2031.39598	2031.39551	-0.23
c34+IrC21H23N	2	2096.91622	2096.91407	-1.03
c35+IrC21H23N	2	2162.43646	2162.43444	-0.93
c36	1	3913.76461	3913.76693	0.59
c36+IrC21H23N	2	2197.95502	2197.95275	-1.03
z2	1	*230.13734	230.13736	0.09
z3	1	*361.17783	361.17779	-0.11
z4	1	*492.21831	492.21822	-0.18
z5	1	*593.26599	593.26615	0.27
z6	1	706.35005	706.35056	0.72
z7	1	853.41847	853.41913	0.77

z8	1	*982.46106	982.46143	0.38
z10	1	1226.58224	1226.58111	-0.92
z11	1	1342.61701	1342.61839	1.03
z11+IrC21H23N	2	912.38122	912.38477	3.89
z12+IrC21H23N	2	968.41934	968.42247	3.23
z13	1	*1156.74875	1156.74974	0.86
z13+IrC21H23N	3	1019.44709	1019.44799	0.88
z14	1	1612.76239	1612.75497	-4.60
z14+IrC21H23N	2	1047.95559	1047.95775	2.06
z15	1	1727.81314	1727.81512	1.15
z15+IrC21H23N	2	1104.97705	1104.97913	1.88
z17	1	1899.86155	1899.86621	2.45
z17+IrC21H23N	2	1191.00349	1191.00826	4.01
z25+IrC21H23N	2	1634.68600	1634.68374	-1.38
z27+IrC21H23N	2	1755.25732	1755.25353	-2.16
z28+IrC21H23N	2	1819.77862	1819.77917	0.30
z29+IrC21H23N	2	1855.29717	1855.29276	-2.38
z30+IrC21H23N	2	1919.81847	1919.81382	-2.42
z31+IrC21H23N	2	1970.34231	1970.33989	-1.23
z33	1	*3670.64271	3670.64638	1.00
z33+IrC21H23N	2	2076.39407	2076.38820	-2.83
z34+IrC21H23N	2	2139.91944	2139.91543	-1.87
z35+IrC21H23N	2	2168.43018	2168.43742	3.34
z36+IrC21H23N	3	1483.65056	1483.64853	-1.37
	2	2224.97221	2224.97716	2.22
IrC21H23N	1	*480.14309	480.14302	-0.15
IrC21H23N+H	1	481.15092	481.15087	-0.10
IrC21H23N+SCH3	1	527.13864	527.13862	-0.04
IrC21H23N+SCH3+H	1	528.14646	528.14582	-1.21
			Mean (ppm)	-0.21
			St. Dv. (ppm)	1.82

Curriculum Vitae

Yulin Qi

Email: yulin.qi@warwick.ac.uk

Education:

Ph.D. Chemistry

University of Warwick, Department of Chemistry, Coventry, United Kingdom

Nov/2010-July/2013

Thesis title: Advanced Methods in Fourier Transform Ion Cyclotron Resonance Mass Spectrometry

Supervisor: Professor Peter B. O'Connor

M.Sc. Pharmaceutical Analysis

University of Warwick, Department of Chemistry, Coventry, United Kingdom

Oct/2009-Sep/2010

Thesis title: Phase Correction of Fourier Transform Ion Cyclotron Resonance Mass Spectra using MatLab

Supervisor: Professor Peter B. O'Connor

B.Sc. Pharmacy

Shanghai University of Traditional Chinese Medicine, Shanghai, China

Sep/2005-June/2009

Publications:

1. **Qi, Y.**; Thompson, C.; Van Orden, S.; O'Connor, P., Phase Correction of Fourier Transform Ion Cyclotron Resonance Mass Spectra Using MatLab. *J. Am. Soc. Mass Spectrom.* **2011,** *22* (1), 138-147. link
2. **Qi, Y.**; Barrow, M. P.; Van Orden, S. L.; Thompson, C. J.; Li, H.; Perez-Hurtado, P.; O'Connor, P. B., Variation of the Fourier Transform Mass Spectra Phase Function with Experimental Parameters. *Anal. Chem.* **2011,** *83* (22), 8477-8483. link
3. **Qi, Y.**; Barrow, M. P.; Li, H.; Meier, J. E.; Van Orden, S. L.; Thompson, C. J.; O'Connor, P. B., Absorption-Mode: The Next Generation of Fourier Transform Mass Spectra. *Anal. Chem.* **2012,** *84* (6), 2923-2929. link
4. **Qi, Y.**; Witt, M.; Jertz, R.; Baykut, G.; Barrow, M. P.; Nikolaev, E. N.; O'Connor, P. B., Absorption-Mode Spectra on the Dynamically Harmonized Fourier Transform Ion Cyclotron Resonance Cell. *Rapid Commun. Mass Spectrom.* **2012,** *26* (17), 2021-2026. link
5. **Qi, Y.**; Li, H.; Wills, R. H.; Perez-Hurtado, P.; Yu, X.; Kilgour, D. P. A.; Barrow, M. P.; Lin, C.; O'Connor, P. B., Absorption-Mode Fourier Transform Mass Spectrometry: the Effects of Apodization and Phasing on Modified Protein Spectra. *J. Am. Soc. Mass Spectrom.* **2013,** *24* (6), 828-834. link
6. **Qi, Y.**; Liu, Z.; Li, H.; Sadler, P. J.; O'Connor, P. B., Mapping the Protein-Binding Sites for Novel Iridium(III) Anticancer Complexes Using Electron Capture Dissociation. *Rapid Commun. Mass Spectrom.* **Acceptd**.
7. **Qi, Y.**; O'Connor, P. B., Data Processing in Fourier Transform Ion Cyclotron Resonance Mass Spectrometry. **Submitted**.

8. Kilgour, D. P. A.; Wills, R. H.; **Qi, Y.**; O'Connor, P. B., Autophaser: An Algorithm for Automated Generation of Absorption Mode Spectra for FT-ICR MS. *Anal. Chem.* **2013,** *85* (8), 3909-3911. link
9. Li, H.; Lin, T.-Y.; Van Orden, S. L.; Zhao, Y.; Barrow, M. P.; Pizarro, A. M.; **Qi, Y.**; Sadler, P. J.; O'Connor, P. B., Use of Top-Down and Bottom-Up Fourier Transform Ion Cyclotron Resonance Mass Spectrometry for Mapping Calmodulin Sites Modified by Platinum Anticancer Drugs. *Anal. Chem.* **2011,** *83* (24), 9507-9515. link

10. Li, H.; Zhao, Y.; Phillips, H. I. A.; **Qi, Y.**; Lin, T.-Y.; Sadler, P. J.; O'Connor, P. B., Mass Spectrometry Evidence for Cisplatin As a Protein Cross-Linking Reagent. *Anal. Chem.* **2011,** *83* (13), 5369-5376. link
11. Jia, J.-Y.; Zhang, M.-Q.; Liu, Y.-M.; Liu, Y.; Liu, G.-Y.; Li, S.-J.; Lu, C.; Weng, L.-p.; **Qi, Y.-L.**; Yu, C., Pharmacokinetics and bioequivalence evaluation of two losartan potassium 50-mg tablets: A single-dose, randomized-sequence, open-label, two-way crossover study in healthy Chinese male volunteers. *Clin. Ther.* **2010,** *32* (7), 1387-1395. link

Presentations:

1. **Qi, Y.**; Van Orden, S. L.; Thompson, C. J.; O'Connor, P. B., Absorption-Mode Fourier Transform Mass Spectrometry: Advantages for Protein and Petroleum Spectra. **2012 BMSS Conference.** Alderley Park, United Kingdom. Apr. 16-18, 2012.
2. **Qi, Y.**; Barrow, M. P.; Meier, J. E.; Van Orden, S. L.; Thompson, C. J.; O'Connor, P. B., Absorption-Mode Fourier Transform Mass Spectrometry: Advantages for Spectra of Modified Proteins. **10th European Fourier Transform Mass Spectrometry Workshop.** Coventry, United Kingdom. Apr. 1-5, 2012.
3. **Qi, Y.**; Van Orden, S. L.; Thompson, C. J.; O'Connor, P. B., Variation of Fourier Transform Mass Spectra Phase Function with Experimental Parameters. **2011 BMSS Conference.** Cardiff, United Kingdom. Sep. 11-14, 2011.
4. **Qi, Y.**; Van Orden, S. L.; O'Connor, P. B., Broadband Phase Correction of FT-ICR Mass Spectra and the Parameters Controlling the Phase Function. **59th ASMS Conference on Mass Spectrometry.** Denver, United States of America, June 5-9, 2011
5. Li, H.; Zhao, Y.; Phillips, H. I.; **Qi, Y.**; Sadler, P. J.; O'Connor, P. B., Mass spectrometry evidence for cisplatin as a cross-linking reagent (Poster). **8th UppCon Conference on Electron Capture and Transfer Dissociation.** Villars-sur-Ollon, Switerland, Feb. 6-10, 2011

Awards:

1. BMSS Travel Award for the 2012 BMSS Conference. Alderley Park, United Kingdom. Apr. 16-18, 2012.
2. BMSS Travel Award for the 2011 BMSS Conference. Cardiff, United Kingdom. Sep. 11-14, 2011.

Bibliography

1. McLafferty, F. W.; Turecek, F., *Interpretation of mass spectra*. 4th edition.; University Science Books: 1993.
2. McLafferty, F. W.; Fridriksson, E. K.; Horn, D. M.; Lewis, M. A.; Zubarev, R. A., Biomolecule Mass Spectrometry. *Science* **1999,** *284* (5418), 1289-1290.
3. Dempster, A. J., A New Method of Positive Ray Analysis. *Physical Review* **1918,** *11* (4), 316-325.
4. Aston, F. W., A Positive Ray Spectrograph. *Phil. Mag. Ser. 6* **1919,** *38*, 707-716.
5. Squires, G., Francis Aston and the Mass Spectrograph. *Journal of the Chemical Society, Dalton Transactions* **1998,** *0* (23), 3893-3900.
6. Moyer, S. C.; Budnik, B. A.; Pittman, J. L.; Costello, C. E.; O'Connor, P. B., Attomole Peptide Analysis by High-Pressure Matrix-Assisted Laser Desorption/Ionization Fourier Transform Mass Spectrometry. *Anal. Chem.* **2003,** *75* (23), 6449-6454.
7. Nikolaev, E. N.; Jertz, R.; Grigoryev, A.; Baykut, G., Fine Structure in Isotopic Peak Distributions Measured Using a Dynamically Harmonized Fourier Transform Ion Cyclotron Resonance Cell at 7 T. *Anal. Chem.* **2012,** *84* (5), 2275-2283.
8. Fenn, J. B.; Mann, M.; Meng, C. K.; Wong, S. F.; Whitehouse, C. M., Electrospray Ionization–Principles and Practice. *Mass Spectrom. Rev.* **1990,** *9* (1), 37-70.
9. Karas, M.; Bachmann, D.; Hillenkamp, F., Influence of the Wavelength in High-Irradiance Ultraviolet Laser Desorption Mass Spectrometry of Organic Molecules. *Anal. Chem.* **1985,** *57* (14), 2935-2939.
10. Karas, M.; Bachmann, D.; Bahr, U.; Hillenkamp, F., Matrix-Assisted Ultraviolet Laser Desorption of Non-Volatile Compounds. *Int. J. Mass Spectrom. Ion Processes* **1987,** *78* (0), 53-68.
11. Tanaka, K.; Waki, H.; Ido, Y.; Akita, S.; Yoshida, Y.; Yoshida, T.; Matsuo, T., Protein and Polymer Analyses up to m/z 100 000 by Laser Ionization Time-Of-Flight Mass Spectrometry. *Rapid Commun. Mass Spectrom.* **1988,** *2* (8), 151-153.

12. Fenn, J. B.; Mann, M.; Meng, C. K.; Wong, S. F.; Whitehouse, C. M., Electrospray Ionization for Mass Spectrometry of Large Biomolecules. *Science* **1989,** *246* (4926), 64-71.
13. Schier, G. M.; Halpern, B.; Milne, G. W. A., Characterization of Dipeptides by Electron Impact and Chemical Ionization Mass Spectrometry. *Biol. Mass Spectrom.* **1974,** *1* (4), 212-218.
14. Munson, M. S. B.; Field, F. H., Chemical Ionization Mass Spectrometry. I. General Introduction. *J. Am. Chem. Soc.* **1966,** *88* (12), 2621-2630.
15. Ghaderi, S.; Kulkarni, P. S.; Ledford, E. B.; Wilkins, C. L.; Gross, M. L., Chemical Ionization in Fourier Transform Mass Spectrometry. *Anal. Chem.* **1981,** *53* (3), 428-437.
16. Karas, M.; Hillenkamp, F., Laser Desorption Ionization of Proteins with Molecular Masses Exceeding 10,000 Daltons. *Anal. Chem.* **1988,** *60* (20), 2299-2301.
17. Dettmer, K.; Aronov, P. A.; Hammock, B. D., Mass Spectrometry-Based Metabolomics. *Mass Spectrom. Rev.* **2007,** *26* (1), 51-78.
18. Zhao, Y.; Kent, S. B. H.; Chait, B. T., Rapid, Sensitive Structure Analysis of Oligosaccharides. *Proceedings of the National Academy of Sciences* **1997,** *94* (5), 1629-1633.
19. Jurinke, C.; Oeth, P.; Boom, D., MALDI-TOF Mass Spectrometry. *Mol. Biotechnol.* **2004,** *26* (2), 147-163.
20. Kirpekar, F.; Nordhoff, E.; Larsen, L. K.; Kristiansen, K.; Roepstorff, P.; Hillenkamp, F., DNA Sequence Analysis by MALDI Mass Spectrometry. *Nucleic Acids Res.* **1998,** *26* (11), 2554-2559.
21. Zenobi, R.; Knochenmuss, R., Ion Formation in MALDI Mass Spectrometry. *Mass Spectrom. Rev.* **1998,** *17* (5), 337-366.
22. Karas, M.; Krüger, R., Ion Formation in MALDI: The Cluster Ionization Mechanism. *Chem. Rev.* **2003,** *103* (2), 427-440.
23. Caldwell, R. L.; Caprioli, R. M., Tissue Profiling by Mass Spectrometry: A Review of Methodology and Applications. *Mol. Cell. Proteomics* **2005,** *4* (4), 394-401.
24. McDonnell, L. A.; Heeren, R. M. A., Imaging Mass Spectrometry. *Mass Spectrom. Rev.* **2007,** *26* (4), 606-643.

25. Whitehouse, C. M.; Dreyer, R. N.; Yamashita, M.; Fenn, J. B., Electrospray Interface for Liquid Chromatographs and Mass Spectrometers. *Anal. Chem.* **1985,** *57* (3), 675-679.
26. Bruins, A. P.; Covey, T. R.; Henion, J. D., Ion Spray Interface for Combined Liquid Chromatography/atmospheric Pressure Ionization Mass Spectrometry. *Anal. Chem.* **1987,** *59* (22), 2642-2646.
27. Chowdhury, S. K.; Katta, V.; Chait, B. T., An Electrospray-Ionization Mass Spectrometer with New Features. *Rapid Commun. Mass Spectrom.* **1990,** *4* (3), 81-87.
28. Nielen, M. W. F.; Buijtenhuijs, F. A., Polymer Analysis by Liquid Chromatography/Electrospray Ionization Time-of-Flight Mass Spectrometry. *Anal. Chem.* **1999,** *71* (9), 1809-1814.
29. Colton, R.; Traeger, J. C., The Application of Electrospray Mass Spectrometry to Ionic Inorganic and Organometallic Systems. *Inorg. Chim. Acta* **1992,** *201* (2), 153-155.
30. Loo, J. A., Electrospray Ionization Mass Spectrometry: a Technology for Studying Noncovalent Macromolecular Complexes. *Int. J. Mass Spectrom.* **2000,** *200* (1–3), 175-186.
31. Brenton, A.; Godfrey, A., Accurate Mass Measurement: Terminology and Treatment of Data. *J. Am. Soc. Mass Spectrom.* **2010,** *21* (11), 1821-1835.
32. Barrow, M. P.; Burkitt, W. I.; Derrick, P. J., Principles of Fourier Transform Ion Cyclotron Resonance Mass Spectrometry and its Application in Structural Biology. *Analyst* **2005,** *130* (1), 18-28.
33. Aebersold, R., A Mass Spectrometric Journey into Protein and Proteome Research. *J. Am. Soc. Mass Spectrom.* **2003,** *14* (7), 685-695.
34. Biemann, K., The Coming of Age of Mass Spectrometry in Peptide and Protein Chemistry. *Protein Sci.* **1995,** *4* (9), 1920-1927.
35. Rodgers, R. P.; McKenna, A. M., Petroleum Analysis. *Anal. Chem.* **2011,** *83* (12), 4665-4687.
36. March, R. E.; Todd, J. F. J., *Quadrupole Ion Trap Mass Spectrometry*. 2nd ed.; Wiley: New York ; Chichester, 2005.
37. Hoffmann, E. d.; Stroobant, V., *Mass spectrometry : Principles and Applications*. 3rd ed.; Wiley ; Chichester : John Wiley: Hoboken, N.J., 2007.

38. Stafford Jr, G. C.; Kelley, P. E.; Syka, J. E. P.; Reynolds, W. E.; Todd, J. F. J., Recent Improvements in and Analytical Applications of Advanced Ion Trap Technology. *Int. J. Mass Spectrom. Ion Processes* **1984,** *60* (1), 85-98.
39. March, R. E., Quadrupole Ion Traps. *Mass Spectrom. Rev.* **2009,** *28* (6), 961-989.
40. Guilhaus, M., Special Feature: Tutorial. Principles and Instrumentation in Time-Of-Flight Mass Spectrometry. Physical and Instrumental Concepts. *J. Mass Spectrom.* **1995,** *30* (11), 1519-1532.
41. Weickhardt, C.; Moritz, F.; Grotemeyer, J., Time-of-Flight Mass Spectrometry: State-of-the-Art in Chemical Analysis and Molecular Science. *Mass Spectrom. Rev.* **1996,** *15* (3), 139-162.
42. Comisarow, M. B.; Marshall, A. G., Frequency-Sweep Fourier Transform Ion Cyclotron Resonance Spectroscopy. *Chem. Phys. Lett.* **1974,** *26* (4), 489-490.
43. Comisarow, M. B.; Marshall, A. G., Fourier Transform Ion Cyclotron Resonance Spectroscopy. *Chem. Phys. Lett.* **1974,** *25*, 282-283.
44. Amster, I. J., Fourier Transform Mass Spectrometry. *J. Mass Spectrom.* **1996,** *31* (12), 1325-1337.
45. Marshall, A. G.; Hendrickson, C. L.; Jackson, G. S., Fourier Transform Ion Cyclotron Resonance Mass Spectrometry - A Primer. *Mass Spectrom. Rev.* **1998,** *17* (1), 1-35.
46. Nikolaev, E.; Boldin, I.; Jertz, R.; Baykut, G., Initial Experimental Characterization of a New Ultra-High Resolution FTICR Cell with Dynamic Harmonization. *J. Am. Soc. Mass Spectrom.* **2011,** *22* (7), 1125-1133.
47. Wang, Y.; Shi, S. D. H.; Hendrickson, C. L.; Marshall, A. G., Mass-Selective Ion Accumulation and Fragmentation in a Linear Octopole Ion Trap External to a Fourier Transform Ion Cyclotron Resonance Mass Spectrometer. *Int. J. Mass Spectrom.* **2000,** *198* (1–2), 113-120.
48. Syka, J. E. P.; Marto, J. A.; Bai, D. L.; Horning, S.; Senko, M. W.; Schwartz, J. C.; Ueberheide, B.; Garcia, B.; Busby, S.; Muratore, T.; Shabanowitz, J.; Hunt, D. F., Novel Linear Quadrupole Ion Trap/FT Mass Spectrometer: Performance Characterization and Use in the Comparative Analysis of Histone H3 Post-translational Modifications. *J. Proteome Res.* **2004,** *3* (3), 621-626.

49. Gauthier, J. W.; Trautman, T. R.; Jacobson, D. B., Sustained Off-Resonance Irradiation for Collision-Activated Dissociation Involving Fourier Transform Mass Spectrometry. Collision-Activated Dissociation Technique that Emulates Infrared Multiphoton Dissociation. *Anal. Chim. Acta* **1991,** *246* (1), 211-225.
50. Little, D. P.; Speir, J. P.; Senko, M. W.; O'Connor, P. B.; McLafferty, F. W., Infrared Multiphoton Dissociation of Large Multiply Charged Ions for Biomolecule Sequencing. *Anal. Chem.* **1994,** *66* (18), 2809-2815.
51. Zubarev, R. A.; Kelleher, N. L.; McLafferty, F. W., Electron Capture Dissociation of Multiply Charged Protein Cations - a Nonergodic Process. *J. Am. Chem. Soc.* **1998,** *120* (13), 3265-3266.
52. Marshall, A. G.; Schweikhard, L., Fourier Transform Ion Cyclotron Resonance Mass Spectrometry: Technique Developments. *Int. J. Mass Spectrom. Ion Processes* **1992,** *118–119* (0), 37-70.
53. Holliman, C. L.; Rempel, D. L.; Gross, M. L., Detection of High Mass-to-Charge Ions by Fourier Transform Mass Spectrometry. *Mass Spectrom. Rev.* **1994,** *13* (2), 105-132.
54. Sheng, L.-S.; Shew Sanford, L.; Winger Brian, E.; Campana Joseph, E., A New Generation of Mass Spectrometry for Characterizing Polymers and Related Materials. In *Hyphenated Techniques in Polymer Characterization*, American Chemical Society: 1994; Vol. 581, pp 55-72.
55. Marshall, A. G., Ion Cyclotron Resonance and Nuclear Magnetic Resonance Spectroscopies: Magnetic Partners for Elucidation of Molecular Structure and Reactivity. *Acc. Chem. Res.* **1996,** *29* (7), 307-316.
56. Senko, M. W.; Hendrickson, C. L.; Emmett, M. R.; Shi, S. D. H.; Marshall, A. G., External Accumulation of Ions for Enhanced Electrospray Ionization Fourier Transform Ion Cyclotron Resonance Mass Spectrometry. *J. Am. Soc. Mass Spectrom.* **1997,** *8* (9), 970-976.
57. Lebrilla, C. B.; Amster, I. J.; McIver Jr, R. T., External Ion Source FTMS Instrument for Analysis of High Mass Ions. *Int. J. Mass Spectrom. Ion Processes* **1989,** *87* (1), R7-R13.
58. Beu, S. C.; Laude, D. A., Elimination of Axial Ejection during Excitation with a Capacitively Coupled Open Trapped-Ion Cell for Fourier Transform Ion Cyclotron Resonance Mass Spectrometry. *Anal. Chem.* **1992,** *64* (2), 177-180.

59. Caravatti, P.; Allemann, M., The 'Infinity Cell': A New Trapped-Ion Cell with Radiofrequency Covered Trapping Electrodes for Fourier Transform Ion Cyclotron Resonance Mass Spectrometry. *Org. Mass Spectrom.* **1991,** *26* (5), 514-518.
60. Brown, L. S.; Gabrielse, G., Geonium theory: Physics of a Single Electron or Ion in a Penning Trap. *Reviews of Modern Physics* **1986,** *58* (1), 233-311.
61. Dehmelt, H., Experiments with an Isolated Subatomic Particle at Rest. *Reviews of Modern Physics* **1990,** *62* (3), 525-530.
62. van Agthoven, M. A.; Delsuc, M.-A.; Rolando, C., Two-Dimensional FT-ICR/MS with IRMPD as Fragmentation Mode. *Int. J. Mass Spectrom.* **2011,** *306* (2–3), 196-203.
63. van Agthoven, M. A.; Chiron, L.; Coutouly, M.-A.; Delsuc, M.-A.; Rolando, C., Two-Dimensional ECD FT-ICR Mass Spectrometry of Peptides and Glycopeptides. *Anal. Chem.* **2012,** *84* (13), 5589-5595.
64. Anders, L. R.; Beauchamp, J. L.; Dunbar, R. C.; Baldeschwieler, J. D., Ion-Cyclotron Double Resonance. *The Journal of Chemical Physics* **1966,** *45* (3), 1062-1063.
65. Lin, C.; Cournoyer, J.; O'Connor, P., Use of a Double Resonance Electron Capture Dissociation Experiment to Probe Fragment Intermediate Lifetimes. *J. Am. Soc. Mass Spectrom.* **2006,** *17* (11), 1605-1615.
66. Marshall, A. G.; Roe, D. C., Theory of Fourier Transform Ion Cyclotron Resonance Mass Spectroscopy: Response to Frequency-Sweep Excitation. *The Journal of Chemical Physics* **1980,** *73* (4), 1581-1590.
67. Hofstadler, S. A.; Laude Jr, D. A., Trapping and Detection of Ions Generated in a High Magnetic Field Electrospray Ionization Fourier Transform Ion Cyclotron Resonance Mass Spectrometer. *J. Am. Soc. Mass Spectrom.* **1992,** *3* (6), 615-623.
68. Qi, Y.; Thompson, C.; Van Orden, S.; O'Connor, P., Phase Correction of Fourier Transform Ion Cyclotron Resonance Mass Spectra Using MatLab. *J. Am. Soc. Mass Spectrom.* **2011,** *22* (1), 138-147.
69. Comisarow, M. B., Signal Modeling for Ion Cyclotron Resonance. *J. Chem. Phys.* **1978,** *69*, 4097-4104.

70. Cody, R. B.; Kinsinger, J. A., Making Use of Information Contained in Folded-Back Peaks to Identify Low Mass Ions in Fourier Transform Mass Spectrometry. *Anal. Chem.* **1986,** *58* (3), 670-671.
71. Marshall, A. G.; Verdun, F. R., *Fourier Transforms in NMR, Optical, and Mass Spectrometry: A User's Handbook*. Elsevier: Amsterdam, 1990; p 460.
72. Bristow, A. W. T., Accurate Mass Measurement for the Determination of Elemental Formula—A Tutorial. *Mass Spectrom. Rev.* **2006,** *25* (1), 99-111.
73. Kaiser, N. K.; Savory, J. J.; McKenna, A. M.; Quinn, J. P.; Hendrickson, C. L.; Marshall, A. G., Electrically Compensated Fourier Transform Ion Cyclotron Resonance Cell for Complex Mixture Mass Analysis. *Anal. Chem.* **2011,** *83* (17), 6907-6910.
74. Shi, S. D.-H.; Hendrickson, C. L.; Marshall, A. G., Counting Individual Sulfur Atoms in a Protein by Ultrahighresolution Fourier Transform Ion Cyclotron Resonance Mass Spectrometry: Experimental Resolution of Isotopic Fine Structure in Proteins. *Proceedings of the National Academy of Sciences* **1998,** *95* (20), 11532-11537.
75. Qi, Y.; Witt, M.; Jertz, R.; Baykut, G.; Barrow, M. P.; Nikolaev, E. N.; O'Connor, P. B., Absorption-Mode Spectra on the Dynamically Harmonized Fourier Transform Ion Cyclotron Resonance Cell. *Rapid Commun. Mass Spectrom.* **2012,** *26* (17), 2021-2026.
76. Marshall, A. G.; Hendrickson, C. L.; Shi, S. D. H., Peer Reviewed: Scaling MS Plateaus with High-Resolution FT-ICRMS. *Anal. Chem.* **2002,** *74* (9), 252 A-259 A.
77. Schaub, T. M.; Hendrickson, C. L.; Horning, S.; Quinn, J. P.; Senko, M. W.; Marshall, A. G., High-Performance Mass Spectrometry: Fourier Transform Ion Cyclotron Resonance at 14.5 Tesla. *Anal. Chem.* **2008,** *80* (11), 3985-3990.
78. Hendrickson, C. L.; Hofstadler, S. A.; Beu, S. C.; Laude Jr, D. A., Initiation of Coherent Magnetron Motion Following Ion Injection into a Fourier Transform Ion Cyclotron Resonance Trapped Ion Cell. *Int. J. Mass Spectrom. Ion Processes* **1993,** *123* (1), 49-58.
79. Kaiser, N. K.; Bruce, J. E., Reduction of Ion Magnetron Motion and Space Charge using Radial Electric Field Modulation. *Int. J. Mass Spectrom.* **2007,** *265* (2–3), 271-280.

80. Vladimirov, G.; Hendrickson, C.; Blakney, G.; Marshall, A.; Heeren, R. A.; Nikolaev, E., Fourier Transform Ion Cyclotron Resonance Mass Resolution and Dynamic Range Limits Calculated by Computer Modeling of Ion Cloud Motion. *J. Am. Soc. Mass Spectrom.* **2012,** *23* (2), 375-384.
81. Marshall, A. G., Theoretical Signal-to-Noise Ratio and Mass Resolution in Fourier Transform Ion Cyclotron Resonance Mass Spectrometry. *Anal. Chem.* **1979,** *51*, 1710-1714.
82. Marshall, A. G.; Comisarow, M. B.; Parisod, G., Relaxation and Spectral Line Shape in Fourier Transform Ion Resonance Spectroscopy. *The Journal of Chemical Physics* **1979,** *71* (11), 4434-4444.
83. Qi, Y.; Barrow, M. P.; Van Orden, S. L.; Thompson, C. J.; Li, H.; Perez-Hurtado, P.; O'Connor, P. B., Variation of the Fourier Transform Mass Spectra Phase Function with Experimental Parameters. *Anal. Chem.* **2011,** *83* (22), 8477-8483.
84. Drader, J. J.; Shi, S. D. H.; Blakney, G. T.; Hendrickson, C. L.; Laude, D. A.; Marshall, A. G., Digital Quadrature Heterodyne Detection for High-Resolution Fourier Transform Ion Cyclotron Resonance Mass Spectrometry. *Anal. Chem.* **1999,** *71* (20), 4758-4763.
85. Craig, E. C.; Santos, I.; Marshall, A. G.; Nibbering, N. M. M., Dispersion versus Absorption (DISPA) Method for Automatic Phasing of Fourier Transform Ion Cyclotron Resonance Mass Spectra. *Rapid Commun. Mass Spectrom.* **1987,** *1* (2), 33-37.
86. Ernst, R. R.; Bodenhausen, G.; Wokaun, A., *Principles of Nuclear Magnetic Resonance in One and Two Dimensions*. Oxford University Press: London, 1987; p 610.
87. Comisarow, M. B.; Marshall, A. G., Selective-Phase Ion Cyclotron Resonance Spectroscopy. *Can. J. Chem.* **1974,** *52* (10), 1997-1999.
88. B. Cody, R.; A. Kinsinger, J.; Ghaderi, S.; Amster, I. J.; W. McLafferty, F.; E. Brown, C., Developments in Analytical Fourier-Transform Mass Spectrometry. *Anal. Chim. Acta* **1985,** *178*, 43-66.
89. Qi, Y.; Barrow, M. P.; Li, H.; Meier, J. E.; Van Orden, S. L.; Thompson, C. J.; O'Connor, P. B., Absorption-mode: The Next Generation of Fourier Transform Mass Spectra. *Anal. Chem.* **2012,** *84* (6), 2923-2929.

90. Marshall, A. G.; Hendrickson, C. L., Fourier Transform Ion Cyclotron Resonance Detection: Principles and Experimental Configurations. *Int. J. Mass Spectrom.* **2002,** *215* (1–3), 59-75.
91. Fukushima, E.; Roeder, S. B. W., *Experimental pulse NMR : a nuts and bolts approach*. Addison-Wesley Publishing Co.: Reading, Mass., 1981; p 539p.
92. Derome, A. E., *Modern NMR techniques for chemistry research*. Pergamon: Oxford, 1987.
93. Kilgour, D. P. A.; Wills, R.; Qi, Y.; O'Connor, P. B., Autophaser: An Algorithm for Automated Generation of Absorption Mode Spectra for FT-ICR MS. *Anal. Chem.* **2013,** *85* (8), 3903-3911.
94. Beu, S. C.; Blakney, G. T.; Quinn, J. P.; Hendrickson, C. L.; Marshall, A. G., Broadband Phase Correction of FT-ICR Mass Spectra via Simultaneous Excitation and Detection. *Anal. Chem.* **2004,** *76* (19), 5756-61.
95. Xian, F.; Hendrickson, C. L.; Blakney, G. T.; Beu, S. C.; Marshall, A. G., Automated Broadband Phase Correction of Fourier Transform Ion Cyclotron Resonance Mass Spectra. *Anal. Chem.* **2010,** *82* (21), 8807-8812.
96. Xian, F.; Corilo, Y. E.; Hendrickson, C. L.; Marshall, A. G., Baseline Correction of Absorption-Mode Fourier Fransform Ion Cyclotron Resonance Mass Spectra. *Int. J. Mass Spectrom.* **2012,** *325–327* (0), 67-72.
97. Xiang, X.; Grosshans, P. B.; Marshall, A. G., Image Charge-Induced Ion Cyclotron Orbital Frequency Shift for Orthorhombic and Cylindrical FT-ICR Ion Traps. *Int. J. Mass Spectrom. Ion Processes* **1993,** *125* (1), 33-43.
98. Craig, E. C.; Marshall, A. G., Automated Phase Correction of FT NMR Spectra by Means of Phase Measurement Based on Dispersion versus Absorption Relation (DISPA). *J. Magn. Reson.* **1988,** *76*, 458-475.
99. Bracewell, R. N., *The Fourier transform and its applications*. 3rd ed.; McGraw-Hill: New York, 1999.
100. Marshall, A. G., Convolution Fourier Transform Ion Cyclotron Resonance Spectroscopy. *Chem. Phys. Lett.* **1979,** *63* (3), 515-518.
101. Ledford, E. B.; White, R. L.; Ghaderi, S.; Gross, M. L.; Wilkins, C. L., Convolution-Based Phase Correction in Fourier Transform Mass Spectrometry. *Anal. Chem.* **1980,** *52* (7), 1090-1094.

102. Brenna, J. T.; Creasy, W. R., Experimental Evaluation of Apodization Functions for Quantitative Fourier Transform Mass Spectrometry. *Int. J. Mass Spectrom. Ion Processes* **1989,** *90* (2), 151-166.
103. Lee, J. P.; Comisarow, M. B., Advantageous Apodization Functions for Magnitude-Mode Fourier Transform Spectroscopy. *Appl. Spectrosc.* **1987,** *41* (1), 93-98.
104. Lee, J. P.; Comisarow, M. B., Advantageous Apodization Functions for Absorption-Mode Fourier Transform Spectroscopy. *Appl. Spectrosc.* **1989,** *43* (4), 599-604.
105. Qi, Y.; Li, H.; Wills, R.; Perez-Hurtado, P.; Yu, X.; Kilgour, D. A.; Barrow, M.; Lin, C.; O'Connor, P., Absorption-Mode Fourier Transform Mass Spectrometry: The Effects of Apodization and Phasing on Modified Protein Spectra. *J. Am. Soc. Mass Spectrom.* **2013,** *24* (6), 828-834.
106. Bartholdi, E.; Ernst, R. R., Fourier Spectroscopy and the Causality Principle. *Journal of Magnetic Resonance (1969)* **1973,** *11* (1), 9-19.
107. Cooley, J. W.; Tukey, J. W., An Algorithm for the Machine Calculation of Complex Fourier Series. *Mathematics of computation* **1965**, 297-301.
108. Lee, H.-N.; Marshall, A. G., Theoretical Maximal Precision for Mass-to-Charge Ratio, Amplitude, and Width Measurements in Ion-Counting Mass Analyzers. *Anal. Chem.* **2000,** *72* (10), 2256-2260.
109. Comisarow, M. B.; Lee, J., Phase Distortions In Absorption-Mode Fourier Transform Ion Cyclotron Resonance Spectra. *Anal. Chem.* **1985,** *57* (2), 464-468.
110. Savitski, M. M.; Ivonin, I. A.; Nielsen, M. L.; Zubarev, R. A.; Tsybin, Y. O.; Håkansson, P., Shifted-Basis Technique Improves Accuracy of Peak Position Determination in Fourier Transform Mass Spectrometry. *J. Am. Soc. Mass Spectrom.* **2004,** *15* (4), 457-461.
111. Reinhold, B.; Reinhold, V., Electrospray Ionization Mass Spectrometry: Deconvolution by an Entropy-Based Algorithm. *J. Am. Soc. Mass Spectrom.* **1992,** *3* (3), 207-215.
112. Senko, M. W.; Beu, S. C.; McLafferty, F. W., Determination of Monoisotopic Masses and Ion Populations for Large Biomolecules from Resolved Isotopic Distributions. *J. Am. Soc. Mass Spectrom.* **1995,** *6* (4), 229-233.

113. Zhang, Z.; Marshall, A., A Universal Algorithm for Fast and Automated Charge State Deconvolution of Electrospray Mass-to-Charge Ratio Spectra. *J. Am. Soc. Mass Spectrom.* **1998,** *9* (3), 225-233.
114. Comisarow, M. B.; Melka, J. D., Error Estimates for Finite Zero-Filling in Fourier Transform Spectrometry. *Anal. Chem.* **1979,** *51* (13), 2198-2203.
115. Yarlagadda, R. K. R., *Analog and Digital Signals and Systems*. Springer: New York, 2010.
116. Oppenheim, A. V.; Schafer, R. W., *Discrete-Time Signal Processing*. 3rd ed., International ed.; Pearson Education: Upper Saddle River, N.J. ; Harlow, 2010.
117. Beauchamp, J. L.; Anders, L. R.; Baldeschwieler, J. D., Ion-Molecule Reactions in Chloroethylene by Ion Cyclotron Resonance Spectroscopy. *J. Am. Chem. Soc.* **1967,** *89* (18), 4569-4577.
118. Francl, T. J.; Sherman, M. G.; Hunter, R. L.; Locke, M. J.; Bowers, W. D.; McIver Jr, R. T., Experimental Determination of the Effects of Space Charge on Ion Cyclotron Resonance Frequencies. *Int. J. Mass Spectrom. Ion Processes* **1983,** *54* (1–2), 189-199.
119. Ledford, E. B.; Rempel, D. L.; Gross, M. L., Space Charge Effects in Fourier Transform Mass Spectrometry. II. Mass Calibration. *Anal. Chem.* **1984,** *56* (14), 2744-2748.
120. Shi, S. D. H.; Drader, J. J.; Freitas, M. A.; Hendrickson, C. L.; Marshall, A. G., Comparison and Interconversion of the Two Most Common Frequency-to-Mass Calibration Functions for Fourier Transform Ion Cyclotron Resonance Mass Spectrometry. *Int. J. Mass Spectrom.* **2000,** *195–196* (0), 591-598.
121. Flora, J. W.; Hannis, J. C.; Muddiman, D. C., High-Mass Accuracy of Product Ions Produced by SORI-CID Using a Dual Electrospray Ionization Source Coupled with FTICR Mass Spectrometry. *Anal. Chem.* **2001,** *73* (6), 1247-1251.
122. Belov, M. E.; Zhang, R.; Strittmatter, E. F.; Prior, D. C.; Tang, K.; Smith, R. D., Automated Gain Control and Internal Calibration with External Ion Accumulation Capillary Liquid Chromatography-Electrospray Ionization-Fourier Transform Ion Cyclotron Resonance. *Anal. Chem.* **2003,** *75* (16), 4195-4205.

123. Jeffries, J. B.; Barlow, S. E.; Dunn, G. H., Theory of Space-Charge Shift of Ion Cyclotron Resonance Frequencies. *Int. J. Mass Spectrom. Ion Processes* **1983,** *54* (1–2), 169-187.
124. Easterling, M. L.; Mize, T. H.; Amster, I. J., Routine Part-Per-Million Mass Accuracy for High-Mass Ions: Space-Charge Effects in MALDI FT-ICR. *Anal. Chem.* **1999,** *71* (3), 624-632.
125. Taylor, P. K.; Amster, I. J., Space Charge Effects on Mass Accuracy for Multiply Charged ions in ESI–FTICR. *Int. J. Mass Spectrom.* **2003,** *222* (1–3), 351-361.
126. Aizikov, K.; Mathur, R.; O'Connor, P. B., The Spontaneous Loss of Coherence Catastrophe in Fourier Transform Ion Cyclotron Resonance Mass Spectrometry. *J. Am. Soc. Mass Spectrom.* **2009,** *20* (2), 247-256.
127. Aizikov, K.; O'Connor, P. B., Use of the Filter Diagonalization Method in the Study of Space Charge Related Frequency Modulation in Fourier Transform Ion Cyclotron Resonance Mass Spectrometry. *J. Am. Soc. Mass Spectrom.* **2006,** *17* (6), 836-843.
128. Masselon, C.; Tolmachev, A. V.; Anderson, G. A.; Harkewicz, R.; Smith, R. D., Mass Measurement Errors Caused by “Local” Frequency Perturbations in FTICR Mass Spectrometry. *J. Am. Soc. Mass Spectrom.* **2002,** *13* (1), 99-106.
129. Wong, R. L.; Amster, I. J., Experimental Evidence for Space-Charge Effects between Ions of the Same Mass-to-Charge in Fourier-Transform Ion Cyclotron Resonance Mass Spectrometry. *Int. J. Mass Spectrom.* **2007,** *265* (2–3), 99-105.
130. Wineland, D. J.; Dehmelt, H. G., Principles of the Stored Ion Calorimeter. *J. Appl. Phys.* **1975,** *46* (2), 919-930.
131. Muddiman, D. C.; Oberg, A. L., Statistical Evaluation of Internal and External Mass Calibration Laws Utilized in Fourier Transform Ion Cyclotron Resonance Mass Spectrometry. *Anal. Chem.* **2005,** *77* (8), 2406-2414.
132. Williams, D. K.; Muddiman, D. C., Parts-Per-Billion Mass Measurement Accuracy Achieved through the Combination of Multiple Linear Regression and Automatic Gain Control in a Fourier Transform Ion Cyclotron Resonance Mass Spectrometer. *Anal. Chem.* **2007,** *79* (13), 5058-5063.

133. O'Connor, P. B.; Costello, C. E., Internal Calibration on Adjacent Samples (InCAS) with Fourier Transform Mass Spectrometry. *Anal. Chem.* **2000,** *72* (24), 5881-5885.
134. B. Cody, R. Method for External Calibration of Ion Cyclotron Resonance Mass Spectrometers. United States Patent 4933547, 2012/04/21, 1990.
135. Williams Jr, D. K.; Chadwick, M. A.; Williams, T. I.; Muddiman, D. C., Calibration Laws based on Multiple Linear Regression Applied to Matrix-Assisted Laser Desorption/Ionization Fourier Transform Ion Cyclotron Resonance Mass Spectrometry. *J. Mass Spectrom.* **2008,** *43* (12), 1659-1663.
136. Smith, D.; Kharchenko, A.; Konijnenburg, M.; Klinkert, I.; Paša-Tolić, L.; Heeren, R. A., Advanced Mass Calibration and Visualization for FT-ICR Mass Spectrometry Imaging. *J. Am. Soc. Mass Spectrom.* **2012,** *23* (11), 1865-1872.
137. Chen, R.; Cheng, X.; Mitchell, D. W.; Hofstadler, S. A.; Wu, Q.; Rockwood, A. L.; Sherman, M. G.; Smith, R. D., Trapping, Detection, and Mass Determination of Coliphage T4 DNA Ions by Electrospray Ionization Fourier Transform Ion Cyclotron Resonance Mass Spectrometry. *Anal. Chem.* **1995,** *67* (7), 1159-1163.
138. Kaiser, N.; Quinn, J.; Blakney, G.; Hendrickson, C.; Marshall, A., A Novel 9.4 Tesla FTICR Mass Spectrometer with Improved Sensitivity, Mass Resolution, and Mass Range. *J. Am. Soc. Mass Spectrom.* **2011,** *22* (8), 1343-1351.
139. Laukien, F. H., The Effects of Residual Spatial Magnetic Field Gradients on Fourier Transform Ion Cyclotron Resonance Spectra. *Int. J. Mass Spectrom. Ion Processes* **1986,** *73* (1–2), 81-107.
140. Natarajan, V., Penning Trap Mass Spectroscopy at 0.1 ppb. **1993**.
141. Nikolaev, E. N.; Gorshkov, M. V., Dynamics of Ion Motion in an Elongated Cylindrical Cell of an ICR Spectrometer and the Shape of the Signal Registered. *Int. J. Mass Spectrom. Ion Processes* **1985,** *64* (2), 115-125.
142. Pan, Y.; Ridge, D. P.; Rockwood, A. L., Harmonic Signal Enhancement in Ion Cyclotron Resonance Mass Spectrometry using Multiple Electrode Detection. *Int. J. Mass Spectrom. Ion Processes* **1988,** *84* (3), 293-304.
143. Hendrickson, C.; Beu, S.; Laude, D., Two-Dimensional Coulomb-Induced Frequency Modulation in Fourier Transform Ion Cyclotron

Resonance: A Mechanism for Line Broadening at High Mass and for Large Ion Populations. *J. Am. Soc. Mass Spectrom.* **1993,** *4* (12), 909-916.

144. Mathur, R.; O'Connor, P. B., Artifacts in Fourier Transform Mass Spectrometry. *Rapid Commun. Mass Spectrom.* **2009,** *23* (4), 523-529.

145. Zhang, L.-K.; Rempel, D.; Pramanik, B. N.; Gross, M. L., Accurate Mass Measurements by Fourier Transform Mass Spectrometry. *Mass Spectrom. Rev.* **2005,** *24* (2), 286-309.

146. Chow, K. H.; Comisarow, M. B., Frequency (Mass) Errors and Phase Dependence in Magnitude-Mode Apodized Fourier Transform--Ion Cyclotron Resonance Spectra. *Int. J. Mass Spectrom. Ion Processes* **1989,** *89* (2-3), 187-203.

147. Kaur, P.; O'Connor, P., Algorithms for Automatic Interpretation of High Resolution Mass Spectra. *J. Am. Soc. Mass Spectrom.* **2006,** *17* (3), 459-468.

148. Schmidt, A.; Gehlenborg, N.; Bodenmiller, B.; Mueller, L. N.; Campbell, D.; Mueller, M.; Aebersold, R.; Domon, B., An Integrated, Directed Mass Spectrometric Approach for In-Depth Characterization of Complex Peptide Mixtures. *Mol. Cell. Proteomics* **2008,** *7* (11), 2138-2150.

149. Brown, S. C.; Kruppa, G.; Dasseux, J.-L., Metabolomics Applications of FT-ICR Mass Spectrometry. *Mass Spectrom. Rev.* **2005,** *24* (2), 223-231.

150. Marshall, A. G.; Guan, S. H., Advantages of High Magnetic Field For Fourier Transform Ion Cyclotron Resonance Mass Spectrometry. *Rapid Commun. Mass Spectrom.* **1996,** *10* (14), 1819-1823.

151. Kaiser, N.; Skulason, G.; Weisbrod, C.; Bruce, J., A Novel Fourier Transform Ion Cyclotron Resonance Mass Spectrometer with Improved Ion Trapping and Detection Capabilities. *J. Am. Soc. Mass Spectrom.* **2009,** *20* (5), 755-762.

152. Brustkern, A.; Rempel, D.; Gross, M., An Electrically Compensated Trap Designed to Eighth Order for FT-ICR Mass Spectrometry. *J. Am. Soc. Mass Spectrom.* **2008,** *19* (9), 1281-1285.

153. Mathur, R.; O'Connor, P. B., Design and Implementation of a High Power RF Oscillator on a Printed Circuit Board for Multipole Ion Guides. *Rev. Sci. Instrum.* **2006,** *77* (11), 114101-114101-7.

154. Mathur, R.; Knepper, R.; O'Connor, P., A Low-Noise, Wideband Preamplifier for a Fourier-Transform Ion Cyclotron Resonance Mass Spectrometer. *J. Am. Soc. Mass Spectrom.* **2007,** *18* (12), 2233-2241.
155. Guo, X.; Duursma, M.; Al-Khalili, A.; McDonnell, L. A.; Heeren, R. M. A., Design and Performance of a New FT-ICR Cell Operating at a Temperature Range of 77-438 K. *Int. J. Mass Spectrom.* **2004,** *231* (1), 37-45.
156. Lin, T. Y.; Green, R. J.; O'Connor, P. B., A gain and Bandwidth Enhanced Transimpedance Preamplifier for Fourier-Transform Ion Cyclotron Resonance Mass Spectrometry. *Rev. Sci. Instrum.* **2011,** *82* (12), 124101.
157. Blakney, G. T.; Hendrickson, C. L.; Marshall, A. G., Predator Data Station: A Fast Data Acquisition System for Advanced FT-ICR MS Experiments. *Int. J. Mass Spectrom.* **2011,** *306* (2-3), 246-252.
158. Senko, M. W.; Canterbury, J. D.; Guan, S. H.; Marshall, A. G., A High-Performance Modular Data System For Fourier Transform Ion Cyclotron Resonance Mass Spectrometry. *Rapid Commun. Mass Spectrom.* **1996,** *10* (14), 1839-1844.
159. Klerk, L. A.; Broersen, A.; Fletcher, I. W.; van Liere, R.; Heeren, R. M. A., Extended Data Analysis Strategies for High Resolution Imaging MS: New Methods to Deal with Extremely Large Image Hyperspectral Datasets. *Int. J. Mass Spectrom.* **2007,** *260* (2-3), 222-236.
160. Taban, I. M.; van der Burgt, Y. E. M.; Duursma, M.; Takáts, Z.; Seynen, M.; Konijnenburg, M.; Vijftigschild, A.; Attema, I.; Heeren, R. M. A., A Novel Workflow Control System for Fourier Transform Ion Cyclotron Resonance Mass Spectrometry Allows for Unique on-the-fly Data-Dependent Decisions. *Rapid Commun. Mass Spectrom.* **2008,** *22* (8), 1245-1256.
161. Kaur, P.; O'Connor, P. B., Quantitative Determination of Isotope Ratios from Experimental Isotopic Distributions. *Anal. Chem.* **2007,** *79* (3), 1198-1204.
162. Comisarow, M. B., Comprehensive Theory for ICR Power Absorption: Applications to Line Shapes for Reactive and Non-Reactive Ions. *J. Chem. Phys.* **1971,** *55*, 205-217.
163. Marshall, A. G., Theory for Ion Cyclotron Resonance Absorption Line Shapes. *J. Chem. Phys.* **1971,** *55*, 1343-1354.

164. Xian, F.; Hendrickson, C. L.; Blakney, G. T.; Beu, S. C.; Marshall, A. G., Effects of Zero-Filling and Apodization on Absorption-Mode FT-ICR Mass Spectra. In *59th ASMS Conference on Mass Spectrometry & Allied Topics*, Denver, CO, USA, 2011.

165. Wills, R.; Habtemariam, A.; Sadler, P. J.; O'Connor, P., Mapping the Binding Sites of Organometallic Ruthenium Anticancer Compounds on Peptides using FTICR Mass Spectrometry. *J. Am. Soc. Mass Spectrom.* **2012**, submitted.

166. Grothe, R. A. Esitimation of Ion Cyclotron Resonance Parameters in Fourier Transform Mass Spectrometry. Patent 20090278037A1, 2009.

167. Rockwood, A. L.; Van Orden, S. L.; Smith, R. D., Rapid Calculation of Isotope Distributions. *Anal. Chem.* **1995,** *67* (15), 2699-2704.

168. Barrow, M. P.; Witt, M.; Headley, J. V.; Peru, K. M., Athabasca Oil Sands Process Water: Characterization by Atmospheric Pressure Photoionization and Electrospray Ionization Fourier Transform Ion Cyclotron Resonance Mass Spectrometry. *Anal. Chem.* **2010,** *82* (9), 3727-3735.

169. Savory, J. J.; Kaiser, N. K.; McKenna, A. M.; Xian, F.; Blakney, G. T.; Rodgers, R. P.; Hendrickson, C. L.; Marshall, A. G., Parts-Per-Billion Fourier Transform Ion Cyclotron Resonance Mass Measurement Accuracy with a "Walking" Calibration Equation. *Anal. Chem.* **2011,** *83* (5), 1732-1736.

170. Weisbrod, C. R.; Kaiser, N. K.; Skulason, G. E.; Bruce, J. E., Excite-Coupled Trapping Ring Electrode Cell (eTREC): Radial Trapping Field Control, Linearized Excitation, And Improved Detection. *Anal. Chem.* **2010,** *82* (14), 6281-6286.

171. Ledford Jr., E. B.; Ghaderi, S.; White, R. L.; SpencerR.B.; Kulkarni, P. S.; Wilkins, C. L.; Gross, M. L., Exact Mass Measurement by Fourier Transform Mass Spectrometry. *Anal. Chem.* **1980,** *52* (3), 463-468.

172. O'Connor, P. B.; Speir, J. P.; Senko, M. W.; Little, D. P.; McLafferty, F. W., Tandem Mass Specatrometry of Carbonic Anhydrase (29 kDa). *J. Mass Spectrom.* **1995,** *30* (1), 88-93.

173. Kelleher, N. L., Peer Reviewed: Top-Down Proteomics. *Anal. Chem.* **2004,** *76* (11), 196 A-203 A.

174. Horn, D. M.; Zubarev, R. A.; McLafferty, F. W., Automated Reduction and Interpretation of High Resolution Electrospray Mass Spectra of Large Molecules. *J. Am. Soc. Mass Spectrom.* **2000,** *11* (4), 320-32.
175. Perez-Hurtado, P.; O'Connor, P. B., Deamidation of Collagen. *Anal. Chem.* **2012,** *84* (6), 3017-3025.
176. Li, H.; Zhao, Y.; Phillips, H. I. A.; Qi, Y.; Lin, T.-Y.; Sadler, P. J.; O'Connor, P. B., Mass Spectrometry Evidence for Cisplatin As a Protein Cross-Linking Reagent. *Anal. Chem.* **2011,** *83* (13), 5369-5376.
177. Li, H.; Lin, T.-Y.; Van Orden, S. L.; Zhao, Y.; Barrow, M. P.; Pizarro, A. M.; Qi, Y.; Sadler, P. J.; O'Connor, P. B., Use of Top-Down and Bottom-Up Fourier Transform Ion Cyclotron Resonance Mass Spectrometry for Mapping Calmodulin Sites Modified by Platinum Anticancer Drugs. *Anal. Chem.* **2011,** *83* (24), 9507-9515.
178. Li, X.; Yu, X.; Costello, C. E.; Lin, C.; O'Connor, P. B., Top-Down Study of β2-Microglobulin Deamidation. *Anal. Chem.* **2012,** *84* (14), 6150-6157.
179. König, S.; Fales, H. M., Calibration of Mass Ranges up to *m/z* 10,000 in Electrospray Mass Spectrometers. *J. Am. Soc. Mass Spectrom.* **1999,** *10* (3), 273-276.
180. Hannis, J.; Muddiman, D., A Dual Electrospray Ionization Source Combined with Hexapole Accumulation to Achieve High Mass Accuracy of Biopolymers in Fourier Transform Ion Cyclotron Resonance Mass Spectrometry. *J. Am. Soc. Mass Spectrom.* **2000,** *11* (10), 876-883.
181. Loo, J. A., Studying Noncovalent Protein Complexes by Electrospray Ionization Mass Spectrometry. *Mass Spectrom. Rev.* **1997,** *16* (1), 1-23.
182. Habtemariam, A.; Melchart, M.; Fernández, R.; Parsons, S.; Oswald, I. D. H.; Parkin, A.; Fabbiani, F. P. A.; Davidson, J. E.; Dawson, A.; Aird, R. E.; Jodrell, D. I.; Sadler, P. J., Structure−Activity Relationships for Cytotoxic Ruthenium(II) Arene Complexes Containing N,N-, N,O-, and O,O-Chelating Ligands. *J. Med. Chem.* **2006,** *49* (23), 6858-6868.
183. Leymarie, N.; Costello, C. E.; O'Connor, P. B., Electron Capture Dissociation Initiates a Free Radical Reaction Cascade. *J. Am. Chem. Soc.* **2003,** *125* (29), 8949-8958.

184. O'Connor, P. B.; Lin, C.; Cournoyer, J. J.; Pittman, J. L.; Belyayev, M.; Budnik, B. A., Long-Lived Electron Capture Dissociation Product Ions Experience Radical Migration via Hydrogen Abstraction. *J. Am. Soc. Mass Spectrom.* **2006,** *17* (4), 576-585.

185. Perez-Hurtado, P.; O'Connor, P. B., Differentiation of Isomeric Amino Acid Residues in Proteins and Peptides using Mass Spectrometry. *Mass Spectrom. Rev.* **2012,** *31* (6), 609-625.

186. Melvin B, C., Cubic Trapped-Ion Cell for Ion Cyclotron Resonance. *International Journal of Mass Spectrometry and Ion Physics* **1981,** *37* (2), 251-257.

187. Kofel, P.; Allemann, M.; Kellerhals, H.; Wanczek, K. P., Coupling of Axial and Radial Motions in ICR Cells during Excitation. *Int. J. Mass Spectrom. Ion Processes* **1986,** *74* (1), 1-12.

188. Gabrielse, G.; Haarsma, L.; Rolston, S. L., Open-Endcap Penning Traps for High Precision Experiments. *Int. J. Mass Spectrom. Ion Processes* **1989,** *88* (2–3), 319-332.

189. Tolmachev, A.; Robinson, E.; Wu, S.; Kang, H.; Lourette, N.; Paša-Tolić, L.; Smith, R., Trapped-Ion Cell with Improved DC Potential Harmonicity for FT-ICR MS. *J. Am. Soc. Mass Spectrom.* **2008,** *19* (4), 586-597.

190. Rockwood, A. L.; Van Orden, S. L.; Smith, R. D., Ultrahigh Resolution Isotope Distribution Calculations. *Rapid Commun. Mass Spectrom.* **1996,** *10* (1), 54-59.

191. Nikolaev, E. N.; Miluchihin, N. V.; Inoue, M., Evolution of an Ion Cloud in a Fourier Transform Ion Cyclotron Resonance Mass Spectrometer during Signal Detection: its Influence on Spectral Line Shape and Position. *Int. J. Mass Spectrom. Ion Processes* **1995,** *148* (3), 145-157.

192. Schweikhard, L.; Marshall, A., Excitation Modes for Fourier Transform-Ion Cyclotron Resonance Mass Spectrometry. *J. Am. Soc. Mass Spectrom.* **1993,** *4* (6), 433-452.

193. McIver Jr, R. T.; Hunter, R. L.; Bowers, W. D., Coupling a Quadrupole Mass Spectrometer and a Fourier Transform Mass Spectrometer. *Int. J. Mass Spectrom. Ion Processes* **1985,** *64* (1), 67-77.

194. Wang, D.; Lippard, S. J., Cellular Processing of Platinum Anticancer Drugs. *Nat. Rev. Drug Discov.* **2005,** *4* (4), 307-320.
195. Kelland, L., The Resurgence of Platinum-Based Cancer Chemotherapy. *Nat. Rev. Cancer* **2007,** *7* (8), 573-584.
196. Hu, W.; Luo, Q.; Wu, K.; Li, X.; Wang, F.; Chen, Y.; Ma, X.; Wang, J.; Liu, J.; Xiong, S.; Sadler, P. J., The Anticancer Drug Cisplatin can Cross-Link the Interdomain Zinc Site on Human Albumin. *Chem. Commun.* **2011,** *47* (21), 6006-6008.
197. Safaei, R.; Howell, S. B., Copper Transporters Regulate the Cellular Pharmacology and Sensitivity to Pt drugs. *Crit. Rev. Oncol. Hematol.* **2005,** *53* (1), 13-23.
198. Meggers, E., Exploring Biologically Relevant Chemical Space with Metal Complexes. *Curr. Opin. Chem. Biol.* **2007,** *11* (3), 287-292.
199. Peacock, A. F. A.; Habtemariam, A.; Moggach, S. A.; Prescimone, A.; Parsons, S.; Sadler, P. J., Chloro Half-Sandwich Osmium(II) Complexes: Influence of Chelated N,N-Ligands on Hydrolysis, Guanine Binding, and Cytotoxicity. *Inorg. Chem.* **2007,** *46* (10), 4049-4059.
200. Scolaro, C.; Chaplin, A. B.; Hartinger, C. G.; Bergamo, A.; Cocchietto, M.; Keppler, B. K.; Sava, G.; Dyson, P. J., Tuning the Hydrophobicity of Ruthenium(ii)-Arene (RAPTA) Drugs to Modify Uptake, Biomolecular Interactions and Efficacy. *Dalton Trans.* **2007,** (43), 5065-5072.
201. Richens, D. T., Ligand Substitution Reactions at Inorganic Centers. *Chem. Rev.* **2005,** *105* (6), 1961-2002.
202. Liu, Z.; Habtemariam, A.; Pizarro, A. M.; Fletcher, S. A.; Kisova, A.; Vrana, O.; Salassa, L.; Bruijnincx, P. C. A.; Clarkson, G. J.; Brabec, V.; Sadler, P. J., Organometallic Half-Sandwich Iridium Anticancer Complexes. *J. Med. Chem.* **2011,** *54* (8), 3011-3026.
203. Liu, Z.; Salassa, L.; Habtemariam, A.; Pizarro, A. M.; Clarkson, G. J.; Sadler, P. J., Contrasting Reactivity and Cancer Cell Cytotoxicity of Isoelectronic Organometallic Iridium(III) Complexes. *Inorg. Chem.* **2011,** *50* (12), 5777-5783.
204. Liu, Z.; Habtemariam, A.; Pizarro, A. M.; Clarkson, G. J.; Sadler, P. J., Organometallic Iridium(III) Cyclopentadienyl Anticancer Complexes Containing C,N-Chelating Ligands. *Organometallics.* **2011,** *30* (17), 4702-4710.

205. Kröning, R.; Lichtenstein, A. K.; Nagami, G. T., Sulfur-Containing Amino Acids Decrease Cisplatin Cytotoxicity and Uptake in Renal Tubule Epithelial Cell Lines. *Cancer Chemother. Pharmacol.* **2000,** *45* (1), 43-49.
206. Ivanov, A. I.; Christodoulou, J.; Parkinson, J. A.; Barnham, K. J.; Tucker, A.; Woodrow, J.; Sadler, P. J., Cisplatin Binding Sites on Human Albumin. *J. Biol. Chem.* **1998,** *273* (24), 14721-14730.
207. Tsybin, Y.; Quinn, J.; Tsybin, O.; Hendrickson, C.; Marshall, A., Electron Capture Dissociation Implementation Progress in Fourier Transform Ion Cyclotron Resonance Mass Spectrometry. *J. Am. Soc. Mass Spectrom.* **2008,** *19* (6), 762-771.
208. Belov, M.; Gorshkov, M.; Udseth, H.; Smith, R., Controlled Ion Fragmentation in a 2-D Quadrupole Ion Trap for External Ion Accumulation in ESI FTICR Mass Spectrometry. *J. Am. Soc. Mass Spectrom.* **2001,** *12* (12), 1312-1319.
209. Zubarev, R. A.; Horn, D. M.; Fridriksson, E. K.; Kelleher, N. L.; Kruger, N. A.; Lewis, M. A.; Carpenter, B. K.; McLafferty, F. W., Electron Capture Dissociation for Structural Characterization of Multiply Charged Protein Cations. *Anal. Chem.* **2000,** *72* (3), 563-573.
210. Zubarev, R. A., Reactions of Polypeptide Ions with Electrons in the Gas Phase. *Mass Spectrom. Rev.* **2003,** *22* (1), 57-77.
211. Kelleher, N. L.; Lin, H. Y.; Valaskovic, G. A.; Aaserud, D. J.; Fridriksson, E. K.; McLafferty, F. W., Top Down versus Bottom Up Protein Characterization by Tandem High-Resolution Mass Spectrometry. *J. Am. Chem. Soc.* **1999,** *121* (4), 806-812.
212. Li, H.; Wells, S. A.; Jimenez-Roldan, J. E.; Römer, R. A.; Zhao, Y.; Sadler, P. J.; O'Connor, P. B., Protein Flexibility is Key to Cisplatin Crosslinking in Calmodulin. *Protein Sci.* **2012,** *21* (9), 1269-1279.